MPM SCIENTIFIC JOURNAL

ISSN 1605-2730
E-ISSN 1605-8119

MATERIALS PHYSICS AND MECHANICS

Vol. 53, No. 4, 2025

MATERIALS PHYSICS AND MECHANICS

"Materials Physics and Mechanics" Editorial Office:
Phone: +7(812)552 77 78, ext. 224 **E-mail:** mpmjournal@spbstu.ru **Web-site:** http://www.mpm.spbstu.ru

International scientific journal "**Materials Physics and Mechanics**" is published by Peter the Great St. Petersburg Polytechnic University in collaboration with Institute for Problems for Mechanical Engineering in the Russian Academy of Sciences in both hard copy and electronic versions. The journal provides an international medium for the publication of reviews and original research papers written in English and focused on the following topics:

- Mechanics of composite and nanostructured materials.
- Physics of strength and plasticity of composite and nanostructured materials.
- Mechanics of deformation and fracture processes in conventional materials (solids).
- Physics of strength and plasticity of conventional materials (solids).
- Physics and mechanics of defects in composite, nanostructured, and conventional materials.
- Mechanics and physics of materials in coupled fields.

Owner organizations: Peter the Great St. Petersburg Polytechnic University; Institute of Problems of Mechanical Engineering RAS.

Materials Physics and Mechanics is indexed in Chemical Abstracts, Cambridge Scientific Abstracts, Web of Science Emerging Sources Citation Index (ESCI) and Elsevier Bibliographic Databases (in particular, SCOPUS).

МЕХАНИКА И ФИЗИКА МАТЕРИАЛОВ

Materials Physics and Mechanics

Том 53, номер 4, 2025 год

Учредители:
ФГАОУ ВО «Санкт-Петербургский политехнический университет Петра Великого»
ФГБУН «Институт проблем машиноведения Российской академии наук»

Тел.: +7(812)552 77 78, доб. 224 **E-mail:** mpmjournal@spbstu.ru **Web-site:** http://www.mpm.spbstu.ru

Тематика журнала

Международный научный журнал "Materials Physics and Mechanics" издается Санкт-Петербургским политехническим университетом Петра Великого в сотрудничестве с Институтом проблем машиноведения Российской академии наук в печатном виде и электронной форме. Журнал публикует обзорные и оригинальные научные статьи на английском языке по следующим тематикам:

- Механика композиционных и наноструктурированных материалов.
- Физика прочности и пластичности композиционных и наноструктурированных материалов.
- Механика процессов деформации и разрушения в традиционных материалах (твердых телах).
- Физика прочности и пластичности традиционных материалов (твердых тел).
- Физика и механика дефектов в композиционных, наноструктурированных и традиционных материалах.
- Механика и физика материалов в связанных полях.

Редколлегия принимает статьи, которые нигде ранее не опубликованы и не направлены для опубликования в другие научные издания. Все представляемые в редакцию журнала "Механика и физика материалов" статьи рецензируются. Статьи могут отправляться авторам на доработку. Не принятые к опубликованию статьи авторам не возвращаются.

Журнал "Механика и физика материалов" ("Materials Physics and Mechanics") включен в систему цитирования Web of Science Emerging Sources Citation Index (ESCI), SCOPUS и РИНЦ.

Contents

MATERIALS PHYSICS AND MECHANICS RESEARCH ARTICLE

Submitted: April 24, 2025 **Revised: July 21, 2025** **Accepted: August 11, 2025**

Experimental investigations on the milling characteristics of Cu alloys and additively manufactured CuCrZr

S.R. Mundla [1], S. Arungalai Vendan [2] ✉, C.P. Paul [3], A.K. Shettigar [1], S.C. Jambagi [1]

[1] National Institute of Technology Karnataka, Surathkal, India

[2] Department of Electronics and Communication, Dayananda Sagar University, Bangalore, India

[3] Raja Ramana Centre for Advanced Technology, Indore, India

✉ arungalaisv@yahoo.co.in

ABSTRACT

Copper is one of the widely used materials in various fields such as automotive, electronics, aviation, etc. The inherent property of copper makes it useful in wide variety of applications. The features on different components using the copper material can be made using different manufacturing techniques. However, post processing is one of the inevitable steps in any manufacturing process. Machining is one of the widely used post processing. There are multiple varieties of milling process. Among them, end milling process is widely used for making the slots. Three important process parameters in end milling process are depth of cut, cutting rate and feed rate. In this experimental approach, the copper is subjected to end milling operation by varying the aforementioned input parameters. In this fast-moving world, any manufacturing industry aims to produce the features with good dimensional accuracy with minimal amount of tool wear. Hence, the output responses selected are surface roughness and the tool wear. This research investigates the machining behavior of pure copper (Cu) and additively produced CuCrZr alloys to assess how fabrication methods affect processability. Pure copper, recognized for exceptional thermal / electrical conductivity, is compared against additively manufactured CuCrZr, which retains copper's advantages while offering improved strength and wear resistance through alloy composition. During the milling process the following parameters such surface quality, cutting forces, tool degradation, and removal rates are reviewed through proper analysis. Compared to commercial copper, CuCrZr is more difficult to machine because it requires precise control over machining parameters to attain superior surface quality during milling. It is found that the CS and FR parameters balance material removal rate while controlling surface quality in both materials. As–built CuCrZr finds demand in high–performance applications such as heat exchangers, rocket engine components, and electrical contacts wherein strength, excellent thermal conductivity and additive manufacturability are critical.

KEYWORDS

CuCrZr • milling • as built • surface roughness • depth of cut

Citation: Mundla SR, Arungalai Vendan S, Paul P, Shettigar AK, Jambagi SC. Experimental investigations on the milling characteristics Cu alloys and additively manufactured. *Materials Physics and Mechanics*. 2025;53(4): 1–21.
http://dx.doi.org/10.18149/MPM.5342025_1

Introduction

Widespread usage of copper across multiple industrial sectors is due to unique metal properties such as electrical conductivity, malleability, and thermal conductivity. In manufacturing, copper is employed in the production of industrial machinery [1], precision instruments, and heat exchangers. The transportation sector also depends on copper for the construction of vehicle radiators [2] and braking systems [3].

Machining copper presents numerous challenges due to thermal and electrical properties of the material. Copper is utilized majorly in various applications due to its electrical and thermal conductivity, plasticity, and elongation [4,5]. Notable complications are observed during the machining process of copper due to its electrical properties and the properties of softness and ductility. Optimal choice of tools and machining techniques and process parameters is imperative to minimise tool degradation, distortion, burr development and retain accurate dimension. Copper's maximum heat transfer capability develops complications during the time of machining, resulting in loss of material's integrity and tool degradation. Thermal management becomes essential by adopting efficient lubricant and coolant systems. Copper is susceptible to built-up edge (BUE) formation as it shows tendency to bond with cutting tool surfaces. Necessity for specialized tool coatings and optimized cutting velocities arises due to the occurrence of BUE, which results in acceleration of tool wear and degradation of surface quality [6]. It is difficult to process copper with significant advantages due to the following properties such as softness and malleability. Manufacturing techniques such as drilling, milling and turning are used for the fabrication of accurate components mostly used in safety critical application in aerospace domain. Maintaining a balance is essential during the copper matching due to copper's physical complexity for achieving appropriate integrity and accurate dimension for usage across various industrial sectors.

Machining procedures play a vital role in customizing copper (Cu) components for versatile applications across various spectrum of industries. Different techniques are deployed, each demonstrating its unique pros and cons. Machining processes classified under mechanical, facilitates the removal of material through mechanical modes, are widely adopted in copper machining. These processes involve drilling, turning, grinding, and milling. Milling is a machining technique that uses rotary cutters to remove material out of the workpiece. Milling offers several advantages while placing it as a preferred choice for Cu machining. It illustrates high precision, allowing for ease of fabrication of intricate shapes and profiles [7]. Besides, milling yields exceptional surface finishes, thereby eliminating any supplementary finishing procedures [8]. It illustrates high efficiency, and is well-suited for large scale production [9]. Advancements in tooling and cutting techniques have enhanced the tool life. Additionally, milling demonstrates adaptability through end and face milling, that offers distinct advantages. End milling, engages the bottom of the cutter, whereas face milling comprises of cutting with the sides of the cutter [10,11]. This features places milling as a potential machining process to handle a diverse range of tasks, that comprises machining flat surfaces, complex profiles and slots [12].

End milling presents is a prominent technique for the required ablation from raw materials. The variations of the key process parameters, controls the end milling of additively manufactured copper [13]. These parameters play a crucial role in the outcome of the machining process. Typically, a higher cutting speed (CS) can improve material removal efficiency and minimize tool contact time, thereby enhancing the surface finish. Optimizing the feed rate (FR) has the potential to influence tool wear and chip evacuation. Optimizing these parameters is essential to ensure efficient and precise machining. Tool wear and machined product evenness, measured in the form of roughness are important in the end milling for additively manufactured copper [14,15]. Lower surface roughness

is preferred as it facilitates production of smoother and more precise parts. The tool wear impacts the tool longevity and the efficiency of the machining process. Higher tool wear forces frequent tool changes, leading to increased downtime and incurs additional costs. Henceforth it is imperative to monitor and regulate tool wear and surface roughness to attain successful end milling product.

After detailed literature survey, it may be observed that minimal work is presented on optimizing the end milling process parameters for copper-based materials. Hence, in this study, the copper is subjected to end milling operation by varying three input parameters. The input process parameters are varied in five levels. The impact of input parameters on the tool condition and product quality is reported. Further, Cu Cr Zr is additively manufactured and milling experiments are performed similar to those performed or Cu. The comparative results are presented in the paper. The experiments are designed based on the central composite rotable design technique.

Materials and Methods

The end milling experiments are carried out on the copper plate. During experimentation, steel tools with a wide speed range are deployed for the machining or ablation operation. FR, CS, and depth of cut (DoC) varied during the experimentations, and the tool wear and surface roughness are calculated. A systematic approach that considers the material properties and intended process outputs is considered when choosing machining settings for milling commercial copper (Cu) and CuCrZr that has been additively produced. The foundation for parameter selection also accounts for the milling behaviour of commercial copper and Cu Cr Zr alloys, such as the impact of process parameters on the resultant microstructures. Additionally, mechanical, thermal, and physical properties of the material are carefully examined, as are material-specific factors like porosity, work hardening, and anisotropy. The process parameter window is then fine-tuned by preliminary trials, and performance is subsequently optimized using structured experiments utilizing Taguchi factorial design. The parametric range is selected based on the tool catalogue and the initial preliminary trials calculated based on trial and error. Subsequently, the parameters are chosen from optimized parametric window based on the data obtained from the experiments. Consequently, the trials are carried out based on the central composite rotable methodology. Input process parameters are varied in five levels during the experimentation. Each experiment with a specific parametric set up

Fig. 1. Cu sample after milling operations

is repeated thrice, and the mean value is reported. The surface roughness is measured using a 3D profilometer (Make: Bruker) and the tool wear is estimated using the optical microscope (Make: Leica). Figure 1 shows the Cu sample after milling operations are performed.

Preliminary experimentation

The primary objective of the initial/preliminary experimentation is to determine the optimal range of the parameters in which the responses are effective. It is observed from the literature that FR has the most significant parameter that influences the product surface quality followed by CS and DoC. The variation of the FR during experimentation is in accordance to the tool makers catalogue. It is desirable to obtain the least surface roughness for the applications. It may be concluded that the range in which the FR can be varied may lie between 100 to 250 m/min.

Influence of FR on machined surface

The linear speed at which the cutting tool (represented by FR) moves along the workpiece during the process of milling, influences the resulting surface roughness in copper machining. Figure 2 provides valuable insights into the dependency of surface roughness on the FR with the key objective being the attainment of lower surface roughness, a major consideration in precision machining.

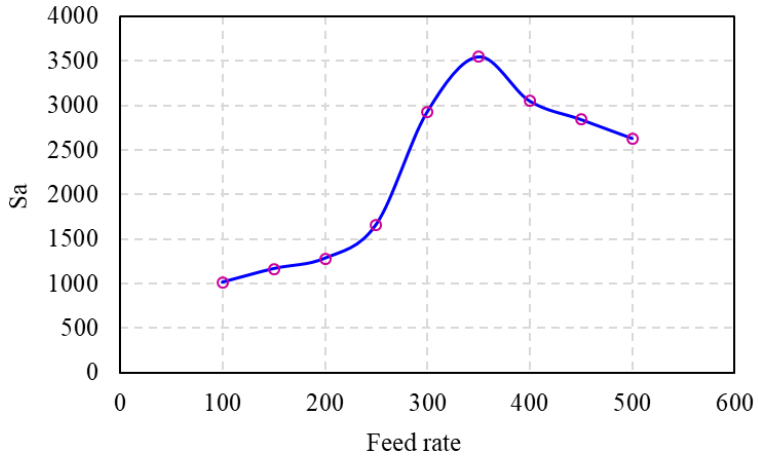

Fig. 2. Effect of FR on the 3D average S_a

From Fig. 2, it can be observed that mean S_a (machine surface quality) is increasing with the increase in FR from 100 to 350 m/min and then progressively decreases as the FR is increased to 500 m/min. This clearly indicates that higher FRs yield smoother surface finishes. It may also be noted that within the data, there is an occurrence of a peak in surface roughness at an intermediate FR, specifically at 350 m/min, where S_a reaches 3551.55 nm. This suggests that there exists an optimal range of FRs that minimizes surface roughness. Increasing the FR beyond this optimal point, may result in rougher surfaces due to factors such as increase tool wear or increased cutting forces, indicating a subtle balance between FR and surface finish.

Influence of CS on machine surface quality

3D surface roughness is measured and recorded using optical metrology tools by capturing the height variation (*z*-axis) across a defined area (*x*-*y* plane) of the sample surface. These values of height are processed to calculate area surface roughness parameters according to standards. CS (rpm) controls the resulting surface roughness in the machining processes of copper. Figure 3 shows the influence of CS on the average Sa. It is observed from the figure that the average Sa drops down with rise in CS from 950 to 2500 rpm and then decreases further as the CS is increased to 3000. Subsequently, a declining trend may be observed as the CS increases to 3500 rpm. It is preferred to obtain the least surface roughness for the applications. Therefore, the FR range can be varied between 500 to 3000 rpm.

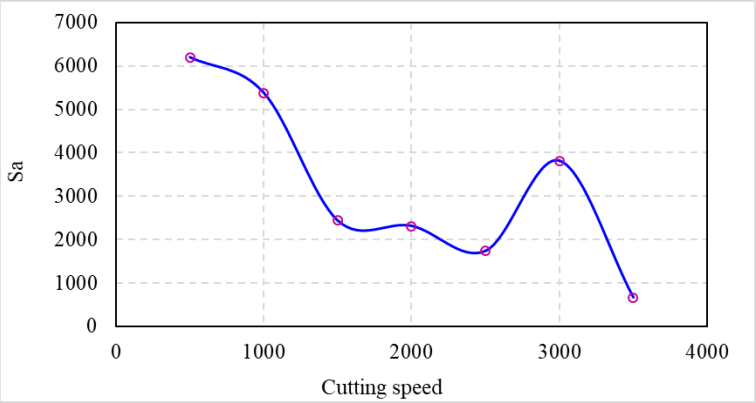

Fig. 3 Effect of CS on 3D average S_a

Analysing Fig. 3, it may further be note that initially, as the CS increases from 500 to 3000 rpm, there is a decline in surface roughness value. At a constant FR of 300 m/min and a DoC of 0.5 mm, S_a decreases progressively from 6197.25 to 1737.88 nm. However, it may be noted that a slight deviation is in the data at 3500 rpm, where surface roughness increases to 3812.33 nm. This anomaly may be due to the fact that there may be a threshold beyond which further increases in CS can have a detrimental effect on surface finish. Factors viz., tool wear, vibrations or excessive heat generation could be contributing to this deviation.

Influence of DoC on surface quality

DoC (measured in mm) is a key parameter in the machining processes of copper that governs the machined product quality. The impact of DoC on the average S_a is shown in Fig. 4. It may be observed that the average unevenness increases with the increase in cutting depth from 0.2 to 0.3 mm and on further increasing the depth, S_a decreases and then increases as the DoC is increased to 0.8 mm. It is preferred to have the least surface roughness for the applications. Therefore, the FR can be varied between 0.3 to 0.8 mm.

Analysing the data from Fig. 4, it is evident that as the DoC increases from 0.2 to 0.8 mm while maintaining a constant CS of 2000 rpm and a FR of 300 m/min, S_a exhibits a consistent decreasing trend. The reducing surface roughness with increasing DoC may be attributed to different factors. The depth of cut being larger allows for more efficient

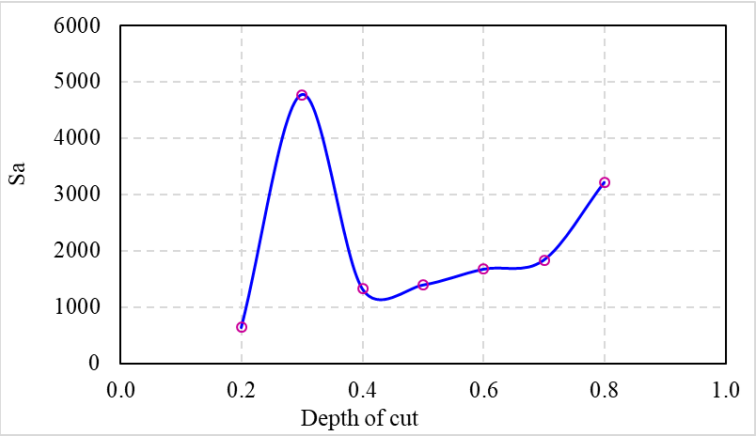

Fig. 4 Influence of DoC on the 3D average S_a

material removal, reducing the number of tools passes that is necessary to complete the machining operation. This will eventually minimize the cumulative effects of tool wear and cutting forces, leading to improved surface finish. Beyond a threshold point, increasing the depth of cut may result in diminishing returns or even deteriorating surface finish. This is due to the fact that increasing cutting forces, heat generation, and the potential for tool deflection, negatively impacts the surface quality.

CCRD results with discussion

The experiments are carried out using the central composite rotable design technique. Each input parameter is varied in five levels, and the output responses are record. The experimental design followed for the experimentation is shown (Table 1).

Table 1 Experimental plan according to central composite rotable design with surface roughness

Std	Run	CS, rpm	FR, m/min	Depth of cut, mm	3D-surface roughness (S_a), nm	Cutting forces		
						Fx	*Fy*	*Fz*
8	1	2500	200	0.7	3496.55	-11.64	-40.37	0.9
2	2	2500	100	0.4	1914.9	-6.54	-19.23	2.81
17	3	1750	150	0.55	2181.85	-12.05	-47.58	2.35
19	4	1750	150	0.55	2780.2	-6.87	-20.66	0.34
14	5	1750	150	0.8	4800.28	-22.16	-64.02	-0.08
20	6	1750	150	0.55	2495.16	-12.69	-24.4	-2.15
15	7	1750	150	0.55	2477.7	-17.01	-60.57	-4.82
6	8	2500	100	0.7	2377.25	-11.13	-29.92	0.59
18	9	1750	150	0.55	2507.8	-16.29	-70.83	0.59
12	10	1750	235	0.55	3972.4	-1.58	-8.55	-1.35
13	11	1750	150	0.3	1952.3	-2.01	-10.42	3.27
7	12	1000	200	0.7	5982.2	-5.76	-24.25	5.27
1	13	1000	100	0.4	2860.72	-2.91	-12.98	3.48
9	14	490	150	0.55	5440.6	-13.61	-41.84	1.63
4	15	2500	200	0.4	3279.59	-11.57	-31.72	2.35
10	16	3010	150	0.55	2802	-12.31	-31.1	3.09
3	17	1000	200	0.4	4501.15	-11.43	-32.08	4.48
11	18	1750	65	0.55	1530.7	-7	-19.82	1.88
5	19	1000	100	0.7	3386.05	-8.55	-26.53	-0.43
16	20	1750	150	0.55	2258.2	-7.42	-25.23	1.76

From the above data, an equation is generated. The equation is as follows: SA = +6437.66676 – 2.97654·CS + 7.10099·FR – 11785.15146·DoC – 0.005842·CS·FR – – 1.47452·CS·DoC + 11.83883·FR·DoC + 0.001051·CS^2 + 0.041299·FR^2 + 14768.16485·$D0C^2$.

Influence of FR on milled product evenness with varying DoC

Upon closer observation of the data in Fig. 5 it becomes evident that FR, when coupled with varying DoC, yields interesting reports on surface roughness. The dataset comprises of runs with FR ranging from 65 to 235 m/min, each carried out at various DoC settings.

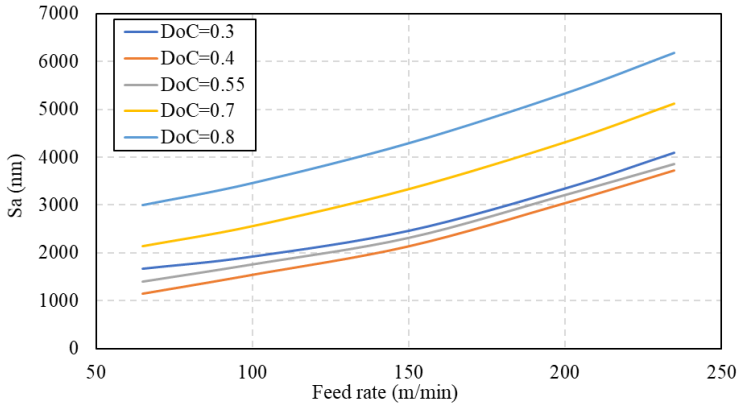

Fig. 5. Effect of FR on average area S_a at varying DoC

It may be noticed that for a given DoC, as FR increases, surface roughness decreases. Higher FR improve the more efficient chip evacuation and reduced tool contact time with the workpiece, resulting in reduced surface roughness. However, it is also to be noted that this trend is not uniform across all trials, and the influence of FR is also dependent upon DoC. The data reveals cases where the effect of DC on SA is prominent. In Run 5 with DoC of 0.8 mm, an increase in FR from 150 to 235 m/min results in a substantial rise in roughness (S_a) from 4800.28 to 5472.4 nm. This nonconformity from trend suggests that, for specific scenarios and DoC settings, higher FR yielding a lower surface roughness isn't certain as conditions vary.

Furthermore, it is recorded that the ideal FR for achieving lower roughness varies with the DoC cut. Runs 3 and 10, both executed at a DoC of 0.55 mm. While Run 3, with a FR of 150 m/min, yields a S_a value of 2181.85 nm, Run 10, with a higher FR of 235 m/min, results in a higher S_a value of 3972.4 nm. This discrepancy highlights the need for a systematic and cautious approach, that accounts not only FR but also the DoC during the process of optimizing the surface finish in copper machining.

One of the main reasons behind the decrease in S_a with higher FR is the effect on chip formation and evacuation. FR, measured in m/min, controls the rate at which the cutting tool advances through the workpiece. A higher FR leads to the generation of smaller, and more manageable chips. It is easy to evacuate these smaller chips from the cutting zone, reducing the likelihood of chip recutting and minimizing surface irregularities. Effective chip evacuation is a critical factor in accomplishing a smooth surface finish owing to the fact that the recutting chips may introduce unwanted imperfections and marks on the workpiece. With the increase in the FR, the rate at which

chips are produced bring into line better with the tool's ability to evacuate them, that results in reduced recutting and enhanced surface quality.

Higher FR values reduce the dwell time (the duration of tool-workpiece contact) during each pass of the cutting tool. Shorter dwell time is desired. Firstly, it decreases the heat build-up at the cutting edge of the tool, that may lead to thermal distortion and negatively affect the surface quality. Secondly, by reducing the duration of tool-workpiece contact it minimizes tool wear.

Influence of FR on surface roughness with varying CS

From Fig. 6, it becomes evident that the combination of FR and the CS, is significant in accomplishing a particular surface quality of machined copper components. The dataset comprises of FR varying from 65 to 235 m/min, performed at different CSs. Typically, as FR increases, S_a machined product irregularities decrease. This establishes the importance of FR in accomplishing smoother surface finishes during copper machining. Higher FR facilitate the attainment of efficient chip evacuation and reduces the dwell time of the machining tool on the work surface, that contributes to the reduction in surface roughness.

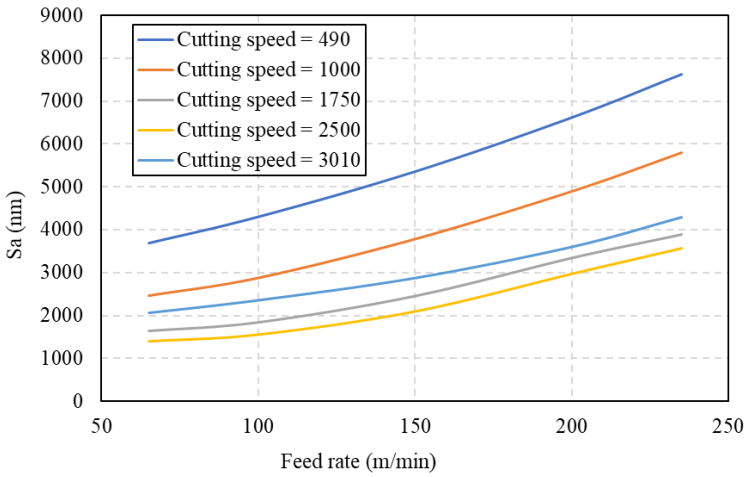

Fig. 6. Effect of FR on average S_a at varying CS

The data recordings also reveal that the impact of CS on S_a is prominent. In the case of Run 16 with a CS of 3010 rpm, an increase in FR from 150 to 235 m/min results in a significant decrease in surface roughness from 2802 to 3972.4 nm. This clearly demonstrates how the effect of FR can be altered by CS, and higher CSs can increase the impact of FR on surface roughness. Besides, it's vital to consider the interaction between CS and FR in achieving the desired surface finish. In the case of Run 14 with a CS of 490 rpm, a relatively low FR of 150 m/min leads to a high surface roughness of 5440.6 nm. Nevertheless, in contrast, Run 15 with a similar CS but a higher FR of 200 m/min results in a lower surface roughness of 3279.59 nm.

The key reason for the decrease in surface roughness with increasing FR is its effect on chip formation and evacuation. FR (m/min) controls the rate at which the cutting tool advances through the workpiece. Generation of smaller, more manageable chips is typically observed for a higher FR. It is easier to evacuate these smaller chips from the

cutting zone, thereby reducing the chip recutting and minimizing surface irregularities. Efficient chip evacuation is a critical factor in accomplishing a smooth surface finish owing to the fact that recutting chips introduces unwanted marks and imperfections on the workpiece. Additionally, a higher FR led to the reduction in dwell time. It decreases the opportunity for heat to build up at the machining tool surface or the edge which can lead to thermal distortion and adversely affect surface quality. It also minimizes withering of the cutting tool by reducing the duration of tool-workpiece contact. Tool wear alters the sharpness of the tool and increases the friction, both of which may negatively impact surface finish.

Effect of CS on surface roughness with varying DoC

A careful examination of the plot (Fig. 7) reveals that the choice of CS, when clubbed with variations in DoC, majorly influences the surface roughness of machined copper components. The dataset comprises of trials carried out at a wide range of CSs, from 490 to 3010 rpm, with each run featuring different depth of cut settings. In general, as CS increases, S_a is observed to decrease. In the case of Run 16 with a CS of rpm and DoC of 0.55 mm, the resulting surface roughness is 2802 nm. This clearly establishes how higher CSs lead to smoother surface finishes by ensuring efficient material removal and reducing tool contact time with the workpiece. Nevertheless, the data also reveals that the effect of DoC on machined product surface evenness cannot be neglected. In case of Run 5 with a DoC of 0.8 mm, an increase in CS from 1750 to 2500 rpm results in a substantial rise in surface roughness, from 4800.28 to 3496.55 nm. This observation infers that the impact of CS on surface quality can be regulated by the DoC. Trials 2 and 17, carried out at similar CSs but with different DoC settings, illustrate this point. Run 2, with a DoC of 0.4 mm and a CS of 2500 rpm, yields a S_a value of 1914.9 nm. In contrast, Run 17, with a similar CS but a deeper DoC of cut of 0.4 mm, results in a notably higher S_a value of 4501.15 nm. One key factor driving the improvement of surface evenness at higher CS is the efficiency of material removal. As CS rises, the tool removes material more rapidly, leading to a reduction in the thickness of material left behind in each pass.

A higher CS accelerates material removal and minimises the negative effects of tool wear on surface quality. The reduction in surface roughness with higher CSs is also

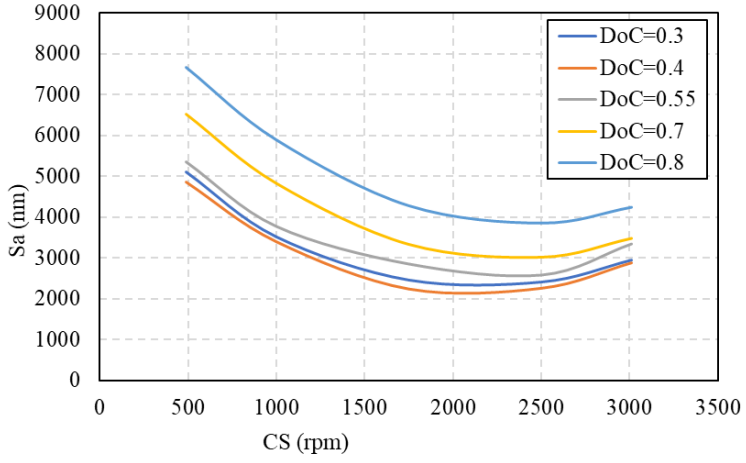

Fig. 7. Effect of feed rate on average S_a roughness at varying DoC

governed by the minimization of cutting forces. Cutting forces are the forces that are exerted on the tool during machining and those forces may cause tool deflection and workpiece deformation. When CS is increased, the duration of tool-workpiece contact is reduced, resulting in lower cutting forces. This reduction contributes to a smoother surface finish by reducing the instances of workpiece vibrations and deformations. However, the impact of CS on the surface should be determined along with the variation of DoC. DoC which specifies the thickness of material removed during each pass of the cutting tool, plays a vital role in regulating the correlation between them. With the increase in DoC, it may counter the benefits of higher CS.

A deep cut removes more material, even for a moderate CS. This results in a higher surface roughness, as observed in Run 5, where a rise in CS from 1750 to 2500 rpm led to a rise in surface roughness. The DoC in this case (0.8 mm) significantly influenced material removal, overshadowing the effects of increased CS. Furthermore, the interaction between CS and DoC governs the machined surface characteristics. Runs 2 and 17 illustrate this point, as both were carried out at a similar CS but with different DoC settings. In Run 2, with a DoC of 0.4 mm and a CS of 2500 rpm, a relatively low surface roughness of 1914.9 nm was accomplished. However, in Run 17, with a similar CS but a deeper DoC (0.4 mm), the roughness increased significantly to 4501.15 nm.

Effect of CS variation on Sa with varying feed rate

The dataset provided in Fig. 8 can be utilised to explore the dependencies between CS and surface roughness with the variations in the FR. The requirement of the copper milling process is lower surface roughness. The obtained data indicates that CS, when combined with changes in FR, goenrs the surface roughness of machined copper components. The dataset includes the experimental trails conducted with variation of CSs, ranging from 490 to 3010 rpm, with each run featuring different FR settings.

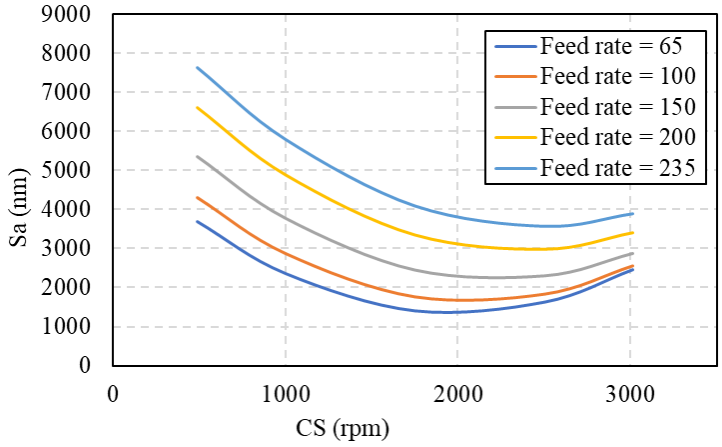

Fig. 8. Effect of CS on average S_a at varying FRs

As CS increases, roughness is observed to decrease. For instance, in Run 16 with a CS of 3010 rpm and a FR of 150 m/min, the resulting surface roughness is 2802 nm. This highlights the significance of higher CSs to promote smoother surface finishes by enhancing material removal efficiency and reducing tool contact time with the workpiece. However, the data also reveals that the impact of FR on product roughness should not be

underestimated. For instance, in Run 15 with a CS of 2500 rpm, a lower FR of 100 m/min leads to a higher surface roughness of 3279.59 nm, whereas increasing the FR to 200 m/min results in a notably lower S_a value.

The reduction in Sa with increasing CS can be due to several key factors. Firstly, increased CS promotes the chip evacuation, ensuring prompt removal of the metal remnants from the cutting zone. Also, higher CSs reduce the dwell time of the cutting tool on the workpiece, minimizing the tool wear and heat build-up. The combination of these effects results in smoother surface finishes when CS is increased. FR has its own significance on the surface roughness, even with varying CS. In the trial 15, a CS of 2500 rpm is maintained, but the FR is varied. When the FR is set at 100 m/min, the resulting surface roughness is 3279.59 nm. However, when the FR is increased to 200 m/min, a notably lower Sa value is achieved. This observation infers that the effect of CS on Sa may be modulated by the chosen FR. In cases like Run 15, where the FR is increased, the reduction in Sa is significant, indicating that FR adjustments can compensate for variations in CS.

CS primarily affects material removal efficiency by determining the speed at which the cutting tool engages the workpiece. Higher CSs can help achieve smoother surfaces by reducing tool contact time and minimizing heat generation. The FR influences the rate at which the tool advances through the workpiece. A higher FR can promote chip evacuation, reduce tool wear, and mitigate heat-related issues. However, excessively high FRs can also lead to issues such as tool breakage or poor chip formation. Runs 2 and 8, executed at a similar FR but with different CSs, illustrate this point. Run 2, with a CS of 2500 rpm and a FR of 100 m/min, yields a S_a value of 1914.9 nm. In contrast, Run 8, with a similar FR but a higher CS of 2500 rpm, results in a S_a value of 2377.25 nm. This highlights the need to carefully balance both parameters to optimize surface quality in copper machining.

Effect of DoC on roughness of product with varying FR

The variation patterns observed in Fig. 9 illustrate the correlation of DoC and machined product roughness (S_a), considering variations in FR. The dataset comprises trials executed at varying DoC, ranging from 0.3 to 0.8 mm, each paired with different FR

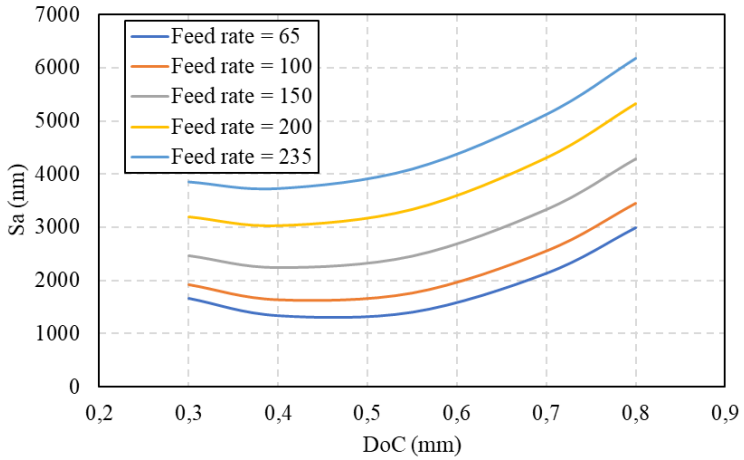

Fig. 9. Effect of DoC on average area surface roughness at varying FRs

settings. The DoC, in conjunction with changes in FR significantly influences the surface roughness of machined copper components.

As the DoC increases, surface roughness is observed to decrease. For example, in Run 5, with a DoC of 0.8 mm and a FR of 150 m/min, the resulting surface roughness is 4800.28 nm. Larger values of DoC contribute to smoother surface finishes by efficiently removing more material per pass and minimizing tool contact time with the workpiece. The variations also indicate the impact of FR variations on the machined surface at differing DoC. In Run 15, a DoC of 0.4 mm is maintained, but the FR is varied. When the FR is set at 100 m/min, the resulting surface roughness is 3279.59 nm. However, when the FR is increased to 200 m/min, a notably lower S_a value is achieved.

This observation suggests that the influence of DoC on Sa can be modulated by the chosen FR. In cases like Run 15, where FR is increased, the reduction in S_a is substantial, indicating that FR adjustments can compensate for variations in DoC. The correlation and combined effect of DoC and FR rate can be analysed by considering the balance between material removal and tool-workpiece interaction.

A comparative analysis of milling behaviour in copper and additively manufactured CuCrZr

Optimisation and selection of the optimal approach for machining for copper and additively manufactured CuCrZr requires comparative analysis of their properties. CuCrZr demands more precise machining parameters and tools, due to its enhanced properties [16,17]. This section describes the experimental analysis of 3D printing of Cu Cr Zr using laser powder bed fusion (LPBF) technique. This study involves the following procedures: 3D printing a 110 × 110 × 8 mm^3 plate; wire-cut EDM (electrical discharge machining) to reduce its dimension to 55 × 110 × 8 mm^3; milling operations.

Experiment

The chemical properties of CuCrZr materials and the mechanical properties of the as-built sample is presented in Tables 2 and 3. CuCrZr has high strength and good machinability. With these characteristics, it is commonly used in applications such as heat exchangers, electrical contacts, and aerospace components.

Table 2. Chemical composition of CuCrZr

Element	Min	Max
Cr	0.5	1.2
Zr	0.03	0.3
Fe		0.08
Si		0.1
Cu	Balance	

Table 3. Mechanical properties of as-built CuCrZr sample

Test	Unit	As-built	Remarks
Tensile strength	*Rm*, MPa	190 ± 20	Tensile test according to ISO 6892–1:2009B
Yield strength	R_pO, MPa	150 ± 20	
Elongation break	*A*, %	36 ± 4	
Modulus of elasticity	*E*, GPa	125 ± 20	
Vickers hardness	*HV10*	90 ± 2	Hardness testing according to DIN EN ISO 6507–1

LPBF printing technology for CuCrZr

CuCrZr material is prepared in the form of powder for the printing process. CuCrZr powder typically has a specific particle size distribution to ensure good flowability and density during printing. The LPBF process involves laser power to heat and fuse layers of CuCrZr powder to form the part. The laser moves in a precise pattern, layer by layer, to build up the part. The machine used for this study is STLE 400 (Fig. 10) and the parameters used for building the part is presented in Table 4. The typical layer thickness for LPBF is in the range of 20–100 µm, depending on the printer's capabilities and the desired part resolution. The initial 3D-printed plate is 110 × 110 × 8 mm^3. The LPBF process allows for the creation of complex geometries, but in this case, a simple plate structure is being produced, which will subsequently be subjected to WEDM.

Fig. 10. STLR 400 machine deployed for preparing CuCrZr part

Table 4. Parametric Settings for as-built CuCrZr sample

Parameters	Value
Powder, W	370
Scan speed, mm/S	500
Hatch distance, µm	80
Layer thickness, µm	30
Spot size, µm	80
Build plate temperature, °	180

Wire-cut EDM process

EDM uses an electrically charged wire (usually copper or brass) to erode material from the workpiece. The wire is continuously fed through the part while submerged in a dielectric fluid (such as deionized water) to cool the process and flush away debris. Wire-cut EDM allows for very fine and intricate cuts with high precision and minimal thermal distortion. The wire acts as an electrode that removes material through rapid electrical discharges, leaving behind a very clean and accurate cut surface. In this study, after printing the 110 × 110 × 8 mm^3 CuCrZr plate, the wire-cut EDM is used to trim the plate to a final dimension of 55 × 110 × 8 mm^3. Figure 11 shows as–built CuCrZr sample subjected to milling with the numbers marked indicating the trials and the process parametric range used for them.

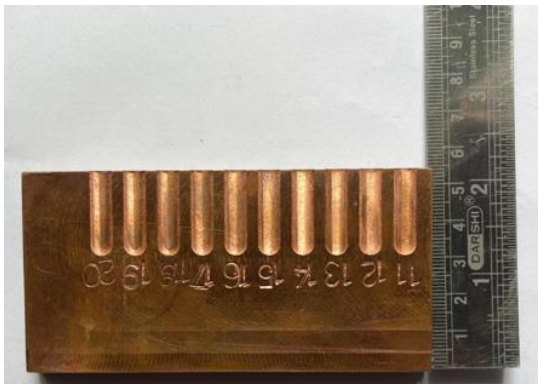

Fig 11. Sample as–built CuCrZr subjected to milling

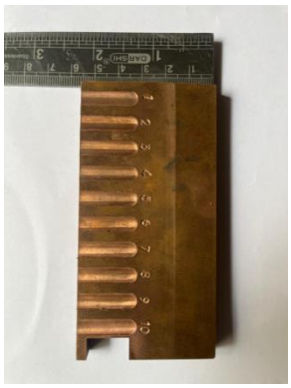

Fig. 12. A section removed for analysis from as-built CuCrZr

The following caution was adopted during the experimentation:

1. CuCrZr has high thermal conductivity, which can lead to thermal stresses during the printing process. These stresses must be carefully managed through optimal printing parameters.
2. LPBF parts often require post-processing steps like wire-cut EDM or machining to achieve the final dimensions and surface finish. This can be time-consuming and costly.
3. CuCrZr powder can be expensive and handling the powder carefully to avoid contamination and ensure consistent quality.

Milling operation of as built-CuCrZr

Additive manufacturing (AM) of CuCrZr, a high-performance copper alloy with superior thermal and electrical conductivity, has become popular for the generation of intricate geometries in aerospace, automotive, and fusion technology [18–20]. Methods such as laser powder bed fusion (LPBF) are widely practiced, albeit with challenges owing to the high reflectivity and thermal conductivity of copper, necessitating high-power lasers and processing conditions to be optimized. Post-processing operations like heat treatment and hot isostatic pressing are commonly utilized to improve mechanical properties and remove porosity. CuCrZr milling is employed to obtain high dimensional precision and surface quality, particularly following AM, although the greater hardness of the alloy in the aged condition can contribute to tool wear [19,21,22]. The combination of AM and high-precision milling allows complex, high-performance parts with high tolerances and high-quality surfaces to be fabricated [23–26].

Experimentation involving the milling of as-built CuCrZr focuses on evaluating the significance and influence of various machining parameters, such as FR, CS, and cutting forces on product quality and DoC. cut. During the process of milling, copper's high thermal conductivity paves way for efficient heat dissipation, thereby minimizing the thermal loads on the workpiece and tool. Contrary to that, additively manufactured CuCrZr illustrates reduced and anisotropic thermal conductivity owing to microstructural variations that eventually lead to localized heat accumulation. This may have impact on the dimensional stability, tool wear, and surface quality. A thorough understanding of these thermal behaviours is essential for optimizing machining strategies. The goal is to optimize machining conditions for improved efficiency, precision, and durability of CuCrZr

Table 5. Experimental plan according to central composite rotable design with surface roughness for CuCrZr

Std	Run	CS, rpm	FR, m/min	Cutting forces			As-built CU	
				Fx	*Fy*	*Fz*	Depth of cut, mm	3D-surface roughness (S_a), µm
8	1	2500	200	−2.03	-19.43	-3.34	0.7	0.78
2	2	2500	100	−0.15	-14.57	-3.67	0.4	0.73
17	3	1750	150	-0.64	-27.15	-3.75	0.55	6.97
19	4	1750	150	-0.42	-15.36	-3.69	0.55	5.96
14	5	1750	150	-5.26	-54.6	-16.06	0.8	6.38
20	6	1750	150	-2.64	-24.44	-10.51	0.55	6.3
15	7	1750	150	-3.19	-26.54	-7.51	0.55	6.67
6	8	2500	100	-5.81	-30.98	-11.08	0.7	0.54
18	9	1750	150	-4.86	-58.44	-10.21	0.55	6.99
12	10	1750	235	-2.11	-21.91	-5.87	0.55	5.72
13	11	1750	150	-0.49	-12.52	-1.69	0.3	6.5
7	12	1000	200	-0.45	-19.39	-2.76	0.7	2.16
1	13	1000	100	-6.8	-10.24	-0.16	0.4	1.74
9	14	490	150	-9.67	-41.45	-10.55	0.55	2.93
4	15	2500	200	-5.21	-20.42	-4.32	0.4	1.15
10	16	3010	150	-7.15	-18.46	-3.54	0.55	0.57
3	17	1000	200	-13.85	-22.19	-4.55	0.4	2.32
11	18	1750	65	-11.89	-16.95	-2.06	0.55	6.05
5	19	1000	100	-14.6	-11.52	0.53	0.7	1.61
16	20	1750	150	-17.18	-15.67	-0.39	0.55	6.64

components in demanding industrial applications. The following table shows the experimental trials for milling of as-built CuCrZr based of design of experiments. Figure 12 shows CuCrZr sample where a milled portion is removed for analysing the DoC and product quality. Table 5 records the DoC and Sa for various trails of milling conducted on as-built CuCrZr. During milling, cutting forces were measured using a dynamometer which was mounted beneath the workpiece to record forces along all the directions. The dynamometer was connected to data acquisition system to capture real-time force signals during machining. Measurements were recorded for varying cutting parameters to examine their influence on machining behaviour.

Results and Discussion

Table 5 is analysed for understanding the parametric correlation between the process input parameters and output parameters which are the surface roughness and DoC. Correlation statistical algorithms are used to analyse the parametric interdependencies while Pearson's coefficient is used to arrive at a comparative heat map for milling parametric correlations and comparisons between Cu and CuCrZr samples. Figure 13 shows the relation between CS and surface roughness.

In milling operations of as-built CuCrZr, surface roughness typically decreases as CS increases, up to an optimal point. At higher CSs, the material is removed more efficiently,

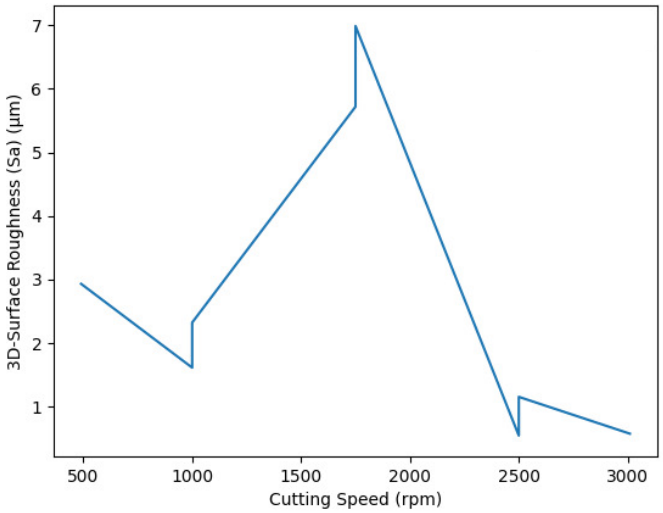

Fig. 13. Cutting speed vs. surface roughness

allowing for smoother cuts and reducing the likelihood of tool marks on the surface. However, if the CS is too high, it can cause excessive heat generation, leading to thermal damage, work hardening, and increased tool wear, which may worsen machined product quality. The relationship between CS and roughness is thus dependent on finding an optimal CS that balances material removal efficiency and tool performance while minimizing surface imperfections. Figure 14 shows the relation between FR and S_a.

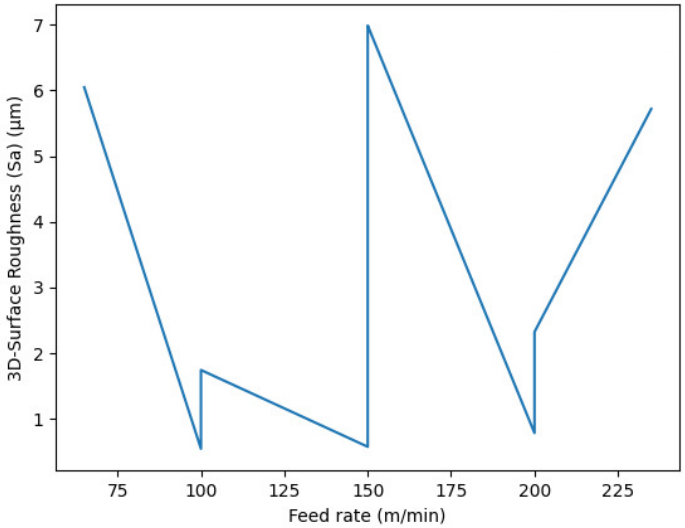

Fig. 14. Feed rate vs. surface roughness

The dependency of surface roughness on the FR for as-built CuCrZr (copper chromium zirconium) can be critical in determining the efficiency and quality of manufacturing processes such as milling or turning. Additive manufacturing (e.g., laser powder bed fusion) of CuCrZr may exhibit different surface roughness characteristics compared to traditional machining due to the material's microstructure and layer bonding. When studying the FR vs. surface roughness relationship for as-built CuCrZr, the key takeaway is that lower FRs generally result in better surface finishes (i.e., lower surface roughness), but at the cost of slower material removal. Understanding the

interplay of machining parameters and material characteristics is critical for optimizing the process to balance efficiency and surface quality. The bar chart (Fig. 15) shows comparison of surface roughness (R_a) for commercial Cu and additively manufactured CuCrZr at varying feed rates, with error bars illustrating standard deviation. Highly anisotropic or harder materials like as-built CuCrZr result in rougher surfaces and higher tool loads as compared to softer materials like commercial Cu.

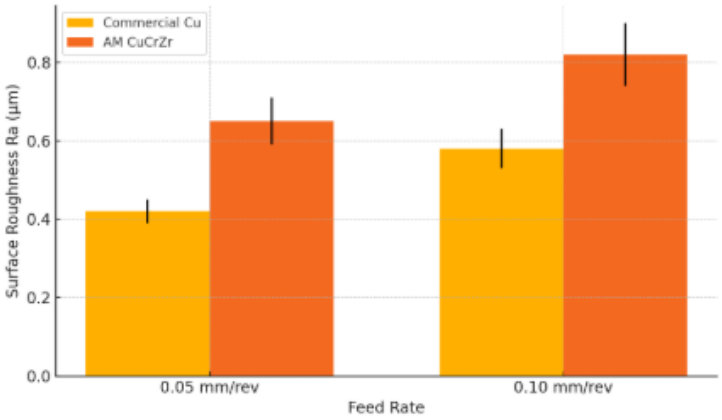

Fig. 15. Surface roughness comparison with deviation

Microscopic analysis of milled samples of Cu and as-built CuCrZr

SEM (scanning electron microscopy) analysis of the milled commercial Cu surface (Fig. 16(a)) illustrated smooth, continuous tool marks with negligible surface defects. This emphasizes stable chip formation and better heat dissipation owing to high conductivity. In contrary, the milled as-built CuCrZr surface demonstrated micro-tearing, smeared areas, and some material sticking, owing to its lower and uneven thermal conductivity, hardened microstructure and internal porosity. These characteristics reveal more tool-material contact and localized heat build-up during the process of machining.

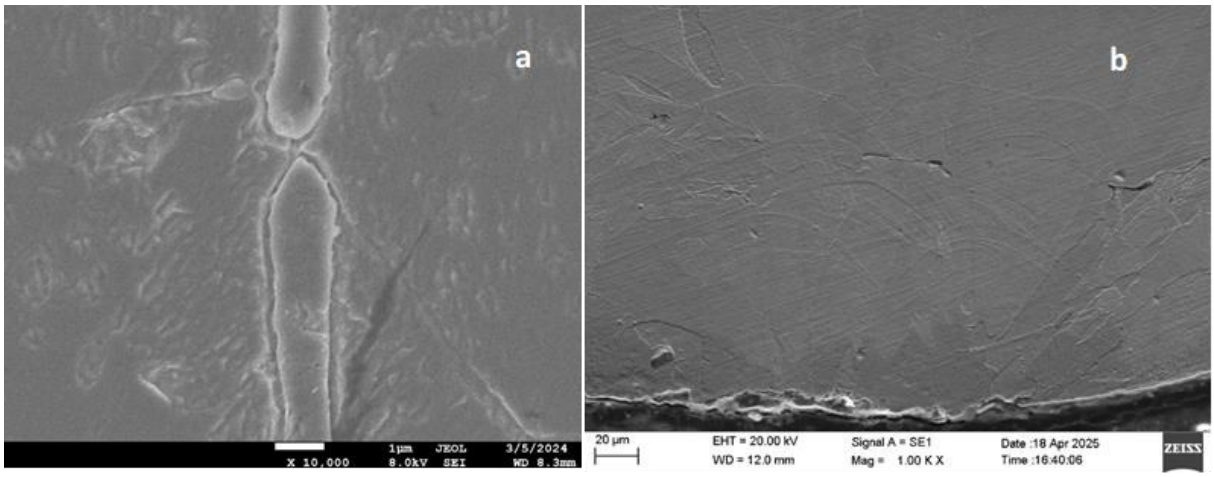

Fig. 16. SEM images of milled sample of Cu (a) and as-built CuCrZr (b)

Comparison between milling operation parametric performance for Cu and as-built CuCrZr

A Pearson correlation heat map is a visual representation of the correlation coefficients between multiple variables in a dataset. Each cell in the heatmap shows the correlation value between a pair of variables, with colour shading indicating the strength and direction of the correlation.

Analysis of the milling performance and parametric differences observed in copper (Cu) and as-built CuCrZr (copper chromium zirconium) in terms of dependency between CS and surface roughness and FR depicts the following observations:

1. Dependency of surface roughness on CS for Cu: surface roughness varies inversely with respect to CS increases, as higher speeds allow for finer, more continuous and uniform cuts. High thermal conductivity of copper causes efficient heat dissipation, thus minimizing tool wear resulting in maintaining surface finish at higher speeds [26,27]. Optimal CS needs to be maintained to avoid excessive heat generation and resultant thermal damage that may increase surface roughness. The less hardness property of copper makes this effect less significant.
2. Dependency of surface roughness on CS for CuCrZr: improvement in surface finish with increasing CS is less observed in CuCrZr, due to its nature of being stronger and harder than commercially available copper. This results in more heat generation due to its alloying elements, and is thus prone to significant thermal damage and tool wear. The optimal CS is thus lower compared to copper, to avoid poor surface finish due to work hardening and increased tool wear.

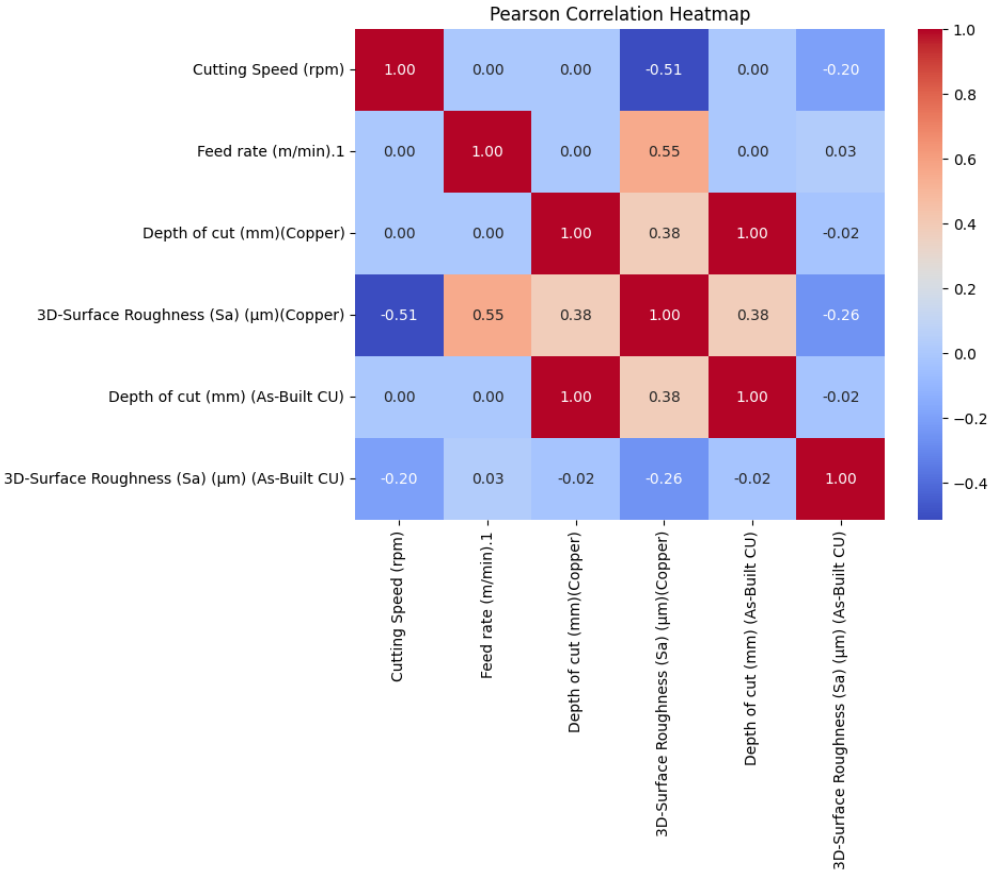

Fig. 17. Pearson correlation heat map

3. Dependency of surface roughness on FR for copper (Cu): surface roughness is observed to be directly proportional to FR. With higher FR, the tool makes rough excisions, resulting in deeper tool marks and a higher surface roughness. Reducing the FR allows for finer in deeper tool marks and a higher surface roughness. Reducing the FR allows for finer cuts, as the tool has more time for precise shaping of the material.
4. Dependency of surface roughness on FR for CuCrZr: owing to the high strength and hardness of CuCrZr, higher FR results in increased surface roughness due to higher cutting forces and less effective material removal, resulting in increased surface roughness. Optimum value of FR is needed for the tool to cut through the material, as lower range of FR can increase wear or even cause tool breakage at sub optimum rates [28,29]. Table 6 shows the parametric correlation of CS and FR vs DoC and surface roughness respectively for Cu and as-built CuCrZr. Based on the correlation coefficients, the heat map is generated. Figure 17 shows the Pearson's correlation heat map.

Table 6. Parametric comparison of milling for Cu and as-built CuCrZr

	DoC, mm		**3D-S_a, µm**	
	As-built	Copper	As-built	Copper
CS	0	0	-0.2	-0.51
Feeding rate	0	0	0.03	0.55

Conclusions

The experimental observations and the comparative study between copper and alloyed CuCrZr offer valuable insights into the interdependencies between material properties and the process parameters of DoC, CS, and product surface quality in copper machining. Additively manufactured CuCrZr differs significantly in properties with respect to commercial copper and requires optimal balance of the process parameters. It is observed that in both materials, optimal cutting parameters of CS, FR control the surface quality while balancing material removal rate and tool wear. However, CuCrZr generally requires more precise control of these parameters to ensure better surface quality obtained with the milling operations. This makes the machining process more challenging for CuCrZr as compared to commercial copper. This analysis has enabled establishment of dependencies and correlations between parameters involved in machining processes of Cu and its alloyed form CuCrZr, contributing to enhanced precision and efficiency in manufacturing. Future investigations can be focussed on the analysis of additional variables like tool material, geometry, coolant utilization, and other machining techniques for ensuring quality of the final product. As-built CuCrZr is used in high-performance applications like heat exchangers, rocket engine parts, and electrical contacts due to its strength, good thermal conductivity, and suitability for additive manufacturing.

CRediT authorship contribution statement

Subba Reddy Mundla: experimentation, sample preparation, testing and characterization, parametric analysis; **Arungalai S. Vendan**: experimentation, ML based parametric analysis, paper writing, technical interpretations; **C. P. Paul**: ideation, experimentation, testing and analysis; **Arun K. Shettigar**: idea for experimentation, technical inputs,

technical interpretation of results, guiding in paper writing; **Sudhakar C. Jambagi**: idea for experimentation, technical inputs, technical interpretation of results, guiding in paper writing.

Conflict of interest

The authors declare that they have no conflict of interest.

References

1. Sivasubramaniyam V, Ramasamy S, Venkatraman M, Gatto G, Kumar A. Carbon Nanotubes as an Alternative to Copper Wires in Electrical Machines: A Review. *Energies.* 2023;16: 3665.
2. Hu H, Chang S, Li Y, Li X. Design and thermal characteristic test of a temperature control system for spacecraft precision instrument. *International Journal of Refrigeration.* 2023;146: 462–470.
3. Barros LY, Poletto JC, Neis PD, Ferreira NF, Pereira CHS. Influence of copper on automotive brake performance. *Wear.* 2019;426: 741–749.
4. Raab SJ, Guschlbauer R, Lodes MA, Körner C. Thermal and electrical conductivity of 99.9 % pure copper processed via selective electron beam melting. *Advanced Engineering Materials.* 2016;18(9): 1661–1666.
5. Seo D, Ogawa K, Sakaguchi K, Miyamoto N, Tsuzuki Y. Parameter study influencing thermal conductivity of annealed pure copper coatings deposited by selective cold spray processes. *Surface and Coatings Technology.* 2012;206(8–9): 2316–2324.
6. Çakıroğlu R, Günay M. Analysis of surface roughness and energy consumption in turning of C17500 copper alloy under different machining environments and modellings with response surface method. *Proceedings of the Institution of Mechanical Engineers, Part E: Journal of Process Mechanical Engineering.* 2023;237(2): 207–219.
7. O'Toole L, Kang CW, Fang FZ. Precision micro-milling process: state of the art. *Advanced Manufacturing.* 2021;9(2): 173–205.
8. Choudhury SK, Bajpai JB. Investigation in orthogonal turn-milling towards better surface finish. *Journal of Materials Processing Technology.* 2005;170(1–2): 487–493.
9. Palos CMM, Mariño-Gámez AE, Acosta-González G-E, Hernández MB, García-Villarreal S, Franco LF, García-Ortiz L, Aguilar-Martínez JA. Large-scale production of ZnO nanoparticles by high energy ball milling. *Physica B: Condensed Matter.* 2023;656: 414776.
10. Schueler GM, Engmann J, Marx T, Haberland R, Aurich JC. Burr formation and surface characteristics in micro-end milling of titanium alloys. In: Aurich J, Dornfeld D. (eds.) *Burrs-Analysis, Control and Removal. Proceedings of the CIRP International Conference on Burrs, 2–3 April 2009, University of Kaiserslautern, Germany.* Berlin, Heidelberg: Springer; 2010. p.129–138.
11. Rao B, Dandekar CR, Shin YC. An experimental and numerical study on the face milling of Ti–6Al–4V alloy: Tool performance and surface integrity. *Journal of Materials Processing Technology.* 2011;211(2): 294–304.
12. Sridharan N, Shah JJ. Recognition of multi axis milling features: part I-topological and geometric characteristics. *Journal of Computing and Information Science in Engineering.* 2004;4(3): 242–250.
13. Hayajneh MT, Tahat MS, Bluhm J. A study of the effects of machining parameters on the surface roughness in the end-milling process. *Jordan Journal of Mechanical and Industrial Engineering.* 2007;1(1): 1–7.
14. Sorgato M, Bertolini R, Bruschi S. On the correlation between surface quality and tool wear in micro–milling of pure copper. *Journal of Manufacturing Processes.* 2020;50: 547–560.
15. Li H, Lai X, Li C, Feng J, Ni J. Modelling and experimental analysis of the effects of tool wear, minimum chip thickness and micro tool geometry on the surface roughness in micro-end-milling. *Journal of Micromechanics and Microengineering.* 2008;18(2): 025006.
16. Edwards DJ, Singh BN, Tähtinen S. Effect of heat treatments on precipitate microstructure and mechanical properties of a Cu Cr Zr alloy. *Journal of Nuclear Materials.* 2007;367: 904–909.
17. Bai Y, Zhao C, Zhang Y, Chen J, Wang H. Additively manufactured Cu Cr Zr alloy: Microstructure, mechanical properties and machinability. *Materials Science and Engineering: A.* 2021;819: 141528.
18. Chen J, Wang J, Xiao X, Wang H, Chen H, Yang B. Contribution of Zr to strength and grain refinement in Cu Cr Zr alloy. *Materials Science and Engineering: A.* 2019;756: 464–473.

19. Wallis C, Buchmayr B. Effect of heat treatments on microstructure and properties of Cu Cr Zr produced by laser-powder bed fusion. *Materials Science and Engineering: A.* 2019;744: 215–223.
20. Lipa M, Durocher A, Tivey R, Huber T, Schedler B, Weigert J. The use of copper alloy Cu Cr Zr as a structural material for actively cooled plasma facing and in vessel components. *Fusion Engineering and Design.* 2005;75: 469–473.
21. Tang X, Chen X, Sun F, Li L, Liu P, Zhou H, Fu S, Li A. A study on the mechanical and electrical properties of high-strength Cu Cr Zr alloy fabricated using laser powder bed fusion. *Journal of Alloys and Compounds.* 2022;924: 166627.
22. Brotzu A, Felli F, Pilone D, Paolozzi A, Paris C, Iacoviello F, Bellini C, Di Cocco V. Study of the fracture behavior of a Cu Cr Zr alloy. *Material Design & Processing Communications.* 2020;2(5): e113.
23. Polozov IA, Borisov EV, Sufiiarov VS, Popovich AA. Selective laser melting of copper alloy. *Materials Physics and Mechanics.* 2020;43(1): 65–71.
24. Kumar N, Bharti A, Kumar A, Nigam A. Effect of process parameters on the crystal parameters of Cu-Zn spinel-ferrites. *Materials Physics and Mechanics.* 2021;47(1): 65–73.
25. Rudskoi AI, Zolotov AM, Parshikov RA. Severe plastic deformation influence on engineering plasticity of copper. *Materials Physics and Mechanics.* 2018;38(1): 64–68.
26. Zhang B, Zhang ZG. Mechanical properties, electrical conductivity and microstructure of CuCrZr alloys treated with thermal stretch process. *Transactions of Nonferrous Metals Society of China.* 2015;25(7): 2285–2292.
27. Candela V, Tocci M, Ischia G, Valentini F, Mutanen A, Candela S, Lehtonen H, Hongisto J, Syvänen T, Dima R, Ottelin J. Understanding microstructure and properties evolution in additively manufactured Cu Cr Zr alloy to obtain a high-performance material. *Materials Characterization.* 2025;222: 114811.
28. Feng H, Jiang H, Yan D, Rong L. Effect of continuous extrusion on the microstructure and mechanical properties of a Cu Cr Zr alloy. *Materials Science and Engineering: A.* 2013;582: 219–224.
29. Kuai Z, Li Z, Liu B, Chen Y, Lu S, Tang X, Liu T. Selective laser melting of Cu Cr Zr alloy: processing optimisation, microstructure and mechanical properties. *Journal of Materials Research and Technology.* 2022;19: 4915–4931.

MATERIALS PHYSICS AND MECHANICS RESEARCH ARTICLE

Submitted: July 28, 2025 **Revised: September 12, 2025** **Accepted: September 25, 2025**

Predicting the flexural strength of 3D-printed geopolymer reinforced concrete using machine learning techniques

M. Hematibahar [1], M. Kharun [2], R.S. Fediuk [3,4]✉, N.I. Vatin [5], M.G. Porvadov [6], L.S. Sabitov [2]

[1] Department of Architecture, Restoration and Design, RUDN University, Moscow, Russia

[2] Moscow State University of Civil Engineering, Moscow, Russia

[3] Far Eastern Federal University, Vladivostok, Russia

[4] Vladivostok State University, Vladivostok, Russia

[5] Peter the Great St. Petersburg Polytechnic University, St. Petersburg, Russia

[6] Perm Military Institute of the National Guard Troops of the Russian Federation, Perm, Russia

✉ roman44@yandex.ru

ABSTRACT

Both geopolymer concrete and 3D printing are innovative trends in construction materials science. This study investigates the prediction of 3D printed geopolymer reinforced concrete due to lack of information and studies on the prediction of 3D printed geopolymer reinforced concrete. This study investigated for the first time the flexural strength of 3D printed reinforced concrete through compressive strength with concrete mix design. Rigid, Lasso, elastic net, random forest, gradient boosting, decision tree, support vector machine regression and k-nearest neighbor are examined in this study. Considering to this study, compressive strength and flexural strength have more than 0.97 relationship. Moreover, the best result was for gradient boosting, random forest and k-nearest neighbor with 0.85 and 0.89.

KEYWORDS

3D printing concrete • 3D printing reinforced concrete • auxetic • geopolymer • prediction

***Funding**. This research was funded by the Ministry of Science and Higher Education of the Russian Federation within the framework of the state assignment No 075-03-2025-256 dated 16 January 2025, Additional agreement No 075-03-2025-256/1 dated 25 March 2025, FSEG-2025-0008.*

Citation: Hematibahar M, Kharun M, Fediuk RS, Vatin NI, Porvadov MG, Sabitov LS. Predicting the flexural strength of 3D-printed geopolymer reinforced concrete using machine learning techniques. *Materials Physics and Mechanics*. 2025;53(4): 22–34.
http://dx.doi.org/10.18149/MPM.5342025_2

Introduction

Geopolymer concrete is a type of green concrete that reduces the negative effects of using concrete and cement, which is why many researchers use geopolymer concrete [1]. Cement production and use releases large amounts of carbon dioxide into the atmosphere, while geopolymer concrete can reduce this amount by eliminating cement [2].

The geopolymer concrete has high potential strength such as high compressive strength, low alkaline expansion, low shrinkage and etc. [3,4]. Amin et al. [5] studied the geopolymer concrete with fly ash, metakaolin, and slag. They found that compressive strength is more than 60 MPa, tensile strength is more than 6.2 MPa and flexural strength

is more than 9.2 MPa. Silica fume and micro silica, with a high percentage of silicon, can improve mechanical properties such as compressive strength of geopolymer concrete [6]. Wu et al. [7] analyzed geopolymer concrete with silica fume and sodium silicate as activator. They found that compressive strength can achieve more than 43.63 MPa. Adding microsilica and silica fume as powder form to geopolymer concrete can create aluminosilicate (N-A-S-H) geopolymer gel. In addition, sodium silicate solution as an activator is a good option for addition to geopolymer concrete [8]. Gel products are calcium silicate gel (C-S-H) converted to calcium aluminosilicate gel (C-A-S-H) [9].

De Oliveira et al. [10] have proven the high durability of geopolymers. Mintsaev et al. [11] studied features of the synthesis of construction geopolymer composites. A. Jan et al. [12] found that when 0.25 % polypropylene fibers (PPF) were added to geopolymer concrete, the compressive strength improved by more than 3.73 %. Some studies show that different types of fiber such as steel, basalt and etc. can improve the mechanical properties of concrete such as compressive, tensile and flexural strengths [13–15]. According to Levkina and Titova [16], the use of innovative products, such as geopolymers, can become an impetus for the development of small businesses in the regions.

Despite the above studies, there is a lack of information and research on the prediction of 3D printed geopolymer reinforced concrete. This study first investigated the flexural strength of 3D printed geopolymer reinforced concrete through compressive strength with concrete mix design. This study considers the stiff methods, lasso, elastic net, random forest, gradient boosting, decision tree, support vector regression and K-nearest neighbors. It is necessary to identify the relationship between compressive strength and flexural strength. The aim of the study is to predict the flexural strength of 3D-printed reinforced concrete using machine learning methods. The tasks were:

1. Establishing the relationship between the compressive and flexural strengths of concrete and identifying the best predictive models.
2. Identifying the influence of various factors on the mechanical properties of 3D-printed reinforced concrete.
3. Determining the potential for the innovative results obtained.

Materials and Methods

Materials

This study was conducted on geopolymer concrete containing microsilica and sodium silicate. In this research, in order to investigate the effect of microsilica geopolymer concrete and different aggregates, fine and coarse aggregates were mixed in different proportions (Fig. 1). Sodium silicate was sprayed on the concrete as an activator during the curing period due to the creation of an alkaline environment due to the creation of a geopolymer activator. Table 1 shows the mixture design of current study concrete.

Methodology

The compressive strength is based on the ASTM C109 [17] for cube (5 × 5 × 5 cm^3), and flexural strength as three-point bending strength as prism (16 × 4 × 4 cm^3) [18].

Table 1. Current study mixture design

Sample	Micro silica, kg/m³	Water, kg/m³	Fine aggregate, kg/m³	Coarse aggregate, kg/m³	Marble powder, kg/m³	Glass powder, kg/m³	Super-plasticizer, kg/m³
CF100	600	370	1180	0	150	200	55.5
CF80	600	370	944	236	150	200	55.5
CF60	600	370	708	472	150	200	55.5
CF40	600	370	472	708	150	200	55.5
CF20	600	370	236	944	150	200	55.5
CF0	600	370	0	1180	150	200	55.5

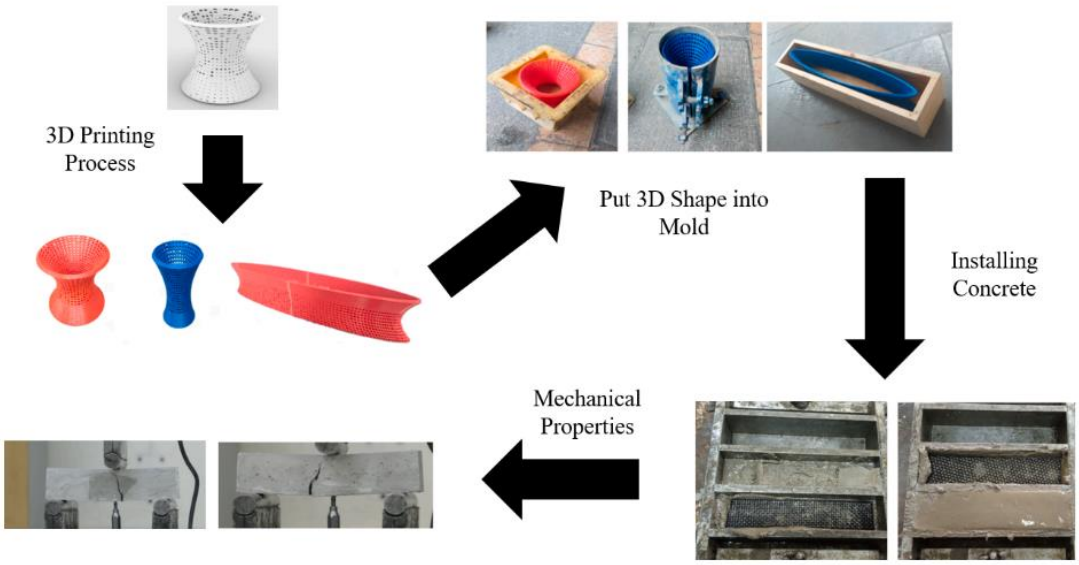

Fig. 1. Scheme of 3D printed reinforced concrete based on [18,19]

Regressions

In this study, Rigid, Lasso, elastic net, dissection tree, random forest, GBoost, SVR and KNN used (Table 2).

Table 2. Current study mixture design

Regression	Alpha	max_ depth	min_ samples_ leaf	min_ samples_ split	_estimators	learning_ rate	C	gamma	kernel
Ridge	0.615	–	–	–	–	–	–	–	–
Lasso	0.885	–	–	–	–	–	–	–	–
Random forest	–	20	1	4	50	–	–	–	–
Gradient boosting	–	9	–	4	50	0.124	–	–	–
SVR	–	–	–	–	–	–	92.76	10.0	rbf

In this term, ridge regression illustrated in Eq. (1) decreases errors and obtains more accuracy [20,21]:

$$v = \delta_0 + \delta_1 w_1 + \delta_2 w_2 + \delta_3 w_3 + \delta_4 w_4 + \varepsilon + \lambda\sum(\delta_1^2 + \delta_2^2 + \delta_3^2 + \delta_4^2), \quad (1)$$

where v is the dependent variable, w is the independent variable, δ_0 is the y-intercept and δ_1 is the regression coefficient representing the change in v concerning the change in w, also called the slope, and λ is the ridge regression penalty ratio, ε is the error term, $\sum(\delta_i^2)$ represents the sum of the squares of the coefficients.

Lasso regression means least absolute shrinkage and selection operator (LASSO). Lasso regression is a usual regression for solving multicollinearity issues, while unlike ridge regression, results in some coefficient predictions are equal to zero. Equation (2) shows the Lasso regression equation [21,22]:

$$v = \delta_0 + \delta_1 w_1 + \delta_2 w_2 + \delta_3 w_3 + \delta_4 w_4 + \varepsilon + \lambda\sum|\delta_1| + |\delta_2| + |\delta_3| + |\delta_4|, \quad (2)$$

Support vector machine (SVM) is a classification method for machine learning. In fact, support vector regression is solving problem by SVM as a regression. SVR can solve nonlinear and problems with high-dimensional [23–25].

Elastic net is a linear regression that combines two types of penalty functions to refine the best predictions. The best prediction is analyzed by the Scikit-learn package with a parameter in the range [0,1]. This algorithm is much closed for lasso prediction as the minimum contraction and selection operator. This algorithm reduces the complexity of the algorithm [26,27].

Decision tree is used for classification and prediction as a regression algorithm. In this algorithm, direct nodes are considered as root nodes and internal nodes are called leaf nodes. Usually, nodes in direct tree algorithm predict data category or direct data [28–30].

K-nearest neighbor is a supervised machine learning algorithm that solves problems with a small amount of data, usually for classification, but other studies also use it as regression. KNN solves the problem by finding the distance between the query and all the examples in the data by selecting a certain number of examples (*k*) close to the query, then averaging the labels in the case of a regression problem. The k-nearest neighbor algorithm is as follows [31]:

$$\bar{y} = \frac{1}{k}\sum_{j=1}^{k} y_i, \quad (3)$$

where y_i are actual values of the output characteristic and x_i are training examples attributes, x is test point, k is the number of nearest instances.

Random forest is an effective method that gives consistent answers. The reliability of the random forest method is related to the nature. Random forest is an advanced method related to decision trees with high efficiency [32,33]. All types of regression are applied to find the best prediction result to find the optimal and best result.

Validation

To find the verified prediction, the correlation coefficient (R^2) as expressed in Eq. (3), mean absolute errors (MAE), and root mean squared errors (RMSE) have been established [34]:

$$R^2 = 1 - \frac{\sum(y-\hat{y})^2}{\sum^n(y-\bar{y})^2}. \quad (4)$$

RMSE calculates the average deviation of each actual data point and the predicted results [35]:

$$RSME = \sqrt{\frac{1}{n}\sum^n(y-\hat{y})^2}. \quad (5)$$

Data collection

To data collection in this study, concrete mixture designs and concrete mechanical properties have been selected as the main parameter, in fact, compressive strength known as main character and the flexural strength known as the predictive character. This study used 3D printing study to collect data to find the concrete mixture and mechanical properties [18,19,36–39]. Due to lack of information about 3D printed reinforced concrete, Gaussian Noise has been selected to increase data more than 2000 with regard pervious data study.

Results

Hyperparameter and data

This heat map visually shows the distribution and intensity of different properties or components in a concrete mixture. A colour spectrum is used to highlight differences, with warm colours (such as red) representing higher values and cool colours (such as blue) representing lower values. This helps to quickly identify patterns, correlations, or anomalies in the data.

Figure 2 heat map visually displays the relationships between the various components of concrete and its mechanical properties. Correlation values close to 1 indicate a strong and direct relationship between the variables, while values close to (-1) indicate a strong and inverse relationship. For example, the strong negative correlation between water and compressive strength (-0.94) indicates that increasing the amount of water significantly reduces the compressive strength of concrete. On the other hand,

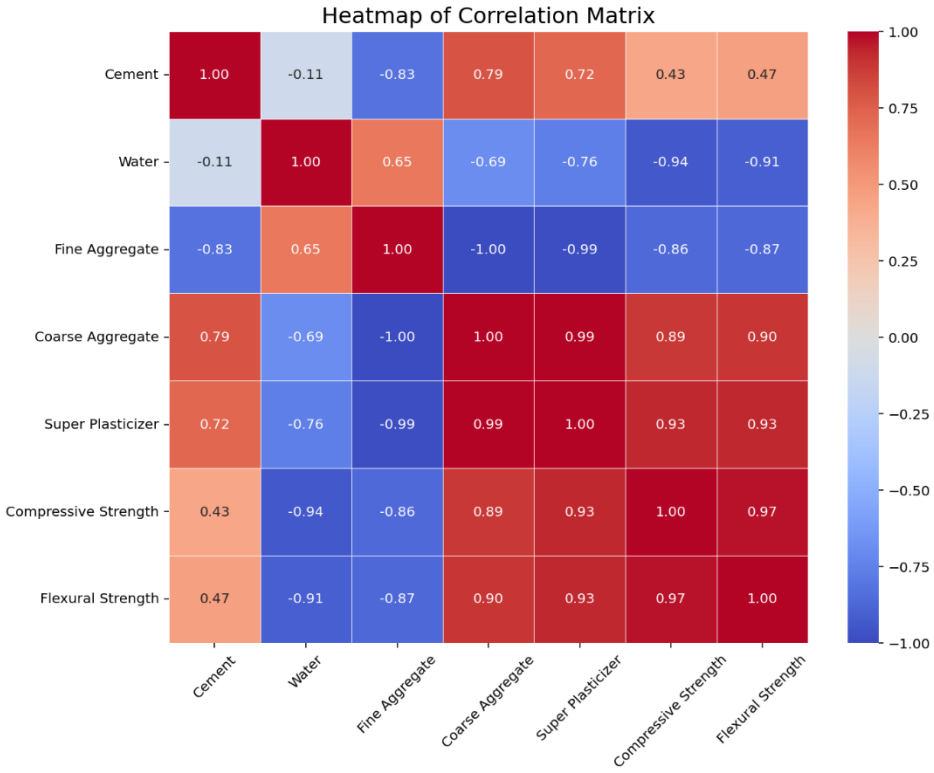

Fig. 2. Heatmap of concrete

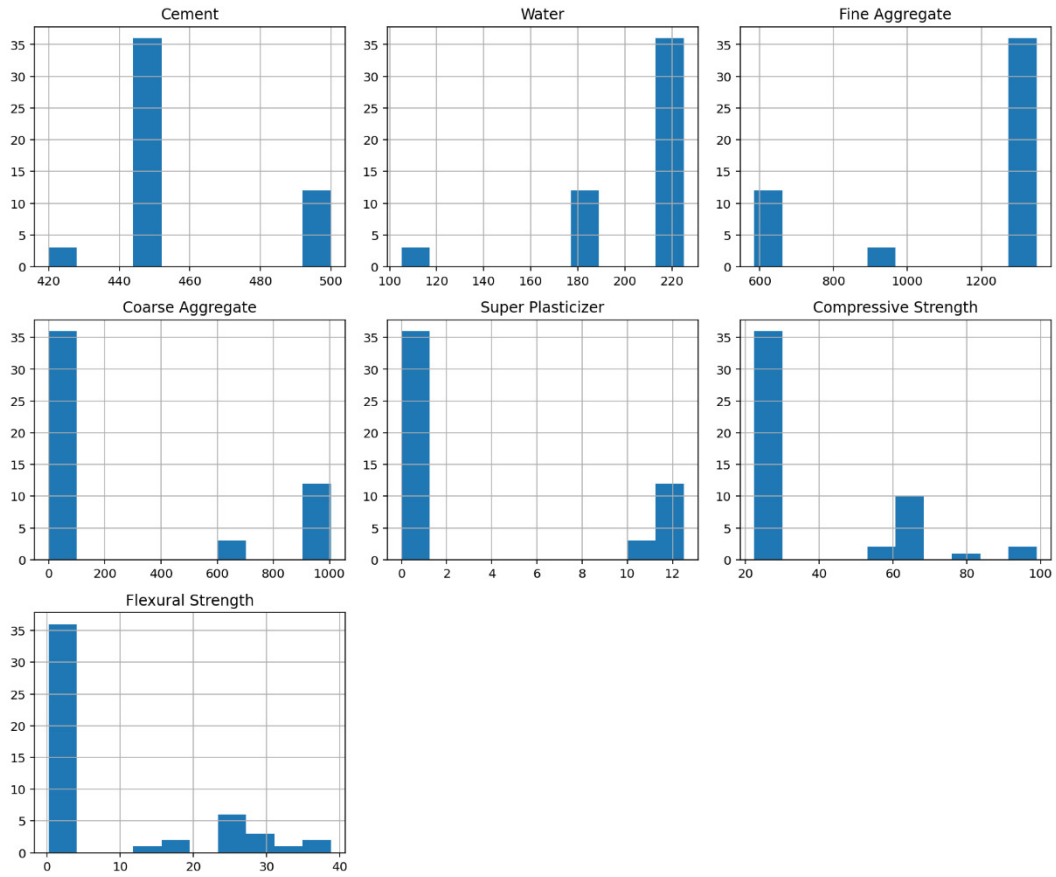

Fig. 3. Data distribution of current study

the positive correlation between coarse aggregate and compressive strength (0.89) indicates a positive effect of this material on increasing strength. Moreover, flexural strength and compressive strength have more than 0.97 positive effect. According to heat map water and fine aggregates have negative effect on the compressive and flexural strength, which means increasing fine aggregates and water can decrease the compressive and flexural strengths.

Figure 3 shows the distribution of the data collected in this study. This graph visually shows the dispersion and concentration of data related to concrete mix design and its mechanical properties. By examining this graph, it is possible to identify patterns in the data and use it for further analysis.

In the second part, Fig. 3 shows how the data is distributed across different ranges. This distribution helps researchers better understand the relationship between different variables, such as the compressive and flexural strengths of concrete. It can also reveal outliers or unusual data that may affect the results.

Finally, Fig. 3 serves as an auxiliary tool to verify the quality of the data used in machine learning models. By viewing this graph, researchers can ensure that the data has been collected in a balanced and representative manner, which increases the accuracy of the predictions made by the models.

Figure 4 in this study shows the scatter plot between flexural strength, compressive strength and other related data. These plots are plotted in pairs to clearly show the linear or nonlinear relationships between different variables. In the second part, Fig. 4 shows

how other factors such as cement content, water and aggregates affect the strength of concrete. For example, increasing the water content reduces the compressive and flexural strengths, while cement and coarse aggregates have a positive effect on the strength of concrete. These relationships help researchers to understand the factors affecting the mechanical properties of concrete and design prediction models more accurately.

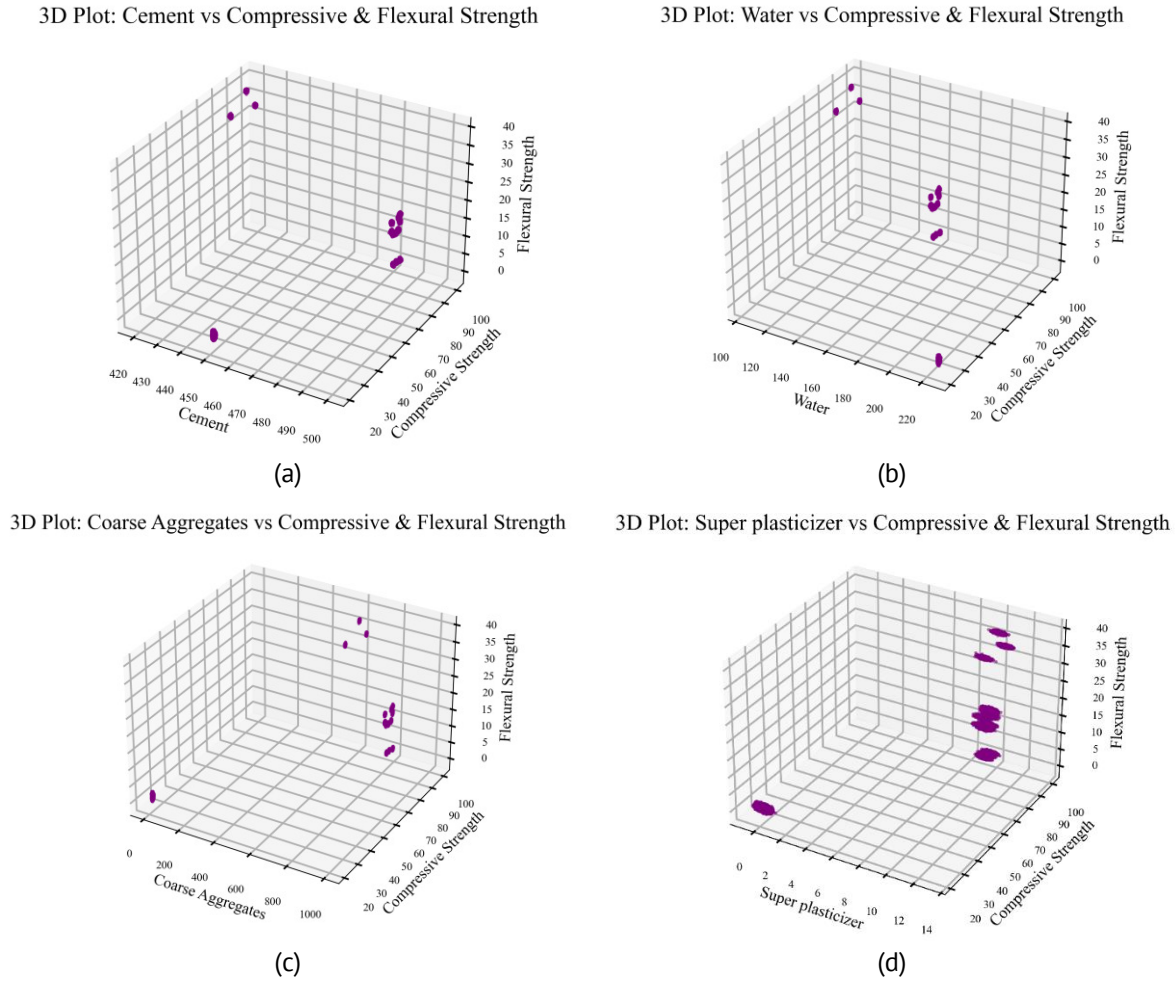

Fig. 4. The scatter plot between flexural strength, compressive strength and other data: (a) cement, (b) water, (c) coarse aggregates, (d) super plasticizer

Finally, Fig. 4 is used as an aid to validate data and machine learning models. By comparing the dispersion of the actual and predicted data, we can evaluate the accuracy of different models. These graphs also show that some models, such as Gradient Boosting and Random Forest, were able to identify patterns in the data well and provide more accurate predictions.

Figure 5(a) shows a multi-bar diagram of the gradient reinforcement model that ranks the factors affecting a system (i.e., concrete strength). In this diagram, cement is identified as the most important factor (around 0.35) as the key factor, while fine aggregate and water are in the next ranks. Other products such as superplasticizer and coarse aggregate have negligible or close to zero effects. These results indicate that the model considers cement as the most important variable in its prediction.

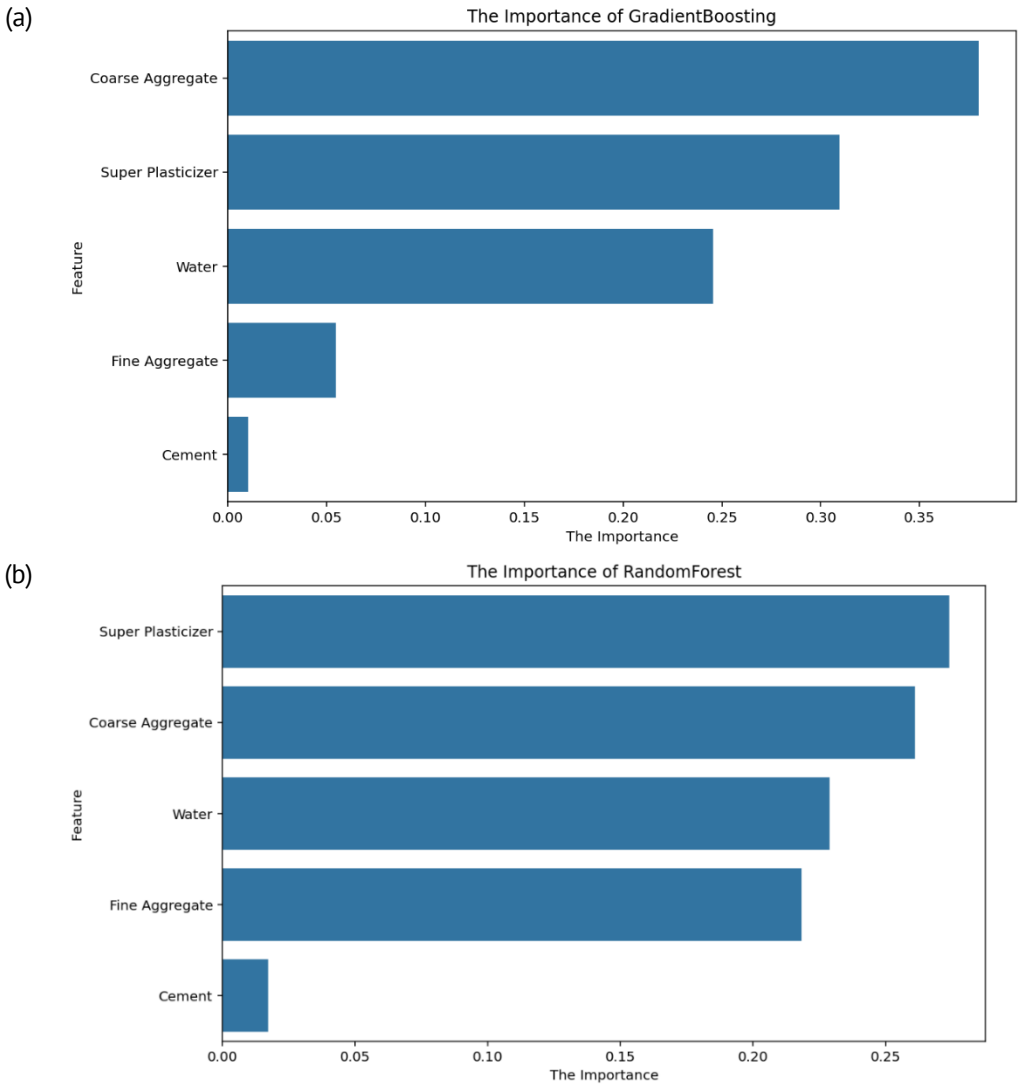

Fig. 5. The importance and features: (a) GBoost; (b) random forest

Figure 5(b) shows the importance of variables in the random forest model, indicating the influence of each factor on the model predictions. In this plot, cement is identified as the most influential variable with an importance of about 0.25. This is followed by fine aggregate and water with an importance of about 0.15 and 0.10, respectively. Other variables such as super plasticizer, coarse aggregate and unspecified Feature are less important, with some of them having a negligible impact on the model. These results indicate that cement plays a key role in the predictions of this model.

Regressions

All regression results are shown in Fig. 6. Considering to regression results the most data are divided by to clusters, however in KNN and random forest regressions three clusters are existed. In the first cluster, data are complex and close together, while data in the middle of data set are scatters.

Table 3 compares the performance of eight different regression models based on two metrics: r^2 (coefficient of determination) and RMSE (root mean square error). The models

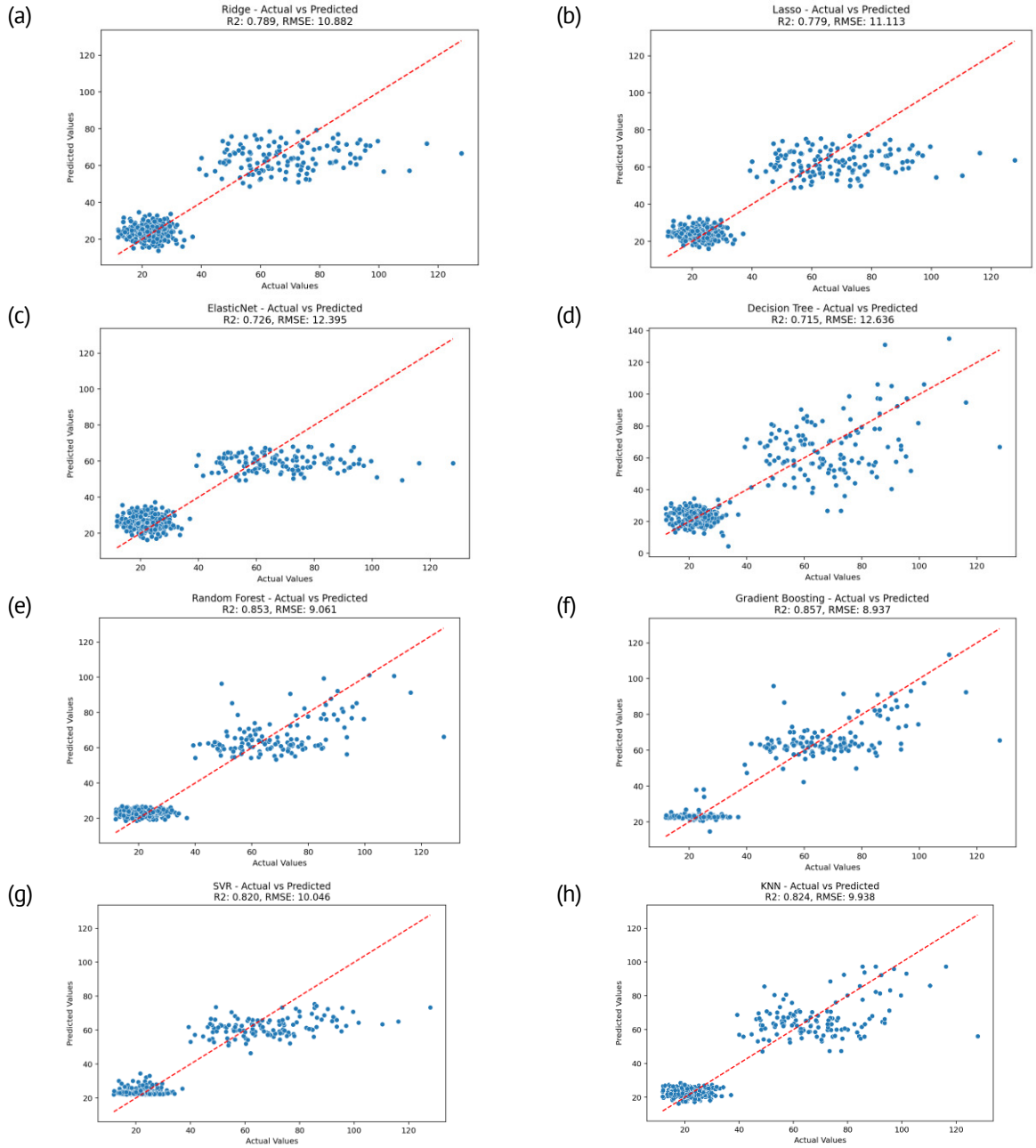

Fig. 6. Regression results: (a) Rigid; (b) Lasso; (c) elastic net; (d) dissection tree; (e) random forest;(f) GBoost; (g) SVR; (h) KNN

Table 3. Regression results of current studies

Regression	R^2	**RSME**
Rigid	0.78	10.88
Lasso	0.77	11.11
Elastic net	0.12	12.39
Decision tree	0.71	12.63
Random forest	0.85	9.06
GBoost	0.85	8.93
SVR	0.81	10.04
KNN	0.89	9.93

studied include ridge regression (Rigid), lasso (Lasso), elastic net (elastic net), decision tree (decision tree), random forest (random forest), gradient boosting (GBoost), support vector regression (SVR), and k-nearest neighbour (KNN). Among these models, GBoost and random forest performed best with R^2 of 0.85 and RMSE of 8.93 and 9.06, respectively. these results indicate that these two models are able to explain the variance of the data and have low prediction error.

In contrast, the elastic net model has the weakest performance with a very low r^2 (0.12) and a high RMSE (12.39), which is probably due to the model not matching the data structure or its parameters being incorrectly set. The rigid, lasso and SVR models have average performance with r^2 values between 0.77, 0.81, and RMSE between 10.04 and 11.11. Although these models are acceptable, they have lower accuracy than GBOOST and random forest. Also, the KNN model has a relatively high RMSE (9.93) despite a high r^2 (0.89), which may be overfitting in some data.

Finally, it can be concluded that GBOOST is recommended as the best model, as it has the highest r^2 and lowest RMSE, which provides a good balance between accuracy and generalizability. However, the final model choice also depends on the specific project needs and computational costs. For example, if the interpretability of the model is important, random forest is a better option, while KNN may be more suitable for low-dimensional data. Also, tuning the hyperparameters of weaker models such as elastic net can help improve their performance.

The Taylor plot clearly shows that the GBoost and Random Forest models have higher accuracy in predicting flexural strength compared to other models. The best results of regression were for KNN, Random Forest and GBoost. Other studies are investigated on this type of regressions. For example, Zhu et al. [40] studies basalt fiber reinforced concrete with PSO-KNN method, they found that this method have more than 0.96 and 0.98 accuracy with R^2. Elastic Net was a powerful regression, however in this

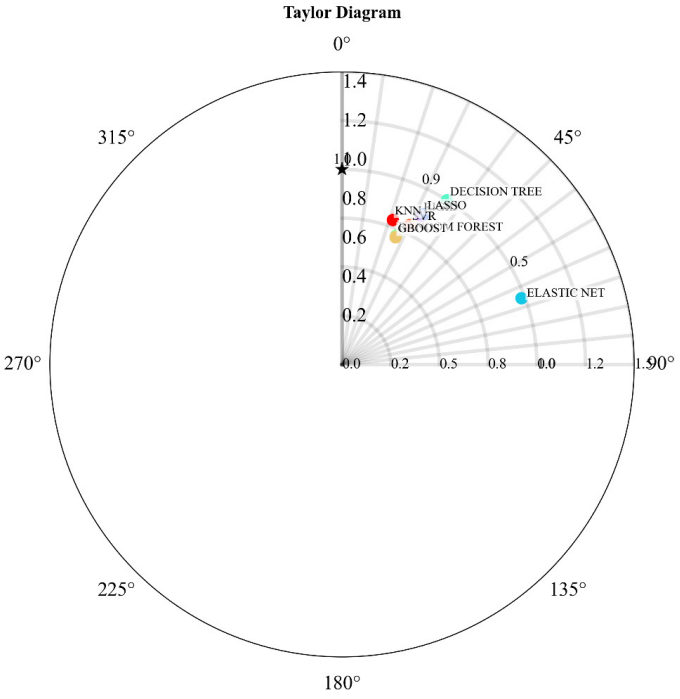

Fig. 7. Taylor diagram

study result of this regression was 0.12, while other studies show that when concrete predicted with Elastic Net regression, result is more than 0.98 [27]. These two models are located near the centre of the plot and have high correlation, indicating a good match between the actual data and the data predicted by these algorithms. In contrast, models such as Elastic Net, which are further away from the reference point, show poorer prediction performance. The use of the Taylor plot in this study is an effective visual tool for making the final decision in choosing the most appropriate machine learning algorithm (Fig. 7).

The obtained results are in good agreement with the results of independent authors, for example [41]. The obtained results are applicable in the design of 3D printed reinforced concrete.

Conclusions

This study investigated the prediction of flexural strength of 3D printed reinforced concrete using machine learning techniques.

1. The results showed that there is a strong relationship between the compressive and flexural strengths of concrete with a correlation coefficient of more than 0.97, which allows for more accurate prediction of flexural strength. Also, the gradient strengthening, random forest, and KNN models were identified as the best predictive models with R^2 values of 0.85, 0.85, and 0.89, respectively.
2. Among the key findings of this study was the significant effect of cement as the most important factor on concrete strength and the negative effect of water and fines on mechanical properties. These results not only help to better understand the behavior of 3D printed reinforced concrete but also provide valuable guidance for optimizing concrete mixing designs in the future. Also, the use of machine learning methods in this field is a new step towards increasing accuracy and reducing laboratory costs.
3. Finally, as one of the first comprehensive studies on the prediction of flexural strength of 3D printed reinforced concrete, this research paves the way for future research in this field. Despite the promising results, there is a need to develop more accurate models with more extensive data and to investigate the influence of other parameters such as fiber type and printing geometries.

CRediT authorship contribution statement

Mohammad Hematibahar: writing – review & editing, writing – original draft; **Makhmud Kharun**: writing – original draft, conceptualization; **Roman S. Fediuk**: writing – original draft, investigation; **Nikolai I. Vatin**: writing – original draft, supervision; **Maxim G. Porvadov**: writing – original draft, data curation; **Linar S. Sabitov**: writing – review & editing, writing – original draft.

Conflict of interest

The authors declare that they have no conflict of interest.

References

1. Esparham A, Vatin NI, Kharun M, Hematibahar M. A Study of Modern Eco-Friendly Composite (Geopolymer) Based on Blast Furnace Slag Compared to Conventional Concrete Using the Life Cycle Assessment Approach. *Infrastructures*. 2023;8(3): 58.
2. Kim T, Tae S, Roh S. Assessment of the CO_2 Emission and Cost Reduction Performance of a Low-Carbon-Emission Concrete Mix Design Using an Optimal Mix Design System. *Renew. Sustain. Energy Rev.* 2013;25: 729–741.
3. Chen C, Zhang X, Hao H, Sarker PK. Experimental and Numerical Study of Steel Fibre Reinforced Geopolymer Concrete Slab under Impact Loading. *Engineering Structures*. 2025;322: 119096.
4. Asante B, Wang B, Yan L, Kasal B. Optimized Mix Design and Fire Resistance of Geopolymer Recycled Aggregate Concrete under Elevated Temperatures. *Case Studies in Construction Materials*. 2025;22: e04401.
5. Amin M, Elsakhawy Y, Abu El-Hassan K, Abdelsalam BA. Behavior Evaluation of Sustainable High Strength Geopolymer Concrete Based on Fly Ash, Metakaolin, and Slag. *Case Studies in Construction Materials*. 2022;16: e00976.
6. Feng Y, Zhang Q, Chen Q, Wang D, Guo H, Liu L, Yang Q. Hydration and Strength Development in Blended Cement with Ultrafine Granulated Copper Slag. *PLoS ONE*. 2019;14(4): e0215677.
7. Wu X, Shen Y, Hu L. Formance of Geopolymer Concrete Activated by Sodium Silicate and Silica Fume Activator. *Case Studies in Construction Materials*. 2022;17: e01513.
8. Akeed MH, Qaidi S, Ahmed HU. Ultra-High-Performance Fiber-Reinforced Concrete Part II: Hydration and Microstructure [J]. *Case Stud. Constr. Mater.* 2022;17: e01289.
9. Fu C, Ye H, Zhu K, Fang D, Zhou J. Alkali Cation Effects on Chloride Binding of Alkali-Activated Fly Ash and Metakaolin Geopolymers. *Cement and Concrete Composites*. 2020;114: 103721.
10. de Oliveira LB, Marvila MT, Pereira EC, Vieira CMF, de Azevedo ARG, Fediuk R. Durability of geopolymers with industrial waste. *Case Studies in Construction Materials*. 2022;16: e00839.
11. Mintsaev MSh, Murtazaev SAY, Salamanova MSh, Saidumov MS, Murtazaev ISA. Features of the synthesis of construction geopolymer composites. *Construction Materials and Products*. 2025;8(2): 6.
12. Jan A, Khubaib M, Ahmad I. Evaluation of Effect of Polypropylene on the Mechanical Properties of Concrete. *International Journal of Innovative Science and Research Technology*. 2018;3(1): 194–202.
13. Abdallah S, Fan M, Zhou X, Le Geyt S. Anchorage Effects of Various Steel Fibre Architectures for Concrete Reinforcement. *Int. J. Concr. Struct. Mater.* 2016;10: 325–335.
14. Guo X, Xiong G. Resistance of Fiber-Reinforced Fly Ash-Steel Slag Based Geopolymer Mortar to Sulfate Attack and Drying-Wetting Cycles. *Constr. Build. Mater.* 2021;269: 121326.
15. ASTM International. ASTM C 109. *Standard Test Method for Compressive Strength of Hydraulic Cement Mortars (Using 2-in. or [50-Mm] Cube Specimens)*. West Conshohocken, PA: ASTM International: 2017.
16. Levkina EV, Titova NY. The Analysis of the Financial Condition of Small Business and the Ways of its Development in the Primorsky Territory. *IOP Conference Series: Earth and Environmental Science*. 2019;272(3): 032185.
17. National Standard of the People's Republic of China. GB/T 17671. *Method of Testing Cements-Determination of Strength*. Beijing, China: Standardization Administration of the People's Republic of China; 1999.
18. Hematibahar M, Hasanzadeh A, Vatin NI, Kharun M, Shooshpasha I. Influence of 3D-Printed Reinforcement on the Mechanical and Fracture Characteristics of Ultra High-Performance Concrete. *Results Eng.* 2023;19: 101365.
19. Hematibahar M, Milani A, Fediuk R, Amran M, Bakhtiary A, Kharun M, Mousavi MS. Optimization of 3D-Printed Reinforced Concrete Beams with Four Types of Reinforced Patterns and Different Distances. *Engineering Failure Analysis Journal*. 2025;168: 109096.
20. Abhishek T. Comparative Assessment of Regression Models Based On Model Evaluation Metrics. *International Research Journal of Engineering and Technology*. 2021;8(9): 853–860.
21. Enwere K, Nduka E, Ogoke U. Comparative Analysis of Ridge, Bridge and Lasso Regression Models In the Presence of Multicollinearity. *IPS Intelligentsia Multidisciplinary Journal*. 2023;3(1): 1–8.
22. Melkumova L, Shatskikh S. Comparing Ridge and LASSO Estimators for Data Analysis. *Procedia Engineering*. 2017;201: 746–755.
23. Kennedy J, Eberhart R. Particle Swarm Optimization. In: *Proceedings of ICNN'95 - International Conference on Neural Networks*. 1995. p.1942–1948.
24. Smola AJ, Scholkopf BA. A Tutorial on Support Vector Regression. *Stat. Comput.* 2004;14: 199–222.
25. Huang Y, Lei Y, Luo X, Fu C. Prediction of Compressive Strength of Rice Husk Ash Concrete: A Comparison of Different Metaheuristic Algorithms for Optimizing Support Vector Regression. *Case Studies in Construction Materials*. 2023;18: e02201.

26. Zou H, Hastie T, Stat JR. Regularization and Variable Selection via the Elastic Net. *Soc. Series B Stat. Methodol.* 2005;67: 301–320.
27. Shahrokhishahraki M, Malekpour M, Mirvalad S, Faraone G. Machine Learning Predictions for Optimal Cement Content in Sustainable Concrete Constructions. *Journal of Building Engineering.* 2024;82: 108160.
28. Myles AJ, Feudale RN, Liu Y, Woody NA, Brown SD. An Introduction to Decision Tree Modeling. *J. Chemom. A J. Chemom. Soc.* 2004;18(6): 275–185.
29. Song YY, Ying L. Decision Tree Methods: Applications for Classification and Prediction. *Shanghai Arch. Psychiatry.* 2015;27(2): 130.
30. Hematibahar M, Kharun M, Beskopylny A, Stel'makh S, Shcherban E, Razveeva I. Analysis of Models to Predict Mechanical Properties of High-Performance and Ultra-High-Performance Concrete Using Machine Learning. *Journal of Composites Science.* 2024;8: 287.
31. Beskopylny AN, Stel'makh SA, Shcherban' EM, Mailyan LR, Meskhi B, Razveeva I, Chernil'nik A, Beskopylny N. Concrete Strength Prediction Using Machine Learning Methods CatBoost, k-Nearest Neighbors, Support Vector Regression. *Appl. Sci.* 2022;12(21): 10864.
32. Sun Y, Li G, Zhang I, Qian D. Prediction of the Strength of Rubberized Concrete by an Evolved Random Forest Model. *Adv. Civil Eng.* 2019;2019: 198583.
33. Ganesh AC, Mohana R, Loganathan P, Kumar VM, Kırgız MS, Nagaprasad N, Ramaswamy K. Development of Alkali Activated Paver Blocks for Medium Traffic Conditions Using Industrial Wastes and Prediction of Compressive Strength Using Random Forest Algorithm. *Sci. Rep.* 2023;13: 15152.
34. Karl P. Notes on Regression and Inheritance in the Case of Two Parents. In: *Proceedings of the Royal Society of London.* 1895. p.240–242.
35. Hastie T, Tibshirani R, Friedman J. *The Elements of Statistical Learning: Data Mining, Inference, and Prediction.* Springer; 2013.
36. Momeni K, Vatin NI, Hematibahar M, Gebre T. Differences between 3D Printed Concrete and 3D Printing Reinforced Concrete Technologies: A Review. *Frontiers in Built Environment* 2025, 10, doi:
37. Hematibahar M, Hasanzadeh A, Kharun M, Beskopylny AN, Stel'makh SA, Shcherban' EM. The Influence of Three-Dimensionally Printed Polymer Materials as Trusses and Shell Structures on the Mechanical Properties and Load-Bearing Capacity of Reinforced Concrete. *Materials.* 2024;17(14): 3413.
38. Hematibahar M, Vatin NI, Hamid TJ, Gebre TH. Effect of Using 3D-Printed Shell Structure for Reinforcement of Ultra-High-Performance Concrete. *Structural Mechanics of Engineering Constructions and Buildings*. 2023;19(5): 534–547.
39. Chiadighikaobi PC, Hasanzadeh A, Hematibahar M, Kharun M, Mousavi MS, Stashevskaya AN, Adedapo Adegoke M. Evaluation of the Mechanical Behavior of High-Performance Concrete (HPC) Reinforced with 3D-Printed Trusses. *Results Eng.* 2024;22: 102058.
40. Zhu M, Lin J, Cao G, Zhang J, Zhang X, Zhou J, Gao Y. Prediction of Constitutive Model for Basalt Fiber Reinforced Concrete Based on PSO-KNN. *Heliyon*. 2024;10: e32240.
41. Amran M, Onaizi AM, Makul N, Abdelgader HS, Tang WC, Alsulam BT, Alluqmani AE, Gamil Y. Shrinkage mitigation in alkali-activated composites: A comprehensive insight into the potential applications for sustainable construction. *Results in Engineering.* 2023;20: 101452.

MATERIALS PHYSICS AND MECHANICS RESEARCH ARTICLE

Submitted: October 5, 2024 **Revised: May 21, 2025** **Accepted: August 1, 2025**

Structural behavior of reinforced concrete beams incorporating cocopeat as a partial sand replacement

T.Q.K. Lam [1] ✉, M.T. Nguyen [2], H.K. Lam [1], K.S. Sreekeshava [3]

[1] Mien Tay Construction University, Vinh Long, Vietnam

[2] Vinh Long Water Supply Joint Stock Company, Vinh Long, Vietnam

[3] Jyothy Institute of Technology, Visvesvaraya Technological University, Belagavi, India

✉ lamkhai@mtu.edu.vn

ABSTRACT

This study investigated the reinforced concrete beams' structural behavior when the sand aggregate is partially replaced with coconut peat also known as cocopeat. The concrete mixes were prepared by 0, 20, 50 and 100 % variation levels of replacement. Flexural loading tests were conducted on the reinforced concrete beams by also considering the variations in stirrup spacing and main bar diameters. The results indicated that, replacement up to 20 % of sand with hardened cocopeat maintained acceptable structural performance with those with 20 % replacement presented a comparable load bearing capacity and crack resistance to control specimen. Greater than 20 % replacement level exhibited significant reduction in strength and stiffness. The results also revealed that closer stirrup spacing, and larger diameter steel bars overcome the limitations of cocopeat content, improving the beam performance. The study supports the potential use of cocopeat as partial sand replacement in sustainable concrete construction.

KEYWORDS

construction materials • cocopeat • sand content • hardening method • sand aggregate

Citation: Lam TQK, Nguyen MT, Lam HK, Sreekeshava KS. Structural behavior of reinforced concrete beams incorporating cocopeat as a partial sand replacement. *Materials Physics and Mechanics*. 2025;53(4): 35–52. http://dx.doi.org/10.18149/MPM.5342025_3

Introduction

The depletion of natural sand resources globally, mainly spearheaded by rapid urbanization and infrastructure development, has increased the demand for use of sustainable alternatives in concrete production. In Mekong Delta region of Vietnam, this issue has led to intrusion of government agencies and research institutions, to bring in policies to promote the use of sea sand, crushed sand and recycled aggregates and also revise the existing material standards [1,2]. Despite the efforts, there is a long way to reach the goal of achieving a fully sustainable and structurally viable alternative to natural sand.

Recent studies have explored a wide variety of alternative construction materials including limestone, fly ash, iron slag, thermal ash, recycled aggregates and composite additives such as fiberglass and carbon fibers [3–9]. These materials have exhibited promising outcomes by increasing concrete strength and durability. Addition of steel and synthetic fibers have exhibited improved tensile and flexural strength in reinforced concrete structures [10], whereas material efficiency is achieved from hollow mortar concrete [11]. Natural fibers including coir and jute have been utilised for low strength application-based cements [12–17].

Ongoing studies are investigating the use of local sand (from sand dunes) and sea sand as alternatives to traditional sand in concrete production. Some researchers have studied these sands as replacements for river sand in concrete for rural traffic works, helping to reduce the pressure on sand usage [18–21].

Research from BLDEA in India focuses on "Recent trends in replacing natural sand with different types of sand". The study finds that adding copper slag enhances compressive, tensile, and flexural strength in concrete. Concrete density increases with copper slag use, and the flexural strength of beams improves significantly by 21 to 51 % when replacing sand with copper slag. Additionally, using waste sand from the casting industry, bricks, and mining dust as sand substitutes noticeably improves concrete's compressive and flexural strength [22].

Artificial sand production involves crushing natural rocks such as limestone, laterite, granite, and gravel into particles with a modulus similar to natural sand. This material shows comparable characteristics to natural sand, making it a viable alternative for concrete production. Artificial sand has become popular in Europe and Japan, effectively reducing dependence on natural sand and addressing sand scarcity. It enhances concrete quality and minimizes the environmental impact of sand mining [23–26].

Recycled sand production uses various raw materials, including concrete, bricks, tiles, and soil and rocks from previous construction projects. Manufacturing industries like iron, steel, and glass production also generate waste sand that can be repurposed into recycled sand [27]. Studies indicate that recycled sand has potential applications in construction, building materials, and transportation infrastructure. It can also produce lightweight concrete, offering excellent sound and heat insulation [28–31].

Numerous studies are currently exploring the use of coconut fiber (Fig. 1) as a reinforcing material in concrete and its application in unburnt and pavement bricks [32]. Additionally, projects utilize lightweight concrete for benefits such as weight reduction, soundproofing, insulation, and decoration. Using coconut peat as a sand substitute in concrete offers several advantages, including weight reduction and environmental protection. Ben Tre, recognized for its extensive coconut growing area in Vietnam, reports a projected coconut area of over 78,000 hectares by the end of 2022. Coconut fiber is a significant export product for the province, with exports reaching nearly 49,000 tonnes in 2019 and around 45,000 tons in 2020. A coconut shell consists of 30 % coconut fiber and 70 % cocopeat. Cocopeat, with a size range of 0.01 to 0.46 mm and a density of 1.15–1.46 g/cm^3, is notable for its exceptional water absorption capacity [33,34].

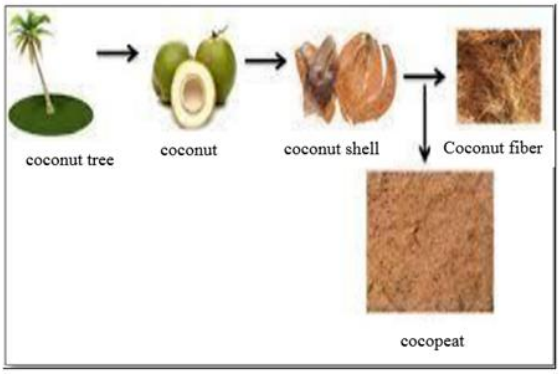

Fig. 1. Coconut fiber and cocopeat. Based on [35]

Numerous studies have investigated the use of coconut fiber as an alternative to sand in concrete. While research on using cocopeat as a sand replacement is limited, it presents a promising area for further exploration. Existing studies have mainly focused on the mechanical properties and durability of concrete with coconut fiber as a partial or complete substitute for sand. Avinash Singh and his colleagues [36] conducted an experimental study showing that incorporating coconut fiber at a rate of 5 % by weight of cement significantly improved the compressive and tensile strength of concrete. Another study examined how coconut fiber affects concrete's mechanical properties and its ability to enhance the bond between concrete and steel reinforcement. This research found that the optimal amount of coconut fiber to add ranged from 0.6 to 1.2 % of the total mass, depending on the desired properties of the final product [37].

Researchers have also explored using the water absorption properties of cocopeat, along with other by-products such as shells and rice husk ash, to develop eco-friendly permeable concrete and produce large-sized unburnt bricks. These products combine cement, stone powder, coal slag, and coconut fiber [38,39].

One study aimed to evaluate the mechanical strength of concrete grade M25, according to Indian standards, by substituting 10 % of sand with cocopeat. The results revealed a notable increase in compressive strength for concrete made with cocopeat treated with a 2 % NaOH solution for 1 h, compared to conventional concrete. On the 28th day, the compressive strength improved by approximately 15.39 % compared to concrete without NaOH treatment [40,41].

Another study assessed the effects of replacing sand with cocopeat in reinforced concrete beams. Researchers tested nine samples of reinforced concrete beams, labeled D1 to D9, with dimensions of 15 × 20 × 120 cm^3. Each beam was reinforced with four D10-CB400-V steel bars and had D6-CB240-T steel stirrups. The researchers used the "hardening method" to incorporate cocopeat as a sand aggregate replacement in the concrete.

Irrespective of numerous studies examining the coconut fiber in concrete, very limited studies have been performed on analyzing the structural performance of reinforced concrete beams when cocopeat is used as sand replacement. The main objective of this study is to evaluate the flexural behavior of the RC beams by varying the cocopeat contents and reinforcement configurations.

The objectives include:

1. Preparation and testing of concrete beams with different cocopeat replacements ratios.
2. Analysis of the influence of stirrups spacing and steel bar diameter on structural performance.
3. Determination of optimal replacement level of sand with cocopeat for maintaining the structural integrity.

Materials and Methods

Materials

Cocopeat, a by-product derived from the husks of coconuts, was used in this study as a partial or full replacement for fine aggregate in the concrete mixtures. Cocopeat has unique properties, including a bulk density of 70–100 kg/m^3, high water retention capacity of 600–800 % due to its porous structure, and an organic content of 20–30 %

lignin and cellulose, making it lightweight. The cocopeat particles were sieved to pass through a 2.5 mm sieve and retained by a 0.63 mm sieve. For comparison, natural river sand served as the control fine aggregate. The sand used in the study had a bulk density of 1600–1700 kg/m^3, a fineness modulus of 2.3–3.1, and particles that passed through a 4.75 mm sieve, with low water absorption, typically around 1–2 %.

Ordinary portland cement (OPC) was the binding material in the concrete mix, with key properties such as a grade of OPC 42.5, a specific gravity of 3.15, and fineness passing through a 90 μm sieve. The cement had an initial setting time of 30 min, a final setting time of about 600 min, and a compressive strength of around 42.5 MPa after 28 days. Crushed stone was used as the coarse aggregate in the concrete, with properties including a maximum size of 20 mm, a bulk density of 1450–1550 kg/m^3, and a specific gravity of 2.65–2.75. Its water absorption was low, at 0.5–1.0 %, and it had a crushing value of less than 30 %, indicating its suitability for structural applications.

The water used in the concrete mix was potable, free from impurities, and appropriate for mixing and curing. Its pH level ranged from 6.5 to 8.5, ensuring neither excessive acidity nor alkalinity. The water-to-cement ratio for all beam samples was maintained at approximately 0.57, ensuring adequate hydration of the cement while providing the necessary workability for the concrete.

Steel reinforcement for the concrete beams was provided according to the specified stirrup spacing for each beam, which ranged between s100, s150, and s150–s200. This reinforcement was essential for ensuring the structural integrity of the beams and improving their load-bearing capacity. High-yield strength deformed steel bars of Grade 60 were used for the reinforcement, which offered high resistance to tensile forces. The diameter of the steel bars varied based on the specific design of each beam, typically ranging from 10 to 16 mm. The yield strength of the steel was approximately 420 MPa, contributing to the overall durability and performance of the reinforced concrete beams under loading conditions.

Hardening process of cocopeat

A total of 120 kg of cocopeat particles hardened with cement was obtained by repeatedly performing the hardening process. The particles were meticulously selected to ensure they remained on the 0.63 mm sieve and passed through the 2.5 mm sieve. Table 1 indicates the optimal water quantity used for hardening the cocopeat with cement.

Table 1. Optimal water content for hardening cocopeat with cement

Cocopeat, g	Cement, g	Optimal amount of water, ml	Finished product, g
100	500	400	760–800

The process of hardening cocopeat with cement involved the following steps:
Step 1: the coconut shells were dried in the sun for one day. A 2.5 mm sieve was used to separate the cocopeat (see Fig. 2).
Step 2: 100 g of cocopeat was measured and wet with 100 ml of water (Fig. 3).
Step 3: 100 g of cement was weighed and mixed thoroughly with the wet cocopeat obtained in Step 2 (Fig. 4).

(a) (b)

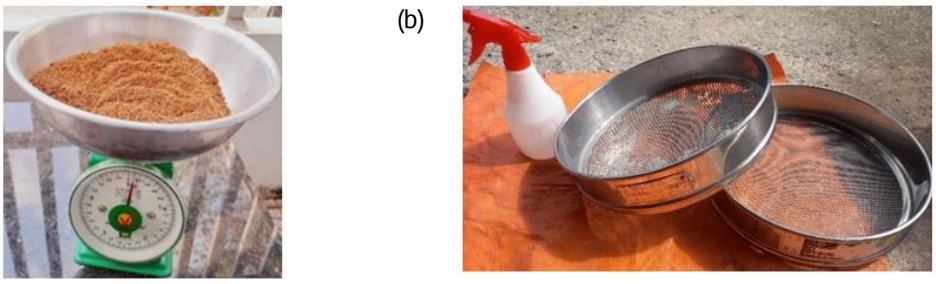

Fig. 2. Cocopeat after step 1 processing: (a) determine the weight of cocopeat, (b) 2.5 mm sieves

Fig. 3. Cocopeat after wetting with 100 ml of water

Fig. 4. Cocopeat after mixing with 100 g of cement

Fig. 5. Combine the cocopeat and cement mixture

Step 4: after 15 min, the mixture is combined. The resulting particles passed through the 2.5 mm sieve and were retained by the 0.63 mm sieve (Fig. 5): (a) cocopeat after wetting (Fig. 3), (b) cocopeat and cement mixture after combining (Fig. 4), (c) final cocopeat and cement mixture after sieving (Fig. 5).

Step 5: the particles that passed through the 1.5 mm sieve were wetted by spraying water evenly over their surface. These particles were mixed with 60 g of cement, repeating the process as in Step 4, until they passed through the 2.5 mm sieve but were retained by the 0.63 mm sieve.

Step 6: the mixture is allowed to solidify for 24 h. Then, the hardened particles are sieved. The final product consisted of particles that pass through the 2.5 mm sieve and retained by the 0.63 mm sieve (Fig. 6).

(a) (b)

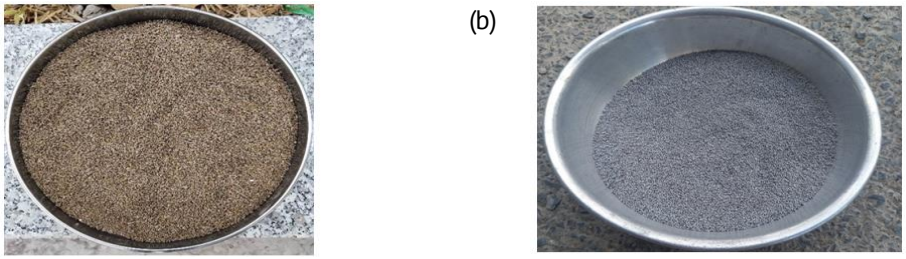

Fig. 6. Cocopeat hardened with cement: (a) finished product remaining on 0.63 mm sieve, (b) finished cocopeat granules have been hardened with cement

Design of reinforced concrete beams

The study involved nine reinforced concrete beams, with variations in stirrup spacing and proportions of cocopeat replacing sand as a fine aggregate and is denoted from D1 to D9 (group 1: D1, D2, D3, D4; group 2: D5, D6, D7, D8; group 3: D9 (Fig. 7)). Table 2 summarizes

the beam compositions, detailing the amounts of sand, cocopeat, cement, stone, and water used. The mix design for all specimens was kept constant across each group, with only the fine aggregate (sand/cocopeat ratio) and stirrup spacing varied. Details of each experimental reinforced concrete beam are summarized in Table 2 below.

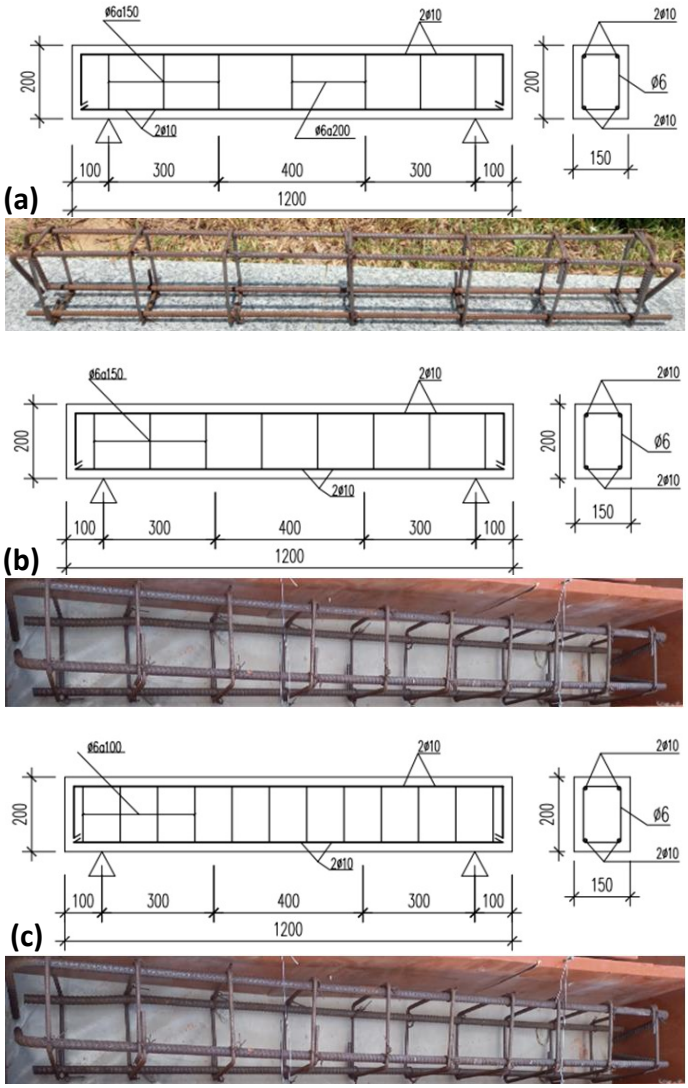

Fig. 7. Design of reinforced concrete beams: (a) group 1 beams, (b) group 2 beams, (c) group 3 beam

Table 2. Details of reinforced concrete beams

Sample groups	Label	Stirrup spacing	$\mu_{cocopeat}$, %	Sand, kg	Cocopeat, kg	Cement, kg	Stone, kg	Water, l
Group 1 Fig. 7(a)	D1	s150-s200	0	22.00	0.00	12.96	43.99	7.38
	D2	s150-s200	20	17.60	4.40	12.96	43.99	7.38
	D3	s150-s200	50	11.00	11.00	12.96	43.99	7.38
	D4	s150-s200	100	0.00	22.00	12.96	43.99	7.38
Group 2 Fig. 7(b)	D5	s150	0	22.00	0.00	12.96	43.99	7.38
	D6	s150	20	17.60	4.40	12.96	43.99	7.38
	D7	s150	50	11.00	11.00	12.96	43.99	7.38
	D8	s150	100	0.00	22.00	12.96	43.99	7.38
Group 3 Fig. 7(c)	D9	s100	50	11.00	11.00	12.96	43.99	7.38

Fig. 8. Formwork and reinforcement processing

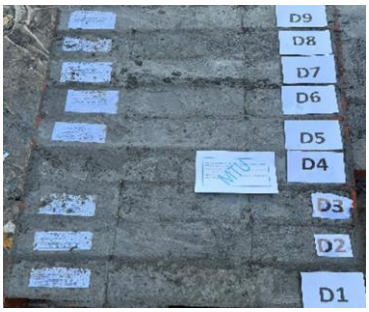

Fig. 9. Reinforced concrete beams

The steel reinforcement for the beams was processed according to the specifications outlined in Table 2 and depicted in Fig. 8. After the reinforcement was properly placed and secured, formwork was installed to shape the beams. Once the reinforcement and formwork were ready, concrete was poured into the forms to create the reinforced concrete beams, as shown in Fig. 9.

Testing procedure of reinforced concrete beams

The analysis of concrete samples with varying percentages of cocopeat as a sand replacement was conducted using a JEOL JSM-IT500HR Scanning Electron Microscope. This advanced equipment allows for high-resolution imaging, enabling detailed examination of the microstructural features of the samples. The samples were prepared for optimal imaging, allowing for insights into transition zones, voids, and crack patterns within the concrete matrix.

The experiment assessed various parameters, including the force applied to the beam, the deflection at the midpoint, and the deformation on both sides of the beam. The experiments aimed to evaluate and compare the bearing capacity of each beam. Beams D1 through D9, made of 28–day–old concrete, were subjected to loading using hydraulic jacks applied at two concentrated points until the beams were completely destroyed. Before testing, the reinforced concrete beams were coated with a layer of white lime to facilitate the observation of crack formation and development on the surface, as well as to enable accurate measurement of crack length and width.

Once the setup and equipment were in place, pressure was applied to the structure using a 50-ton hydraulic jack. This jack, operated by an electric pump, was equipped with an oil pressure gauge ranging from 0 to 10,000 Psi (700 Bar or 500 kN). The bearing capacity of the reinforced concrete beams was calculated based on loading levels of 300, 500, 700, 1000, 1400, 2000, and 2500 Psi. At each loading level, the gauge data were recorded, including displacement (V-1), compression zone deformation (PDT-1 and PDT- 2), and tension zone deformation (PDT-3 and PDT-4). It was crucial to carefully observe crack formation and accurately measure their length and width.

Results and Discussion

SEM analysis

The analysis of concrete samples with varying percentages of cocopeat as a sand replacement was conducted using scanning electron microscopy (SEM).

0 % cocopeat sample: SEM images (Fig. 10) show a dense and smooth matrix with well-defined boundaries. The concrete exhibits minimal porosity and few voids, resulting in strong and cohesive bonding within the matrix. The cracks that appear are predictable and minimal. The interfacial transition zones (ITZ) are smooth and well-integrated, and there are few to no micro spheroids, with shapes being well-defined and uniform.

20 % cocopeat sample: SEM analysis reveals a slightly rougher texture with minor irregularities due to the incorporation of cocopeat (Fig. 11). There is a slight increase in porosity and voids compared to the 0 % cocopeat sample, leading to a slight reduction in bonding strength. Crack patterns show minor irregularities. The ITZ displays minor roughness but remains largely cohesive. Few micro spheroids are present, mostly irregular in shape, and the overall shapes are less uniform.

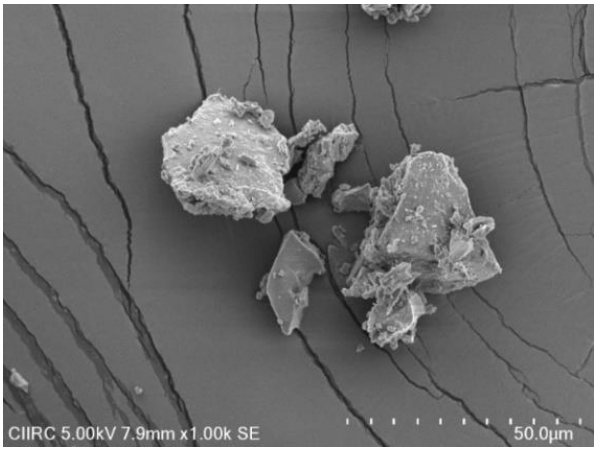

Fig. 10. SEM Image for 0% cocopeat sample

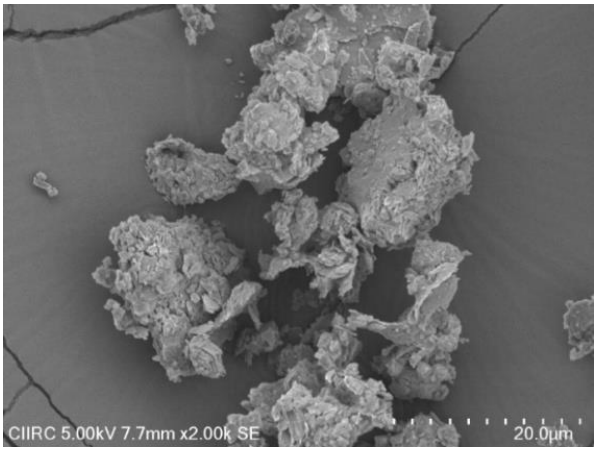

Fig. 11. SEM Image for 20% cocopeat sample

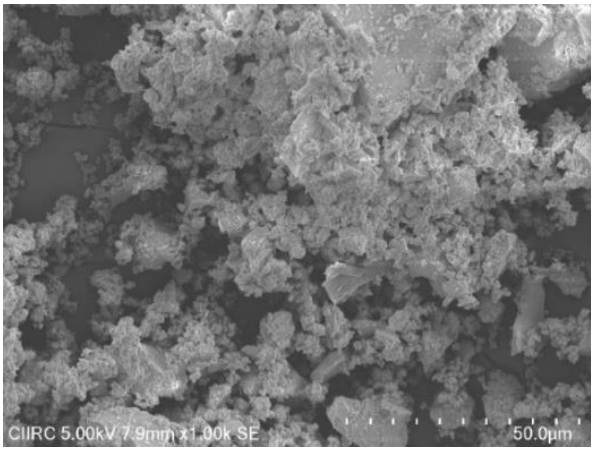

Fig. 12. SEM Image for 50% cocopeat sample

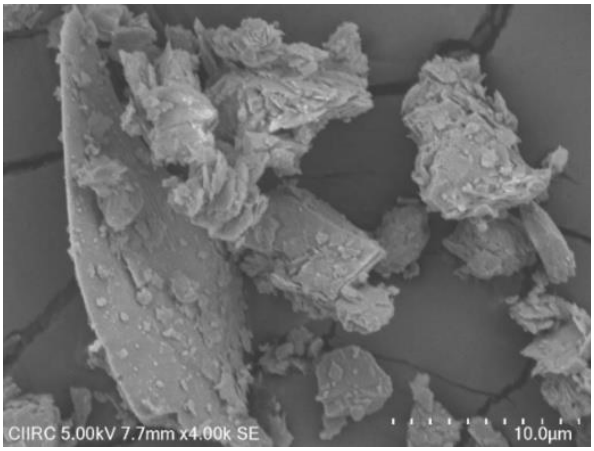

Fig. 13. SEM Image for 100% cocopeat sample

50 % cocopeat sample: SEM images (Fig. 12) indicate a noticeably rougher texture with increased irregularities and surface roughness. Significant voids and higher porosity are evident due to the equal ratio of cocopeat. Bonding quality is reduced with more noticeable disruptions in the matrix. Pronounced and branched cracks develop, and the ITZ shows increased voids and rough bonding. There is an increase in micro spheroids, predominantly irregular, and the shapes are largely irregular throughout the matrix.

100 % cocopeat sample: SEM results show a highly irregular and porous texture due to the complete substitution of sand with cocopeat (Fig. 13). Large voids and very high porosity are observed, resulting in poor bonding quality. Extensive and highly irregular cracks develop. The ITZ is poorly integrated with significant voids. Many micro spheroids are present, mostly irregular in shape, and the shapes within the matrix are predominantly irregular.

Load and vertical displacement relationship between normal concrete beams and beams using cocopeat

In Group 1, observations from Figs. 14–16 revealed key insights into the performance of the reinforced concrete beams. The beams incorporating cocopeat (D2, D3, and D4) displayed reduced displacement compared to the control beam (D1) at equivalent load levels, indicating improved resistance to deformation. Figure 14 shows the setup of the measuring equipment used to capture displacement and deformation. Figures 15 and 16 further illustrate the differences in crack formation and propagation between beams with varying percentages of cocopeat replacement. Notably, the beams with higher cocopeat content showed a delay in crack initiation and slower crack propagation, demonstrating better crack control and overall structural performance compared to the control sample.

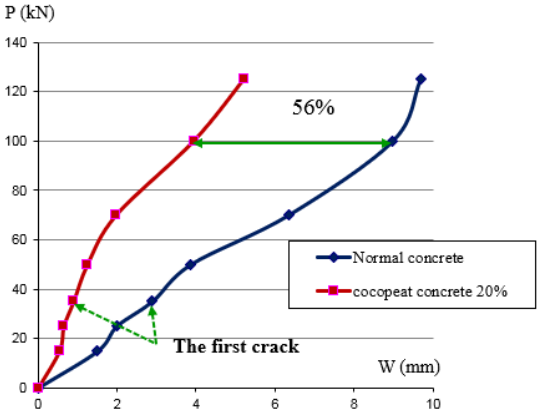

Fig. 14. Vertical displacement of beam D1 and beam D2

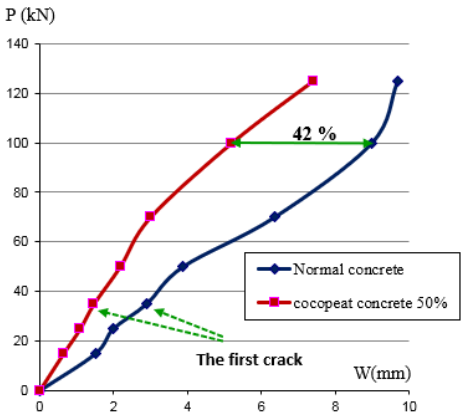

Fig. 15. Vertical displacement of beam D1 and beam D3

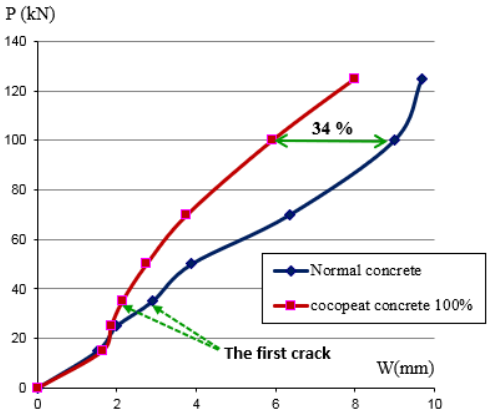

Fig. 16. Vertical displacement of beam D1 and beam D4

In Group 2, observations from Figs. 17–19 highlight that using cocopeat as a replacement for sand in reinforced concrete beams led to reduced displacement compared to conventional concrete beams under the same load conditions. At a load of 100 kN, Beam D6 exhibited 45 % less displacement than Beam D5, while Beam D7 showed a 44 % reduction, and Beam D8 demonstrated a 31 % decrease in displacement. Initial cracking was observed in all beams (D5, D6, D7, and D8) at a load of 35 kN. Significant damage to all beams occurred when the load surpassed 125 kN, marking the onset of structural failure.

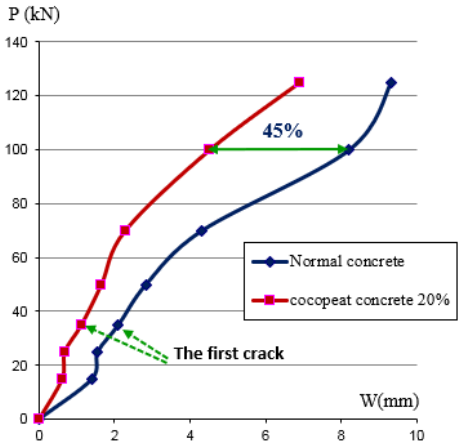

Fig. 17. Vertical displacement of beam D5 and beam D6

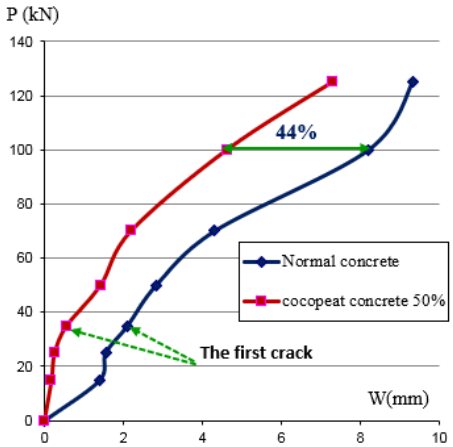

Fig. 18. Vertical displacement of beam D5 and beam D7

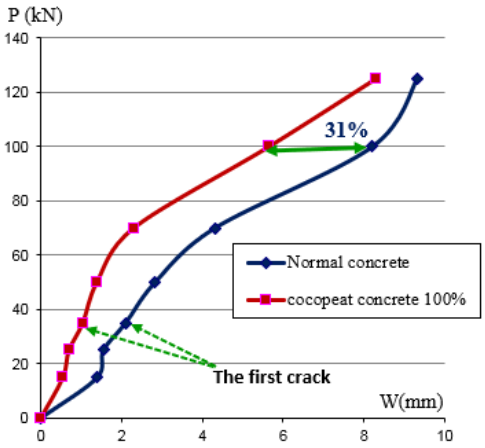

Fig. 19. Vertical displacement of beam D5 and beam D8

This study shows that the "cocopeat particle hardening method" using cement (Fig. 6), following the cocopeat production process described in the one of the previous sections, and the sand / cocopeat ratio (Table 2) have improved the performance of these reinforced concrete beams.

Effect of cocopeat content on vertical displacement in beams

Observations from Figs. 20 and 21 reveal that beams D3 (which incorporates 50 % cocopeat in place of sand) and D4 (which utilizes 100 % cocopeat) exhibit identical vertical displacements. Similarly, the vertical displacement of Beams D6, D7, and D8 is also the

same. In Group 1, Beam D2 (with 20 % cocopeat replacing sand) displays the smallest vertical displacement when compared to Beams D1, D3, and D4. In Group 2, Beam D6 (also with 20 % cocopeat replacing sand) shows the least vertical displacement among Beams D5, D6, D7, and D8. The data from Group 1 (Fig. 20) indicate that a 20 % substitution of sand with cocopeat in reinforced concrete beams results in the lowest displacement compared to other configurations. Likewise, the data from Group 2 (Fig. 21) confirm that replacing 20 % of sand with cocopeat in the reinforced concrete beam achieves the smallest displacement, highlighting its highly effective performance.

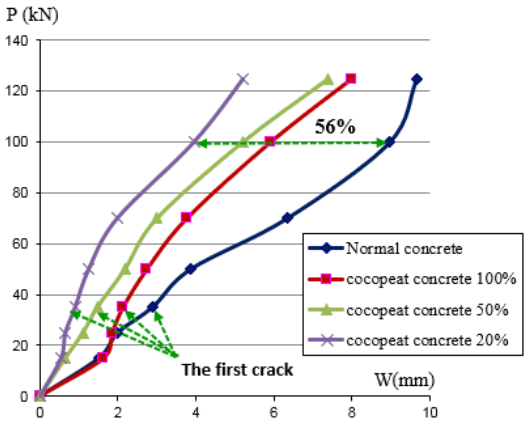

Fig. 20. Vertical displacement of beams D1, D2, D3, D4

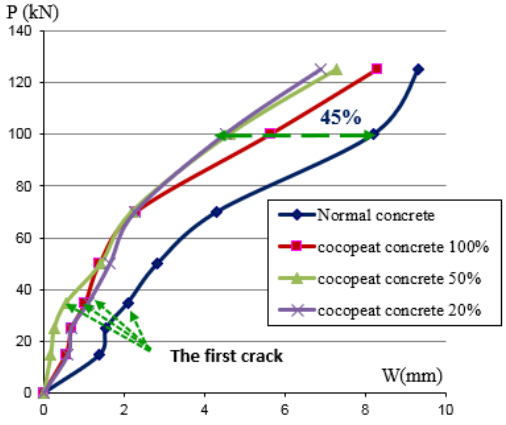

Fig. 21. Vertical displacement of beams D5, D6, D7, D8

Effect of stirrup spacing on vertical displacement of beams

In normal concrete, the beam with a stirrup spacing of 150 mm demonstrates less displacement compared to the beam with a stirrup spacing of 150–200 mm (Fig. 22). When 50 % cocopeat is used as a substitute for sand, the vertical displacements of the beams are similar. However, the reinforced concrete (RC) beam with a stirrup spacing of 100 mm exhibits lower displacement than the RC beam with a spacing of 150 mm. Similarly, the RC beam with a spacing of 150 mm shows less displacement compared to the beam with a spacing of 150–200 mm (Fig. 23). Furthermore, cracks in Beam D9 were first observed at an applied force of 50 kN, while Beams D3 and D7 experienced initial cracking at 35 kN.

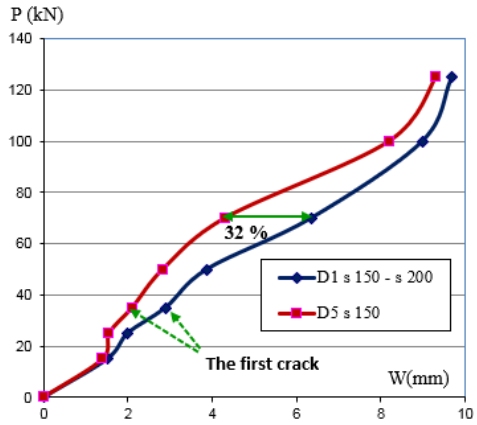

Fig. 22. Vertical displacement of beam D1 and beam D5

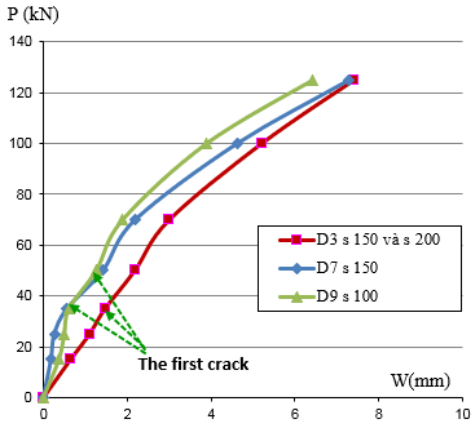

Fig. 23. Vertical displacement of beam D3, D7 and beam D9

The displacement observed in the reinforced concrete beam with stirrup spacings of 150–200 mm (Beam D3) is greater than that of the other beams (Beams D7 and D9), despite all beams having the same concrete aggregate composition. Nonetheless, the displacements of Beams D3, D7, and D9 are in agreement with one another. Additionally, a stirrup spacing of 100 mm leads to delayed crack formation and enhances the load-bearing capacity of the beam prior to failure, in comparison to the other beam configurations.

Load and deformation relationships in beams

Compression zone deformation is shown in Figs. 24 and 25. Based on the diagrams in Figs. 24 and 25, several key observations emerge. The deformation in the compression zone of reinforced concrete beams with varying percentages of cocopeat replacing sand demonstrates similar results across the board. Notably, using cocopeat as a replacement for sand results in reduced deformation in the compression zone compared to normal concrete. When the applied force is below 25 kN, the deformation in the compression zones of all reinforced concrete beams remains nearly identical. However, the most significant differences in deformation occur at a load level of 125 kN. At this load level, the deformation value shows an 85 % difference between Beam D1 (normal concrete) and Beam D2 (20 % cocopeat), and an 89 % difference between Beam D5 and Beam D6.

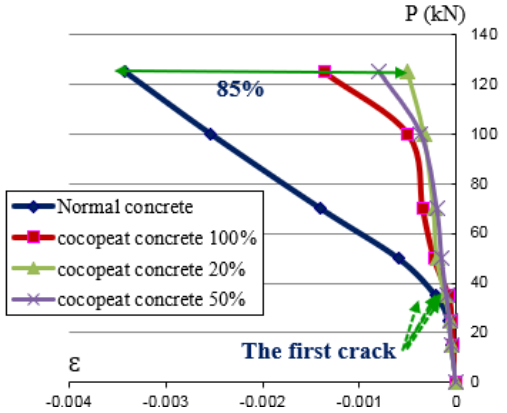

Fig. 24. Compression zone deformation of beams D1, D2, D3 and D4

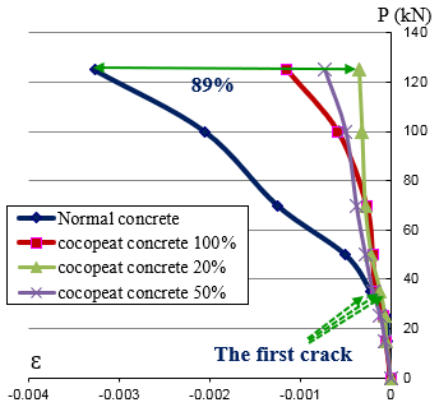

Fig. 25. Compression zone deformation of beams D5, D6, D7 and D8

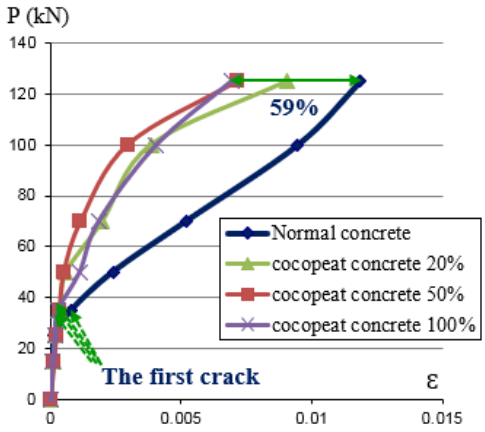

Fig. 26. Tensile deformation of beams D1, D2, D3 and D4

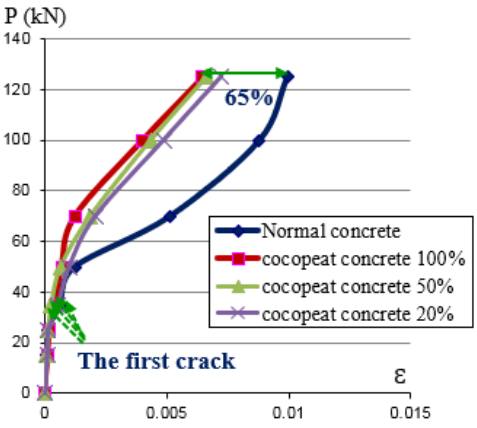

Fig. 27. Tensile deformation of beams D5, D6, D7 and D8

The diagrams in Figs. 26 and 27 reveal several important insights regarding the tensile zone deformation of reinforced concrete beams. The tensile deformation remains consistent across different percentages of cocopeat used as a replacement for sand. Notably, substituting sand with cocopeat leads to reduced tensile zone deformation compared to conventional concrete. For forces applied below 25 kN, the tensile deformation values are similar across all reinforced concrete beams. However, the most significant differences in tensile deformation are observed at a load level of 125 kN, where there is a 59 % difference between Beam D1 (normal concrete) and Beam D4 (100 % cocopeat), and a 65 % difference between Beam D5 and Beam D8. Tensile deformation is shown in Figs. 26 and 27.

Development and propagation of cracks in beams

The test results indicate that all reinforced concrete beams, from Beam D1 to Beam D8, initiated their first cracks under a load of P = 700 Psi (equivalent to 35 kN). In contrast, Beam D9 exhibited its initial crack at a higher load of P = 1000 Psi (equivalent to 50 kN), as demonstrated in Figs. 28 and 29. These observations are consistent with prior research on crack formation and propagation in reinforced concrete beams subjected to short-term loads [42], as well as studies on deflection and cracking in flexural concrete beams [43]. The cracks predominantly appear at the center of the beam and near the points of force application, with vertical cracks developing in the middle of the beam and diagonal cracks forming at 45 degrees in the support areas. As the load intensifies, both the length and width of these cracks increase, as depicted in Fig. 30. Specifically, at a load of 35 kN, the crack width measures 0.02 mm, which expands to 0.70 mm at a load level of 125 kN, as illustrated in Figs. 30 and 31.

General comments

The SEM results demonstrate that as the percentage of cocopeat increases in the concrete mix, the texture becomes progressively rougher and more porous. The addition of cocopeat leads to a noticeable increase in voids and irregularities within the matrix, which adversely affects the bonding strength and structural integrity. Concrete with 50 and 100 % cocopeat shows significant reductions in cohesiveness and an increase in irregularities and micro spheroids, leading to less predictable crack patterns and reduced overall performance compared to the 0 and 20 % cocopeat samples:

1. The deformation in both tensile and compressive zones of reinforced concrete beams, whether using varying percentages of cocopeat as a replacement for sand or using normal concrete, shows comparable values.
2. Replacing sand with cocopeat in reinforced concrete beams leads to reduced deformation in both tensile and compressive zones compared to beams made with normal concrete.
3. All tested reinforced concrete beams exhibit greater tensile strain compared to compressive strain.
4. The maximum deformation in the compression zone for beams using cocopeat instead of sand is 1.37 %, significantly lower than the deformation in beams made with normal concrete, which is 3.27 % (equivalent to ε_{cu} = 3.5 % for normal concrete).

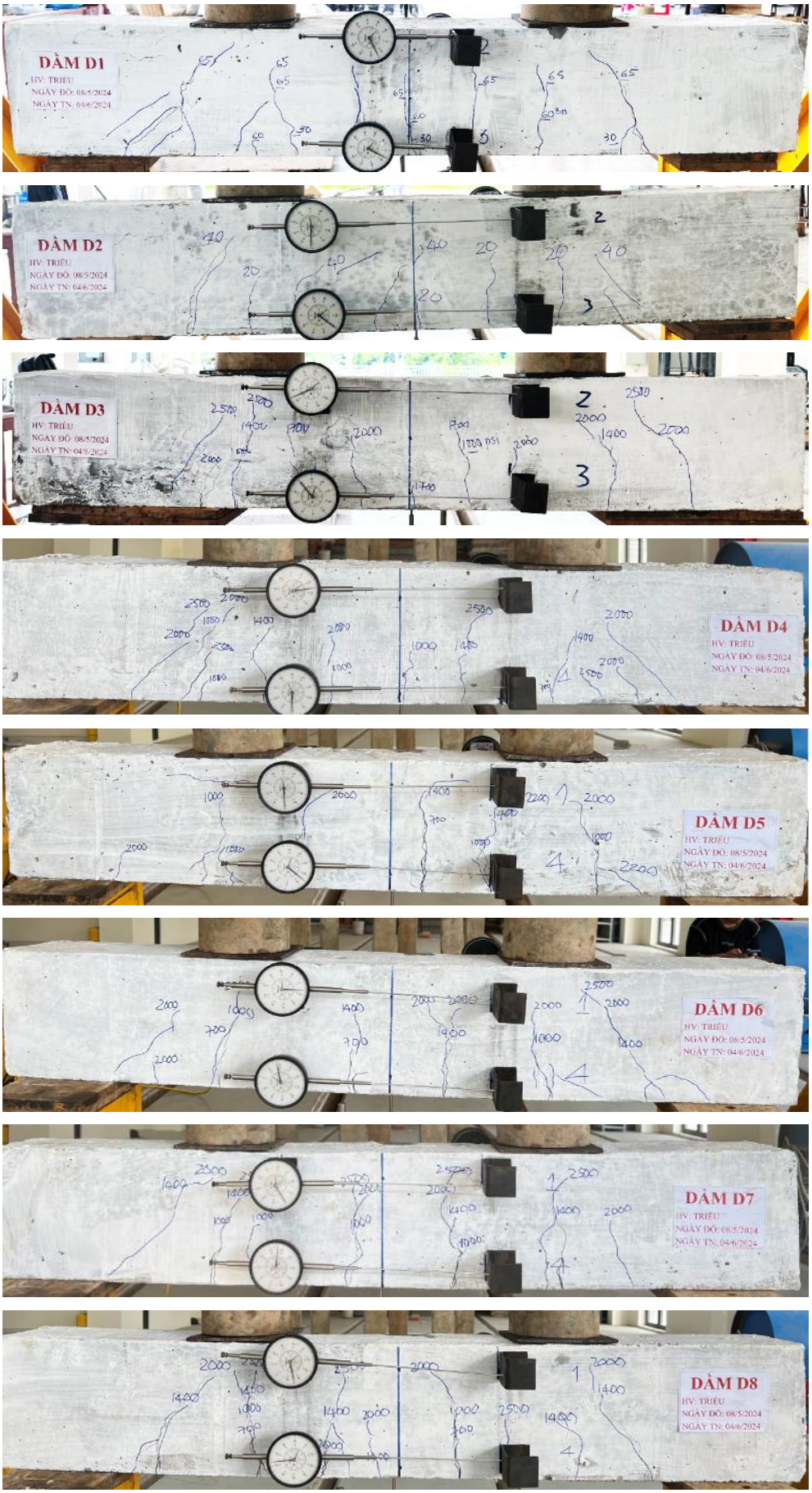

Fig. 28. Formation and propagation of cracks in reinforced concrete beams

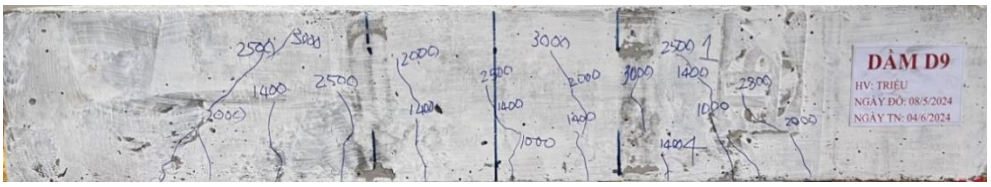

Fig. 29. Cracks of D9 reinforced concrete beams

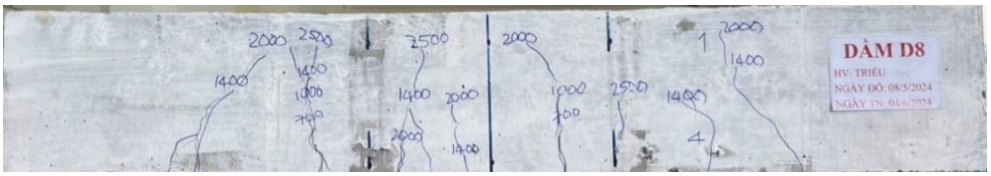

Fig. 30. Cracks of D8 reinforced concrete beam

Fig. 31. Measure the crack width of D8 reinforced concrete beam

These findings align closely with the results from the study [43]. For instance, cracks appeared in all normal concrete B15 beams under compression when a load of 35 kN was applied, and damage occurred in the beams subjected to loads exceeding 110 kN.

Conclusions

This study demonstrates that cocopeat particles, hardened with cement, can effectively substitute sand in concrete production:

1. The SEM results reveal that increasing the proportion of cocopeat in the concrete mix results in a rougher and more porous texture. Higher cocopeat content introduces more voids and surface irregularities, which negatively impacts the bond strength and structural stability. Concrete samples with 50 and 100 % cocopeat exhibit significant increases in irregularities and micro spheroids, leading to unpredictable crack patterns and reduced performance compared to those with 0 and 20 % cocopeat.
2. Specifically, replacing 20 % of the sand with hardened cocopeat in reinforced concrete beams yields load-bearing capacities comparable to those of normal concrete beams.
3. The study found that the characteristics of deflection, deformation, and crack formation and propagation in reinforced concrete beams with a stirrup spacing of 200 mm were similar to those with stirrup spacings of 100 and 150 mm. This similarity underscores the practical implications for the design and arrangement of stirrups in reinforced concrete beam construction.

4. Replacing sand with cocopeat at varying levels 20, 50, and 100 % led to an increase in vertical displacement between spans of the reinforced concrete beams. However, this increase was less pronounced compared to beams made without cocopeat.
5. Cracking was observed when the load reached 35 kN, and all beams from D1 to D8 failed under loads exceeding 125 kN.

The encouraging results of using cocopeat as a sand substitute in concrete highlight its potential for sustainable construction. A focused roadmap for future research can include several key areas: optimizing cocopeat proportions by experimenting with varying ratios (e.g., 10, 30, 50 %) to determine the best mix for strength and durability; assessing long-term performance under different environmental conditions and evaluating how the material ages over time; and conducting a life-cycle cost analysis to compare cocopeat-enhanced concrete with traditional methods, focusing on material and labor costs. Additionally, researchers should measure the environmental impact by analyzing reductions in carbon footprint and resource usage and exploring waste reduction opportunities.

CRediT authorship contribution statement

Thanh-Quang-Khai Lam: writing – review & editing, investigation, supervision; **Minh-Trieu Nguyen**: conceptualization, investigation, data curation; **Hoang-Khang Lam**: investigation, writing – original draft; **K.S. Sreekeshava**: SEM analysis, writing – editing.

Conflict of interest

The authors declare that they have no conflict of interest.

References

1. Government E-newspaper. 2024. *There is a mechanism to encourage the use of materials to replace natural sand*. Available from: https://baochinhphu.vn/da-co-co-che-khuyen-khich-su-dung-vat-lieu-thay-the-cat-tu-nhien-102221229145659446.htm [Accessed 15th January 2024].
2. Vietnam Association of Building Materials. 2023. *Promoting the development of crushed sand and recycling of construction waste in the southern provinces*. Available from: http://hoivlxdvn.org.vn/news/thuc-day-phat-trien-cat-nghien-va-tai-che-phe-thai-xay-dung-tai-cac-tinh-phia-nam-498012.html [Accessed 15th January 2023].
3. Thuy NTB, Son HT, Thinh PQ, Uyen NN. Use of wet fly ash with high loss on ignition content to replace sand in mortar. *Journal of Science.* 2022;17(2): 103–111.
4. Hung NT, Hung NS, Thach VH, Khuong LPT. Behavior of reinforced concrete beams using recycled aggregates and fly ash admixtures strengthening with CFRP sheets. *Journal of Materials & Construction.* 2023;13(01): 77–81.
5. Selyutina N, Petrov YuV. Dynamic behaviour of concrete and mortar at high strain rates. *Materials Physics and Mechanics.* 2013;18(2): 101–107.
6. Morozov VI, Pukharenko YuV, Yushin AV. The numerical investigations of double-span concrete beams strengthened with fiber reinforced plastics across the oblique section. *Materials Physics and Mechanics.* 2017;31(1/2): 40–43.
7. Pukharenko YuV, Letenko DG, Nikitin VA, Morozov VI. Obtaining the nanomodifier for cement composites based on the "DEALTOM" carbon nanotubes. *Materials Physics and Mechanics.* 2017;31(1/2): 59–62.
8. Witjaksana B. Additional steel fibers in concrete mixture: studies of compressive and tensile strength of concrete. *Materials Physics and Mechanics.* 2018;37(1): 104–108.
9. Bragov AM, Gonov ME, Lamzin DA, Lomunov AK, Modin IA. Response of fine-grained fiber-reinforced concretes under dynamic compression. *Materials Physics and Mechanics.* 2021;47(6): 962–967.
10. Ly LP. *Research on manufacturing lightweight structural concrete using polystyrene aggregate. Doctoral Thesis in Engineering.* Institute of Construction Science and Technology, Hanoi; 2019.

11. Le Anh LA, Nguyen Ninh NN, Nguyen Tan NT. Study on geopolymer concrete based fly ash and slag of thermal plant and foam agent H2O2. *Journal of Materials & Construction.* 2021;04: 6–12.
12. Yen VH, Bach VT. *Research on utilizing agricultural waste as construction materials. Master's thesis.* Ho Chi Minh City University of Technology; 2010.
13. Huyen NTB. *Research on green material production from plastic waste and agricultural waste.* Ho Chi Minh City University of Food Technology. 2013;01: 1–5.
14. Khe DT, Nhung LT. Application of coconut fiber and rice husk in the production technology of unburnt wall panels. *Journal of Science Technology and Food.* 2015;05: 121–126.
15. Vu TQ. *Study on the effect of coconut fiber on the strength of concrete. Master's Thesis.* Danang: Danang University; 2019.
16 An DT. *Research on using sulfate-resistant cement and Co Chien river sand in the mix to produce concrete for salt-intruded works in Tra Vinh province. Master's Thesis.* Danang: Danang University; 2019.
17. Ahn NT, Truong LNP. Mechanical properties of natural fiber concrete in the Mekong delta. *Journal of Materials & Construction.* 2021;2: 35–42.
18. Quang NT, Cuong TV, Tan NN, Tan NH, Giang NH. An experimental study on the effect of the proportions of recycled coarse aggregates on the evolution of concrete compressive strength and Young's modulus. *Journal of Science and Technology in Civil Engineering.* 2021;15(1V): 48–59.
19. Ratnayake NP, Puswewala UGA, Chaminda SP, Ekanayaka EMTM, Jayawardene MN. Evaluation of the potential of sea sand as an alternative to river sand or concrete production in Sri Lanka. *Journal of Geological Society of Sri Lanka.* 2014;16: 109–117.
20. Tuan HQ. Characteristics and applications of going sand in Soc Trang province as fine aggregate in concrete. *Journal of Transportation Science and Technology.* 2019;34: 57–64.
21. Le Viet LV, Phan Van PV. Research on the possibility of using sea sand as aggregate for concrete. *Journal of Materials & Construction.* 2021;1: 18–24.
22. Sankh AC, Biradar PM, Naghathan SJ, Ishwargol MB. Recent Trends in Replacement of Natural Sand With Different Alternatives. *IOSR Journal of Mechanical and Civil Engineering.* 2014;1: 59–66.
23. Arasu AN, Vivek S, Robinson J, Ranjith TT. Experimental analysis of waste foundry sand in partial replacement of fine aggregate in concrete. *International Journal of ChemTech Research.* 2017;10(8): 605–622.
24. Labcare. 2022. *Using artificial sand to replace natural sand*. Available from: https://labcare.com.vn/thay-the-cat-tu-nhien-bang-cat-nhan-tao [Accessed 10th April 2024].
25. Anh TD, Dung PV. *Evaluation of the relationship between grain size of artificial sand and concrete strength.* Quang Binh; 2021.
26. Dung LV, Kien TT, Thanh DT, Lam NB. Experimental research to estimate the application of crushed limestone sand for concrete of axial loading R-C column. *Journal of Science and Technology in Civil Engineering.* 2021;15(3V): 93–103.
27. Le Viet LV, Pham Huu PH, Phan Van PV, Nguyen Van NV. Some mechanical properties and durability of concrete using sea sand and fly ash. *Journal of Materials & Construction.* 2022;12(03): 13–21.
28. Lam T. *Production and consumption of artificial sand: Difficult input, narrow output.* Available from: https://vnbusiness.vn/thi-truong/san-xuat-tieu-thu-cat-nhan-tao-kho-dau-vao-hep-dau-ra-1095944.html [Accessed 10th April 2024].
29. Bahoria BV, Parbat DK, Naganaik PB. Replacement of natural sand in concrete by waste products : a state of art. *Journal of Environmental Research And Development.* 2013;7(4A): 1651–1657.
30. Thang NC, Phong NH, Tuan NV, Tung PH, Lan LN. The effect of lightweight aggregates recycled from construction and demolition wastes to some properties of lightweight concrete. *Journal of Science and Technology in Civil Engineering.* 2019;13(4V): 94–102.
31. Tuan NK, Nhat LD, Thoi NT, Khai PQ, Khanh NV. Utilizing recycled aggregate and autoclaved aerated concrete to develop paving block concrete. *Journal of Science and Technology in Civil Engineering.* 2020;14(4V): 106–117.
32. Nguyen LN. *Research on manufacturing large-sized unburnt bricks from a mixture of cement, stone powder, coal slag and coconut fiber. Master's Thesis.* Danang: Danang University; 2019.
33. Ramakrishna G, Thirumalai S. Impact strength of a few natural fibre reinforced cement mortar slabs: A comparative study. *Cement and Concrete Composites.* 2005;27: 547–553.
34. Trung V. *Coconut industry development*. Available from: http://www.cesti.gov.vn/images/cesti/files/STINFO/Nam2014/So10/Trang%204-10.pdf [Accessed 10th April 2024].
35. Le P. *Vietnam's coconut fiber exports increase by 272 %*. Available from: https://toquoc.vn/xuat-khau-xo-dua-cua-viet-nam-tang-272-20220822101536735.htm [Accessed 10th April 2024].
36. Ravindranath DA. Coir pith wealth from waste a reference. In: *Proc. of India International Coir Fair (IICF2016), 15–18 July 2016.* 2016.

37. Fitriadi N, Balkhaya, Rizal M, Fonna S. Physical and thermal characteristics of coco peat fibre reinforced polyurethane composite for insulation box in marine application. *Journal of Engineering Science and Technology.* 2022;17(6): 3787 – 3799.
38. Yadav SK, Singh A. An Experimental Study on Coconut Fiber Reinforced Concrete. *International Research Journal of Engineering and Technology.* 2019;06(05): 2250 – 2254.
39. Syed H, Nerella R, Madduru SRC. Role of coconut coir fiber in concrete. *Materials Today: Proceedings.* 2020;27: 1104-1110.
40. Bureau of Indian Standards. IS 10262 – 2009. *Concrete Mix Proportioning-Guidelines*. 2009.
41. Priyadarshini V, Felixkala T, Depaa RAB, Hemamaline A, Xavier JF, Babu KS, Arthi AJJ. Experimental investigation on properties of coir pith and its influence as partial replacement of fine aggregate in concrete. *Materials Today: Proceedings.* 2021;45(7): 6903 – 6906.
42. Tung P, Dao P, Tung D, Quang N. A study on the appearance and development of the vertical crack of the reinforced concrete beam under short-term loading. *Journal of Science and Technology in Civil Engineering.* 2018;12(2): 3 – 10.
43. Hoa TTN, Hiep DV, The PT. Experimental study on deflection and cracks of reinforced by concrete beams GFRP bars under bending. *Journal of Construction Science and Technology.* 2021;4: 14 – 21.

MATERIALS PHYSICS AND MECHANICS RESEARCH ARTICLE

Submitted: November 24, 2024 **Revised: April 4, 2025** **Accepted: May 12, 2025**

Experimental investigation and development of sustainable natural fiber based reinforced composite

Y.K. Sahu✉, T.V. Arjunan, S. Singh, S. Vishwas

Guru Ghasidas Vishwavidyalaya (Central University), Bilaspur, India

✉ yugendra88sahu@gmail.com

ABSTRACT

Sustainable development goal is the development of such as materials, which might not drop the negative impact over the environment, ecology and society and has long resiliency or life if bring into use. In today's era, the world is concentrating on alternative materials that are naturally recyclable and friendly to the environment. In place of synthetic fibres, renewable natural fibres now offer an alternative polymer composite material. Pollution of the environment has become unavoidable due to the toxic gas emissions from burning large quantities of residual rice straw fibres. As we know that natural fiber and epoxy resin is ascertained as momentous composite material amongst other composite materials due to its multipurpose usage in engineering, versatility cum unique mechanical properties, low-cost fabrication, renewable, biodegradable, and recyclable. In the presented research work, analysis of mechanical Behavior, of rice straw and bamboo fiber hybrid composite. To analysis same, in this research work a hybrid composite was created by first treating rice straw fibre with sodium hydroxide in an alkali process and then combining the treated rice straw sheet in stacking sequences with bamboo fiber. The testing results show that the specific tensile strength and flexural strength of rice straw fiber combined with bamboo fiber is greater than another hybrid composite. In addition to that, the hardness of rice straw fiber combined with bamboo fiber is also found greater than the other hybrid composite. The discussed hybrid composite fabrication scheme, testing, analysis and results represented graphically throughout the presented research work.

KEYWORDS

natural fiber • mechanical behavior • alkali treatment • sustainable material development

Citation: Sahu YK, Arjunan TV, Singh S, Vishwas S. Experimental investigation and development of sustainable natural fiber based reinforced composite. *Materials Physics and Mechanics*. 2025;53(4): 53–65. http://dx.doi.org/10.18149/MPM.5342025_4

Introduction

The sustainable material development (SMD) stated to develop the materials, which have sustainability if usage to fabricate goods/products such as making the ply, bed, doors of houses etc under least cost along with promoting the minimum pollution [1]. It is seen that the construction sectors are a major contributor to socio-economic development is interdependent pillar of sustainability. The materials provide the best reliable construction if material is good in nature [2]. It is seen that the composite materials are available in broad range for different civil engineering work, products' fabrications. The reinforcing matrix material is identified as a prominent sustainable material within the contemporary context. Composite materials derived from natural fibers are typically selected in various industrial applications [3]. This phenomenon transpires due to reduced expenses and density, environmental sustainability, recyclability, and low mass. The predominant cereal crop is Oryza sativa, and the external layer of rice straw is classified as a byproduct of agricultural practices [4]. Most waste is burned, which pollutes

Publisher: Peter the Great St. Petersburg Polytechnic University

the air then this wastage is utilised commercially to avoid this. Additionally, it can be used to produce biofuel, paper, fertiliser, and animal feed [5]. The reinforcement materials have the strength as well as stiffness and matrix material have capability to transfer the stresses [6]. Natural fibers are readily available and easily sourced. Collaborative efforts between industries and researchers aim to replace synthetic fibers with natural alternatives in response to environmental concerns and increasing global demand [7]. S. Kirubai et al. [8] analysis of mechanical behavior on natural fiber-based silica filled hybrid composite material. This study the effect of filler material on silica with jute and Rice straw hybrid composites. The outcome demonstrates that the fibre matrix interface was enhanced by combining natural fibre with synthetic filler. Preeti Beniwal et al. [9] advancement in the tensile characteristics of composites made of polylactic acid and reinforced by rice straw fibres. When the modified fibres were added to polylactic acid (PLA), composite films were produced that demonstrated improved thermal stability and crystallinity. The mechanical tests showed that the film of tensile strength had improved by 95 % and that its toughness had improved by roughly 600 %, thus improving compatibility among the matrix material and reinforcement. Singh et al.' [10] analysis the performance of rice straw reinforced fiber composite material. As a result, shows, that the improper usage of rice straw directly affects both material costs and environmental protection. Rice straw has been identified as a potential energy source and a useful waste product with a number of specific advantages as research is shifting towards reducing carbon footprints. Bowen Feng et al. [11] analysis the behavoir of alkali treatment rice straw reinforcement cement composites. The right amount of rice straw fibres additive greatly enhanced the modified cement specimens, while an excessive amount of the reserve impact was seen. These findings support theoretical research on the utilisation of rice straw fibres in cemented composites and reduce the environmental pollution generated by those fibres. Santosh Kumar et al. [12] analysis the wear behaviour of polylactic acid (PLA) composites supplemented with rice straw fibres. The experimental results show that applied stress and fibre loading significantly affect composite wear loss. Wear loss increases with a rise in applied normal load, Still, when fibre loading increases, the composites' abrasive wear loss decreases. M.H.M. Hamdan et al. [13] investigated the mechanical parameters of a PLA polymer composite reinforced with rice husk filler and treated with maleic anhydride, polypropylene, and polyethylene, they found that tensile and flexural strength of the composite decreased with increasing rice husk concentration. Eduardo Cesar Pachla et al. [14] studied that the rice husk and rice straw are used sustainably in cellular composites. Straw was added, which decreased the compressive strength by 15 % while increasing the flexural strengths. When rice straw was added, sound absorption increased, and the sound lining values were statistically comparable. Yashas et al. [15] studied the polymers matrix composite and stated that the matrix material is non-bio deformable and might attain the biodegradable by moderately changing fibers with natural fibers. Newly, Wang et al. [16] examined the tensile strength characteristics of natural fibre reinforced polymer composites and noted that while natural fibre tensile strength attributes are good, they can be changed when using synthetic fibres, such as carbon or glass, to reinforce plastic materials. Rong et al. [17] studied the effects of chemical behaviours of fiber epoxy composite and stated that the bond among the fibers and matrix scan be improved by emphasizing the chemical

behavior. Arpitha et al. [18] moderately changed the glass fiber with bamboo fiber and considered the effects of hybridization, and indicated that the fillers added natural fiber epoxy composites gives major progress in mechanical property. Rajesh et al. [19] explained that the surface treatment by NaOH and the hybridization increase the mechanical behavior of polymer composites matrerial. Megahed et al. [20] studied the mechanical behavior of rice straw and glass fiber reinforced epoxy composite. The alkali treatment method was used for making rice straw sheet. Ranjan et al. [21] investigated the mechanical properties of rice straw fiber hybrid epoxy reinforced biodegradable composite. The presence of lignin in rice straw causes poor bonding among the fiber and matrix material. Zhang et al. [22] studied about the fabrication and treatment process of lignocellulosic reinforced particleboard composite (made from rice straw and coir fiber). The treating composite material is increasing the wet ability of the rice straw surfaces on surface smaller contact angle. Xie et al. [23] studied the rice straw fiber and bamboo fiber, which are used as reinforcement cement-based composite. The mechanical property of the composite can be enhanced using fiber, the authors stated. Vijaya et al. [24] investigated that, the mechanical property of bamboo glass fibers hybrid composite material increases the ecological. Ismail et al. [25] investigate the mechanical behavior of rice straw fiber-based hybrid composite. The authors tested the three-point bending strength of rice straw reinforced composites material and concluded that flexural strength increases with the enhancement of a polyvinyl alcohol percentage in a composite material. Nguyen and Mangat [26] studied that, the analysis the property of rice straw fiber based reinforced with alkali-active cementitious composites. sodium hydroxide (NaOH) was used to treat the rice straw fibre. The rice straw fiber has a very optimistic effect on the alkali treatment process in the composite. Lokesh et al. [27] analysed the mechanical property of bamboo fiber-based reinforced polymer hybrid composite material. The author found that the flexural strength of bamboo fiber epoxy resin is increasing with increasing fiber loading. The impact property of a composite material is increasing with the rise of fiber, contained in composite. Tensile property, flexural property, and impact property are highly affected by the sodium hydroxide-treated fibers used [28].

The objective of this study is to develop a sustainable hybrid composite using rice straw and bamboo fibers reinforced with epoxy resin. It aims to reduce agricultural waste and environmental pollution by utilizing renewable natural fibers. The research focuses on enhancing mechanical properties such as tensile strength, flexural strength, and hardness through hybridization. Overall, the goal is to promote eco-friendly, cost-effective, and high-performance bio-based composite materials.

Materials and Method

Materials

Rice straw. The rice crop residue is light in weight as well as biodegradable and the most appropriate for the filler in the composite material. The rice straw (Table 1) is using in the place of plastic fiber in composite material. Nowadays almost everyone uses harvesters for harvesting crops, and after that, they leave the crop residue there. Then burn it to sow the next crop. The burning of the rice straw causes the emission of toxic fumes,

and two to three months later the clouds are black. Due to which the environment is gated populated. Hence, the rice straw is easily collected, and it is available for free [28].

Bamboo. Bamboo fiber (Table 1) is widely used as reinforcement material in the composite because it is a predominant behavioral property, such as strong, flexible, antibacterial, and biodegradable. The sweat is very quickly absorbed and evaporated by the bamboo fiber. Bamboo fiber is luxurious, shiny, and breathable. The micro-hole is present in the cross-segment of the bamboo fiber which is loading to as moisture absorption and ventilation [29].

Table 1. Chemical property of rice straw and bamboo fiber [30,31]

Property	Density, g/cm^3	Young modulus, GPa	Poisson ratio	Cellulose, wt. %	Hemicellulose, wt. %	Lignin, wt. %
Rice straw fiber	1.6	2.427	1.0	38.94	20.95	6.922
Bamboo fiber	0.9	35–46	0.35	42.3–49.1	24.1–27.7	23.8–26.1

Epoxy resin and hardener. Epoxy is a polymer type of matrix material. The basic function of epoxy resin is to hold the fibers together and transfer the load between the fibers. Epoxy resin (Table 2) is widely used in manufacturing applications because of its property like toughness, strong adhesion. In this, epoxy resin LY556 and curing agent hardener HY951 are used for making the composite. The resin and hardener were mixing with a ratio of 10:1 [32].

Table 2. Property of epoxy resin [33,34]

Sr.no.	Property	Epoxy resin
1	Density, g/cm^3	1.10–1.41
2	Young modulus, GPa	3
3	Poisson ratio	0.4

Making sheets from rice straw fibers

The rice straw was collected from or on the farm. Impurity ware was removed, and the alkali treatment process was conducted at home. In the alkali treatment process, the adhesion property of fiber is improved. After removing impurities, the straw was cut into 5 mm length as in Fig. 1(a). Then the rice straw was washed by running water and removed from the waste material in the straw. Then the rice straws are soaked in 2 wt. % of sodium NaOH for 36 h. Sodium hydroxides are buying 250 g near the store. Rice straw is treated with sodium hydroxide and breakdown of a bundle of smaller fiber. This developed the rough surface structure that causes enhanced fiber-matrix adhesion between fiber and matrix. Then the rice straw was boiled for 2 h until the rice straw becomes soft, as shown in Fig. 1(b). Then the rice straw fiber was washed with thoroughly running water. Then the rice straws are crushed with a pestle as shown in Fig. 1(c). After crush, the rice straws are put into the mould. The mesh passed through the roller to remove the excess quantity of water shown in Fig. 1(d). Then the water come-out through the screen. Then the rice straw is uniformly distributed into the mould shown in Fig. 1(e). Then rice straw fiber dried into the sunray. The alkali treatment process was completed [32,35].

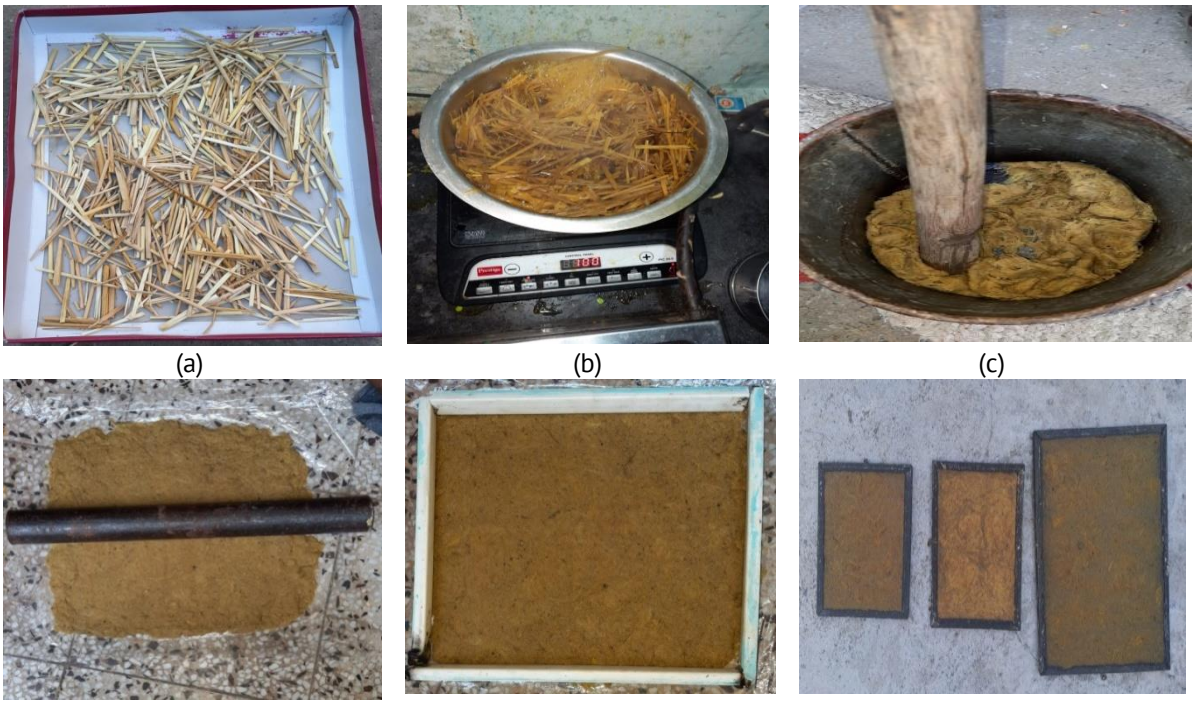

Fig. 1. Development of sheets from rice straw fiber

Fabrication process

In this research, the hand-lay-up method was using to fabricate the composite plate (Table 3). The most popular and affordable open moulding method is hand-lay-up technique because it required fewer amounts of apparatus. It is suitable for making an extensive variety of composite product from small to large. In this method, two mild steel plates are used, and the dimension of the plate is 200 × 150 mm^2. Resin and hardener mixed with the proportion is 10:1. Then the mixtures is stirred until the mixture attains a notable amount of heat. This mixture is prepared with the help of a weighing machine. Then a small amount of wax is applied to the plate. Then the fiber is placed between the plates. Both the plate is fastened with screw and tight with nut for curing in 30 h [36].

Table 3. Composition of wt. % of fiber and epoxy resin

Sr. No.	Sample code	Stacking sequence	Fiber, wt. %		Resin, wt. %
			Rice Straw	Bamboo	
1	RBR143	Rice straw / bamboo / rice straw	26.7	13.3	60
2	RB110	Rice straw / bamboo	20	20	60
3	RR100	Rice straw / rice straw	40	0	60
4	BRB214	Bamboo / rice straw / bamboo	13.3	26.7	60

Characterization

Tensile test. The tensile test measured the ultimate strength, maximum breaking strength, maximum extension, and decrease in area. The purpose of tensile testing is to select the material for an application, new product development, and proof of concept. The universal testing machine conducts the tensile test. Flat samples are typically used for the tensile test [37]. The normally used sample shapes are the straight side kind by

end tab. The sample is using for testing is shown in Fig 2. Tensile tests were performed using a 10-ton capacity universal testing machine of model UTB9103 in accordance with ASTM D638 at standard. The sample dimensions 165 × 12 × 4 mm^3 as per the standard recommendation. The gauge length of the specimen is 60 mm and crosshead speed of 1 mm/min. All the testing is conducted on CIPET Raipur [38,39].

Fig. 2. Composite plate

Flexural test. The stress a material immediately before it yields in a flexure test is known as its flexural strength. It represents maximum stress experiences inside the material on its instant of yield. The material can resist deformation under the load [40]. A three-point bending test is used for determining flexural strength. This test is performed using a universal testing apparatus in accordance with ASTM D790. The sample dimensions 127 × 12 × 4 mm^3 as per the standard recommendation. The span length of the specimen is 50 mm and crosshead speed of 1 mm/min [41].

Hardness test. Hardness is the resistance of a material to localized plastic deformation. The hardness testing evaluates material properties, like strength, and wear resistances [42]. It determines whether a materials or materials behaviour is suitable for purpose you required. The performance of the hardness test is pressing the indenter into surface of the material. It determines by measuring the depth of indenter penetration. Shore hardness test is used to measure the hardness in this research [43,44].

Results and Discussion

Tensile strength

Table 4 shows the various properties of RR100, RB110, RBR143 and BRB214, such as tensile stress, and strain. Table 4 demonstrates that the tensile properties of reinforced composite material decreased with increasing fiber volume percentage due to improper bonding among the rice straw fiber and epoxy. It is found that the ultimate tensile stress of sample RR100 is 12.7 MPa and RB110 is 11.8 MPa. It can be seen that the increasing fiber wt. % of the composite reduced the tensile properties of the composite. It has been observed that the ultimate stress of RR100 is greater than RB110. It is found that the ultimate tensile stress sample RBR143 is 1.21 MPa and BRB214 is 13.5 MPa. It has been observed that the ultimate stress and strain of RBR143 is lesser than BRB214. In this

study the maximum tensile strength was obtained increasing the wt. % of the resin. BRB214 sample has highest tensile property. Alkali treatment of rice straw fiber is also increasing the tensile properties of the composite. The comparative study of sample RR100 and RB110 are illustrated in Fig. 3. It is found that the ultimate tensile stress of sample RR100 is 12.7 MPa and RB110 is 11.8 MPa. It has been observed that the ultimate stress of RR100 is greater than RB110. Whereas the elongation of RB110 is better than RR100. It has also been observed that two layers of rice straw shows the excellent tensile properties and RB110 is more ductile than the RR100.

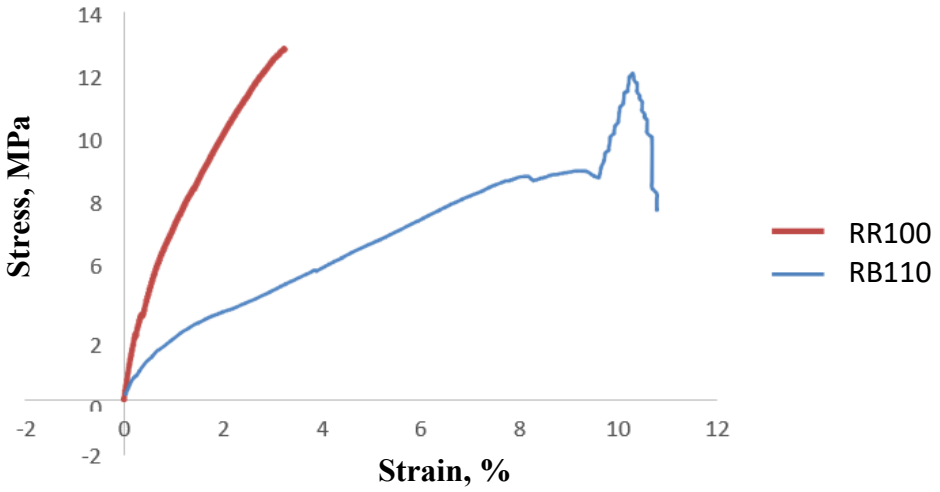

Fig. 3. Tensile strength comparison of sample RR100 and RB110 composite

Table 4. Tensile properties of tested hybrid composite

Sample	RR100 (S1)	RB110 (S2)	RBR143 (S3)	BRB214 (S4)
Ultimate stress, MPa	12.7	11.8	1.21	13.5
Ultimate strain, %	3.38	13.9	1.09	8.11

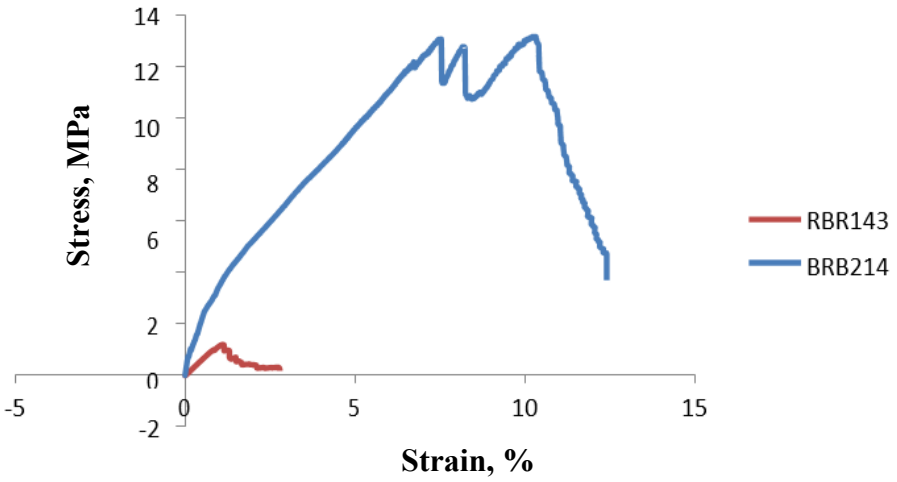

Fig. 4. Tensile strength comparison of sample RBR100 and BRB110 composite

The comparative study of sample RBR143 and BRB214 are illustrated in Fig. 4. In this graph, it is found that the ultimate tensile stress sample RBR143 is 1.21 MPa and BRB214 is 13.5 MPa. It has been observed that found that BRB214 has excellent tensile properties. Sample RBR214 has resin wt. % is more than the other sample than adhesion quality of this composite is more. The stress strain curve found from tensile test of hybrid composite is shown in a single graph for comparison. The tensile strength found to be highest for sample BRB214 and lowest for RBR143. The tensile strain found to be highest for sample RB110 and lowest for RBR143. Figure 5 shows all composition and demonstrated that the following sequences are as under:
Tensile stress=> BRB214>RR100>RB110>RBR143.
Tensile strain=> RB110>BRB214>RR100>RBR143.

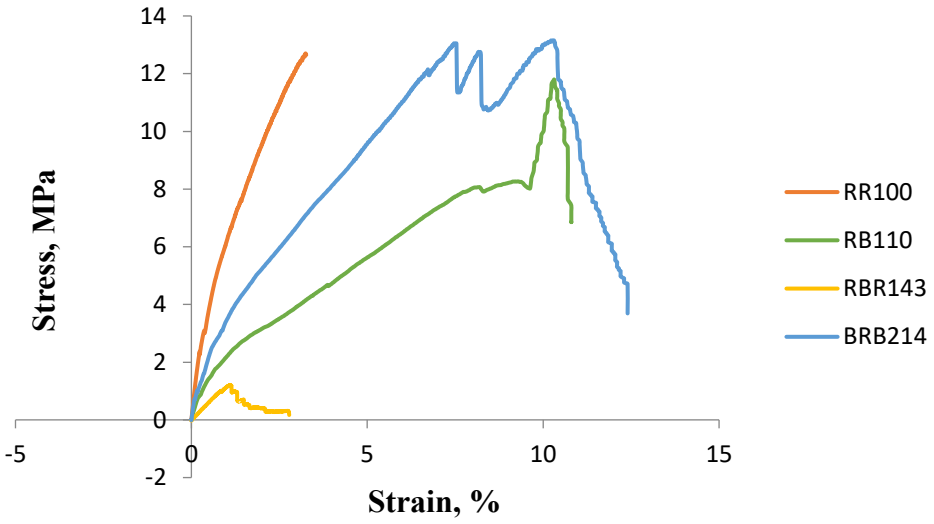

Fig. 5. Tensile strength comparison for all hybrid composite

Flexural property

Table 5 shows the various properties of RR100, RB110, RBR143 and BRB214, such as flexural stress, and strain. It is found that the ultimate stress of the sample RR100 is 8.35 MPa and RB110 is 6.49 MPa. Table 5 shows that the flexural properties of reinforced composite material decreased with increasing fiber volume percentage due to improper bonding among the rice straw fiber and epoxy. It has been observed that the ultimate stress and strain of RR100 is greater than RB110. It is found that the ultimate stress of the sample RBR143 is 5.49 MPa and BRB214 is 8.3 MPa. It has been observed that the ultimate stress and strain of RBR143 is lesser than BRB214. The comparative study of sample RR100 and RB110 are illustrated in Fig. 6. It is found that the ultimate stress of the sample RR100 is 8.35 MPa and RB110 is 6.49 MPa. From the graph in Fig. 6 it can also be seen that the value of flexural strength reduced from 36 to 52 %. This is because of improved in fiber volume and reduces the epoxy resin presence among the composite material. The value of flexural strength reduced with increasing fiber wt. % in the composite. It has been observed that the ultimate stress and strain of RR100 is greater than RB110. It has also been observed that two layers of rice straw shows the excellent flexural properties and RB110 is more ductile than the RR100.

Table 5. Flexural properties of tested hybrid composite

Sample id	RR100 (S1)	RB110 (S2)	RBR143 (S3)	BRB214 (S4)
Ultimate stress, MPa	8.35	6.49	5.49	8.3
Ultimate strain, %	3.262	1.056	1.87	3.734

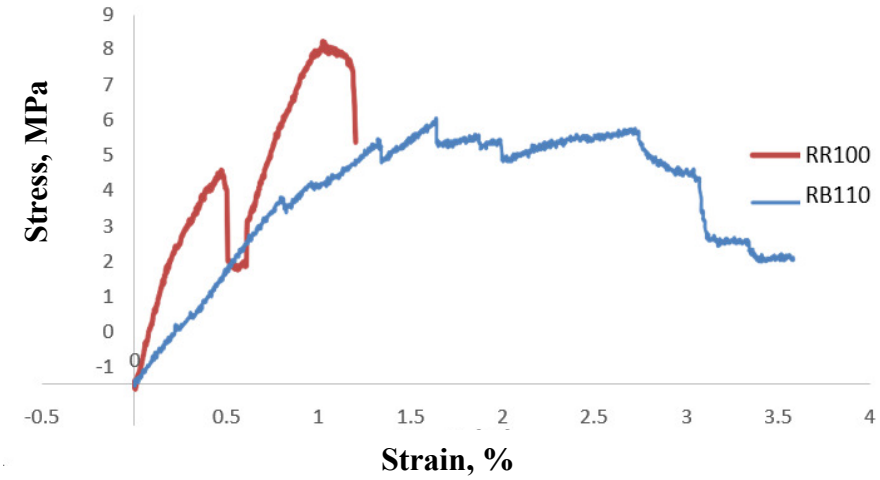

Fig. 6. Flexural strength comparison of sample RR100 and RB110 composite

The comparative study of sample RBR143 and BRB214 are illustrated in Fig. 7. The introduction of the alkali treatment of rice straw fiber increases the bonding of fiber and resin hence it increases flexural strength of the composite. It is found that the ultimate stress of the sample RBR143 is 5.49 MPa and BRB214 is 8.3 MPa. It has been observed that the ultimate stress and strain of RBR143 is lesser than BRB214. It has also been observed that BRB214 has the excellent flexural properties. The stress-strain curve found from flexural test of hybrid composite is shown in a single graph for comparison. The flexural strength found to be highest for sample RR100 and lowest for RBR143. The tensile strain found to be highest for sample BRB214 and lowest for RB110. From Fig. 8 shows all the composition and demonstrated that the following sequences are as under:
Ultimate stress=> RR100>BRB214>RB110>RBR143.
Ultimate strain=> BRB214>RR100>RBR143>RB110.

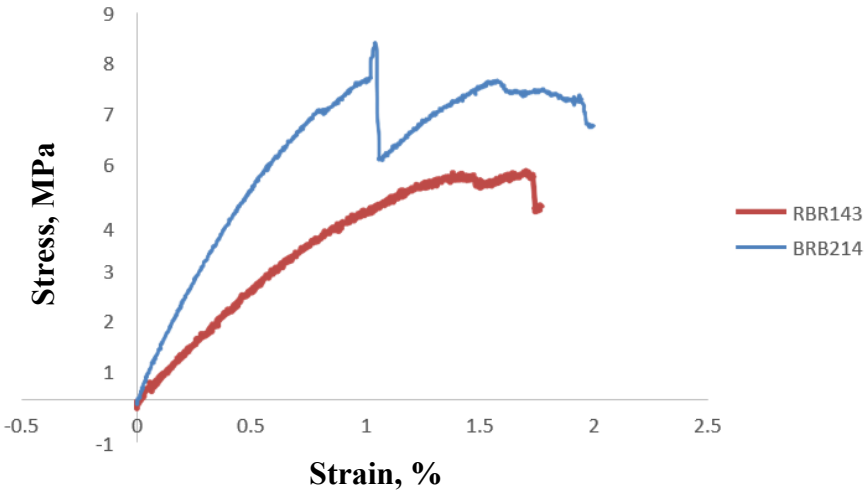

Fig. 7. Flexural strength comparison of sample RBR100 and BRB110 composite

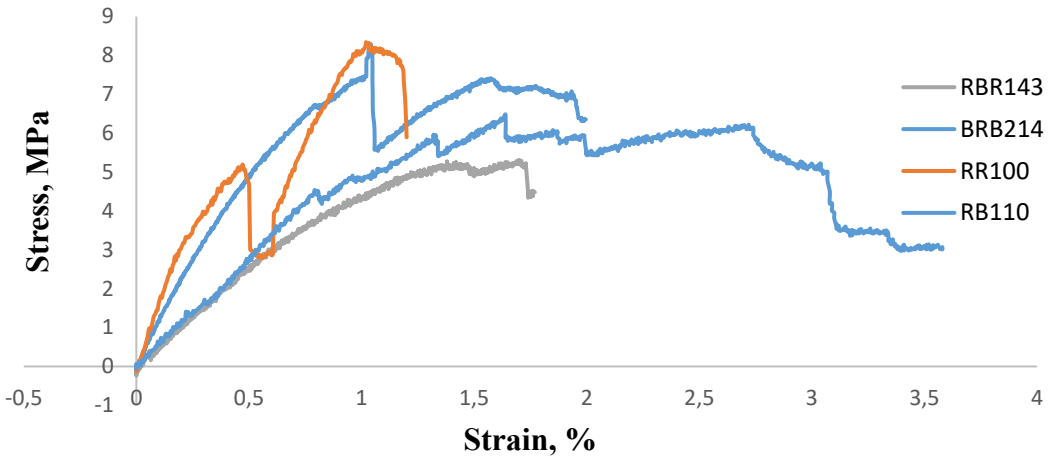

Fig. 8. Flexural strength comparison for all hybrid composite

Hardness test result

Shore hardness test is used to measure the hardness in this research. It analyses a material's resistance to an indenter-like spring-loaded needle penetrating it. An equipment known as a durometer is used to perform the shore hardness test. It loads an indenter using a calibrated spring. Then the hardness is then determined by the indenter's penetration depth under load. The specimen BRB214 is a maximum value of hardness (Fig. 9). Table 6 had given the hardness test result value of all hybrid composite fabricated material.

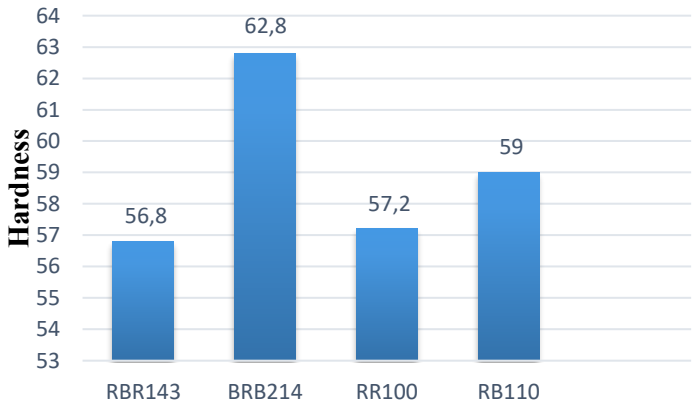

Fig. 9. Hardness test result in bar graph

Table 6. Hardness test result of fabricated material

Sample id	RBR143	BRB214	RR100	RB110
Hardness	56.8	62.8	57.2	59

Conclusion

SMD is found as one of the important fields in today's era. Concern about SMD, the researchers are focusing on developing the materials into two aspects such as materials must have the composition of natural polymers and have the low manufacturing cost and

high resiliency for long period of time targeted the SDG. Natural composites/ polymers reduce by environmental effect and provide healthy life to society as well as ecosystem (promote to social ecology), where on other hand high resiliency means materials have sustainability. Therefore, as results, the authors attempted to fabricate the materials by using natural polymers and tested the mechanical properties of same. In this work, sustainability of said material is measured in the terms of tensile, flexural, hardness of rice straw fiber/bamboo fiber mat/epoxy resin hybrid composites. Random rice straw fibers were changed to mat form with the better distribution to improve the mechanical behavior of the composite.

Based on the testing results, the following conclusions can be a drawn:

1. The successful fabrications of a rice straw sheet and bamboo fiber hybrid epoxy composite.
2. The tensile strength of RR100 composite is 7.6 % more than RB110 and BRB214 composite is 82 % of RBR143.
3. The flexural strength of RR100 composite is 22 % more than RB110 and BRB214 composite is 33 % of RBR143.
4. The hardness value is maximum for BRB214 (62.8) and minimum for RBR143 (56.8).

After comparison, it is summarized that RR100 composite has good tensile as well as flexural strength however in case of hardness BRB214 can be referred for civil engineering field.

Credit authorship contribution statement

All authors contributed to the study conception. Material preparation was performed by **Yugendra Kumar Sahu**, **Shubhra Vishwas**, data collection and analysis were performed by **Yugendra Kumar Sahu**. The supervision of the manuscript by **T.V. Arjunan** and **Samarjit Singh**. All authors read and approved the final manuscript.

Conflict of interest

The authors declare that they have no conflict of interest.

References

1. Agarwal S, Singh S. Production techniques and properties of particulate reinforce metal matrix composites: a review. *Materials Physics and Mechanics.* 2024;52(6): 136–153.
2. Kumar P, Kumar D, Kaur K, Chalisgaonkar R, Singh SS, Gupta M. Investigation of aluminum metal matrix composite fabrication processes: a comparative review. *Materials Physics and Mechanics.* 2024;52(6): 154–170.
3. Mylsamy B, Aruchamy K, Maheshwari A, Palaniappan SK, Siengchin S. Evolution and recent advancements of composite materials in aerospace applications. In: *Applications of Composite Materials in Engineering.* Elsevier; 2025. p.139–167.
4. Velayutham T, Manikandan GK, Aruchamy K, Mylsamy B, Palaniappan SK, Siengchin S. Coating of fibers and polymers with synthetic materials. In: *Surface Modification and Coating of Fibers, Polymers, and Composites.* Elsevier; 2025. p.371–398.
5. Xia T, Huang H, Wu G, Sun E, Jin X, Tang W. The characteristic changes of rice straw fibers in anaerobic digestion and its effect on rice straw-reinforced composites. *Industrial Crops and Products.* 2018;121: 73–79.

6. Noyon MR, Islam R, Rahman MM, Uddin ME, Yeasmin MF, Palaniappan SK, Maafa IM, Yousef A, Siengchin S. Antimicrobial composite materials from waste paper pulp, polyvinyl alcohol and aloe vera extract: sustainable footwear solutions. *Polymer Bulletin.* 2025;82(12): 7057–7076.
7. Muthukutti GP, Singh MK, Palaniappan SK, Vijayananth K, Rangappa SM, Siengchin S. Value-added polymer composites using non-metallic industrial waste: A concise review. *Chemical Engineering Journal.* 2025;512: 162344.
8. Kirubai S, Padmavathy S, Ganesh N, Rajaguru K. Study of mechanical behaviour on jute fiber and rice straw reinforced hybrid silica filled composite material. *Materials Today: Proceedings*. 2022;69: 1206–1212.
9. Beniwal P, Toor AP. Advancement in tensile properties of polylactic acid composites reinforced with rice straw fibers. *Industrial Crops and Products.* 2023;192: 116098.
10. Singh S, Deb J, Sarkar U, Sharma S. $MoSe_2$/multiwalled carbon nanotube composite for ammonia sensing in natural humid environment. *Journal of Hazardous Materials.* 2022;435: 128821.
11. Feng B, Liu J, Lu Z, Zhang M, Tan X. Study on properties and durability of alkali activated rice straw fibers cement composites. *Journal of Building Engineering.* 2023;63: 105515.
12. Kumar S, Varadarajan YS, Shamprasad MS. Three-body abrasive wear behavior of rice straw fibers reinforced PLA composites. *Materials Today: Proceedings.* 2023;92: 322–326.
13. Hamdan MHM, Siregar JP, Rejab MRM, Bachtiar D, Jamiluddin J, Tezara C. Effect of Maleated Anhydride on Mechanical Properties of Rice Husk Filler Reinforced PLA Matrix Polymer Composite. *Int. J. of Precis. Eng. and Manuf.-Green Tech.* 2019;6: 113–124.
14. Pachla EC, Silva DB, Stein KJ, Marangon E, Chong W. Sustainable application of rice husk and rice straw in cellular concrete composites. *Construction and Building Materials*. 2021;283: 122770.
15. Yashas Gowda TG, Sanjay MR, Subrahmanya Bhat K, Madhu P, Senthamaraikannan P, Yogesha B. Polymer matrix-natural fiber composites: An overview. *Cogent Eng.* 2018;5(1): 1446667.
16. Ku H, Wang H, Pattarachaiyakoop N, Trada M. A review on the tensile properties of natural fiber reinforced polymer composites. *Compos. Part B Eng.* 2011;42(4): 856–873.
17. Rong MZ, Zhang MQ, Liu Y, Yang GC, Zeng HM. The effect of fiber treatment on the mechanical properties of unidirectional sisal-reinforced epoxy composites. *Compos. Sci. Technol.* 2001;61(10): 1437–1447.
18. Arpitha GR, Sanjay MR, Senthamaraikannan P, Barile C, Yogesha B. Hybridization effect of sisal/glass/epoxy/filler based woven fabric reinforced composites. *Exp. Tech.* 2017;41(6): 577–584.
19. Rajesh M, Pitchaimani J, Rajini N. Free Vibration Characteristics of Banana/Sisal Natural Fibers Reinforced Hybrid Polymer Composite Beam. *Procedia Eng.* 2016;144: 1055–1059.
20. Megahed M, Ali-Eldin SS, Abd El Moezz SM, Abdalla WS. Synthesis of developed rice straw sheets and glass fiber-reinforced polyester composites. *J. Compos. Mater.* 2020;54(23): 3381–3394.
21. Ranjan C, Ahmed Z, Raj Kumar S, Kumar A, Kumar A, Kumar K. Fabrication and strength analysis of rice straw fibers reinforced epoxy biodegradable composite. *Mater. Today Proc.* 2021;46: 331–335.
22. Zhang L, Hu Y. Novel lignocellulosic hybrid particleboard composites made from rice straws and coir fibers. *Mater. Des.* 2014;55: 19–26.
23. Xie X, Zhou Z, Jiang M, Xu X, Wang Z, Hui D. Cellulosic fibers from rice straw and bamboo used as reinforcement of cement-based composites for remarkably improving mechanical properties. *Compos. Part B Eng.* 2015;78: 153–161.
24. Vijaya Kumar K, Arul Marcel Moshi A, Selwin Rajadurai J. Mechanical property analysis on bamboo-glass fiber reinforced hybrid composite structures under different lamina orders. *Mater. Today Proc.* 2021;45: 1620–1625.
25. Ismail MR, Yassen AAM, Afify MS. Mechanical properties of rice straw fiber-reinforced polymer composites. *Fibers Polym.* 2011;12(5): 648–656.
26. Van Nguyen C, Mangat PS. Properties of rice straw reinforced alkali activated cementitious composites. *Constr. Build. Mater.* 2020;261: 120536.
27. Lokesh P, Surya Kumari TSA, Gopi R, Loganathan GB. A research on mechanical properties of bamboo fiber reinforced polymer composite. *Mater. Today Proc.* 2020;22: 897–903.
28. Singh MK, Palaniappan SK, Suyambulingam I, Rangappa SM, Siengchin S, Marinkovic D. Sustainable Composite Materials For Electric Vehicle Applications: A Comprehensive Review. To be published in *Facta Universitatis, Series: Mechanical Engineering.* [Preprint] 2025. Available from: doi.org/10.22190/FUME240828014S.
29. Hasan KMF, Horváth PG, Bak M, Le DHA, Mucsi ZM, Alpár T. Rice straw and energy reed fibers reinforced phenol formaldehyde resin polymeric biocomposites. *Cellulose.* 2021;28: 7859–7875.
30. Adilhodzhaev A, Igamberdiev B, Kodirova D, Davlyatov S, Marufjonov A, Shaumarov S. The study of the interaction of adhesive with the substrate surface in a new composite material based on modified gypsum and treated rice straw. *European Journal of Molecular & Clinical Medicine.* 2020;7(2): 683–689.

31. Thabah W, Singh AK, Bedi R. Tensile properties of urea treated rice straw reinforced recycled polyethylene terephthalate composite materials. *Materials Today: Proceedings*. 2022;56: 2151–2157.
32. Sahu YK, Arjunan TV, Singh S, Vishwas S. Investigation of shape memory and mechanical properties of MWCNT and graphene nano filler reinforced epoxy composite. *J. Polym. Res.* 2025;32: 298.
33. Agirgan M, Agirgan AO, Taskin V. Investigation of thermal conductivity and sound absorption properties of rice straw fiber/polylactic acid biocomposite material. *Journal of Natural Fibers.* 2022;19(16): 15071–15084.
34. Yang Q, Ruan F, Wu H, Kan C, Wang G, Wang Z, Wang H, Xu Z, Wang H. Effect of Chemical Treatment on Rice Straw Fiber Surface and Properties of Straw/Polylactic Acid Composites. *Journal of Natural Fibers.* 2023;20(2): 2228486.
35. Mat Zubir NH, Ting SS, Santiagoo R, Noimam NZ, Wang J. Tensile properties of rice straw fiber reinforced poly (lactic acid) biocomposites. *Advanced Materials Research*. 2016;1133: 598–602.
36. Chin KM, Ting SS, Lin OH, Owi WT. Extraction of microcrystalline cellulose from rice straw and its effect on polyvinyl alcohol biocomposites film. *AIP Conf. Proc.* 2017;1865(1): 040006.
37. Sharma M, Beniwal P, Toor AP. The effect of rice straw derived microfibrillated cellulose as a reinforcing agent in starch/polyvinyl alcohol/polyethylene glycol biocompatible films. *Materials Chemistry and Physics.* 2022;291: 126652.
38. Jena PK, Bhoi P, Behera R. Mechanical and Thermal Properties of Rice/Wheat Straw Fiber Reinforced Epoxy Composites: A Comparative Study. In: Pradhan P, Pattanayak B, Das HC, Mahanta P. (eds.) *Recent Advances in Mechanical Engineering. Lecture Notes in Mechanical Engineering*. Singapore: Springer; 2022. p.727–735.
39. Mamat Razali NA, Ismail MF, Abdul Aziz F. Characterization of nanocellulose from Indica rice straw as reinforcing agent in epoxy-based nanocomposites. *Polymer Engineering and Science*. 2021;61(5): 1594–1606.
40. Satapathy A, Jha AK, Mantry S, Singh SK, Patnaik A. Processing and characterization of jute-epoxy composites reinforced with SiC derived from rice husk. *Journal of Reinforced Plastics and Composites*. 2010;29(18): 2869–2878.
41. NAM Razali, R Mohd Sohaimi, RNIR Othman, N Abdullah, SZN Demon, L Jasmani, Ya'acob WMHW, Salleh EM, Norizan MN, Halim NA. Comparative study on extraction of cellulose fiber from rice straw waste from chemo-mechanical and pulping method. *Polymers.* 2022;14(3): 387.
42. El-Kassas AM, Elsheikh AH. A new eco-friendly mechanical technique for production of rice straw fibers for medium density fiberboards manufacturing. *International Journal of Environmental Science and Technology*. 2021;18: 979–988.
43. Alcántara JC, González I, Pareta MM, Vilaseca F. Biocomposites from rice straw nanofibers: morphology, thermal and mechanical properties. *Materials*. 2020;13(9): 2138.
44. Yao F, Wu Q, Lei Y, Xu Y. Rice straw fiber-reinforced high-density polyethylene composite: Effect of fiber type and loading. *Industrial Crops and Products*. 2008;28(1): 63–72.

MATERIALS PHYSICS AND MECHANICS RESEARCH ARTICLE

Submitted: July 21, 2025 **Revised: September 1, 2025** **Accepted: September 11, 2025**

Experimental and numerical determination of mechanical properties of porous thermoplastic

I.A. Keresten [1] ✉, P.B. Pirozhnikov [2], I.S. Suranov [1], D.A. Erofeev [2], A.G. Titov [3]

[1] Peter the Great St. Petersburg Polytechnic University, St. Petersburg, Russia

[2] St. Petersburg Institute of Technology (Technical University), St. Petersburg, Russia

[3] Institute of Medical Education of Almazov National Medical Research Centre, St. Petersburg, Russia

✉ keresten@compmechlab.com

ABSTRACT

The main aim of this paper is to experimentally and numerically determine the mechanical properties of thermoplastics that exhibit porosity due to 3D-printing. The mechanical properties of thermoplastics (polyacrylonitrile-co-butadiene-co-styrene, polycarbonate, polyetherimide) were investigated using both tensile testing machine and finite element method. The object of the study is the standard 3D-printed specimen for tensile testing. According to the result of the experimental determination of the stress–strain curves of specimens under partial loading, full unloading and repeated loading, a gradual accumulation of plastic strain was revealed for all considered thermoplastics. A finite element model for testing standard tensile specimens has been developed and validated. As a result of validation, multilinear isotropic hardening material law was identified for all investigated thermoplastics. Measured mechanical properties of porous thermoplastics were compared with properties declared by the manufacturer for the original raw material.

KEYWORDS

thermoplastics • polyacrylonitrile-co-butadiene-co-styrene • polycarbonate • polyetherimide • digital engineering mechanical properties • finite element method

Citation: Keresten IA, Pirozhnikov PB, Suranov IS, Erofeev DA, Titov AG. Experimental and numerical determination of mechanical properties of porous thermoplastic. *Materials Physics and Mechanics*. 2025;53(4): 66–75. http://dx.doi.org/10.18149/MPM.5342025_5

Introduction

In modern mechanical engineering, competitiveness is increasingly driven by the development of advanced materials and their corresponding manufacturing processes. The integration of polymer materials with 3D-printing technology enables the tailoring of unique mechanical properties to meet stringent design limitations on chemistry, weight, volume, and stiffness, which are paramount in aerospace and medical applications [1]. While specific material grades and chemical additives expand the applicability of polymers, they also necessitate detailed performance validation under operational conditions – a requirement effectively addressed through digital engineering technology [2].

3D-printing makes it possible to effectively use the provided volume, ensuring the requirements for strength and rigidity. At the same time, it changes the microstructure of the material and thus transforms the original isotropic material into anisotropic, due to the formation of porosity or orientation of polymer chain fragments [3]. 3D-printing of

thermoplastics changes their physical and mechanical properties, which complicates the prediction of macroscopic reactions of constructures manufactured in such way [4].

It is necessary to note the advantage of thermosetting polymers in terms of the absence of such preconditions for the formation of anisotropy at the micro level due to another manufacturing technology – chemical polymerization.

While the physical, mechanical, and thermal properties of various thermoplastics are well-documented in general reviews [5,6], data for specific material grades – particularly those processed via additive manufacturing remain incomplete. Expanding the database of mechanical properties for various materials is valuable for the scientific and engineering community. 3D-printing significantly alters the properties of the original polymer feedstock. For example, in the article [7], it is shown that the building orientation of a part leads to a change in mechanical properties. Article [8] shows the effect of the layer stacking pattern during 3D-printing on the strength properties. The change in mechanical properties is explained by a different way of forming cavities at the micro level. In addition, for some high-molecular-weight polymers, manufacturing by 3D-printing is accompanied by orientation of polymer chain fragments, leading to the appearance of orthotropic mechanical properties at the macro level. However, the mechanical properties of a part are determined not only by its building orientation during manufacturing by 3D-printing. For example, article [9] shows the effect of various 3D-printing parameters on mechanical properties. In particular, the effect of the following parameters has been studied: layer thickness, thread width, filling density, layer orientation, printing speed and filling structure. The effect of 3D-printing parameters on mechanical properties has been studied not only for homogeneous specimens but also for heterogeneous specimens. Article [10] shows the effect of the infill percentage density and the different printing speed on the tensile properties. Special attention is paid to the effect of non-uniform temperature distribution during 3D-printing on mechanical properties. Article [11] shows the effect of the layer thickness, printing speed and the nozzle temperature on the mechanical properties. Article [12] is devoted to the study of the effect of non-uniform temperature distribution in the workpiece on the mechanical properties of specimens – individual parts of the workpiece. It has been determined that an important factor affecting the mechanical properties of thermoplastics is the time-dependent spatial temperature distribution during 3D-printing. Conversely, heating above the glass transition temperature can anneal these stresses, highlighting the complex relationship between thermal conditions and final mechanical properties.

The methodology of experimental and numerical determination of mechanical properties of standard specimens is well presented in the literature. Article [13] presents the results of experiments which are required for determination of the rheological material model and mechanical properties of standard specimens. Studied material represents a mixture of two types of thermoplastics in different proportions. Article [14] is devoted to the study of the effect of the building orientation of the part during manufacturing by laser stereolithography technology. The possibilities for achieving the best mechanical properties were investigated. In article [15], the mechanical properties of standard specimens of titanium alloy were studied experimentally and numerically using a finite element analysis software system.

This paper is devoted to the experimental and numerical study of the mechanical properties of standard (ISO 527-2:2025) specimens [16], which were manufactured by 3D-printing for specific thermoplastics certified in accordance with ISO 10993–4:2017 [17], namely: ABS–M30i [18,19], PC–ISO [20,21], Ultem 1010 resin [22–24]. Today, one of the methods for identifying the porosity of specimens is scanning electron microscopy of the cross-section of the surface [25,26]. This article studies mechanical properties of thermoplastics with voids and pores formed due to 3D-printing. These defects have been identified by cross-sectional scanning electron microscopy for all considered thermoplastics [27]. The ratio of voids (voids and pores) for ABS-M30i, PC–ISO and Ultem 1010 resin constitute 0.7 (~ 14), 0.4 (~ 20) and 3 (~ 20) % respectively.

Materials and Methods

The object of study is standard (ISO 527-2:2025) specimens, which were manufactured by 3D-printing from thermoplastics certified by standard ISO 10993–4:2017. In particular, the following thermoplastics were considered: polyacrylonitrile-co-butadiene-co-styrene (ABS–M30i, Stratasys Ltd.), polycarbonate (PC–ISO, Stratasys Ltd.) and polyetherimide (Ultem 1010 Resin, Stratasys Ltd.). Detailed information about the manufacturing of the considered thermoplastics, as well as their physical, chemical and surface properties have been presented in [27].

The tensile specimen was designed based on a standard geometry, the key dimensions of which are illustrated in Fig. 1(a). In accordance with this sketch, a full-scale geometric model of the specimen was developed (Fig. 2(b)) using a computer-aided design system SolidWorks (Dassault Systèmes SE). Based on this geometric model, 12 specimens of each considered thermoplastics were 3D-printed (Fig. 1(c)) using a 3D-printer Stratasys Fortus 450 mc (Stratasys Ltd.). Tensile tests were performed on thermoplastic specimens with a working area of 60 mm length, 5.9 mm width, and 3 mm thickness, in accordance with ISO 527-2:2025. Testing was conducted under standard ambient conditions using two Shimadzu universal testing machines (UTMs): a 5 kN AG–Xplus HS equipped with a pantograph and a 50 kN AG–50kNXD with a screw-type clamps. A constant crosshead speed of 1 mm/min was applied, and strain was measured by GL38 extensometer. The cyclic loading tests for mechanical hysteresis analysis (load-unload cycles down to 0.5 MPa) were exclusively performed on the 50 kN screw-type clamp machine, as this test configuration was not feasible with the pantograph clamp system.

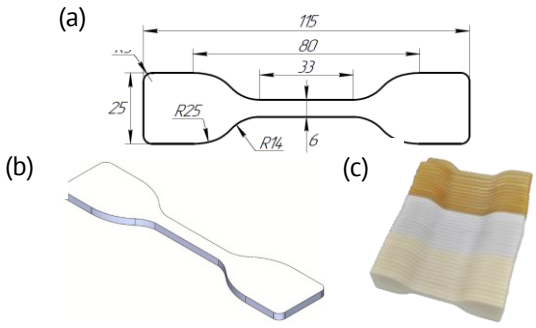

Fig. 1. Specimens: (a) sketch with relevant dimensions in mm; (b) geometric model; (c) 3D-printed specimens

Results and Discussion

Experimental part

An experimental study of the mechanical properties was conducted for standard (ISO 527-2:2025) thermoplastic specimens in the presence of porosity caused by 3D-printing. The following grades of thermoplastics certified in accordance with ISO 10993-4:2017 were considered: ABS–M30i (polyacrylonitrile-co-butadiene-co-styrene), PC–ISO (polycarbonate), Ultem 1010 resin (polyetherimide). Thermoplastics ABS-M30i and PC-ISO could be considered as isotropic materials [18,20], while thermoplastic Ultem 1010 resin is characterized by orthotropy of mechanical properties [22]. Tests for thermoplastic Ultem 1010 resin were conducted in XZ print orientation [22]. Tensile tests were conducted for determination of the mechanical properties in accordance with standard for tensile testing methods of plastics using the machine shown in Fig. 2.

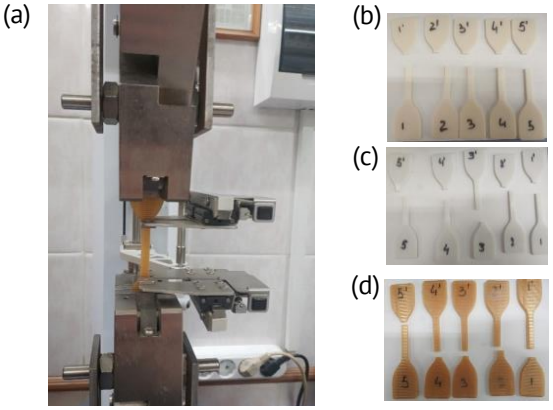

Fig. 2. Photographs of the: (a) tensile testing machine; (b) ABS–M30i specimens; (c) PC–ISO specimens; (d) Ultem 1010 resin specimens

As a result of experiments, stress–strain curves were determined, as well as the elastic modulus, tensile strength and elongation at break, which are given in Table 1. Mechanical properties of all considered thermoplastics are presented in comparison with VESTAKEEP i4 3DF [28] (polyetheretherketone), which is used today in endoprosthetics.

Table 1. Mechanical properties of thermoplastics

Thermoplastic	ABS-M30i	PC-ISO	Ultem 1010 resin	VESTAKEEP i4 3DF
Elastic modulus, MPa	2 400 [18]	2 000 [20]	3 040 [22]	3 500 [28]
Elastic modulus (experiment), MPa	2 203 (-8.2 %) Sd 38	2 094 (+4.7 %) Sd 165	3 257 (+7.1 %) Sd 92	–
Tensile strength, MPa	36 [18]	57 [20]	79.2 [22]	94 [28]
Tensile strength (experiment), MPa	28.4 (-21.1 %) Sd 0.3	49 (-14 %) Sd 0.3	88.6 (+11.9 %) Sd 4	–
Elongation at break, %	4 [18]	4 [20]	4 [22]	5 [28]
Elongation at break (experiment), %	7.7 (+92.5 %) Sd 1.1	5.3 (+32.5 %) Sd 0.2	4.35 (+8.8 %) Sd 0.4	–

As shown in Table 1, the experimentally determined elastic modulus for all studied 3D-printed thermoplastics correlates well with manufacturer datasheet values. The

values of the experimentally determined elastic modulus for all considered thermoplastics correlate with the data sheet, in contrast to the other properties of these materials. A mechanical hysteresis was constructed for the identification of an adequate rheological model for all considered thermoplastics (Fig. 3).

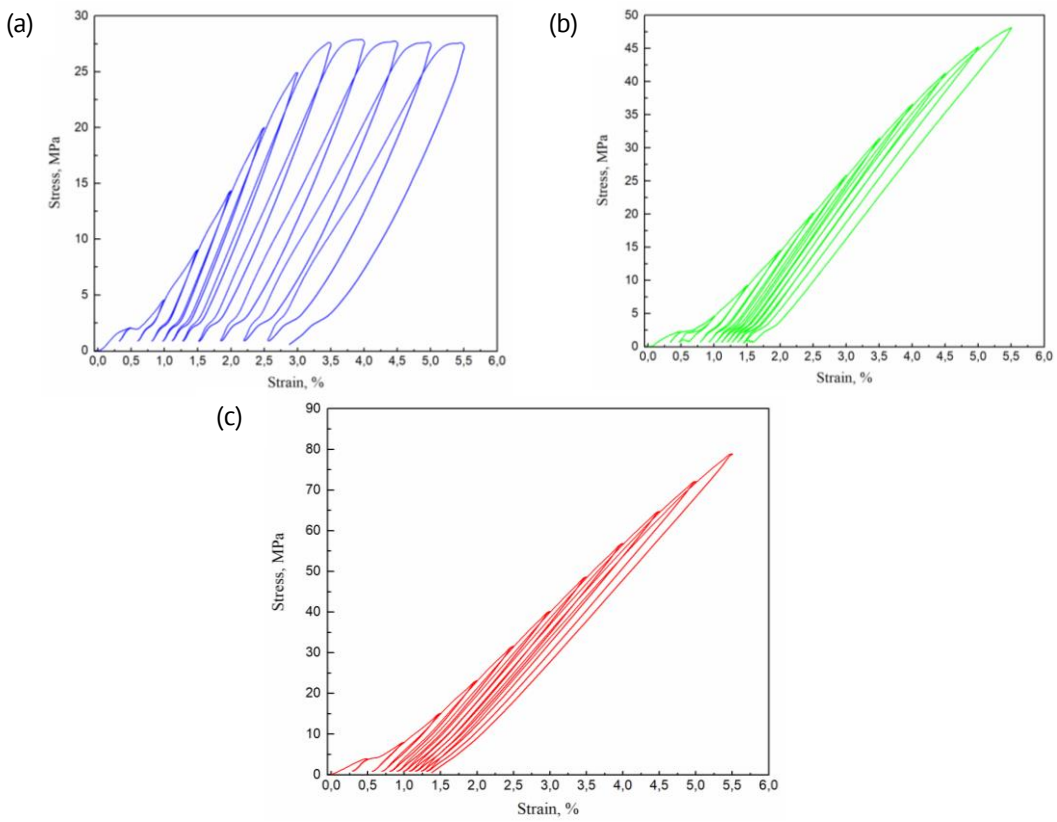

Fig. 3. Experimental stress–strain curves of investigated thermoplastics: (a) ABS-M30i; (b) PC–ISO; (c) Ultem 1010 resin

The experimentally determined tensile strength values for ABS–M30i and PC–ISO are lower than the values presented in data sheets. It is well explained by the presence of the porosity at micro level, which appears due to manufacturing by 3D-prining. This physical phenomenon has been confirmed by scanning electron microscopy of the cross section [27]. In contrast, Ultem 1010 Resin exhibited a less pronounced but opposite trend, which may be partly explained by the orthotropic nature of its feedstock [22]. Coupled with the technological parameters of 3D-printing, it led to a slight strengthening of the material.

The experimentally determined tensile strength values for ABS–M30i and PC–ISO are lower than the values presented in data sheets. It is well explained by the presence of the porosity at micro level, which appears due to manufacturing by 3D-prining. This physical phenomenon has been confirmed by scanning electron microscopy of the cross section [27]. In contrast, Ultem 1010 Resin exhibited a less pronounced but opposite trend, which may be partly explained by the orthotropic nature of its feedstock [22]. Coupled with the technological parameters of 3D-printing, it led to a slight strengthening of the material.

For all considered thermoplastics, an increase in the elongation at break is observed by comparison with data sheets. It is illustrated by the yield plateau on the stress–strain curves. As a result of the analysis of the stress–strain curves in combination with the loops of mechanical hysteresis, all investigated thermoplastics are prone to gradual accumulation of plastic strain under increasing load (Fig. 3).

Numerical part

Also, a numerical study of the mechanical properties of the considered thermoplastics was conducted using the SIMULIA Abaqus/Standard (Dassault Systèmes SE) finite element analysis software system [29–31]. Figure 4(a) shows a finite element model of a standard (ISO 527-2:2025) thermoplastic specimen, which contains about 10^4 linear finite elements (finite element type C3D8R). Figure 4(b) shows a boundary conditions imposed on the model. One edge of the specimen is assumed to be rigidly fixed in clamps, while displacements in the longitudinal direction were applied to the second edge of the specimen.

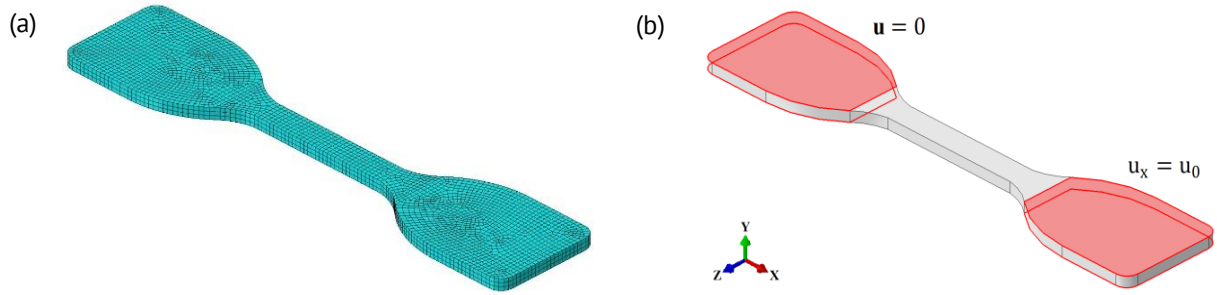

Fig. 4. Computational model of a specimen: (a) finite element model; (b) boundary conditions imposed on the model

An elastic-plastic material model (plastic material model) was chosen to describe the rheological behavior of the considered thermoplastics. The numerical values of the parameters for the multilinear isotropic hardening material law (Table 2) were iteratively identified in accordance with the experimentally determined stress-strain curves.

Table 2. Numerical values of the multilinear isotropic hardening material law

ABS-M30i		PC-ISO		Ultem 1010 resin	
Plastic strain	**Stress, Pa**	**Plastic strain**	**Stress, Pa**	**Plastic strain**	**Stress, Pa**
0	$1.3 \cdot 10^7$	0	$1 \cdot 10^7$	0	$2 \cdot 10^7$
0.0005	$2.1 \cdot 10^7$	0.001	$2 \cdot 10^7$	0.001	$3 \cdot 10^7$
0.0015	$2.5 \cdot 10^7$	0.002	$2.5 \cdot 10^7$	0.002	$4 \cdot 10^7$
0.002	$2.6 \cdot 10^7$	0.004	$3.2 \cdot 10^7$	0.0035	$5 \cdot 10^7$
0.0025	$2.7 \cdot 10^7$	0.0055	$3.6 \cdot 10^7$	0.0055	$6 \cdot 10^7$
0.003	$2.75 \cdot 10^7$	0.0085	$4.05 \cdot 10^7$	0.0085	$7 \cdot 10^7$
0.004	$2.8 \cdot 10^7$	0.0135	$4.55 \cdot 10^7$	0.013	$8 \cdot 10^7$
0.008	$2.85 \cdot 10^7$	0.022	$4.9 \cdot 10^7$	0.019	$8.8 \cdot 10^7$

As a result of the numerical simulation of stretching a standard specimen, the stress-strain state was determined. The following characteristics were determined by finite element method: displacement (Fig. 5(a)), von Mises stress intensity (Fig. 5(b)) and plastic strain (Fig. 5(c)).

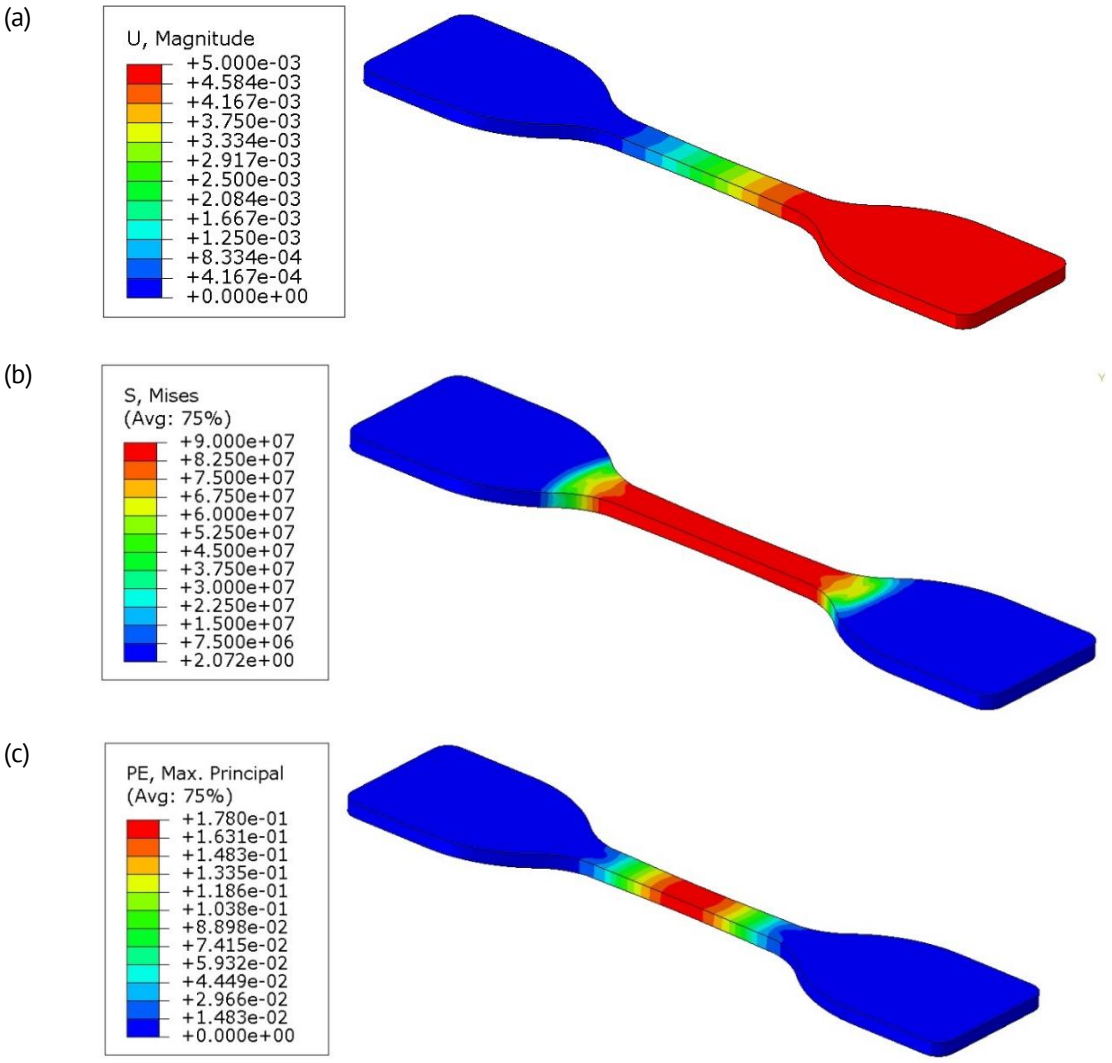

Fig. 5. Stress-strain state of specimen (in case of the Ultem 1010 resin): (a) displacement; (b) von Mises stress intensity; (c) Plastic strain

Modeling was conducted on 6 core desktop computer with Intel i7 CPU and 16 Gb RAM. As a result of the multivariant solution for all considered thermoplastics, numerical values of the multilinear isotropic hardening material law (Table 2) were identified. Thus, the developed digital model for tensile testing of specimens was validated (Fig. 6). The data in the first row of Table 2 delineate the transition from the conditionally safe (elastic) region to the plastic flow zone. In other words, it is safety to say that stress values below 13, 10 and 20 MPa for ABS–M30i, PC–ISO and Ultem 1010 resin thermoplastics respectively do not lead to the formation of plastic strain. Stresses above these values result in the accumulation of plastic strain, which is confirmed by the presence of a mechanical hysteresis loop (Fig. 3).

Comparison of results

As a result of the experimental and numerical study of mechanical properties, stress-strain curves were determined for all considered thermoplastics (Fig. 6). The numerical values of the multilinear isotropic hardening material law for all considered thermoplastics were determined in such a way that the numerical stress-strain curves lie in the middle between the experimental curves whole over the entire deformation.

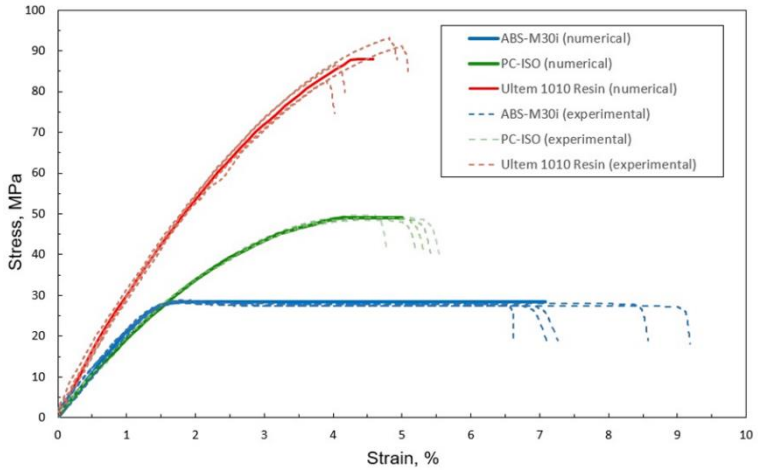

Fig. 6. Experimental and numerically calculated stress-strain curves of investigated thermoplastics: ABS– 30i, PC–ISO, Ultem 1010 resin

From all considered thermoplastics ABS–M30i has the lowest tensile strength. All things being equal, this circumstance does not allow ABS–M30i to be recommended for critical and loaded components of mechanical systems in terms of ensuring strength requirements. It should also be noted that ABS–M30i exhibits explicit yield plateau after exceeding a relative deformation of 1.8 % up to a relative deformation of 7.7 %, which corresponds to failure.

In turn, PC–ISO has the most nonlinear stress–strain curve compared to other considered thermoplastics. PC–ISO has a significantly higher tensile strength compared to ABS–M30i, but it enters the plastic flow zone earlier than considered thermoplastics. As a result of which, it contributes to the formation and accumulation of irreversible deformations and defects during operation under cyclic loads. All things being equal, this circumstance does not allow PC–ISO to be recommended for parts and structures with durability requirements.

From all considered thermoplastics Ultem 1010 resin has the most tensile strength and rigidity. Mechanical properties of Ultem 1010 resin are close to cortical bone tissue and VESTAKEEP i4 3DF (polyetheretherketone), which is used today in endoprosthetics. The difference in the rheological behavior of the studied thermoplastics is directly related to their chemical composition and structure, which is implicit indicated by the value of the glass transition [27]. The lower the glass transition of polymer material, the more explicit the plastic behavior is. These features make it possible to consider Ultem 1010 resin as a promising material for usage in mechanical systems with requirements for strength and durability.

Conclusions

In the presented research paper, the mechanical properties of certified (ISO 10993– 4:2017) thermoplastics ABS–M30i (polyacrylonitrile-co-butadiene-co-styrene), PC–ISO (polycarbonate) and Ultem 1010 Resin (polyetherimide) were investigated using standard (ISO 527-2:2025) specimens, which were manufactured by 3D-printing. The mechanical properties of thermoplastics with voids and pores formed due to 3D-printing have been studied. For all considered thermoplastics stress–strain curves were experimentally constructed, as well as a mechanical hysteresis. Based on the results of the experimental study, an elastic-plastic material model was chosen to adequately describe the rheological behavior of polymer materials. As a result of the numerical study of mechanical properties, a validated digital model for tensile testing of a specimen was developed. Based on the results of the numerical study, the numerical values of the multilinear isotropic hardening material law were identified for all considered thermoplastics. Also, measured mechanical properties of porous thermoplastics after 3D-printing were compared with the properties for the original raw material.

An important scientific result of this article consists in the identification of a rheological model and its numerical parameters for all considered thermoplastics: ABS– M30i, PC–ISO and Ultem 1010 resin. The suggested validated multilinear isotropic hardening material law can be used as part of a digital twin of mechanical systems in various industries. For example, to develop a digital twin of the skeleton-endoprosthesis system for large human joints. As part of further research of mechanical properties of the investigated thermoplastics, several areas of scientific and practical importance can be denoted, for example: durability research; determination of the mechanical properties of wet thermoplastics (for example in saline solution); investigation of the effect of temperature on mechanical properties.

CRediT authorship contribution statement

Ilya A. Keresten: writing – review & editing, writing – original draft, conceptualization, investigation, supervision, data curation; **Pavel B. Pirozhnikov**: writing – review & editing, investigation, supervision; **Ian S. Suranov**: writing – original draft, data curation; **Erofeev A. Daniil**: investigation; **Alexey G. Titov**: conceptualization.

Conflict of interest

The authors declare that they have no conflict of interest.

References

1. Kablov EN. New generation materials represent the basis for innovations, technological leadership and national security of Russia. *Intellect and Technology.* 2016;2(14): 16–21. (In Russian)
2. Haider TP, Völker C, Kramm J, Landfester K, Wurm FR. Plastics of the future? The impact of biodegradable polymers on the environment and on society. *Angewandte Chemie International Edition.* 2019;58(1): 50–62.
3. Ahn S, Montero M, Odell D. Anisotropic material properties of fused deposition modeling ABS. *Rapid Prototyping Journal.* 2002;8(4): 248–257.

4. Malekmotiei L, Voyiadjis GZ, Samadi-Dooki A. Effect of annealing temperature on interrelation between the microstructural evolution and plastic deformation in polymers. *Journal of Polymer Science Part B: Polymer Physics.* 2017;55(17): 1286–1297.
5. Beukelaer HD, Hilhorst M, Workala Ya, Maaskant E, Post W. Overview of the mechanical, thermal and barrier properties of biobased and/or biodegradable thermoplastic materials. *Polymer Testing.* 2022;116: 107803.
6. Kobykhno IA, Kuznetcov DA, Didenko AL, Smirnova VE, Vaganov GV, Ivanov AG, Popova EN, Litvinova LS, Svetlichnyi VM, Vasilyeva ES, Tolochko OV, Yudin VE, Kudryavtsev VV. Multiblock copoly(urethane-amide-imide)s with the properties of thermoplastic elastomers. *Materials Physics and Mechanics.* 2018;40(2): 221–230.
7. Cantrell JT, Rohde S, Damiani D, Gurnani R, DiSandro L, Anton J, Young A, Jerez A, Steinbach D, Kroese C, Ifju PG. Experimental characterization of the mechanical properties of 3D-printed ABS and polycarbonate parts. *Rapid Prototyping Journal.* 2017;23(4): 811–824.
8. Galeja M, Hejna A, Kosmela P, Kulawik A. Static and Dynamic Mechanical Properties of 3D Printed ABS as a Function of Raster Angle. *Materials.* 2020;13(2): 297.
9. Travieso-Rodriguez JA, Jerez-Mesa R, Llumà J, Traver-Ramos O, Gomez-Gras G, Roa Rovira JJ. Mechanical properties of 3D-printing polylactic acid parts subjected to bending stress and fatigue testing. *Materials.* 2019;12(23): 3859.
10. Singh R, Kumar R, Farina I, Colangelo F, Feo L, Fraternali F. Multi-material additive manufacturing of sustainable innovative materials and structures. *Polymers.* 2019;11(1): 62.
11. Yadav P, Dev S, Hussain I, Kumar R. Evaluation of additive manufacturing process parameters for improved mechanical properties of thermoplastic parts. To be published in *Materials Today: Proceedings.* [Preprint] 2022. Available from: doi.org/10.1016/j.matpr.2022.12.150
12. Sun Q, Rizvi GM, Bellehumeur CT, Gu P. Effect of processing conditions on the bonding quality of FDM polymer filaments. *Rapid Prototyping Journal.* 2008;14(2): 72–80.
13. Alzarzouri F, Jabra R, Deri F. Melt rheological behaviour and mechanical properties of poly(lactic acid)/high density polyethylene blends. *Materials Physics and Mechanics.* 2021;47(1): 103–116.
14. Vnuk VV, Ippolitov EV, Kamaev SV, Markov MA, Nikulenko AA, Novikov MM, Cherebylo SA. Study of the influence of technological features of laser stereolithography process on functional characteristics of parts. *Materials Physics and Mechanics.* 2021;47(2): 293–305.
15. Skripnyak VV, Kozulyn AA, Skripnyak VA. The influence of stress triaxiality on ductility of α titanium alloy in a wide range of strain rates. *Materials Physics and Mechanics.* 2019;42(4): 415–422.
16. International Organization for Standardization. ISO 527-2:2025. *Plastics — Determination of tensile properties. Part 2: Test conditions for moulding and extrusion plastics*. ISO; 2025.
17. International Organization for Standardization. ISO 10993–4:2017. *Biological evaluation of medical devices. Part 4: Selection of tests for interactions with blood.* ISO; 2017.
18. *ABS-M30i.* [Data sheet] Stratasys Ltd.; 2021.
19. Khuong TL, Gang Z, Farid M, Yu R. Tensile Strength and Flexural Strength Testing of Acrylonitrile Butadiene Styrene (ABS) Materials for Biomimetic Robotic Applications. *Journal of Biomimetics, Biomaterials and Biomedical Engineering.* 2014;20: 11–21.
20. *PC-ISO.* [Data sheet] Stratasys Ltd.; 2021.
21. Zhang S, Wang B, Meng X, Chen Ya. Mechanical Properties and Fracture Microstructure of Polycarbonate under High Strain Rate Tension. *Materials.* 2023;16(9): 3386.
22. *ULTEM 1010 Resin.* [Data sheet] Stratasys Ltd.; 2020.
23. Zhang Y, Moon SK. Effect of Annealing on Additive Manufactured ULTEM™ 9085 Mechanical Properties. *Materials.* 2021;14(11): 2907.
24. Forés-Garriga A, Pérez MA, Gómez-Gras G, Reyes-Pozo G. Role of infill parameters on the mechanical performance and weight reduction of PEI Ultem processed by FFF. *Materials & Design.* 2020;193(3): 108810.
25. Ziemian S, Okwara M, Ziemian CW. Tensile and fatigue behavior of layered acrylonitrile butadiene styrene. *Rapid Prototyping Journal.* 2015;21(3): 270–278.
26. Madhu G, Bhunia H, Bajpai PK, Chaudhary V. Mechanical and morphological properties of high density polyethylene and polylactide blends. *Journal of Polymer Engineering.* 2014;34(9): 813–821.
27. Erofeev DA, Pirozhnikov PB, Keresten IA, Titov AG. Experimental determination of physical, chemical and surface properties of biocompatible thermoplastic. *Materials Physics and Mechanics.* 2024;52(3): 1–12.
28. *VESTAKEEP i4 3DF.* Evonik Operations GmbH; 2020.
29. *Dassault Systems.* ABAQUS 6.13 Online documentation. 2013.
30. Meknassi RF, Béres G, Lukács Z. Study the near plane strain tensile test specimen using finite element code ABAQUS. *Multidiszciplináris tudományok.* 2022;12(3): 107–116.
31. Borovkov AI, Maslov LB, Zhmaylo MA, Tarasenko FD, Nezhinskaya LS. Finite element analysis for prediction of femoral component strength in hip joint endoprosthesis made from meta-biomaterial. *Materials Physics and Mechanics.* 2024;52(6): 38–60.

MATERIALS PHYSICS AND MECHANICS RESEARCH ARTICLE

Submitted: September 13, 2024 **Revised: August 26, 2025** **Accepted: September 10, 2025**

Double diffusive convection of non-Newtonian nanofluid in porous layer under internal heating

V. Sharma [1], J. Devi [2]✉, R. Kumar [3], V. Sharma [2]

[1] Govt. College, Tissa, Chamba, Himachal Pradesh, India

[2] Himachal Pradesh University, Shimla, India

[3] Kurukshetra University, Kurukshetra, Haryana, India

✉thakurjyoti641@gmail.com

ABSTRACT

The onset of double-diffusive convection in a non-Newtonian nanofluid-saturated porous layer is investigated under the effect of internal heating and various boundary conditions. A non-Newtonian nanofluid is modeled using the Buongiorno framework for nanoparticles combined with the Jeffrey model for viscoelastic fluid behavior. The governing coupled differential equations are reduced to ordinary linear differential equations via the normal mode method, the Boussinesq approximation, and linear stability analysis. Eigenvalue problems are solved using realistic boundary conditions to determine the stationary Rayleigh numbers, which describe the initiation of non-oscillatory convection in terms of non-dimensional controlling parameters. This work is motivated by practical applications in geophysics, energy engineering, and materials science, where non-Newtonian nanofluids in porous layers are subjected to internal heating, such as in geothermal reservoirs, enhanced oil recovery, and thermal management systems. The analysis demonstrates that reduced particle density and internal heating promote convection, whereas porosity, solutal Rayleigh number, concentration Rayleigh number, and modified diffusivity ratio stabilize the system. Furthermore, reduced particle density enhances instability, while the Jeffrey parameter introduces viscoelastic effects that weaken stability without altering convection cell size. These findings provide new insights into the stabilization and destabilization mechanisms of nanofluid systems, with implications for designing advanced energy and material processing technologies.

KEYWORDS

Internal heat source • Jeffrey model • double diffusive convection • porous material

Citation: Sharma V, Devi J, Kumar R, Sharma V. Double diffusive convection of non-Newtonian nanofluid in porous layer under internal heating. *Materials Physics and Mechanics*.2025;53(4): 76–90.
http://dx.doi.org/10.18149/MPM.5342025_6

Introduction

A type of convection called double diffusive convection is driven by two slopes that have different diffusion rates. Several industrial areas are very interested in this phenomenon, such as putting nuclear waste underground, making binary mixtures solid, electrochemistry, magma chambers, the earth's oceans, and oil drilling. This convection also helps us understand how convection works in the sun, where warmth and helium move around at different speeds. A lot of study has been done on the phenomenon of double diffusive convection, especially in relation to salt fingers in oceanic settings. Stern [1] wrote about the conditions that allow rhythmic motion to be seen, meaning that warmer, saltier water is below colder, less dense water. Huppert and Turner [2], on the other hand, found that binary convection (double diffusive convection) can happen with

two parts in the fluid layer and cause motion to stop in the shape of salt-fingers. Dougall [3] did a thorough study on binary convection in a solute-solute pair caused by molecular diffusion. Kafoussias and Williams [4] did a study to look at how the Soret and Dufour factors affected boundary layer flow in laminar mixed convection and mass transport with viscosity that changes with temperature. Kuznetsov and Sheremet [5] also did a numerical study on binary convection in holes with Soret and Dufour effects, taking into account heat transfer through solid walls. Lotfy et al. [6] analyzed Hall current and microtemperature effects on rods, and ramp-type microtemperature heating in rotator semiconductors, highlighting coupled elastic, magnetic, plasma, and thermal interactions. Lotfy et al. [7] applied hyperbolic two-temperature theory in 1D, showing strong effects on displacement, stress, and carrier density. Lotfy and El-Bary [8] extended this to 2D microstretch models under photothermal transport, while Ismail et al. [9] examined variable thermal conductivity impacts on thermal-plasma-elastic waves. These studies underscore the critical role of coupled mechanical, thermal, and electromagnetic effects in optimizing semiconductor behavior.

Researchers are very interested in using nanofluids because they have unique properties that make them better at conducting heat. These properties come from mixing nanoscale particles (such as oxide ceramics, metal carbides, nitrides, and metals or carbon nanotubes) with a base fluid (such as ethylene or triethylene glycols, water, alcohol, and polymer solutions), with Choi [10] being the first person to suggest this idea. These fluids are used for many different things, such as making nano-composites, bio-pharmaceuticals, oil digging, building nanostructures for transportation, and cooling electronics. Nanoparticles come in different types, each with its own unique optical, magnetic, mechanical, and thermal qualities. These include metal oxide ceramics like Al_2O_3 or CuO, ZnO, and TiO_2, nitrides ceramics like AlN or SiN, and metals. A lot of experts have made a lot of models to show how well nanofluids conduct heat. Maxwell [11] was the first person to study the thermal conductivity of colloidal solutions. This is a comparison of the thermal conductivity of fluids and particles. The Lattice Boltzmann model was used by Xuan et al. [12] to look into how heat moves through nanofluids. Buongiorno [13] studied nanofluid transport to find out how the relative speeds of nanoparticles in a normal fluid and a fluid with nanoparticles could be compared. A lot of researchers have used the modified conservation equations of motion to look into how thermal instability starts in nanofluids and nanoparticles, taking into account the effects of Brownian diffusion and thermophoresis. The main goal of the studies was to look into various mixtures of parameters and boundary conditions, either by themselves or with others.

Unlike the Oldroyd-B or Maxwell models, the Jeffrey model employs a single relaxation parameter that efficiently captures the viscoelastic behavior of the fluid without overcomplicating the governing equations. Jeffrey Nanofluid is a type of nanofluid that contains tiny particles mixed into a Jeffrey fluid. A Jeffrey fluid is a non-Newtonian fluid that shows shear thinning behavior, which means that as shear rate increases, viscosity decreases. Adding nanoparticles can improve the fluid's thermal and rheological qualities, which means it can be used in more situations. Some of these uses are making polymers, coatings, and composites better and more durable, controlling spacecraft, satellites, and other aerospace systems, and improving the performance and thermal efficiency of solar collectors and other energy systems. Additionally, Jeffrey

Nanofluid can be used in heat sinks, drug delivery, tissue engineering, and other biological tasks. It can also be used as a drilling fluid or a hydraulic fracturing fluid.

A lot of people are interested in studying double diffusive convection in Jeffrey nanofluid flooded porous layers because it has many uses in energy systems, environmental engineering, and industrial processes. A lot of research has been done to look into what happens when two types of convection mix in a layer that is both fluid and porous and full of nanoparticles. Umavathi and Sasso [14] looked into convection in a binary porous layer that was filled with an Oldroyd nanofluid. Yadav et al. [15] looked into the phenomenon of binary convective motion in a porous layer filled with Kuvshiniski fluid. They found that raising the Kuvshiniski parameter lowers convective heat transfer while raising the thermal Rayleigh number and the solute Rayleigh number increases both heat and mass transfers. Shoaib et al. [16] looked into the two-way flow of nanofluid on a flat, sloped surface that was saturated and porous. To do a full analysis, their study used an AI-based system with a balanced back propagated network. According to the results, as Gr goes up, so does velocity. The magnetic field parameter and angle of inclination, on the other hand, show the reverse trend.

More and more people are interested in studying free convection in fluids that contain internal energy. This is mostly because nuclear power engineering needs to get better all the time. The study of convection caused by internal heat sources has many uses in many fields, such as astrophysics, geophysics, thermal ignition, downsizing electrical parts, fire dynamics, combustion processes, and more. Researchers are looking into how an internal heat source affects the start of thermal convection in different types of fluids because the heat source makes the fluids float more, which changes the way heat and mass move through them. Experiments and computer simulations have both been used to look into how internal warmth affects natural convection in classical fluids. Sparrow et al. [17] looked at how internal warmth affects free convection and found that it makes the fluid layer more likely to become unstable. Watson [18] looked at how both internal heat sources and sinks affected the system and found that both of them made it less stable. Israel-Cookey et al. [19] looked into how thermally unstable a porous fluid layer is when internal warmth is added. The Darcy-Brinkman model was used by Yadav et al. [20] to look at how an internal temperature affects the start of nanofluid convection in a porous medium. The researchers found that the porosity has a calming effect on the system and the nanofluid Lewis number has an unstable effect. Sharma and Sharma [21] examined influence of heat sources and relaxation time on temperature distribution in tissues. Altawallbeh [22] did research on binary convection in a viscoelastic fluid porous layer with an internal heating. They found that when the thermal Rayleigh number is below the critical value, an increase in internal heat causes the Sherwood number to drop. Combined effects of Brownian motion and viscous dissipation on heat transfer and temperature distribution of Al_2O_3 /water nanofluid flow through a porous medium have been explored by Bouazizi and Turki [23]. Sharma and Khator [24,25] explored some problems of renewable sources with regard to power generation planning. A study by Ali et al. [26] used numbers to look into convection in a binary anisotropic porous layer that was rotated and heated from the inside. They found that warmth from the inside speeds up heat transfer, which makes it easier for thermal convection to start inside the system. The nanofluids' viscosity prediction through interaction layer of

particle-media have been investigated by Syzrantsev et al. [27] and draw fundamental understanding of the rheology of nanofluids (dispersions based on SiO_2 and Al_2O_3 nanoparticles). Abo-Dahab et al. [28] studied numerical estimation of the Double diffusive peristaltic flow of non- Newtonian Sisko nanofluid through a porous medium inside a horizontal symmetrical flexible channel under the various impacts due to specific boundary restrictions. Paandurangan et al. [29] investigated the heat and mass transfer in mixed convection peristaltic flow of Casson nanofluid through an asymmetric permeable channel filled with a porous medium in the presence of electro osmosis.

Recent advancements in porous media modeling have highlighted the importance of fractional and nonlocal approaches to capture anomalous diffusion and long-range interactions [30–32]. Such models allow accurate representation of spatio-temporal heat transfer and microstructural effects in complex media. Simultaneously, thermoelastic and viscoelastic nanofluids have gained prominence in energy systems, including solar collectors and thermal management devices, where enhanced heat transfer and stability are crucial [33,34]. Incorporating viscoelastic fluid behavior with advanced nanofluid formulations enables better prediction and control of convective processes, bridging the gap between theoretical modeling and practical energy applications. Raza et al. [35] investigated that nanofluids offer superior thermal conductivity compared to conventional fluids, with hybrid types like Al_2O_3–MWCNT enhancing heat transfer by up to 79 %. Their complex behavior challenges standard numerical methods, making multiscale modeling and AI-based techniques such as ANN, CNN, and RNN essential for predicting thermophysical stability and optimizing performance. Integrating experimental results with computational and AI-driven models is key for developing efficient, scalable nanofluid-based thermal systems.

Although the present study uses classical integer-order derivatives, the framework can be extended to include fractional-order or non-local effects, enabling the modeling of memory-dependent transport and long-range interactions in porous media. Such extensions would allow a more accurate representation of anomalous diffusion and complex thermal responses in nanofluid systems.

Because internal heat sources can be used in many different ways, we looked into how internal heat sources affect the start of binary convection in nanofluids with changed boundary conditions. Using the Jeffrey model with no nanoparticle volumetric flow helps to explain the rheology of the fluids. Unlike earlier works that studied Newtonian nanofluids or simplified viscosity models, our approach captures the influence of viscoelastic effects (through the Jeffrey parameter) together with nanoparticle migration and internal heating. This provides a more realistic framework for non-Newtonian nanofluid convection extending traditional models and offering improved predictive capability for thermoelastic behavior in porous structures.

Mathematical formulation

Two parallel xy lines hold in place a horizontal layer of a binary Jeffrey nanofluid that can't be squished. The temperatures in the lower and upper planes are shown as T_0 and T_1 at $z = 0$ and $z = d$ respectively with $(T_0 > T_1)$. The system is given a small

temperature difference, $\left|\frac{dT}{dz}\right|$ and the nanofluid has a constant heat source inside it, Q_0. The system is also affected by a gravity field, $g(0,0,-g)$ which can be seen in Fig. 1.

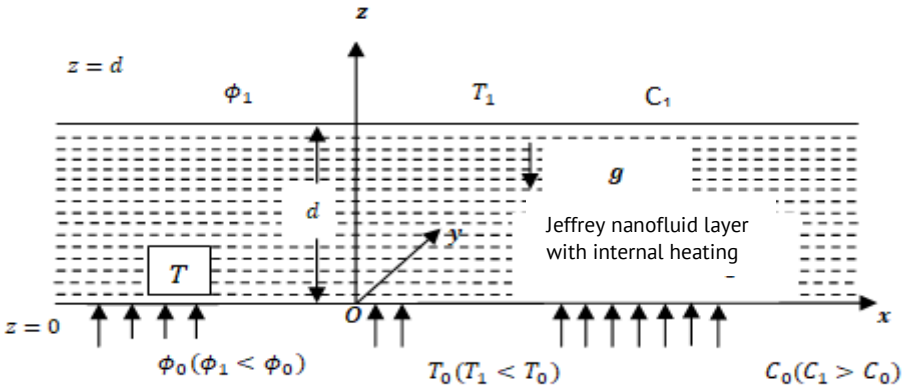

Fig. 1. Geometrical configuration of the system

The model is built under the following assumptions:

1. The nanofluid is incompressible and satisfies the Boussinesq approximation.
2. The porous medium obeys Darcy's law.
3. Fluid rheology follows the Jeffrey viscoelastic model.
4. Nanoparticle transport is governed by the Buongiorno model, including Brownian diffusion and thermophoresis.
5. Heat generation within the porous layer is uniform.
6. All thermophysical properties are constant except density in the buoyancy term.
7. Boundary conditions are taken as realistic experimental configurations. These assumptions simplify the coupled governing equations into an eigenvalue problem, solved by the Galerkin approach.

The equations that describe the flow, concentration, momentum, and thermal energy of Jeffrey nanofluid under the Boussinesq approach are [13,20,36–40]:

$$\nabla \cdot q = 0, \tag{1}$$

$$\frac{\rho}{\varepsilon}\left[\frac{\partial q}{\partial t} + \frac{1}{\varepsilon}(q \cdot \nabla)q\right] = \left[\phi\rho_p + (1-\phi)\rho_f\{1 - \beta(T - T_0) + \beta'(C - C_0)\}\right]g - \nabla p - \frac{\mu}{(1+\lambda)}\frac{q}{k_1}, \tag{2}$$

$$\frac{\partial \phi}{\partial t} + \frac{1}{\varepsilon}(q \cdot \nabla)\phi = \nabla.\left[D_B \nabla\phi + \frac{D_T}{T_0}\nabla T\right], \tag{3}$$

$$(\rho c)_m \frac{\partial T}{\partial t} + \frac{(\rho c)_f}{\varepsilon}(q \cdot \nabla)T = \nabla.(k_T.\nabla T) + (\rho c)_p \nabla T.\left[D_B \nabla\phi_n + \frac{D_T}{T_0}\nabla T\right] + Q_0, \tag{4}$$

$$(\rho c)_m \frac{\partial C}{\partial t} + \frac{(\rho c)_f}{\varepsilon}(q \cdot \nabla)C = \nabla.(k_c.\nabla C). \tag{5}$$

Different symbols in the above equations stand for different amounts of matter. Here, $\boldsymbol{q}$, $\boldsymbol{g}$, T, C, p, $\varepsilon, \lambda, \rho_p$, ρ_f, ϕ, β, β', k_1 and μ stand for the Darcy speed, the acceleration due to gravity, the temperature, the concentration, the pressure, the porosity, the Jeffrey parameter, the density of the nanoparticles, the density of the base fluid, the volume fraction of the nanoparticles, the thermal expansion coefficient, the solute expansion coefficient, the permeability of the porous medium, and the viscosity. Also, $(\rho c)_f$,$(\rho c)_p$,$(\rho c)_m$, D_B, K_T, k_c and D_T stand for the heat capacity of the fluid, the heat capacity of nanoparticles, the heat capacity of the fluid in a porous medium, the Brownian diffusion coefficient, the thermal conductivity, the solute diffusivity, and the

thermophoretic diffusion coefficient. Dufour type and Soret type diffusion are not taken into account. Adding a term called "Q_0" to the heat equation is a typical way to deal with an internal heat source.

It is thought that both limits are stress-free and keep their temperatures the same. There is also a small amount of volume fraction flow of nanoparticles. As a result, the following border conditions must be met:

$$\begin{aligned} &w = 0,\ T = T_0,\ C = C_0,\ D_B\frac{\partial \phi}{\partial z} + \frac{D_T}{T_1}\frac{\partial T}{\partial z} = 0 \ \text{ at } z = 0, \\ &w = 0,\ T = T_1,\ C = C_1,\ D_B\frac{\partial \phi}{\partial z} + \frac{D_T}{T_1}\frac{\partial T}{\partial z} = 0 \ \text{ at } z = d. \end{aligned} \tag{6}$$

This reflects the physical reality that nanoparticles cannot penetrate solid boundaries, making the setup experimentally realizable. The base concentration and solute profiles are assumed linear, representing an initially uniform preparation of the nanofluid. These boundary conditions allow accurate modeling of the coupled transport of heat, solute, and nanoparticles, capturing the essential physics of double-diffusive convection in a confined porous medium while maintaining consistency with laboratory conditions.

Introducing the variables with no dimensions such as:

$$\begin{aligned} &(x^*, y^*, z^*) = \frac{(x,y,z)}{d}, q^* = \frac{d}{\alpha_m}q, \quad t^* = \frac{\alpha_m}{\sigma d^2}t, \quad \phi_n^* = \frac{(\phi_n - \phi_0)}{(\phi_1 - \phi_0)}, \\ &{q_d}^* = \frac{d}{\alpha_m}q_d, C^* = \frac{(C - C_0)}{\Delta C}, T^* = \frac{(T - T_0)}{\Delta T}, p^* = \frac{pk_1}{\mu\alpha_m}, \end{aligned} \tag{7}$$

we can write Eq. (1) through Eq. (5) in a form that doesn't involve dimensions by changing α_m to $\frac{k_T}{(\rho c)_f}$, σ to $\frac{(\rho c)_m}{(\rho c)_f}$ and ΔT to $T_0 - T_1$:

$$\nabla \cdot q = 0, \tag{8}$$

$$\frac{1}{V_a}\left\{\frac{1}{\sigma}\frac{\partial}{\partial t} + \frac{1}{\varepsilon}q.\nabla\right\} q\,\frac{D_a}{\varepsilon P_r} = -\frac{q}{1+\lambda} - \nabla p - R_n\phi - R_m + R_a T - \frac{R_S C}{L_e}, \tag{9}$$

$$\frac{\partial T}{\partial t} + \frac{1}{\varepsilon}(q \cdot \nabla)T = \nabla^2 T + \frac{N_B}{L_n}(\nabla\phi_n.\nabla T) + \frac{N_A N_B}{L_e}(\nabla T.\nabla T) + H_s, \tag{10}$$

$$\frac{1}{\sigma}\frac{\partial \phi}{\partial t} + \frac{1}{\varepsilon}(q \cdot \nabla)\phi = \frac{1}{L_n}\nabla^2\phi + \frac{N_A}{L_n}\nabla^2 T, \tag{11}$$

$$\frac{\partial C}{\partial t} + \frac{1}{\varepsilon}(q \cdot \nabla)C = \frac{1}{L_e}\nabla^2 C. \tag{12}$$

Here $R_m = \frac{[\phi_0\rho_P + (1-\phi_0)\rho\,]gdk_1}{\mu\alpha_m}$ is the basic density Rayleigh number, $R_s = \frac{\rho\, g\beta dk_1(C_0 - C_1)}{\mu^*\alpha_m}$ is the thermal Rayleigh number $N_A = \frac{D_T\,(T_0 - T_1)}{D_B\,T_0\,(\phi_1 - \phi_0)}$ is the modified diffusivity ratio, $N_B = \frac{\varepsilon(\rho c)_P(\phi_1 - \phi_0)}{(\rho c)_f}$ is the modified particle density increment. We have $D_a = \frac{k_1}{d^2}$, the Darcy number, $P_r = \frac{\mu}{\rho\,\alpha_m}$, the Prandtl number, $V_a = \frac{\varepsilon Pr}{Da}$, the Vadasz number, $L_n = \frac{\alpha_m}{D_B}$, the Lewis number, $L_e = \frac{\alpha_m}{k_c}$, the Lewis number due to salinity, $R_a = \frac{\rho\, g\beta dk_1(T_0 - T_1)}{\mu^*\alpha_m}$, the thermal Rayleigh number and $R_n = \frac{(\rho_P - \rho_f)(\phi_1 - \phi_0)gdk_1}{\mu\alpha_m}$, the concentration Rayleigh number. The dimensionless internal heat parameter is shown by The dimensionless internal heat parameter is shown by $H_s = \frac{Q_0 d^2}{k_T\,(T_1 - T_0)}$.

Basic flow and perturbation equations

We look at a nanofluid that doesn't move or settle over time and doesn't have any floating nanoparticles. It is thought that changes in temperature, pressure, and the bulk fraction of nanoparticles only happen in the z-direction. In this case, the answers to Eq. (8) through Eq. (12) lead to this state:

$$q_b = (0,0,0), p = p_b(z), T = T_b(z), \phi = \phi_b(z), C = C_b(z). \tag{13}$$

Using Eq. (13), Eqs. (8)–(12) give:

$$\frac{\partial^2 T_b}{\partial z^2} + \frac{\partial T_b}{\partial z}\left(\frac{N_B}{L_n}\frac{d\phi_b}{dz} + \frac{N_A N_B}{L_e}\frac{\partial T}{\partial z}\right) + H_s = 0, \tag{14}$$

$$N_A \frac{\partial^2 T_b}{\partial z^2} + \frac{\partial^2 \phi_b}{\partial z^2} = 0, \tag{15}$$

$$\frac{1}{L_e}\frac{\partial^2 C_b}{\partial z^2} = 0. \tag{16}$$

When you do a single integration of Eq. (15) with respect to variable z and include the boundary surfaces (6), you get:

$$N_A \frac{\partial T_b}{\partial z} + \frac{\partial \phi_b}{\partial z} = 0. \tag{17}$$

When you plug in Eq. (17) into Eq. (14), you get:

$$\frac{\partial^2 T_b}{\partial z^2} + H_s = 0. \tag{18}$$

When we do a double integration of Eq. (18) with respect to the variable z and keep the border conditions (6) in mind, we get the following result:

$$T_b = \left(\frac{H_s}{2} - 1\right) z - \frac{H_s}{2} z^2 + 1. \tag{19}$$

Putting Eq. (19) into Eq. (17) and integrating gives us:

$$\phi_b = -\frac{N_A}{2}(-2 - 2H_s z + H_s), \tag{20}$$

$$C_b = -z + 1. \tag{21}$$

To check the stability of the physical system under study, tiny changes are made to the starting flow. This lets us look more closely at:

$$q = q_b + q', T = T_b + T', \phi = \phi_b + \phi', C = C_b + C', \tag{22}$$

where $q' = (u', v', w')$, T', $C'$and ϕ' are the changes in physical quantities.

By using Eqs. (19)–(21), along with perturbations from Eq. (22) in Eq. (8)–(12), we get the non-dimensional linear perturbed equations that look like this:

$$\left\{\frac{1}{\sigma V_a}\frac{\partial q}{\partial t}\right\} = -\frac{q}{1+\lambda} - \nabla p - R_n \phi + R_a T - \frac{R_s C}{L_e}, \tag{23}$$

$$\frac{\partial T}{\partial t} + \frac{q}{2\varepsilon}(H_s - 2 - 2H_s z) = \nabla^2 T + \frac{N_B}{2L_n}(H_s - 2 - 2H_s z)\frac{\partial \phi}{\partial z} + \frac{N_A N_B}{2L_n}(H_s - 2 - 2H_s z)\frac{\partial T}{\partial z}, \tag{24}$$

$$\frac{1}{\sigma}\frac{\partial \phi}{\partial t} + \frac{q}{2\varepsilon}(1 - H_s + 2H_s z)N_A = \frac{1}{L_n}\nabla^2 \phi + \frac{N_A}{L_n}\nabla^2 T, \tag{25}$$

$$\frac{\partial C}{\partial t} - \frac{q}{\varepsilon} = \frac{1}{L_e}\nabla^2 C. \tag{26}$$

We get the following expression when we take variable p out of Eq. (23):

$$\left\{\frac{1}{\sigma V_a}\frac{\partial}{\partial t} + \frac{1}{1+\lambda}\right\}\nabla^2 w = \left(-R_n \nabla_1^2 \phi + R_a \nabla_1^2 T - \frac{R_s \nabla_1^2 C}{L_e}\right). \tag{27}$$

To get exact answers for Eqs. (23)–(26), we use a normal mode analysis to look into the changed physical values. In this method, the variables are given horizontal wave numbers and a growth rate as:

$$[[w', T', C', \phi'] = [W, \Theta, \Psi, \Phi](z)\, exp\{st + i(k_x x + k_y y)\}, \tag{28}$$

where k_x, $k_y$and s all mean what they're supposed to.

Using Eq. (28) along with Eqs. (23)–(27) and making sure that conditions (19), (20), and (21) are met, we can get the following set of stability equations:

$$\left(\frac{1}{\sigma V_a}s+\frac{1}{1+\lambda}\right)(D^2-a^2)W=\left[\left\{R_n a^2\phi+R_a a^2 T-\frac{R_s a^2 C}{L_e}\right\}\right], \tag{29}$$

$$s\Theta+\frac{W}{2\varepsilon}(H_s-2-2H_s z)=\left[(D^2-a^2)\Theta+\frac{N_B}{2L_n}(H_s-2-2H_s z)D\Phi+\frac{N_A N_B}{2L_n}(H_s-\right.$$
$$\left.-2-2H_s z)D\Theta\right], \tag{30}$$

$$s\Psi-\frac{W}{\varepsilon}=\frac{1}{L_e}(D^2-a^2)\Psi, \tag{31}$$

$$\frac{1}{\sigma}s\Phi+\frac{W}{2\varepsilon}(1+2H_s z-H_s)N_A=\frac{1}{L_n}(D^2-a^2)\Phi+\frac{N_A}{L_n}(D^2-a^2)\Theta. \tag{32}$$

The boundary conditions (6) change to:

$$W=D^2W=0,\ D\Phi+N_A D\Theta=0,\ \Theta=0,\ \Psi=0,\ D\Psi=0, \text{at } z=0 \text{ and } z=1. \tag{33}$$

There is a linear eigenvalue problem for the temperature Rayleigh number that is made up of Eqs. (29)–(32) and boundary conditions (33). We use the Galerkin method to find exact solutions to Eqs. (29)–(32) that don't are easy and meet the boundary conditions (33). For example:

$$W=A_1\sin\pi z,\ \Theta=B_1\sin\pi z,\ \Phi=-C_1N_A\sin\pi z,\ \Psi=D_1\sin\pi z, \tag{34}$$

where A_1, B_1, C_1 and $D_1$are unknown coefficients.

We can find the thermal Rayleigh number for stationary convection by putting s = 0 in Eqs. (29)–(32) and integrating each equation separately over the range of 0 < z < 1 while applying the boundary conditions (33). There, we have it:

$$R_a^s=\frac{(\pi^2+a^2)\{a^2+\pi^2\}\varepsilon\{(\pi^2+a^2)L_n+H_sN_AN_B(1+N_A)\}}{a^2(1+\lambda)\{(\pi^2+a^2)+H_sN_A^2N_B\}}+\frac{N_A^2\{-(\pi^2+a^2)\{1-L_n\}+H_sN_AN_B\}R_n}{\{(\pi^2+a^2)+H_sN_A^2N_B\}}+$$
$$+\frac{(\pi^2+a^2)\{(\pi^2+a^2)L_n+H_sN_AN_B(1+N_A)\}R_s}{a^2L_n\{(\pi^2+a^2)+H_sN_A^2N_B\}}. \tag{35}$$

Now special cases arise:

Case (I): for case (I), if the fluid base is very thick and doesn't have any heat sources inside it ($\lambda=0, H_s=0$,) Eq. (35) reduces to:

$$R_a^s=\frac{(\pi^2+a^2)^2}{a^2}-\frac{(L_e+\varepsilon)N_AR_n}{\varepsilon}+\frac{R_s}{\varepsilon}, \tag{36}$$

the results found are very similar to those of the previous study by Yadav et al. [20].

Case (II): If there are no nanoparticles or salt, i.e.,$R_s=0, R_n=0, N_A=0$, Eq. (36) gets even smaller, to:

$$R_a^s=\frac{(\pi^2+a^2)^2}{a^2}, \tag{37}$$

the result that was seen is in line with what Lapwood [41] found.

We use a mathematical expression $\left(\frac{dR_a^s}{da^2}\right)_{a^2=a_c^2}=0$ to find the critical wave number and its corresponding critical stationary thermal Rayleigh number R_a^s. This gives us a polynomial equation with the variable a_c^2as:

$$\varepsilon L_n^2(a_c^2)^4+2L_n^2(a_c^2)^3\varepsilon(\pi^2+H_sN_A^2N_B)+(a_c^2)^2H_sL_nN_A^2N_B[\{\varepsilon H_sN_A(1+N_A)N_B+$$
$$+L_n(\pi^2(3)\varepsilon+(1+\lambda)N_A^2R_n)\}-(1+\lambda)\{\pi^2L_n+H_sN_A(1+N_A)N_B\}R_s-$$
$$-H_sN_AN_BL_n\{(1+N_A)(\pi^2\varepsilon)+(1+\lambda)N_A^2R_n-(1+\lambda)N_AR_S\}]-2a_c^2\pi^2\{L_n\pi^2+$$
$$+H_sN_AN_B(1+N_A)\}\{\pi^2\varepsilon L_n+(1+\lambda)\}-\pi^2\{\pi^2+H_sN_A^2N_B\}\{(L_n\pi^2+$$
$$+H_sN_AN_B(1+N_A))(\pi^2\varepsilon L_n+(1+\lambda)R_s)\}=0. \tag{38}$$

If the fluid is regular and there is no salt in it or any internal heating, i.e., $N_A = R_n = 0$, $R_s = 0$ and $H_s = 0$, then Eq. (38) gives us the critical wave number ($a_c = \pi$) and the critical thermal Rayleigh number ($Ra_c = 4\pi^2$), which is very close to what Lapwood [41] suggested.

The effect of the dimensionless parameters H_s, λ, R_s, R_n and L_n on the stationary convection for Jeffrey nanofluid is studied by figuring out $\frac{\partial R_a^S}{\partial H_s}, \frac{\partial R_a^S}{\partial \lambda}, \frac{\partial R_a^S}{\partial R_s}, \frac{\partial R_a^S}{\partial R_n}$ and $\frac{\partial R_a^S}{\partial L_n}$. If you plug in Eq. (35), you get:

$$\frac{\partial R_a^S}{\partial H_s} = \frac{(a^2+\pi^2)[\{1+(1-L_n)N_A\}]N_A N_B[(a^2+\pi^2)\varepsilon+a^2(1+\lambda)N^2{}_A R_n]}{a^2(1+\lambda)\{(a^2+\pi^2)+H_s N_A^2 N_B\}^2}. \tag{39}$$

From Eq. (39) we can see that $\frac{\partial R_a^S}{\partial H_s} > 0$ or < 0 for $1 > L_n$ or $1 < L_n$. But $1 > L_n$ is not possible with the parameter numbers that were chosen. Because of this, an internal heat source makes a machine less stable.

Equation (35), which gives:

$$\frac{\partial R_a^S}{\partial \lambda} = \frac{(a^2+\pi^2)[(a^2)]\varepsilon[(a^2+\pi^2)L_n+H_s N_A N_B(1+N_A)]}{a^2(1+\lambda)^2\{(a^2+\pi^2)+H_s N_A^2 N_B\}}, \tag{40}$$

where Eq. (40) demonstrates that $\frac{\partial R_a^S}{\partial \lambda} > 0$. As a result, the Jeffrey constant makes the system under consideration more stable:

$$\frac{\partial R_a^S}{\partial R_s} = \frac{(a^2+\pi^2)(1+b)[(a^2+\pi^2)L_n+H_s N_A N_B(1+N_A)]}{a^2 L_n\{(1+b)(a^2+\pi^2)+H_s N_A^2 N_B\}}, \tag{41}$$

where Eq. (41) shows that $\frac{\partial R_a^S}{\partial R_s}$ is positive for all wave numbers. Thus, the Rayleigh number due to salinity enhances the stability of system.

$$\frac{\partial R_a^S}{\partial R_n} = \frac{N_A^2[(a^2+\pi^2)(L_n-1)+H_s N_B N_A]}{\{(a^2+\pi^2)+H_s N_B N_A^2\}}. \tag{42}$$

That means $\frac{\partial R_a^S}{\partial R_n}$is positive for L_n greater than 1. In this way, the concentration Rayleigh number makes a system more stable:

$$\frac{\partial R_a^S}{\partial L_n} = \frac{L_n\{(a^2+\pi^2)^2\{a^2+\pi^2\}\varepsilon+a^2(1+\lambda)(a^2+\pi^2)N_A^2 R_n\}}{a^2(1+\lambda)L_n\{(a^2+\pi^2)+N_B H_s N_A^2\}} + \frac{(a^2+\pi^2)^2(1+\lambda)R_s}{a^2(1+\lambda)L_n\{(a^2+\pi^2)+N_B H_s N_A^2\}} - \\ - \frac{(a^2+\pi^2)[(a^2+\pi^2)L_n+H_s N_A N_B(1+N_A)]R_s}{a^2 L^2{}_n\{(a^2+\pi^2)+N_B H_s N_A^2\}}, \tag{43}$$

where Eq. (43) shows that $\frac{\partial R_a^S}{\partial L_n}$is positive for all wave numbers, which implies that L_n has stabilizing influence.

The novelty of this study lies in combining the Jeffrey viscoelastic fluid model with the Buongiorno nanofluid framework to investigate double-diffusive convection under internal heat generation. Internal heating supplies energy directly within the porous nanofluid layer, creating additional buoyancy forces that drive fluid motion even in the absence of external temperature gradients. This reduces the critical thermal Rayleigh number, causing convection to onset earlier and convective cells to grow larger. The Jeffrey viscoelastic fluid, with its elastic (memory) and viscous (damping) characteristics, interacts with buoyancy forces in a manner that amplifies disturbances rather than suppressing them. Interestingly, while previous studies often report that the Jeffrey parameter stabilizes the system and internal heating alone acts as a destabilizing factor, in this study both the Jeffrey viscoelasticity and internal heating contribute to destabilization under the chosen parameters. Consistent with literature, the salinity Rayleigh number continues to act as a stabilizing influence. Together, internal heating and viscoelasticity enhance system

instabilities, initiating convection at lower thermal forcing, while the critical wave number—and hence the characteristic cell size—remains largely unchanged. This combined effect has practical significance for energy and thermal management systems, including solar collectors, geothermal reservoirs, and chemical reactors, where enhanced convection is beneficial, but flow stability must be carefully controlled.

The findings of this study are relevant for engineering systems where heat and mass transfer in nanofluids within porous structures is critical. Potential applications include enhanced oil recovery, geothermal energy extraction, solar thermal collectors, microelectronic cooling, and biomedical devices. The results may guide the design of more stable and efficient thermal systems by identifying conditions that suppress or trigger convection.

Results and Discussion

The thermal instability of binary Jeffrey nanofluid layer in porous medium is conducted by investigating the stationary thermal Rayleigh number, given by Eq. (35) and examining the effects of relevant non-dimensional parameters. The numerical computation of thermal Rayleigh numbers is performed using MATHEMATICA software (version-12), where one non-dimensional parameter is varied while keeping others constant. The parameter values are considered within certain limits. Graphical representations of the calculated results are shown in Figs. 2–8 with a specific focus on a top-heavy distribution of nanoparticles. The current analysis focuses on stationary convection to establish fundamental stability characteristics. The methodology can be adapted to investigate oscillatory and transient modes, offering insights into time-dependent convection, wave propagation, and the evolution of instabilities under varying thermal and solutal conditions.

The impact of Rayleigh number due to salinity, R_s on stationary thermal Rayleigh number R_a^s, in relation to the wave number a in the stationary mode, is depicted in Fig. 2. It is observed from the curves that a rise in the solutal Rayleigh number leads to a notable effect, resulting in an escalation of the thermal Rayleigh number. Therefore, R_s stabilizes

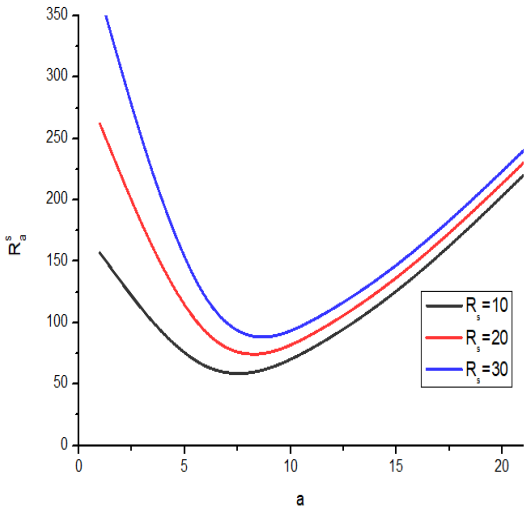

Fig. 2. Comparison ofstationary thermal Rayleigh number R_a^s against wave number a for multiple values of Rayleigh number due to salinity R_s

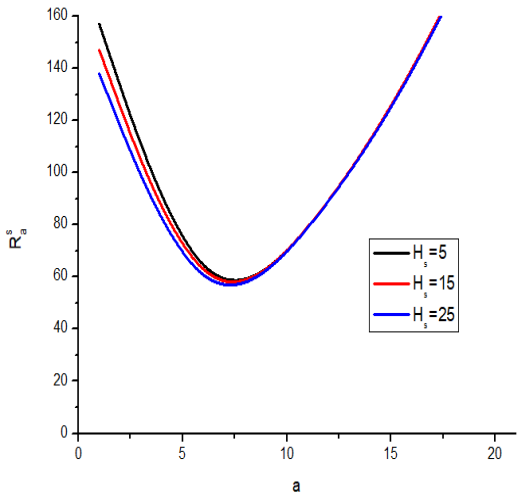

Fig. 3. Comparison ofstationary thermal Rayleigh number R_a^s against wave number a for multiple values of internal heat source H_s

the system. A large solutal Rayleigh number leads to convective instability, where buoyancy forces dominate over diffusive forces. Conversely, a small solutal Rayleigh number enhances the significance of diffusive forces, resulting in a more stable system. Physically, as salinity-induced buoyancy grows, the system resists purely thermal disturbances more effectively, thereby raising the threshold of thermal instability.

Figure 3 depicts the correlation between the internal heating parameter H_s and the thermal Rayleigh number R_a^s in the study. The results indicate that a decrease in the internal heating leads to an increase in R_a^s. As a result, the convective cell size increases, exerting a destabilizing influence on the Jeffrey nanofluid. Furthermore, the internal heat source causes a decrease in the critical wave number, thereby enhancing the convective heat transfer within the system. In physical terms, greater internal heating injects extra energy into the fluid layer, which reduces the critical condition for instability and promotes more vigorous convection in the Jeffrey nanofluid.

A visualization of the relationship between the stationary thermal Rayleigh number, R_a^s and the Jeffrey fluid parameter, λ is presented in Fig. 4. As the Jeffrey parameter increases, it is noted that the stability range for the stationary mode decreases, resulting in a decline in R_a^s. However, despite this increase, the critical wave number remains unchanged. Thus, stronger Jeffrey-type elasticity promotes earlier onset of convection by reducing the required thermal driving, even though it does not change the characteristic size of convective cells.

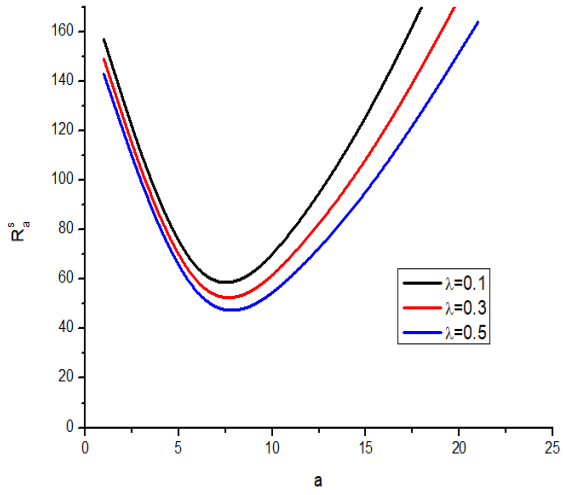

Fig. 4. Comparison ofstationary thermal Rayleigh numberR_a^s against wave number a for multiple values of Jeffrey parameter λ

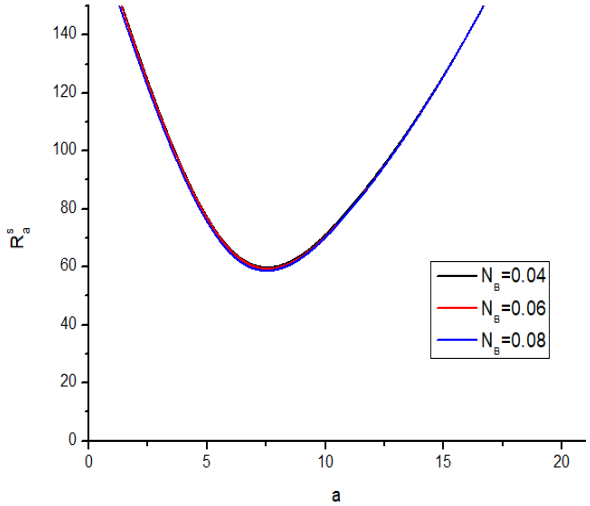

Fig. 5. Comparison ofstationary thermal Rayleigh numberR_a^s against wave number a for multiple values of modified particle density increment N_B

Figure 5 and 6 present the relationship between the modified particle density increment N_B and the concentration Rayleigh number R_n, respectively, with R_a^s. It is observed from Fig. 5 that when the modified particle density experiences a slight decrease, the thermal Rayleigh number increases due to the low value of the term NB^{-1} in the energy equation. This decrease leads to the expansion of convectional cells, thereby destabilizing the system. Conversely, Fig. 6 illustrates that as the concentration Rayleigh number rises, there is a corresponding increase in R_a^s, thus advancing the onset of

stationary convection. While changes in the concentration Rayleigh number affect the critical wave number, the increment in modified particle density does not have any influence on it. Physically, this means that a reduction in modified particle density weakens the stabilizing role of nanoparticles, allowing convection to occur more easily with larger cells. In contrast, an increase in the concentration Rayleigh number enhances solutal buoyancy, which accelerates the onset of convection and also alters the size of convection cells.

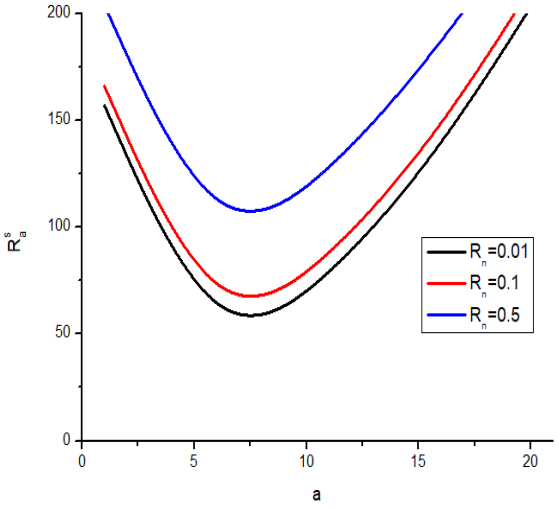

Fig. 6. Comparison of stationary thermal Rayleigh number R_a^s against wave number a for multiple values of concentration Rayleigh number R_n

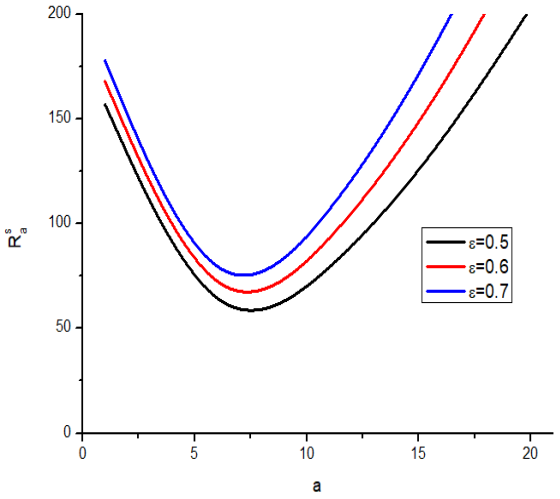

Fig. 7. Comparison of stationary thermal Rayleigh number R_a^s against wave number a for multiple values of porosity ε

In Fig. 7, the impact of medium porosity, ε on the system stability framework is depicted. As the medium porosity increases, the stationary thermal Rayleigh number R_a^s also increases, expanding the region of stability under stationary modes. Consequently, the size of convection cells decreases. Porosity represents the fraction of open space available for fluid flow within the medium. As porosity increases, the medium behaves

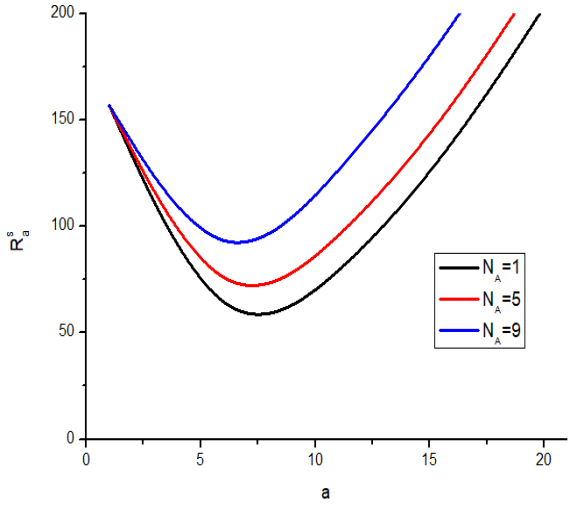

Fig. 8. Comparison of stationary thermal Rayleigh number R_a^s against wave number a for multiple values of modifieddiffusivity ratio N_A

more like a free-fluid layer with reduced resistance from the solid matrix. This facilitates fluid motion, but the enhanced heat transfer stabilizes the system, thereby raising the critical Rayleigh number. Consequently, convection is delayed to higher thermal forcing, and when it sets in, smaller convection cells are formed, allowing more efficient heat transport in the porous environment.

Figure 8 illustrates the impact of modified diffusivity ratio, N_A on R_a^s. An elevation in the modified diffusivity ratio leads to a rise in thermal Rayleigh number, which in turn amplifies the stability region and enlarges the convection cells. Consequently, the system is stabilized by modified diffusivity ratio. Nevertheless, the critical wave number remains unaltered. This implies that the system demands stronger thermal forcing to initiate convection. Although the convection cells grow in size, the fundamental spacing between them, represented by the critical wave number, does not change. In other words, stability is enhanced without altering the basic pattern of convection onset.

The observed trends in our study generally align with prior research, while showing some notable deviations. Previous investigations on viscoelastic nanofluid convection [14,23,42–45] indicate that results depend strongly on the chosen model and parameters. For example, the Jeffrey model in earlier studies (Rana [44]) typically promotes convection,porosity tends to destabilize the system, and the nanofluid parameter modified diffusivity ratio often has negligible influence. In contrast, in our study, the Jeffrey model consistently shows a destabilizing effect, porosity acts oppositely by stabilizing, and modified diffusivity ratio surprisingly produces a pronounced stabilizing effect. The Rayleigh number due to salinity, meanwhile, promotes stability, in agreement with Umavathi et al. [45]. Regarding internal heating, prior studies, including Khalid et al. [42], indicate that internal heat sources generally destabilize the system. Our results corroborate this observation, confirming that internal heating has a destabilizing influence in our configuration as well. These findings highlight the sensitivity of system stability to parameter interactions and emphasize the importance of considering mixed parameter effects when analyzing convection in viscoelastic nanofluids.

Conclusions

This paper investigates the influence of viscoelastic behavior and internal heating on double-diffusive convection in a Jeffrey nanofluid saturated porous medium. By applying linear stability theory and a one-term Galerkin approach, an analytical expression for the stationary thermal Rayleigh number was derived. Key findings reveal that higher concentration and solutal Rayleigh numbers expand the convection domain, internal heating strengthens heat transfer, while increased porosity and diffusivity ratio improve system stability. In contrast, reduced particle density and higher salinity Rayleigh numbers trigger destabilization. The Jeffrey parameter reduces stability without altering the critical wave number, underlining the distinct role of viscoelasticity.

Overall, the results provide new insights into the thermo-diffusion behavior of Jeffrey nanofluids, with potential applications in thermal energy storage, enhanced oil recovery, and polymeric material design. The analytical framework can guide the design of advanced nanofluid systems for engineering applications. Future research may extend

this work to nonlinear regimes, oscillatory instabilities, fractional-order models, and AI-assisted prediction techniques, alongside experimental validation for practical systems.

CRediTauthorshipcontributionstatement

Virender Sharma: writing – review & editing, writing – original draft, data curation; **Jyoti Devi:** writing – review & editing, writing – original draft, Investigation; **Rajneesh Kumar:** conceptualization, supervision; **Veena Sharma:** conceptualization, supervision.

Conflict of interest

The authors declare that they have no conflict of interest.

References

1. Stern ME. The 'salt fountain' and thermohaline convection. *Tellus.* 1960;12(2): 172–175.
2. Huppert HE, Turner JS. Double-diffusive convection. *Journal of Fluid Mechanics.* 1981;106: 290–329.
3. Dougall J. Double diffusive convection caused by coupled molecular diffusion. *Journal of Fluid Mechanics.* 1983;126: 379–397.
4. Kafoussias NG, Williams EW. The effect of temperature-dependent viscosity on free-forced convective laminar boundary layer flow past a vertical isothermal flat plate. *Acta Mechanica.* 1995;110: 123–137.
5. Kuznetsov G, Sheremet M. A numerical simulation of double-diffusive conjugate natural convection in an enclosure. *International Journal of Thermal Sciences and Physical Engineering.* 2011;50(10): 1878–1886.
6. Lotfy K, El-Bary AA, Hassan W, Ahmed MH. Hall current influence of microtemperature magneto-elastic semiconductor material. *Superlattices and Microstructures.* 2020;139: 106428.
7. Lotfy K, Elidy ES, Tantawi RS. Photothermal excitation process during hyperbolic two-temperature theory for magneto-thermo-elastic semiconducting medium. *Silicon.* 2021;13(7): 2275–2288.
8. Lotfy K, El-Bary AA. Magneto-Photo-Thermo-Microstretch Semiconductor Elastic Medium Due to Photothermal Transport Process. *Silicon.* 2022;14(9): 4809–4821.
9. Ismail GM, Gepreel KA, Lotfy K, Mahdy AMS, El-Bary A. Influence of variable thermal conductivity on thermal-plasma-elastic waves of excited microelongatedsemiconductor. *Alexandria Engineering Journal.* 2022;61(12): 12271–12282.
10. Choi SU. Enhancing thermal conductivity of fluids with nanoparticles. In: *Developments and Applications of Non-Newtonian Flows*. 1995. p.231–247.
11. Maxwell JC. On the dynamical theory of gases. *Journal of Phil. Trans. R. Soc. London*. 1866;157: 2678.
12. Xuan Y, Li Q. Heat transfer enhancement of nanofluids. *International Journal of Heat and Mass Transfer.* 2000;21(1): 58–64.
13. Buongiorno J. Convective transport in nanofluids. *Journal of Heat Transfer.* 2006;128(3): 240–250.
14. Umavathi JC, Sasso M. Double diffusive convection in a porous medium layer saturated with an Oldroyd nanofluid. *AIP Conference Proceedings.* 2017;1798: 020166.
15. Yadav D, Kumar Awasthi M, Al-Siyabi M, Al-Nadhairi S, Al-Rahbi A, Al-Subhi M, et al. Double diffusive convective motion in a reactive porous medium layer saturated by a non-Newtonian Kuvshiniski fluid. *Physics of Fluids.* 2022;34(2): 024104.
16. Shoaib M, Rafia T, Raja MAZ, Khan WA, Waqas M. Further analysis of double-diffusive flow of nanofluid through a porous medium situated on an inclined plane: AI-based Levenberg–Marquardt scheme with backpropagated neural network. *Journal of the Brazilian Society of Mechanical Sciences and Engineering.* 2022;44: 227.
17. Sparrow EM, Tsou FK, Kurtz Jr EF. Stability of Laminar Free-Convection Flow on a Vertical Plate. *The Physics of Fluids*. 1965;8(8): 1559–1561.
18. Watson PM. Classical cellular convection with a spatial heat source. *Journal of Fluid Mechanics.* 1968;32(2): 399–411.
19. Israel-Cookey C, Nwaigwe C. Unsteady MHD flow of a radiating fluid over a moving heated porous plate with time-dependent suction. *American Journal of Scientific and Industrial Research.* 2010;1(1): 88–95.
20. Yadav D, Bhargava R, Agrawal GS. Boundary and internal heat source effects on the onset of Darcy–Brinkman convection in a porous layer saturated by nanofluid. *International Journal of Thermal Sciences.* 2012;60: 244–254.
21. Sharma S, Sharma K. Influence of heat sources and relaxation time on temperature distribution in tissues. *International Journal of Applied Mechanics and Engineering.* 2014;19(2): 427–433.

22. Altawallbeh AA. Cross diffusion effect on linear and nonlinear double diffusive convection in a viscoelastic fluid saturated porous layer with internal heat source. *Fluids.* 2021;6(5): 182.
23. Bouazizi L, Turki S. Combined effects of viscous dissipation and Brownian motion on temperature distribution and heat transfer of Al_2O_3/water nanofluid flow through a porous medium. *Materials Physics and Mechanics.* 2021;47(6): 921–936.
24. Sharma S, Khator S. Micro-grid planning with aggregator's role in the renewable inclusive prosumer market. *Journal of Power and Energy Engineering.* 2022;10(4): 47–62.
25. Sharma S, Khator S. Power generation planning with reserve dispatch and weather uncertainties including penetration of renewable sources. *International Journal of Smart Grid and Clean Energy.* 2021;10(4): 292–303.
26. Ali SA, Rudziva M, Sibanda P, Noreldin OAI, Goqo SP, Mthethwa HS. A numerical study of double-diffusive convection in the anisotropic porous layer under rotational modulation with internal heat generation. *International Communications in Heat and Mass Transfer.* 2022;137: 106266.
27. Syzrantsev VV, Arymbaeva AT, Zavjalov AP, Zobov KV. The nanofluids' viscosity prediction through particle-media interaction layer. *Materials Physics and Mechanics.* 2022;48(3): 386–396.
28. Abo-Dahab SM, Mohamed RA, Abd-Alla AM, Soliman MS. Double diffusive peristaltic MHD Siskonanofluid flow through a porous medium in presence of non-linear thermal radiation, heat generation/absorption, and Joule heating. *Scientific Reports.* 2023;13: 1432.
29. Paandurangan B, Parthasarathy SE, Tripathi D, Bég OA. The impact of double-diffusive convection on electroosmotic peristaltic transport of magnetized Casson nanofluid in a porous asymmetric channel. *Zeitschrift für AngewandteMathematik und Mechanik.* 2024;104(9): e202300771.
30. Alanazi K, Abouelregal AE. Thermoelastic behavior of infinite porous media with voids subjected to instantaneous heat Sources: A Spatio-Temporal nonlocal and fractional heat transfer approach. *Ain Shams Engineering Journal.* 2025;16(7): 103377.
31. Xu W, Liu H, Chen L, Zhou Y. Ultrafast diffusion modeling via the Riemann–Liouville nonlocal structural derivative and its application in porous media. *Fractal and Fractional.* 2024;8(2): 110.
32. Zhang X, Zeng S. Time-space fractional porous medium equations with nonlocal nonlinear terms. *Evolution Equations and Control Theory.* 2025;14(6): 1678–1695.
33. Junaid MS, Aslam MN, Khan MA, Saleem S, Riaz MB. Thermal analysis of a viscoelastic Maxwell hybrid nanofluid with graphene and polythiophene nanoparticles: Insights from an artificial neural network model. *Alexandria Engineering Journal.* 2024;94: 193–211.
34. Bocanegra JA, Marchitto A, Misale M. Nanofluids in solar collectors: a comprehensive review focused on its sedimentation. *Clean Technologies and Environmental Policy.* 2025;27(4): 1753–1784.
35. Raza M, Faiz M, Hassan WU, Abbas M, Raza J, Kumail Z, Nawaz T, Shabir S, Jan A, Li FC. AI-powered optimization and numerical techniques for nanofluid heat transfer systems-a review. *Multiscale and Multidisciplinary Modeling, Experiments and Design.* 2024;8(7): 316.
36. Nield DA, Kuznetsov AV. The onset of convection in a horizontal nanofluid layer of finite depth. *European Journal of Mechanics-B/Fluids.* 2010;29(3): 217–223.
37. Nield DA, Kuznetsov AV. The onset of double-diffusive convection in a nanofluid layer. *International Journal of Heat and Fluid Flow.* 2011;32(4): 771–776.
38. Kuznetsov AV, Nield D. The onset of double-diffusive nanofluid convection in a layer of a saturated porous medium. *Transport in Porous Media.* 2010;85: 941–951.
39. Gupta U, Kaur J. Nanofluids rheology for viscoelastic Oldroyd-B fluid: a revised model. *Journal of Physics: Conference Series.* 2020;1531: 012052.
40. Sandeep N, Sulochana C. Momentum and heat transfer behaviour of Jeffrey, Maxwell and Oldroyd-B nanofluids past a stretching surface with non-uniform heat source/sink. *Ain Shams Engineering Journal.* 2018;9(4): 517–524.
41. Lapwood E. Convection of a fluid in a porous medium. *Mathematical Proceedings of the Cambridge Philosophical Society*. 1948;44(4): 508–521.
42. Khalid IK, Mokhtar NFM, Hashim I, Ibrahim ZB, Gani SSA. Effect of internal heat source on the onset of double-diffusive convection in a rotating nanofluid layer with feedback control strategy. *Advances in Mathematical Physics.* 2017;2017(1): 2789024.
43. Rana GC, Thakur RC, Kango SK. On the onset of double-diffusive convection in a layer of nanofluid under rotation saturating a porous medium. *Journal of Porous Media.* 2014;17(8): 88–95.
44. Rana GC. Effects of rotation on Jeffrey nanofluid flow saturated by a porous medium. *Journal of Applied Mathematics and Computational Mechanics.* 2021;20(3): 17–29.
45. Umavathi JC, Sheremet MA, Ojjela O, Reddy GJ. The onset of double-diffusive convection in a nanofluid saturated porous layer: Cross-diffusion effects. *European Journal of Mechanics-B/Fluids.* 2017;65: 70–87.

MATERIALS PHYSICS AND MECHANICS RESEARCH ARTICLE

Submitted: July 16, 2025 **Revised: July 29, 2025** **Accepted: August 22, 2025**

Landau–Lifshitz–Gilbert equation: magnetization of a superparamagnetic particle ensemble in the mean-field approximation

P.V. Kharitonskii [1,2] ✉, N.A. Ivanov [2], L.I. Guzilova [1], K.G. Gareev [1,2]

[1] Ioffe Institute, St. Petersburg, Russia

[2] St. Petersburg Electrotechnical University "LETI", St. Petersburg, Russia

✉ peterkh@yandex.ru

ABSTRACT

A numerical method for solving the Landau–Lifshitz–Gilbert equation for an ensemble of superparamagnetic nanoparticles within the mean-field approximation is presented. The classical fourth-order Runge–Kutta method is employed for the time integration of the equation. The model simulates an ensemble of uniaxial nanoparticles subjected to a constant external magnetic field. It is shown that the proposed approach accurately reproduces the magnetization dynamics: the components perpendicular to the field decay, while the longitudinal component relaxes toward a steady-state value. The results are qualitatively consistent with previously published data obtained using the *Vinamax* simulation software.

KEYWORDS

superparamagnetism • diluted magnet • Landau–Lifshitz–Gilbert equation • mean-field approximation dipole–dipole interaction

Citation: Kharitonskii PV, Ivanov NA, Guzilova LI, Gareev KG. Landau–Lifshitz–Gilbert equation: magnetization of a superparamagnetic particle ensemble in the mean-field approximation. *Materials Physics and Mechanics*. 2025;53(4): 91–98.
http://dx.doi.org/10.18149/MPM.5342025_7

Introduction

Within the framework of micromagnetic theory, a magnet is treated as a mesoscopic medium, in which atomic-scale structural features can be neglected [1]. The magnetic properties of magnetically ordered materials (magnets) are governed by the presence of intrinsic or induced internal magnetic ordering. In the context of the continuum model, this ordering can be represented as a spatial distribution of the macroscopic magnetization per unit volume $\mathbf{M}(\mathbf{r},t)$. The dynamics of the magnetization vector is described by the Landau–Lifshitz–Gilbert (LLG) equation, which accounts for both gyromagnetic effects and dissipative processes. The objective of this study is to perform numerical simulations of magnetization dynamics in systems containing a large number of superparamagnetic particles, within the mean-field approximation of dipole–dipole interactions between them [2–5].

Method for solving the LLG equation

For small single-domain particles, where the magnetization can be considered spatially uniform, the macrospin approximation is applied. The magnetization dynamics of the i-th particle is described by an equation that, taking into account the normalization of the

magnetization vector, reads as follows $\mathbf{m} = \mathbf{M}/I_s$ (I_s is the spontaneous magnetization) takes the form [6]:

$$\frac{\partial \mathbf{m}^{(i)}}{\partial t} = -\gamma \mathbf{m}^{(i)} \times \mathbf{H}_{eff}^{(i)} + \alpha \mathbf{m}^{(i)} \times \frac{\partial \mathbf{m}^{(i)}}{\partial t}, \quad (1)$$

where γ is the gyromagnetic ratio, α is the dimensionless Gilbert damping parameter; $\mathbf{H}_{eff}$ is the effective field acting on the magnetization of the *i*-th particle. The effective field is defined as:

$$\mathbf{H}_{eff}^{(i)} = -\frac{1}{I_S}\frac{\partial U^{(i)}}{\partial \mathbf{m}^{(i)}}, \quad (2)$$

where $U^{(i)}$ is the total energy density (energy per unit volume) of the *i*-th particle.

The total energy density of the *i*-th particle can be written as:

$$U^{(\mathrm{i})} = U_{ext}^{(i)} + U_{anis}^{(i)} + U_d^{(i)}. \quad (3)$$

Here, U_{ext} is the energy in the external field, U_{anis} is the magnetocrystalline anisotropy energy, U_d is the dipole–dipole interaction energy:

$$U_{ext}^{(i)} = -I_s \mathbf{m}^{(i)} \cdot \mathbf{H}_{ext}, \quad (4)$$

$$U_{anis}^{(i)} = K_u \left(1 - \left(\mathbf{m}^{(i)} \cdot \mathbf{e}_u^{(i)}\right)^2\right), \quad (5)$$

$$U_d^{(i)} = -\frac{1}{2} I_s \mathbf{m}^{(i)} \cdot \mathbf{H}_d. \quad (6)$$

In equations (4)–(6), the following notations are used: $\mathbf{H}_{ext}$ is the external magnetic field, K_u is the effective anisotropy constant, $\mathbf{e}_u$ is the unit vector along the uniaxial anisotropy direction of the particle, $\mathbf{H}_d$ is the dipole–dipole interaction field (demagnetizing field).

Accurate evaluation of dipole–dipole interactions remains the principal computational bottleneck in micromagnetic modelling. A brute-force summation of all pairwise interactions require $O(N^2)$ operations for a system of *N* magnetic moments [7]. Two acceleration strategies are now most widely employed: the fast multipole method (FMM) [8–11] and convolution techniques that exploit the fast Fourier transform (FFT) [12–14]. Both approaches reduce the complexity to $O(NlogN)$ while maintaining controllable accuracy. Modern hybrid solvers such as *FastMag* [15] merge FMM or FFT kernels with finite-difference or finite-element discretization and leverage multi-GPU hardware to simulate systems containing up to ~ 10^8 computational cells. Further gains can be realized by re-using the demagnetizing field within multi-stage time integrators through polynomial extrapolation, roughly halving the wall-time of explicit schemes without compromising precision [16]. Despite these advances, current computational resources still limit routine simulations to ensembles of only a few million interacting moments, underscoring the need for new, more scalable algorithms capable of bridging the gap to truly device–scale problems.

According to Eq. (2)–(6), the effective field acting on the magnetization of the *i*-th particle is defined as:

$$\mathbf{H}_{eff}^{(i)} = \mathbf{H}_{ext} + \frac{2K_u}{I_s}\left(\mathbf{m}^{(i)} \cdot \mathbf{e}_u^{(i)}\right)\mathbf{e}_u^{(i)} + \frac{1}{2}\mathbf{H}_d. \quad (7)$$

In this study, the magnetic material is modeled as an ensemble of dipole–dipole interacting superparamagnetic solid spheres with diameter d_0 and volume $V^{(i)}$, each possessing uniaxial anisotropy. The particles are uniformly distributed and fixed within a nonmagnetic matrix shaped as a cylinder of height *d* and radius *R*. The external magnetic field $\mathbf{H}_{ext}$ is applied along the *Oz*-axis, which is aligned with the cylinder's generatrix.

To accurately model superparamagnetic systems, it is essential to account for the influence of thermal fluctuations on the magnetization dynamics. A stochastic term can be introduced into Eq. (1) to describe the effect of thermal fluctuations at nonzero temperature $T \neq 0$. The resulting equation for the *i*-th particle takes the following form:

$$\frac{\partial \mathbf{m}^{(i)}}{\partial t} = -\gamma \mathbf{m}^{(i)} \times \mathbf{H}_{eff}^{*(i)} + \alpha \mathbf{m}^{(i)} \times \frac{\partial \mathbf{m}^{(i)}}{\partial t}, \tag{8}$$

$$\mathbf{H}_{eff}^{*(i)} = \mathbf{H}_{eff}^{(i)} + \mathbf{H}_{therm}^{(i)}. \tag{9}$$

Here $\mathbf{H}^{(i)}_{therm}$ is the stochastic thermal field [17–23], modeled as a Gaussian random process with zero mean and a correlation function that satisfies the fluctuation–dissipation theorem. The stochastic thermal field acting on the *i*-th particle can be expresses as [24–26]:

$$\mathbf{H}_{therm}^{(i)} = \boldsymbol{\eta}^{(i)} \sqrt{\frac{2\alpha k_B T}{\gamma I_s V^{(i)} \Delta t}}, \tag{10}$$

where $\boldsymbol{\eta}^{(i)}$ is a vector, whose components are normally distributed random variables with zero mean, uncorrelated in both space and time; k_B is the Boltzmann constant, Δt is the time step.

Within the framework of the considered model, the components of the effective field acting on the magnetization of the *i*-th particle in the Cartesian coordinate system are defined as:

$$\mathbf{H}_{ext} = (0, 0, H_0), \tag{11}$$

where H_0 is the magnitude of the external magnetic field.

The components of the magnetocrystalline anisotropy field are then given by:

$$\begin{cases} H_{anis,x}^{(i)} = \frac{2K_u}{I_s}\left(\mathbf{m}^{(i)} \cdot \mathbf{e}_u^{(i)}\right) e_x^{(i)}, \\ H_{anis,y}^{(i)} = \frac{2K_u}{I_s}\left(\mathbf{m}^{(i)} \cdot \mathbf{e}_u^{(i)}\right) e_y^{(i)}, \\ H_{anis,z}^{(i)} = \frac{2K_u}{I_s}\left(\mathbf{m}^{(i)} \cdot \mathbf{e}_u^{(i)}\right) e_z^{(i)}, \end{cases} \tag{12}$$

where e_x, e_y, e_z are the components of the unit vector along the uniaxial anisotropy axis.

To account for the influence of dipole–dipole interactions between particles in the ensemble, this work proposes the use of a mean-field method based on the statistical approach developed in [2]:

$$H_{d,z} = -\frac{8\pi}{3} c I_s \left(1 - \frac{3}{2} cos\theta_{max}\right) \zeta, \tag{13}$$

$$\zeta = \sum_{i=1}^{N} m_z^{(i)}, \tag{14}$$

where c is the volume concentration of particles, θ_{max} is the maximum angle between the position vector of a particle and the *Oz*-axis of the cylinder, ζ is the dimensionless magnetization of the ensemble. The use of this method reduces the computational complexity to $O(N)$.

Equation (1) for *i*-th particle in the Cartesian coordinate system is written as:

$$\begin{cases} \frac{\partial m_x}{\partial t} = -\frac{\gamma}{1+\alpha^2}\left[\left(m_y + \alpha m_x m_z\right) H_{eff,z} - \left(m_z - \alpha m_y m_x\right) H_{eff,y} - \alpha\left(m_y^2 + m_z^2\right) H_{eff,x}\right], \\ \frac{\partial m_y}{\partial t} = -\frac{\gamma}{1+\alpha^2}\left[\left(m_z + \alpha m_y m_x\right) H_{eff,x} - \left(m_x - \alpha m_z m_y\right) H_{eff,z} - \alpha\left(m_z^2 + m_x^2\right) H_{eff,y}\right], \\ \frac{\partial m_z}{\partial t} = -\frac{\gamma}{1+\alpha^2}\left[\left(m_x + \alpha m_z m_y\right) H_{eff,y} - \left(m_y - \alpha m_x m_z\right) H_{eff,x} - \alpha\left(m_x^2 + m_y^2\right) H_{eff,z}\right]. \end{cases} \tag{15}$$

When thermal fluctuations are taken into account, the components $\mathbf{H}^{(i)}_{eff}$ in Eq. (15) are replaced with the components $\mathbf{H}^{*(i)}_{eff}$ in accordance with Eq. (9).

To integrate the resulting system of equations (3*N* first-order ordinary differential

equations for N particles), the classical explicit fourth-order Runge–Kutta method [27–29] was employed with a time step of 10^{-12} s, which satisfies the stability criterion. After each integration step, the magnetization vector $\mathbf{m}^{(i)}$ was renormalized to ensure that the condition $|\mathbf{m}^{(i)}| = 1$ is maintained [30].

Results and Discussion

In the numerical experiments, parameters in the CGS unit system were used, corresponding to the magnetic material described in [31] with the damping parameter α chosen according to [24]. The characteristics are listed in Table 1.

Table 1. Key parameters used in the simulation

Parameter	Value
Saturation magnetization I_s, emu/cm^3	480
Anisotropy constant K_u, erg/cm^3	135000
Particle diameter d_0, cm	10^{-6}
Cylinder height d, cm	10^{-4}
Cylinder radius R, cm	$0.5 \cdot 10^{-4}$
Volume concentration c	0.3
Damping parameter α	0.1
External magnetic field H_0, Oe	100…600

The easy axes of magnetization of the particles were uniformly distributed along the six coordinate directions (± x, ± y, ± z), with one-sixth of the particles assigned to each direction, thereby ensuring an initially demagnetized state of the ensemble. As the initial condition, the magnetization of each particle was aligned with its easy axis. The LLG equations were then solved for all particles until a steady-state configuration was reached.

The result of numerical modeling of the magnetization dynamics of the i-th particle, whose easy axis is aligned along the x-axis, in an ensemble of superparamagnetic particles at $T = 0$ K and $H_0 = 600$ Oe is shown in Fig. 1. Figure 2 presents the results for the averaged magnetization vector of the ensemble.

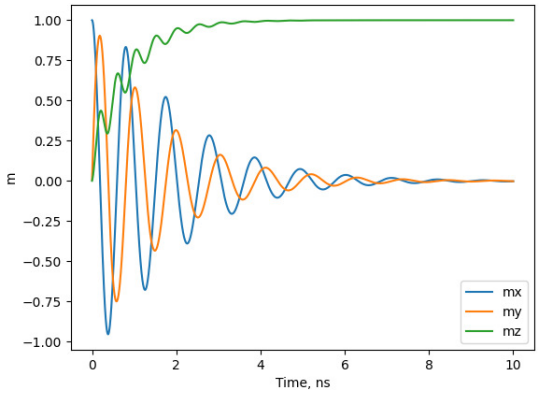

Fig. 1. Time dependence of the components of the normalized magnetization vector of the i-th particle with its easy axis aligned along the x-axis, at $T = 0$ K and $H_0 = 600$ Oe

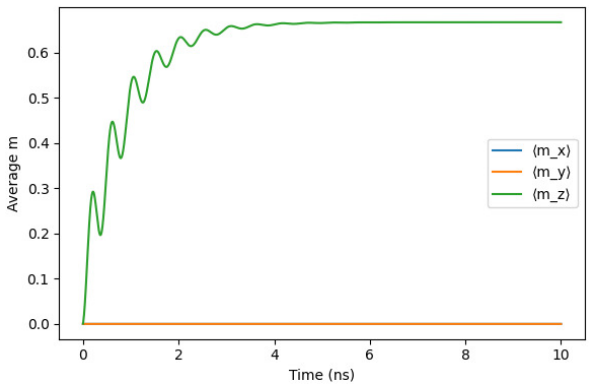

Fig. 2. Time dependence of the components of the ensemble-averaged magnetization at $T = 0$ K and $H_0 = 600$ Oe

The obtained results (Fig. 1) demonstrate the relaxation of m_z toward an equilibrium state and the gradual decay of m_x and m_y. This behavior illustrates the Gilbert damping mechanism and indicates the correct implementation of both anisotropy and dipolar fields within the mean-field approximation. To verify the model, the results were compared with those obtained using *Vinamax* [24], a macrospin simulator that accounts for similar physical effects. The comparison showed qualitative agreement, confirming the physical validity and applicability of the proposed method.

To account for thermal effects in the simulations, Eq. (10) was used, with the vector $\boldsymbol{\eta}^{(i)}$ updated at each time step. The results of numerical modeling of the magnetization dynamics of the i-th particle, whose easy axis is aligned along the x-axis, in an ensemble of superparamagnetic particles at T = 300 K and for H_0 equal to 100, 200 and 300 Oe are presented in Figs. 3, 4, and 5, respectively.

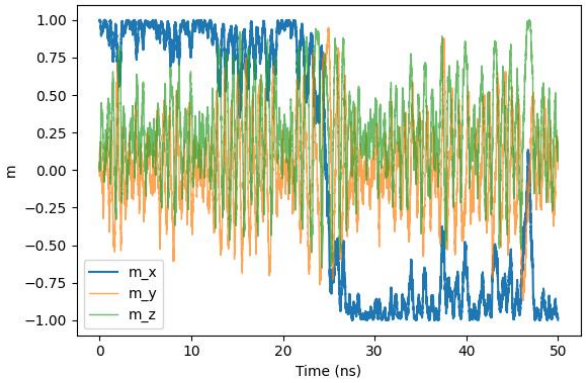

Fig. 3. Time dependence of the components of the normalized magnetization vector of the i-th particle with its easy axis aligned along the x-axis, at T = 300 K and H_0 = 100 Oe

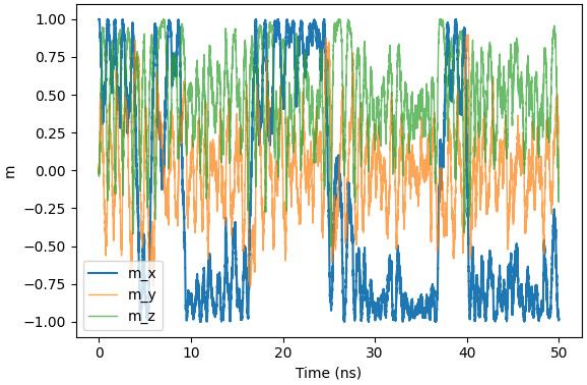

Fig. 4. Time dependence of the components of the normalized magnetization vector of the i-th particle with its easy axis aligned along the x-axis, at T = 300 K and H_0 = 200 Oe

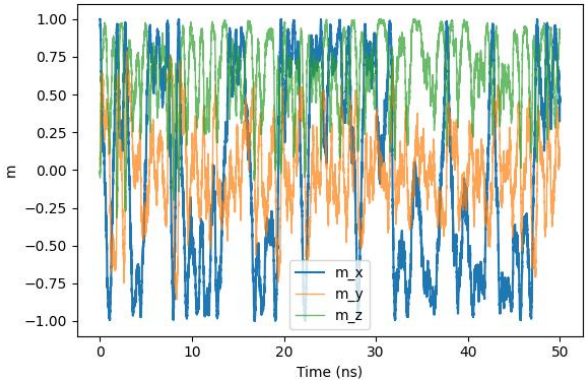

Fig. 5. Time dependence of the components of the normalized magnetization vector of the i-th particle with its easy axis aligned along the x-axis, at T = 300 K and H_0 = 300 Oe

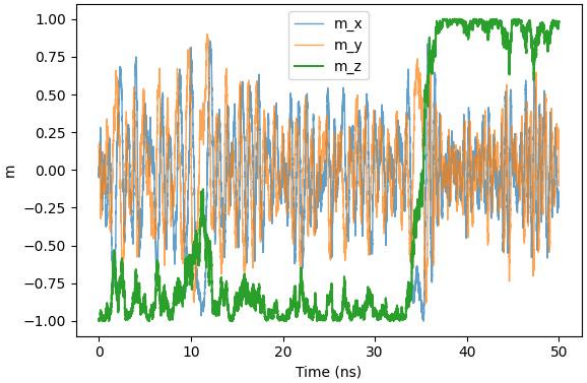

Fig. 6. Time dependence of the components of the normalized magnetization vector of the i-th particle with its easy axis oriented opposite to the z-axis, at T = 300 K and H_0 = 100 Oe

The results of numerical modeling of the magnetization dynamics of the i-th particle, whose easy axis is aligned along the negative z-axis, in an ensemble of superparamagnetic particles at T = 300 K and for H_0 equal to 100, 200 and 300 Oe are presented in Figs. 6, 7, and 8, respectively.

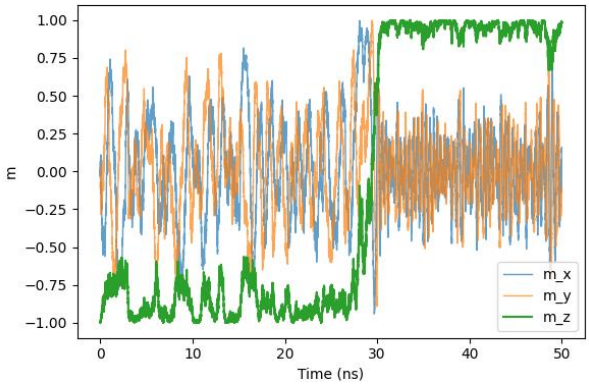

Fig. 7. Time dependence of the components of the normalized magnetization vector of the *i*-th particle with its easy axis oriented opposite to the *z*-axis, at T = 300 K and H_0 = 200 Oe

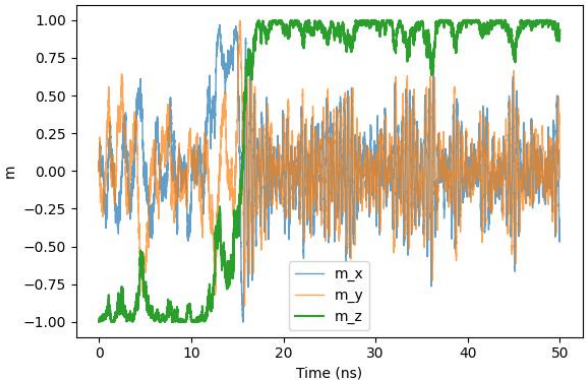

Fig. 8. Time dependence of the components of the normalized magnetization vector of the *i*-th particle with its easy axis oriented opposite to the *z*-axis, at T = 300 K and H_0 = 300 Oe

Analysis of the time dependencies of the magnetization vector components (Figs. 3–8) shows that, under the condition $T > 0$, bistable behavior is observed along the easy anisotropy axis, which is consistent with the classical theory of superparamagnetism. As the magnitude of the external magnetic field increases, the degree of alignment of the magnetic moments along the field direction also increases.

Conclusions

In the study, a numerical method for simulating the dynamics of an ensemble of dipole–dipole interacting superparamagnetic nanoparticles based on the Landau–Lifshitz–Gilbert equation with thermal fluctuations has been proposed and implemented. To describe interparticle interactions, a mean-field approximation was employed, which significantly reduces computational cost.

The integration of the system of equations was carried out using the explicit fourth-order Runge–Kutta method, which ensures numerical stability and accuracy at a small-time step (time step 10^{-12} s). Numerical experiments performed for a diluted ensemble (c = 0.3) of uniaxial superparamagnetic nanoparticles demonstrated that the model accurately captures the relaxation processes: decay of the transverse components of the magnetization vector and convergence of the longitudinal component to an equilibrium state. Comparison with results obtained using the specialized simulation software *Vinamax* [24] confirms the physical validity of the proposed approach.

The simulation results at both zero and room temperature are consistent with classical concepts of superparamagnetism, including bistability along the easy anisotropy axis and enhanced alignment of magnetic moments with increasing external magnetic field strength.

Thus, the proposed method, in combination with the macrospin approximation and the inclusion of thermal fluctuations in the Landau–Lifshitz–Gilbert equation, can be effectively used for numerical analysis of collective magnetic dynamics in diluted magnets composed of superparamagnetic nanoparticles. From the point of view of practical application of the obtained results, a detailed understanding of the magnetization dynamics of structures containing iron oxide in the form of micro- and

nanosized particles can be useful in the development of new generation materials designed to protect against the effects of microwave electromagnetic radiation [32].

CRediT authorship contribution statement

Peter V. Kharitonskii: writing – review & editing, conceptualization; **Nikolai A. Ivanov**: investigation, writing – original draft; **Liubov I. Guzilova**: writing – review & editing; **Kamil G. Gareev**: supervision, writing – review & editing.

Conflict of interest

The authors declare that they have no conflict of interest.

References

1. Coey JMD. *Magnetism and magnetic materials.* Cambridge: Cambridge University Press; 2010.
2. Kharitonskii PV, Setrov EA, Ralin AY. Modeling of hysteresis characteristics of a dilute magnetic with dipole–dipole interaction of particles. *Materials Physics and Mechanics.* 2024;52(2): 142–150.
3. Sánchez FH, Mendoza Zélis P, Arciniegas ML, Pasquevich GA, Fernández van Raap MB. Dipolar interaction and demagnetizing effects in magnetic nanoparticle dispersions: introducing the mean-field interacting superparamagnet model (MFISP Model). *Physical Review B.* 2017;95: 134421.
4. Landi GT. The random dipolar-field approximation for systems of interacting magnetic particles. *Journal of Applied Physics.* 2013;113: 163908.
5. Sánchez FH, Mendoza Zélis P, Arciniegas ML, Pasquevich GA, Fernández van Raap MB. Dipolar interaction and demagnetizing effects in magnetic nanoparticle dispersions: introducing the mean-field interacting superparamagnet model. *Physical Review B.* 2017;95(13): 134421.
6. Gilbert TL. A phenomenological theory of damping in ferromagnetic materials. *IEEE Transactions on Magnetics.* 2004;40(6): 3443–3449.
7. Izotov AV, Belyaev BA, Valikhanov MM, Polenga SV, Stefanyuk AV. Algorithm for calculating the equilibrium state of a ferromagnet based on the Lagrange-multiplier method. *Computational Methods and Programming.* 2012;13(4): 551–559. (In Russian)
8. Greengard L, Rokhlin V. A fast algorithm for particle simulations. *Journal of Computational Physics.* 1987;73(2): 325–348.
9. Zipunova EV, Ivanov AV. On calculation of the demagnetizing field by the fast multipole method. *Preprints of the Keldysh Institute of Applied Mathematics.* 2018;140: 19. (In Russian)
10. Tan X, Baras JS, Krishnaprasad PS. Fast evaluation of demagnetizing field in three-dimensional micromagnetics using multipole approximation. In: Varadan VV. (eds.) *Proc. SPIE 3984, Smart Structures and Materials 2000: Mathematics and Control in Smart Structures, (19 June 2000).* SPIE; 2000. p.195-201.
11. Zhang W, Haas S. Adaptation and performance of the Cartesian coordinates fast multipole method for nanomagnetic simulations. *Journal of Magnetism and Magnetic Materials.* 2009;321(22): 3687–3692.
12. Moutinho JPG. *Micromagnetic device simulation.* Lisbon: Instituto Superior Técnico, Universidade de Lisboa; 2017.
13. Fredkin DR, Koehler TR. Hybrid method for computing demagnetizing fields. *IEEE Transactions on Magnetics.* 1990;26(2): 415–417.
14. Long HH, Ong ET, Liu ZJ, Li EP. Fast Fourier transform on multipoles for rapid calculation of magnetostatic fields. *IEEE Transactions on Magnetics.* 2006;42(2): 295–300.
15. Chang R, Li S, Lubarda MV, Livshitz B, Lomakin V. FastMag: fast micromagnetic solver for large-scale simulations. *CMRR Report.* 2010;34: 16.
16. Lepadatu S. Speeding up explicit numerical evaluation methods for micromagnetic simulations using demagnetizing field polynomial extrapolation. *IEEE Transactions on Magnetics.* 2022;58(5): 1–16.
17. Brown WF. Thermal fluctuations of a single-domain particle. *Physical Review.* 1963;130(5): 1677–1686.
18. García-Palacios JL, Lázaro FJ. Langevin-dynamics study of the dynamical properties of small magnetic particles. *Physical Review B.* 1998;58: 14937–14958.

19. Coffey WT, Kalmykov YuP. Thermal fluctuations of magnetic nanoparticles: Fifty years after Brown. *Journal of Applied Physics.* 2012; 112: 121301.
20. Durhuus FL, Beleggia M, Frandsen C. Conservation laws for interacting magnetic nanoparticles at finite temperature. *Physical Review B.* 2024;109(5): 054421.
21. Coffey WT, Kalmykov YuP, Waldron JT. *The Langevin equation: with applications to stochastic problems in physics, chemistry and electrical engineering.* 2nd ed. Singapore: World Scientific; 2004.
22. Brzuszek K, Ross CA, Janutka A. High-frequency magnetic response of superparamagnetic composites of spherical $Fe_{65}Co_{35}$ nanoparticles. *Journal of Magnetism and Magnetic Materials.* 2023;573: 170651.
23. Berkov DV. Magnetization dynamics including thermal fluctuations: basic phenomenology, fast remagnetization processes and transitions over high-energy barriers. In: Kronmüller H, Parkin S. (eds.) *Handbook of Magnetism and Advanced Magnetic Materials.* Vol. 2: Micromagnetism. Chichester: John Wiley & Sons; 2007. 795–823.
24. Leliaert J, Vansteenkiste A, Coene A, Dupré L, Van Waeyenberge B. Vinamax: a macrospin simulation tool for magnetic nanoparticles. *Medical & Biological Engineering & Computing.* 2015;53(2): 309–317.
25. Vansteenkiste A, Leliaert J, Dvornik M, Helsen M, Garcia-Sanchez F, Van Waeyenberge B. The design and verification of MuMax3. *AIP Advances.* 2014;4(10): 107133.
26. Frantiu MA. *Micromagnetic simulations of magnetic thin films using MuMax3. Bachelor's thesis.* Groningen: University of Groningen; 2019.
27. Gorelov YuN, Kurganskaya LV. *Numerical methods for solving ordinary differential equations (Runge-Kutta method): textbook.* Samara: Samara University Press; 2023. (In Russian)
28. Liu C, Ku Y. A combination of group preserving scheme and Runge-Kutta method for the integration of Landau-Lifshitz equation. *Computer Modeling in Engineering & Sciences.* 2005;9(2): 151–178.
29. Shiach J. Advanced ordinary differential equations & dynamical systems: Runge-Kutta methods. *Online Lecture Notes.* 2020.
30. Botha AE. Stabilisation of the Landau-Lifshitz-Gilbert equation for numerical solution via standard methods. *Scientific Reports.* 2025;15: 15775.
31. Kharitonskii P, Bobrov N, Gareev K, Kosterov A, Nikitin A, Ralin A, Sergienko E, Testov O, Ustinov A, Zolotov N. Magnetic granulometry, frequency-dependent susceptibility and magnetic states of particles of magnetite ore from the Kovdor deposit. *Journal of Magnetism and Magnetic Materials.* 2022;553: 169279.
32. Boiprav OV, Pevneva NA, Ayad H. Development and study of multilayer electromagnetic radiation shields based on powdered oxide-containing materials. *Materials Physics and Mechanics.* 2021;47(1): 123–130.

MATERIALS PHYSICS AND MECHANICS RESEARCH ARTICLE

Submitted: July 2, 2025 **Revised: August 21, 2025** **Accepted: October 3, 2025**

Machinability of nitride ceramics with abrasive powders and their addition to diamond powder

V.I. Burlakov [1], V.G. Artiukh [2], D.A. Kitaeva [2] ✉, N.V. Korihin [2]

[1] Pryazovskyi State Technical University, Mariupol, Russia

[2] Peter the Great St. Petersburg Polytechnic University, St. Petersburg, Russia

✉ dkitaeva@mail.ru

ABSTRACT

Development of modern engineering is related to development and introduction of new materials and progressive technological processes of their treatment. Unique properties of ceramics allow them to be used in various fields of technology, including, as a cutting instrument and the machines, devices, radio and electronic apparatus details. Due to the high hardness of materials, tooling of instrumental purveyances is possible only with synthetic diamonds, but synthetic diamonds are quite expensive there, so it is necessary to solve the problem of replacing expensive materials with cheaper ones. Improvement of ceramics treatment methods is related to study of conformities to law of difficult multivariable process of polishing. Productivity, quality of surface, wear and firmness of instrument, power charges are determined by properties of ceramics, descriptions of diamond instrument, modes and by technological features of equipment. Providing high quality surface at exact ceramic details is a difficult requirement specification. Next to a subzero roughness that is limited to parts of microns, a specific requirement is absence of surface defects (coulisse, microcracks, microcavities). As ceramic materials are fragile then at loading under act of cutting or polishing instruments of good from them tend to spalling. Point loading during a small enough flowage result in that under act of grains of diamond of ceramics, feeling strong mechanical and thermal loading, painted as a result of it there is a ditch width of that exceeds the area of collision of diamond grain with material.

KEYWORDS

vibro-magnetic-abrasive processing • material removal rate • surface roughness • CBN ceramics

Funding. *This work has been supported by the grant of the Russian Science Foundation, RSF 25-19-00921.*

Citation: Burlakov VI, Artiukh VG, Kitaeva DA, Korihin NV. Machinability of nitride ceramics with abrasive powders and their addition to diamond powder. *Materials Physics and Mechanics*. 2025;53(4): 99–110. http://dx.doi.org/10.18149/MPM.5342025_8

Introduction

Problem with processing superhard ceramics is that intensity of its processing depends on presence of artificial diamonds in abrasive mix. Diamond is a rather expensive material. Therefore, the hard material has to be processed more delicately. This issue has been studied by many domestic and foreign researchers. Tamarkin M.A. et al. [1] were engaged in vibration processing in granular abrasive media. Kuzin V.V. [2] studied tools with ceramic cutting plates. Feng Y. et al. [3] investigated manufacturing methods and cutting characteristics of self-lubricating ceramic cutting tools with microtexture. Lebedev V.A. and Dyachenko E.A. [4] were engaged in modeling performance of vibro-abrasive finishing treatment. Khalimonenko A.D. [5] worked on quality control of turning process using cutting ceramic tools. Klimenko S.A. et al. [6] studied surface finishing in production of details. Akulovich L.M. et al. [7] analyzed influence of properties of working technological environment on surface roughness and productivity during magnetic

Publisher: Peter the Great St. Petersburg Polytechnic University

abrasive processing, investigated influence of properties of working technological environment on surface roughness and productivity during magnetic abrasive processing. Arulkirubakaran D. et al. [8] studied texture of cutting tools. Burlakov V.I. et al. [9] explored processing of cutting ceramics. Liu Y. et al. [10] tested cutting tool with certain texture. Savenkov A.A. et al. [11] investigated role of tools with certain texture in improving processing performance. Golobokov A.V. et al. [12] carried out simulation modeling of grinding process of workpieces. Farwaha H. et al. [13] carried out mathematical modeling of processes. Sugihara T. et al. [14] were engaged in development of new CBN cutting tool for high-speed machining. Ranjan P. and Hiremath S. [15] studied role of texture tools in improving machining productivity. Serga G.V. et al. [16] investigated increasing productivity of finishing and hardening machining systems. Cheng K. et al. [17] considered metal machining using the magnetic method. Rogov V.A. and Shkarupa M.I. [18] carried out comparative analysis of mechanical processing of superhard materials by grinding. Slipchenko K. et al. [19] investigated mechanical properties and cutting ability of CBN-based cutting tool. Cheng K.C. et al. [20] were engaged in describing characteristics of magnetic-abrasive method. Sergiev A.P. et al. [21] conducted research of influence of amplitude-frequency characteristics of vibration turning on roughness parameters. Paswan S.K. and Singh A.K. [22] analyzed magnetic abrasive machining. Maksarov V.V. et al. [23] investigated technological features of magnetic abrasive machining under digital technologies. Popov M.A. et al. [24] studied influence of cutting-edge rounding radius on improving quality of surface layer of detail. Filipenko R.A. et al. [25] scrutinized problem of technological quality assurance of edges of flat products using magnetic abrasive machining. Damskiy D.B. et al. [26] conducted assessment of reliability of technological process of vibro-abrasive machining. Tishchenko E.E. et al. [27] developed hardening technologies and coatings. Mordovtsev A.A. [28] conducted assessment of use of vibration processing in conditions of 'smart production'. Rogovenko D.A. [29] was engaged in analysis of schemes and methods for intensifying process of magnetic-abrasive processing of flat surfaces. Purpose of this article is to prove that soft abrasive is capable of taking part in processing of nitride ceramics using the vibration-assisted magnetic abrasive method.

Material and Methods

A promising finishing method is vibration-abrasive machining [1] which allows not only reducing roughness of tool surfaces but also to control size of rounding radius of their cutting edges and relieve residual stress. Until now, there is experience in using such processing in manufacture of cutting tools equipped with a working part made of hard alloys [2,3]. Considering widespread use and high cost of tools made of polycrystalline super hard materials (PSHM) based on cubic boron nitride (CBN) [4,5] improving their manufacturing methods is of significant scientific and practical interest. Vibro-abrasive machining, as a finishing method, which in traditional applications is characterized by high productivity and is effective when it is necessary to ensure high quality of treated surface can be very effective in this case. It should be kept in mind that products made from PSHM have high hardness, are difficult to machine and process of their vibration-

abrasive processing is characterized by a few significant features.

During the process of vibration-assisted magnetic abrasive finishing material being processed and subjected to mechanical abrasive action, influence of magnetic field that is constant in magnitude and direction which has a beneficial effect on properties of surface layer of product. This circumstance allows vibration-assisted magnetic abrasive processing to be distinguished as an independent method of finishing processing [6]. Features of ViMAO method are continuous contact of powder with workpiece surface being processed that reduces cyclic loads on "machine-fixture-tool-workpiece" system and helps to increase accuracy of geometric dimensions and shape of workpiece surface, absence of rigid fastening of abrasive grain in bond that contributes to involuntary leveling of cutting tool relative to shape of surface being processed and eliminates likelihood of critical pressures and temperatures appearing in cutting zone, improving physical and mechanical quality indicators of surface layer of product material, ability to control rigidity of tool and, due to this, ensure regulation of metal removal from forming surface of product; absence of friction of bond on surface of product that significantly reduces temperature in abrasive processing zone, ability to cut with the sharpest edge of magnetic abrasive powder grain (this does not require periodic re-sharpening of the tool), maintaining geometric dimensions within tolerance left for the finishing operation.

Following powders were used as abrasive material: monocorundum, green silicon carbide, black silicon carbide, white electrocorundum, pink electrocorundum, ruby-corundum electrocorundum, sol-gel corundum, normal electrocorundum. In all powders, grain size according to GOST 12 is 150–125 μm. Wide range of abrasives is explained by differences in properties of abrasive powders [7]. Abrasive tools based on electrocorundum are used in roughing and stripping operations for processing workpieces made of materials with a high tensile strength, in finishing and finishing operations for processing workpieces and tools made of various steels, semi-finishing and finishing operations for processing workpieces made of medium- and high-alloy steels, etc. Use of traditional abrasive materials as cutting tools in ViMAO is impossible, since they must have not only abrasive but also high magnetic properties. Use of diamond tools helps to accelerate pace of technical progress and allows introduction of new progressive technological processes that ensure higher precision and quality of processing, increased service life and improved reliability of machines and devices [8].

Compared to conventional abrasives, diamond tools provide increasing accuracy of tool and part processing, increase in tool durability after diamond sharpening by 1.2–2.5 times, increase in labor productivity up to 50 %, improving working conditions and production culture, reduction of processing costs by 1.5–2.0 times. Ultradispersed diamonds (UDD) are nano-diamonds obtained by detonation synthesis under influence of explosion energy [9,10]. Uniqueness of UDD product lies in combination of diamond core structure, diamond hardness, chemical inertness on the one hand and nano-sized particles, rounded shape, developed and active surface on the other one. Unlike natural and known synthetic diamonds, UDD forms multi-level aggregates of varying density and structure depending on environment. UDD suspensions and hydrosols have high aggregation and sedimentation stability. Physicochemical properties of UDD allow identifying main areas of its application: protective electrochemical and chemical coatings in electroplating, friction modifiers in production of lubricating compositions, polishing compounds, fillers

at production of composite polymer materials, sorbents in pharmaceuticals.

Ultra-fine diamonds ensure perfect fit of parts and significantly reduce friction. This allows effect of sliding friction to be replaced by rolling friction. Concentration of ultra-dispersed diamonds can reach $(20–25)\cdot10^{12}$ on an oil film area of 1 cm^2. It is important to note that there is no “abrasive” effect in process of operation of "UltraDiamond" products, since threshold of "abrasiveness" is size of a diamond of 10 nm and more. Therefore, they cannot cause any damage during friction process [11]. Diamond powder is used for production of diamond tools; in addition, it is also used in an unfixed state (in the form of suspensions and pastes).

One of the most common brands is cubic boron nitride ceramics. Cubic boron nitride (CBN) is a super hard material obtained by synthesis at high temperature and pressure. According to properties and performance characteristics CBN differs significantly from synthetic diamond, it is more brittle and has lower strength. Cubic boron nitride is most widely used as a tool material for processing steels and alloys [11–13]. Synthesis of CBN crystals is carried out from supersaturated solutions of boron nitride in melts of alkaline, alkaline earth metals and their compounds. As a rule, spontaneous crystallization from a multicomponent reaction composition is used.

In the process of chip removal during diamond processing ceramics, individual diamond grains are involved in combination with ferromagnetic components. When studying nature of destruction of ceramic surface by diamond grain it was found that grain at the beginning and end of scratch leaves a clear trace without obvious chips along edges of trace. Diamond grain, having sufficient hardness, immediately upon contact with material begins to cut off chips. Middle part of scratch has significant breaks along edges along its entire length. Appearance of chips when a certain depth of grain penetration is reached is explained by the fact that with an increase in cutting depth more and more edges of diamond grain come into work as a result of which micro-cutting forces in zone of its contact with sample material increase and along with formation of highly dispersed chips large areas of breakouts are observed. Forces that arise during finishing determine stability of abrasive tool, quality of processing and allow selection of rational technical parameters [14].

When processing ceramics, condition of surface layer largely depends on cutting forces. Knowledge of patterns of change in the latter allows one to reasonably select optimal processing conditions. Nature of change in cutting forces can also be used to judge physical phenomena occurring in processing zone. Abrasive wear is caused by the fact that product material acts on tool with its contact surfaces, scratching ceramics acting as micro-cutters. Due to high hardness of CBN particles, abrasive wear of tool depends on amount of hard abrasive. Abrasive wear of tool can be associated with phenomenon of "self-wear" [15]. Source of particles that cause "self-wear" is rounded section of tool cutting edge from where particles are removed due to fatigue phenomena and adhesive interaction with material of product and getting onto contact surfaces of tool form their wavy relief. This mechanism determines wear.

Although diamond abrasive wears out due to the specific nature of processing, it does not stop because magnetic field presses sample against tool. Sufficiently high pressure in the cutting zone causes the resulting powder to act as a lapping paste. As a result, a harder material is processed with a softer one and this process is carried out

using the vibration-assisted magnetic abrasive method. Knowing wear intensity of abrasive material, it can be understood that after what time processing will switch to lapping mode and with a soft material. This approach to wear ensures consistent processing of ceramics with virtually any type of abrasive material. Thus, hypothesis about impossibility of processing a hard material with a softer one is not always confirmed. One more thing to note is that abrasive wear which is wear of material under action of abrasive should not be confused with wear of abrasive material. The first one occurs as a result of action of hard abrasive on part, and the second one occurs when soft abrasive is applied to a harder surface [16].

In a free state powder crystallizes into spherical microparticles that corresponds to thermodynamically most favorable form with a minimum surface area and a maximum volume. When using ViMAO method as the main operation in processing of super hard ceramics the process is based on micro-cutting. Micro cutting is processing of part surface layers mainly with an abrasive tool. During the processing, tool is pressed against surface of part with force of 100–200 N that leads to decrease in roughness and increase in wear resistance.

Samples of CBN-based PSHM (Fig. 1) with following dimensions and shapes were processed, namely, square plate 12.7 × 12.7 × 3.0 mm^3 (brand "Borsinit", hardness of 38–40 GPa) and a cylinder ∅ 7.5 × 5.0 mm^2 (brand "Composite 05IT", hardness of 18–20 GPa). During cutting, under influence of forces pressing grain against part, it enters material of part being processed to a depth of *h* and removes chips of length *a* (Fig. 2).

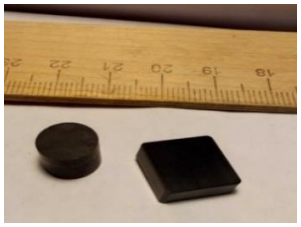

Fig. 1. External appearance of ceramic samples (38–40 GPa)

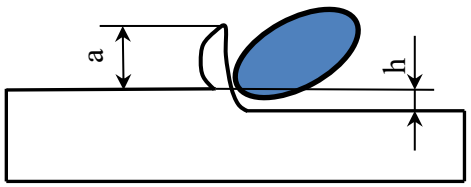

Fig. 2. Scheme of operation of a single grain at ViMAO method

Over time, cutting properties of grains decrease due to their destruction. Therefore, empirical dependence to take into account operating time of magnetic powder can be introduced:

$$1 - e^{-C_u t}, \quad (1)$$

where C_u is the tool life coefficient, *t* is total operating time of magnetic powder.

Then amount of removal Q_c of workpiece surface during time *t* (taking into account wear of powder) can be found using the equation:

$$\Delta Q_c = \Delta V_p = \left[ah\text{arctg}\frac{h\text{tg}\alpha}{a} - r_0^2 \sin\alpha\cos\alpha\right]\frac{ak_c hN\pi rn\rho}{r}\ (1 - e^{-C_u t}). \quad (2)$$

Area of ellipsoid segment of cutting grain in axial section is equal to:

$$S_{segm} = ah\text{arctg}\frac{h\text{tg}\alpha}{a} - r_0^2 \sin\alpha\cos\alpha,\ \alpha = \text{arctg}\frac{x_0}{y_0}. \quad (3)$$

With regard to taking into account all factors influencing processing, it is necessary to introduce a coefficient that depends on formation of chips k_c that is equal to ratio of actual area of metal removed taking into account elastic-plastic deformations of material being processed to area of cutting grain segment [17,18]. Numerical value of coefficient

k_c is determined from reference books on abrasive processing operations.

Then material volume removed from surface of workpiece by one cutting grain will be:

$$V_c = S_c a k_c = \left[a h \operatorname{arctg} \frac{h \operatorname{tg} \alpha}{a} - r_0^2 \sin\alpha \cos\alpha \right] a k_c. \quad (5)$$

Knowing density of material being processed, it is possible to calculate material removal rate Q that is expressed through mass from surface of workpiece by cutting grains arranged in a row [19,20]:

$$Q = V_p = \left[a h \operatorname{arctg} \frac{h \operatorname{tg} \alpha}{a} - r_0^2 \sin\alpha \cos\alpha \right] \frac{a k_c h N \pi r n \rho}{r}. \quad (6)$$

Obtained mathematical dependencies are shown on Fig. 3. Judging by the graph, over time soft abrasive turns into powder, but processing does not end there. Material removal becomes more extended in time, but soft abrasive continues to work.

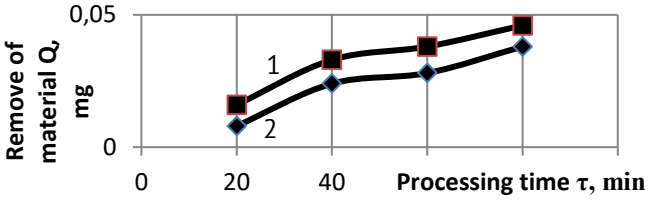

Fig. 3. Dependence of removed material on processing time: 1 – processing with small addition of artificial diamonds; 2 – processing with soft abrasive

Above given dependencies and mathematical models allow to conclude that soft abrasive can process harder material. Process of grinding ceramics can be represented as a set of individual acts of interaction between diamond indenter and brittle body. Although concept of fragility is very relative, high deformation rates and increase in rigidity of stress state diagram can significantly increase fragility of sample being studied while increase in temperature, on the contrary, brings body closer to plastic state. What is important is that these factors act together during processing. Contact area of diamond tool with workpiece can be viewed from three different positions. Firstly, as a nominal contact area determined by the geometric dimensions of interacting bodies. Secondly, as a contour determined by contact areas of individual sections due to macrogeometric deviations of surfaces of tool and workpiece. Thirdly, the actual contact area which is sum of actual contact areas of tool and workpiece as two rough surfaces.

Considering that grinding depth is immeasurably small compared to grinding area and processed material is uniform in three directions it can be argued that contact area of abrasive with sample can be a decisive factor in determining quality and productivity of diamond abrasive processing of super hard ceramics [21].

Diameter of elementary contact spot is determined by below given the equation if microgeometry of grains is practically the same:

$$d = \frac{V \Delta t}{2}, \quad (7)$$

where Δt is contact time of abrasive and sample surface.

Area of elementary contact patch is determined by the equation:

$$\Delta A_r = \frac{\pi}{16} V^2 \Delta t^2. \quad (8)$$

Contact area of abrasive and sample during movement can be calculated:

$$A_r = n' \Delta A_r = \frac{\pi}{16} V^2 \Delta t^2 n', \quad (9)$$

where n' is number of grain projections that came into contact.

Contact time of abrasive and sample surface is determined based on full revolution of electric motor shaft with eccentric since processing was carried out only when ceramic sample passed through abrasive columns and passage was carried out due to vibration action [22]. Number of contact projections was determined by examining imprints of several crystals of hard and soft abrasive materials on cellophane film. Film was placed between abrasive and press, and loading took place (Fig. 4).

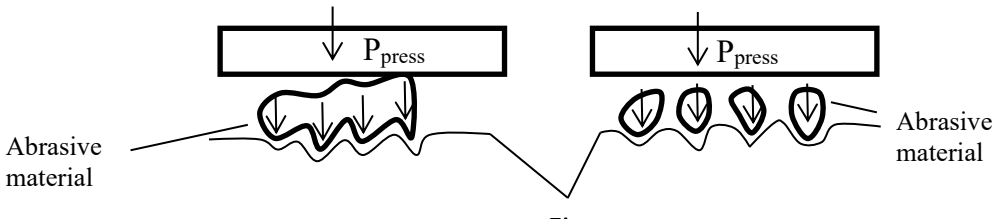

Fig. 4. Scheme for determining number of contact grains when using diamonds

Marks remained on the film at points of contact that were then counted. Thus, calculations were made for soft (A_{rs}) and hard (A_{rh}) abrasives and results were compared: $d_h = \frac{0.9 \cdot 0.022}{2} = 0.05$ mm, $d_s = \frac{0.9 \cdot 0.028}{2} = 0.062$ mm, $\Delta A_{rh} = \frac{3.14}{16} 0.9^2 \cdot 0.022^2 = 7.6 \cdot 10^{-5}$ mm^2, $\Delta A_{rs} = \frac{3.14}{16} 0.9^2 \cdot 0.028^2 = 1.2 \cdot 10^{-4}$ mm^2, $A_{rh} = 5 \cdot \frac{3.14}{16} 0.9^2 \cdot 0.022^2 = 3.9 \cdot 10^{-4}$ mm^2, $A_{rs} = 7 \cdot \frac{3.14}{16} 0.9^2 \cdot 0.028^2 = 8.7 \cdot 10^{-4}$ mm^2.

Analyzing calculated contact area, it can be concluded that contact area of soft abrasive grain is somewhat larger, therefore, processing took place and material removal rate may be somewhat higher than when processing with hard grain [23–25]. This result was also obtained due to the fact that when processing with soft abrasive it is necessary to slightly increase force of pressing tool onto sample. Increasing pressure results in increase of actual contact area of soft abrasive tool with sample. Analysis of dependence shows that material removal is approximately equal both when processing with a soft abrasive and when processing with a harder abrasive.

Use of diamond tool powder in processing of cutting ceramics helps to accelerate pace of technical progress, allows introduction of new progressive technological processes that provide higher precision and quality of processing, increase service life of tool and improve reliability of machines and mechanisms.

Results and Discussion

The research has shown that the most productive method is vibro-abrasive machining with application of magnetic field to working chamber using a suspension containing UDM diamond powder (Fig. 5). This is explained by ability of UDM diamond particles to maintain their cutting ability due to constant microchipping of contact areas as a result of vibration and micro-impact loads in processing zone.

Use of suspensions with monocorundum and diamond powders in different concentrations during vibration-assisted magnetic abrasive processing significantly

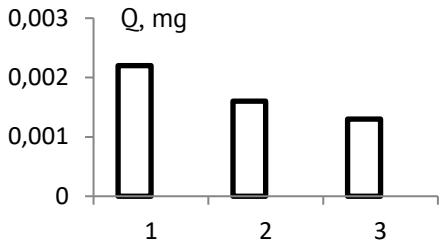

Fig. 5. Influence of diamond powder grade on amount of material removed during ceramic processing: 1 – UDM; 2 – AC6; 3 – ASM

affects amount of material removed from PSHM samples. As can be seen from graph, use of diamond powders in suspension in addition to monocorundum significantly increases removal rate. Figure 6 shows material removal results depending on abrasive material. Analyzing dependence shown on Fig. 6, it can be concluded that synthetic diamond ASM 28/14 that showed high result on its own worked more productively when mixed with monocorundum [26].

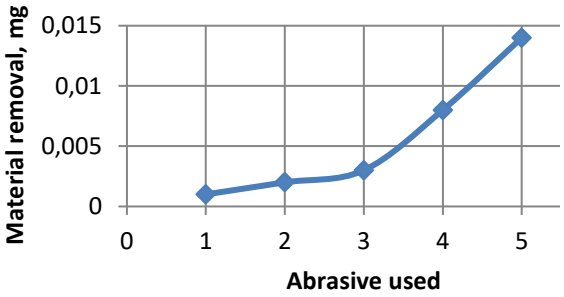

Fig. 6. Material removal from applied abrasive material (mixture): 1 – monocorundum; 2 – monocorundum + white corundum; 3 – monocorundum + 15 % ASM 20/14; 4 – monocorundum + 15 % AC6; 5 – monocorundum + 15 % UDA

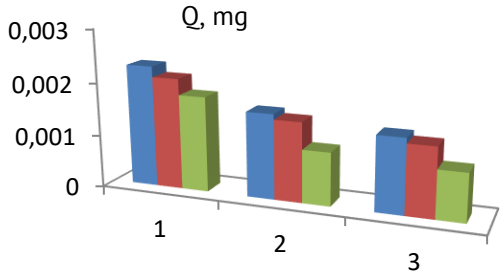

Fig. 7. Influence of diamond powder concentration in suspension on amount of material removed during ceramic processing: 1 – UDM (15, 10, 5 %, respectively); 2 – AC6 (15, 10, 5 % respectively); 3 – ASM (15, 10, 5 % respectively)

As established earlier, material removal depends on physical and mechanical properties of material being processed. Then time for removing micro-roughness will also depend on this parameter. It is possible to determine time for removing microroughness knowing influence of physical and mechanical properties of processed samples during vibration processing and intensity of material removal.

In addition to question of using synthetic diamond as an additive in processing, it was important to find out in what quantity to add synthetic diamond powder. Figure 7 shows dependence of powder concentration on processing intensity. By analyzing dependence conclusion can be drawn about advisability of using certain concentration of diamond powder. When vibration-assisted magnetic abrasive processing of nitride ceramics using suspensions with synthetic diamond powder in concentrations of 10 and 15 % amount of material removed is approximately the same, and it is significantly higher than when using 5 % concentration [27].

Moreover, similar picture is observed when using suspension with any used diamond powder. Finally, it can be said that since difference in removed material with 10 additive and 15 % additive is approximately the same it is more appropriate, based on economic assumptions, to use 10 % additive. Surface roughness was measured in five directions shown on Fig. 8 to eliminate random results. Figure 9 shows surface profiles of samples after 10, 30 and 40 min of processing in one direction.

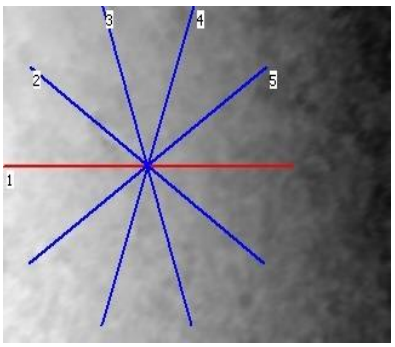

Fig. 8. Orientation of directions for measuring height of microroughness on surface of each sample

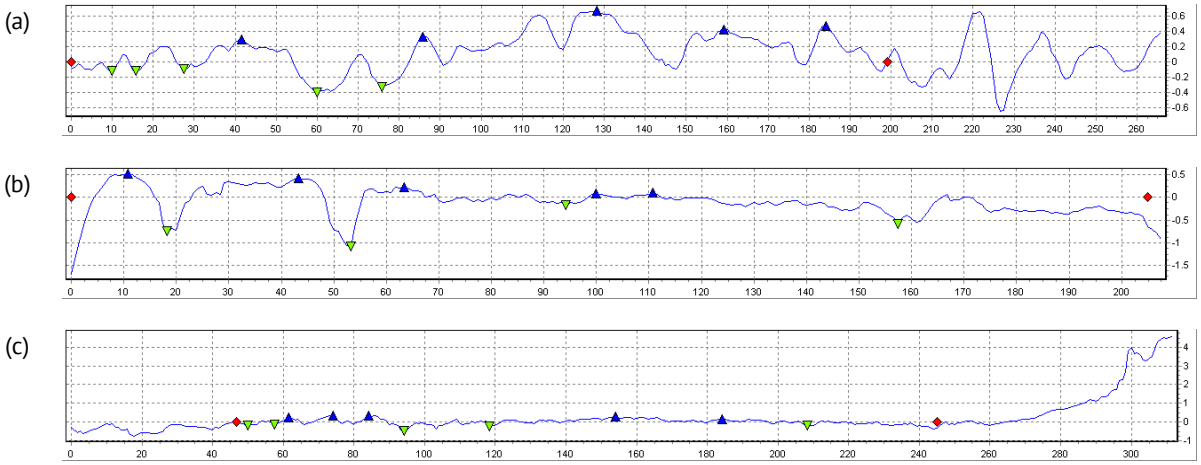

Fig. 9. Surface profiles after (a) 10, (b) 30, and (c) 40 min of processing. R_a = 0.21× 10^3, 0.19× 10^3, and 0.13× 10^3, respectively

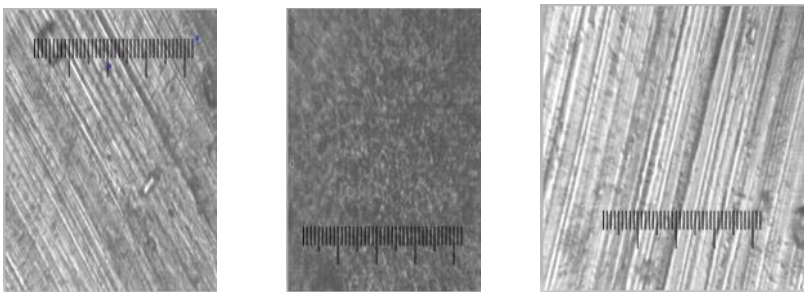

(a) (b) (c)

Fig. 10. Optical microscopy images of sample surface (×500) after (a) 10 , (b) 30, (c) 40 min of processing

Research has shown that according to surface treatment profilograms after 10, 30, and 40 min of work it can be concluded that the lowest roughness was equal to R_a (3) = 0.11 μm after 30 min of treatment. These conclusions are confirmed by images of

fragments of surfaces that were processed. It is evident from them that the most even surface was the one shown on Fig. 5 that corresponds to exactly 30 min of processing. The fragments of surfaces after processing are shown in Fig. 10 [28].

Analyzing profilograms it can be concluded that the highest quality processing occurred with a mixture of monocorundum and UDA diamond powder at concentration of 10 %. Average R_a = 0.11. Profilograms shown above confirm drawings (Fig. 11) made in 3D. They clearly show difference in surface profile of samples treated with different materials [29] diamonds.

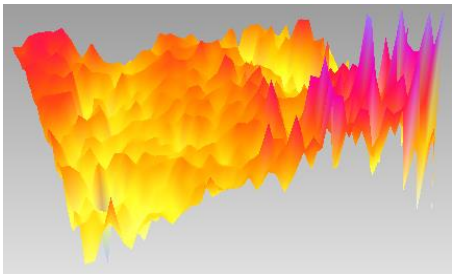

Fig. 11. Plate surface profile (×10^3) after processing in 3D mode: processing time is 30 min. Mixture of UDA diamond powder and monocorundum was used as a tool

Conclusions

1. Process of machining superhard ceramics with softer material is possible with ViMAO due to increase in contact area of abrasive material with sample and increase in pressing force of abrasive material to sample being processed.
2. Obtained mathematical model of machining superhard ceramics with softer material that is possible with ViMAO confirms assumption about processing with softer abrasive.
3. The study demonstrated that using a soft abrasive (monocorundum) in the ViMAO process achieves a material removal rate comparable to that of hard abrasives, albeit requiring approximately 20 % longer processing time to achieve a similar result.
4. Sample surface treated with mixture of monocorundum and UDA diamond powder at concentration of 15 % has more uniform surface compared to other samples.
5. Roughness parameter of ceramic plate after vibration treatment is R_a = 0.11 that is significantly lower compared to other samples.

CRediT authorship contribution statement

Viktor I. Bulakov : conceptualization; **Viktor G. Artiukh** : investigation; **Daria A. Kitaeva** : data curation; **Nikolay V. Korihin** : data curation.

Conflict of interest

The authors declare that they have no conflict of interest.

References

1. Tamarkin MA, Tishchenko EE, Mordovtsev AA, Kokhanyuk A.G. Study of vibration treatment of external and internal surfaces of parts in their preparation for coating. *Strengthening technologies and coatings.* 2021;17(1): 22–26. (In Russian).

2. Kuzin VV. *Instruments with ceramic cutting plates*. Moscow: Yanus-K; 2006. (In Russian)
3. Feng Y, Zhang J, Wang L, Zhang W, Tian Y, Kong X. Fabrication methods and cutting performance of micro-textured self-lubricating ceramic cutting tools by in-situ forming of Al2O3-TiC. *International Journal of Refractory Metals and Hard Materials.* 2017;68: 121–129.
4. Lebedev VA, Dyachenko EA. Model of productivity of vibroabrasive finishing and cleaning processing. In: Babichev AP. (eds.). *Issues of vibration technology*. Rostov-on-Don, Russia: Don State Technical University. 2004. p.17–20. (In Russian)
5. Khalimonenko AD. *Quality management of the turning process with cutting ceramic tools [dissertation abstract]*. St. Petersburg; 2009.
6. Klimenko SA, Kopeykina MYu, Lavrinenko VI, Mayboroda VS, Akulovich LM, Levin ML, Kheifets ML, Khudolei AL, Chizhik SA. *Finishing of surfaces in the production of parts*. Minsk: Belaruskaia navuka; 2017. (In Russian)
7. Akulovich LM, Sergeev LE, Dechko MM. Influence of properties of the working technological environment on the surface roughness and productivity during magnetic abrasive machining. Proceedings of the National Academy of Sciences of Belarus. *Physical-technical series.* 2022;67(1): 39–48. (In Russian)
8. Arulkirubakaran D, Senthilkumar V, Chilamwar VL, Senthil P. Performance of surface textured tools during machining of Al-Cu/TiB2 composite. *Measurement.* 2019;137: 636–646.
9. Burlakcov VI, Burlakova GU, Mazur VA, Manoylov OV. Vibroabrasive treatment of ultra-hard ceramics. *IOP Conference Series: Materials Science and Engineering.* 2021;1164: 012015.
10. Liu Y, Deng J, Wu F, Duan R, Zhang X, Hou Y. Wear resistance of carbide tools with textured flank-face in dry cutting of green alumina ceramics. *Wear.* 2017;372–373: 91–103.
11. Savenkov AA, Shcherbakova AV, Avramchenko AV. The essence of magnetic-abrasive processing and comparative analysis with other processing methods. In: *World of science: Proceedings of the 2nd International scientific-practical conference, Penza, 30 January 2023.* Penza: Nauka i prosveshchenie; 2023. p.62–65. (In Russian)
12. Golobokov AV, Kuznetsov VA, Smirnov AV, Prokop'ev AY. Simulation modeling of the grinding process of instrument bearing blanks made of special corrosion-resistant steels. *STIN.* 2022;S12–2: 28–30. (In Russian)
13. Farwaha HS, Deepak D, Brar GS. Mathematical modeling and process parameters optimization of ultrasonic assisted electrochemical magnetic abrasive machining. *Journal of Mechanical Science and Technology.* 2020;34(12): 5063–5073.
14. Sugihara T, Tanaka H, Enomoto T. Development of a New CBN Cutting Tool for High-Speed Machining of Inconel 718 with Special Focus on Coolant Behavior. *Manufacturing Procedures.* 2017;10: 436–442.
15. Ranjan P, Hiremath SS. Role of textured tool in improving machining performance: A review. *Journal of Manufacturing Processes.* 2019;43: 47–73.
16 Serga GV, Belokur KA, Lebedev VA, Yakovlev DYa. Increasing productivity of technological systems for finishing, cleaning and hardening treatment of parts based on screw rotors. *Strengthening Technologies and Coatings.* 2016;4(136): 16–19. (In Russian)
17. Chen Y, Zheng Y. Design and Characteristics Analysis of Electromagnets Based on ANSYS Maxwell. In: *Proceedings of the 3rd International Symposium on Semiconductor and Electronic Technology (ISSET2024), Xi'an, China, 23–25 August 2024.* IEEE; 2024. p. 108–111.
18. Rogov VA, Shkarupa MI. Comparative analysis of mechanical processing of super hard materials by grinding. *Technology of Mechanical Engineering*. 2009:5: 12–16. (In Russian)
19. Slipchenko K, Petrusha I, Turkevich V, Johansson J, Bushlya V, Stahl J-E. Investigation of the mechanical properties and cutting performance of cBN-based cutting tools with Cr3C2 binder phase. *Procedia CIRP.* 2018;72: 1433–1438.
20. Cheng CK, Chen KY, Tsui HP, Wang AC. Characteristics of the polishing effects for the stainless tubes in magnetic finishing with gel abrasive. *Processes.* 2021;9(9): 1561.
21. Sergiev AP, Vladimirov AA, Shvachkin EG. Study of influence of amplitude-frequency characteristics of vibration turning on roughness parameters. In: Yatsun SF. (eds.) *Vibration technologies, mechatronics and controlled machines: Proceedings of the XII International scientific and technical conference in 2 parts, Part 2, VIBRATSIYA 2016, 18–20 May 2016, Kursk.* Kursk: Southwest State University Press; 2016. p.14–17. (In Russian)
22. Paswan SK, Singh AK. Analysis of finishing performance in rotating magnetorheological honing process with the effect of particles motion. *Proceedings of the Institution of Mechanical Engineers, Part E: Journal of Process Mechanical Engineering.* 2021;235(4): 1104–1118.
23. Maksarov VV, Keksin AI, Filipenko IA, Brigadnov IA. Technological features of magnetic-abrasive processing in terms of digital technologies. *Metalloobrabotka.* 2019;4(112): 3–10. (In Russian)

24. Popov MA, Maksarov VV, Brigadov IA. Influence of the cutting edge rounding radius on improving the quality of the surface layer of a part. *Izvestiia Tula State University*. 2021;9: 30–35.
25. Maksarov VV, Filipenko IA, Shcheglova RA, Brigadnov IA. Technological quality assurance of the edges of flat products by means of magnetic-abrasive finishing of aluminium and its alloys. *Metalloobrabotka*. 2021;3(123): 57–63.
26. Mordovtsev AA, Tamarkin MA, Damsky DB, Avetyan GA. Vibratory finishing application in "smart manufacturing" for manufacturing precision sleeve type products. *Strengthening Technologies and Coatings*. 2022;18(3): 121–124. (In Russian)
27. Tamarkin MA, Tishchenko EE, Troitsky VM, Mordovtsev AA. Preparation of parts for coating by granular abrasive media treatment. *Strengthening Technologies and Coatings*. 2020;16(9): 416–419. (In Russian)
28. Mordovcev AA. Reliability assessment of the manufacturing process of vibro-abrasive treatment in the conditions of digital production. *Transport Engineering*. 2022;6(6): 21–29. (In Russian)
29. Rogovenko DA. Analysis of schemes and methods for intensifying the process of magnetic-abrasive processing of flat surfaces. In: *Research and development in the field of mechanical engineering, energy and management: Proceedings of the XXIII International scientific and technical conference of students, postgraduates and young scientists, 27-28 April 2023, Gomel: in 2 parts. Part 1*. Gomel: GSTU named after P.O. Sukhoi; 2023. p. 20–23. (In Russian)

MATERIALS PHYSICS AND MECHANICS RESEARCH ARTICLE

Submitted: July 12, 2025 **Revised: September 30, 2025** **Accepted: October 7, 2025**

About possibility of using the Roginsky-Schulz and Avrami-Erofeev equations in topokinetic analysis of carbothermic self-recovery of dispersed iron-graphite waste

L.A. Dan [1], V.A. Maslov [1], L.A. Trofimova [1], S.B. Kargin [1], V.G. Artiukh [2], D.A. Kitaeva [2] ✉, N.V. Korihin [2]

[1] Pryazovskyi State Technical University, Mariupol, Russia

[2] Peter the Great St. Petersburg Polytechnic University, St. Petersburg, Russia

✉ dkitaeva@mail.ru

ABSTRACT

Topokinetic analysis of experiment results on carbothermic self-healing of "wustite-graphite" dispersed samples particles was carried out. It was shown a dispersed iron-graphite waste contains metallic iron, iron oxide, carbon and impurities. Observations and calculations made in this work confirmed two-stage nature of process. The first initial stage of the process, at degrees of conversion less than 0.4, can be described by the Roginsky-Schulz or Avrami-Erofeev equations. Apparent activation energy of the initial stage of the process was calculated to be 141.34 kJ/mol. It was found that the Bell-Boudoir reaction is a limiting factor in the process.

KEYWORDS

topokinetic approach • graphite • dispersed iron-graphite waste • cast iron • carbothermic self-healing wustite-graphite

Funding. *This work has been supported by the grant of the Russian Science Foundation, RSF 25-19-00921.*

Citation: Dan LA, Maslov VA, Trofimova LA, Kargin SB, Artiukh VG, Kitaeva DA, Korihin NV. About possibility of using the Roginsky-Schulz and Avrami-Erofeev equations in topokinetic analysis of carbothermic self-recovery of dispersed iron-graphite waste. *Materials Physics and Mechanics*. 2025;53(4): 111–119. http://dx.doi.org/10.18149/MPM.5342025_9

Introduction

Dispersed iron-graphite waste (DIGW) is formed at all stages of cast iron processing. Their formation is associated with decrease in solubility of carbon with decreasing temperature and a number of other processes occurring in liquid iron [1,2]. They contain metallic iron, various iron oxides, carbon and impurities [2,3]. Electron microscopic studies [2] show that particles of dispersed liquid carbon dioxide are graphite plates, to a greater or lesser extent, covered with spherical oxide formations. The main part of oxide inclusions has a size of no more than 160 μm. They are tightly connected to surface of graphite particles and sometimes are located inside them.

This composition and structure of particles explain presence of unique combination of electrical and magnetic properties even in initial dispersed liquid gas phases [4–6]. When applied to graphite which consists of such particles and therefore has magnetic properties term 'magnetic graphite' is used [2]. In this case value of specific saturation magnetization (σ_s) depending on chemical composition of dispersed liquid carbon dioxide is in range from 22 to 45 A·m^2/kg and specific electrical resistance (ρ_v) is in range of

$(4.18–0.46)\cdot10^{-4}$ Ohm·m [2]. The authors position the materials as possessing properties such as radio shielding and radio absorption. An effective method for increasing specific saturation magnetization of DIGW is high-temperature heat treatment that results in formation of metallic iron. Due to this, value of σ_s increases to ~ 180 A·m^2/kg while maintaining low value of ρ_v ~ $2\cdot10^{-4}$ Ohm·m [2]. Efficiency of shielding and absorbing properties increases significantly. Based on this, it is relevant to study kinetic laws of metallization understanding of which will allow for effective control of the process [7].

Materials and Methods

DIGW is a mixture of iron oxides and reducing agent that is graphite. When this mixture is heated above certain temperature process of chemical reduction of iron oxides of dispersed DIGW to metallic iron by carbon contained in them begins. In essence, the process is a carbothermic self-healing one (CTSH). Recovery takes place with participation of solid and gas phases. Therefore, CTSH process can be considered as topochemical.

In [2,8,9] on study of carbothermic self-healing of dispersed DIGW, it was shown that the process occurs in two stages. At the first stage reduction of higher iron oxides to wustite occurs and at the second stage the reduction of wustite to metallic iron occurs. The first stage proceeds quickly. This is followed by induction period during which formation of metallic phase begins followed by its intensive growth. In [9], it is shown that newly formed iron can have a catalytic effect on the process but not immediately and after accumulation of certain minimum amount. Considering high dispersion of oxide component (average size of oxide particles did not exceed 160 μm) of processed material the maximum speed is achieved very quickly. After formation of continuous reaction front beginning of the process deceleration is recorded [9]. Since transformation of magnetite into wustite at temperatures of CTSH occurs almost completely already upon heating of particles to working temperature and the main time of CTSH particles of dispersed DIGW is occupied by reaction FeO → Fe [2,9,10]. This work focuses on topochemical analysis of this reaction occurring at CTSH.

To conduct CTSH of FeO particles wustite-graphite samples were prepared (63.8 % of FeO, 31.2 % of C, 5 % of impurities). Initial dispersed DIGW of mixing section with fraction of less than 160 μm was processed in a quartz reactor without air access for 1.5 h at 820 °C. At this temperature all iron oxides were converted into wustite [9]. Based on differential thermal analysis [9], temperatures above 960 °C were selected as working temperatures for conducting analysis of carbothermic self-healing: 970, 990, 1030 and 1050 °C.

In [2], microstructure of particles of wustite-graphite sample was analyzed after 5, 12, 20 and 40 min after start of carbothermic self-recovery at 1050 °C. Process FeO → Fe was characterized in early stages by formation of areas of metallic phase on surface of oxide. The process then developed with advancement of recovery front into particles and ended with complete recovery. In this case specific saturation magnetization increased monotonically from 0 (initial state) to 168.5 A·m^2/kg after its complete completion after 40 min [2].

Figure 1(a) shows set of curves of recovery degree of wustite (α) during course of experiment constructed according to data of [2]. During the first 5 min measurements were taken for every minute of the experiment then every 5 min. As can be seen from Fig. 1(a) increase in temperature causes shape of the curve to approach a sigmoid.

All curves have three more or less distinct sections, namely, incubation section in which iron nuclei are formed; acceleration section; section in which reaction rate gradually decreases. Similar appearance was shown by curves obtained in [11,12] during reduction of wustite with a hydrogen-helium mixture, in [13] during reduction of hematite to wustite with a gas mixture of N_2, CO, H_2 [13], and in [14] during reduction of hematite with a gas mixture of CO-CO_2.

Analysis of intensity of gas evolution and composition of gas phase for dispersed samples of "wustite-graphite" during CTSH carried out in [2] showed the following. Intensity of gas emission first increased and then decreased during the experiments. CO content was low for entire working temperature range at initial stage of the process. Then it increased and then CO/CO_2 ratio remained constant until end of the experiment. Based on processing of curves shown on Fig. 1(a) rate of recovery of wustite of dispersed samples of “wustite-graphite” at different temperatures of CTSH was calculated.

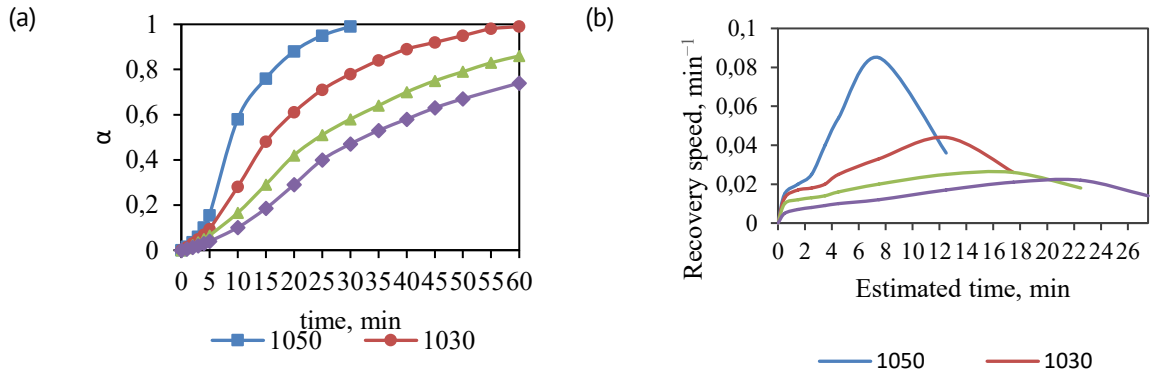

Fig. 1. Kinetics of CTSH of "wustite-graphite" sample [11] (a) and wustite recovery rate of dispersed "wustite-graphite" samples (b)

Calculated curves are shown on Fig. 1(b). Abscissa axis of graph shown on Fig. 1(b) shows calculated time values (average values of interval); ordinate axis shows average recovery rate in time interval. As with intensity of gas evolution, according to [2] rate of wustite recovery during CTSH increased at the beginning of the experiments and then decreased. Increase in temperature in the experiments in studied range leads to an increase in magnitude of recovery rate extremes and their earlier achievement. Thus, at temperature of 970 °C maximum rate of wustite reduction was 0.022 min^{-1} and it was achieved between the 20th and 25th min from beginning of the experiment; at 990 °C the maximum rate was 0.026 min^{-1} and it was achieved between the 15th and 20th min from beginning of the experiment; at 1030 °C the maximum rate was 0.044 min^{-1} and it was achieved between the 10th and 15th min from beginning of the experiment; at 1050 °C the maximum rate was 0.085 $min^{-1}$and it was achieved between the 5th and 10th min from beginning of the experiment. At the same time duration of incubation period decreased. These observations confirm statement about two-stage nature of carbothermic self-healing process made in [2] based on analysis of kinetic curves of CTSH of polydisperse DIGW as well as in studies [13–15].

Joint analysis of Fig. 1 allows to determine proportion of wustite that has transformed into metallic iron by time of reduction process transitions from the first to the second stage. For temperature of 1050 °C it is 0.4; for temperature of 1030 °C it is 0.4; for temperature of 990 °C it is 0.37; for temperature of 970 °C it is 0.36.

Results and Discussion

According to prevailing theory process of reduction of iron oxides by solid carbon is a process involving a gaseous reducing agent [16–18]. Reaction sphere contains solid and gaseous reagents, i.e. the process is topokinetic in nature [13,19]. This is also evidenced by sigmoid form of kinetic curves of CTSH of dispersed particles of "wustite-graphite" shown on Fig. 1(a) as well as CTSH curves of polydisperse DIGW in [2]. It should be kept in mind that the process can be limited both by gasification reaction of carbon contained in sample and by chemical reduction reaction. Taking these considerations into account in order to describe the process of CTSH a topochemical analysis of previously obtained results was carried out in this work.

Modern topokinetic approach to this type of process assumes their two-stage nature [14,15,19]. At the first stage, as a result of interaction of solid and gaseous phases nuclei of reaction product appear on surface of particles, they increase in size, and they merge. The second stage begins after continuous film of reaction product appears on solid particles. Then boundary of reaction proceeds moves deeper into the particles. Since processes occurring at different stages are different, attempts to combine entire process with one general equation led to need to introduce correction factors purpose of which is not to describe the process but to fit equation to obtained experimental curves.

Therefore, by analogy with [12,14,20] each experiment was conditionally divided into two stages, namely, at the first stage the rate increased due to increase of reaction surface and at the second stage the rate decreased due to its decrease. Due to low degree of conversion, the first stage can be called the initial stage, and the second stage can be called the main stage. These stages are separated by the maximum rate.

For topokinetic analysis of available experimental data the Roginsky-Schulz (Eq. (1)) [20] and Avrami-Erofeev (Eq.(2)) [21–23] equations were used in turn to compare results of the analysis:

$$\frac{d\alpha}{d\tau} = k \cdot \alpha^{2/3}; \quad (1)$$

$$\alpha = 1 - exp(-\beta\tau^n), \quad (2)$$

where α is degree of conversion, $d\alpha/d\tau$ is process speed (W), β is a constant that depends on both rate of nucleation and rate of growth of embryos, n is coefficient indicating geometric parameters of embryo growth.

According to [13], one-dimensional, two-dimensional, three-dimensional growth of embryos occurs at n = 1…2, n = 2…3 n = 3…4, respectively. In case when process can be described by Eq. (1) graph in coordinates $W(\alpha^{2/3})$ should have form of a straight line. After carrying out corresponding calculations graphs in coordinates of Roginsky-Schulz equation (Fig. 2) were obtained in form of four straight lines. This speaks in favor of assumptions made about the possibility of applying Roginsky-Schulz equation to the description of the process under consideration. Processing graphs on Fig. 2 allows calculating coefficients k in Eq. (1) for all experimental temperatures and their natural

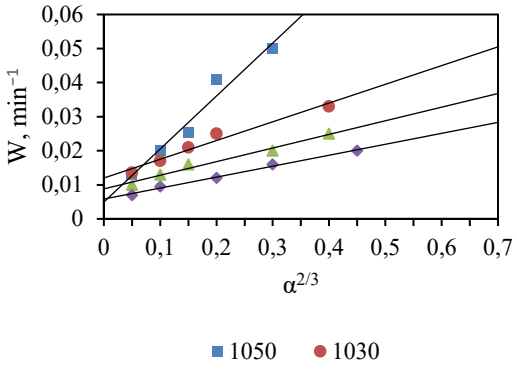

Fig. 2. Graphs in Roginsky-Schulz coordinates

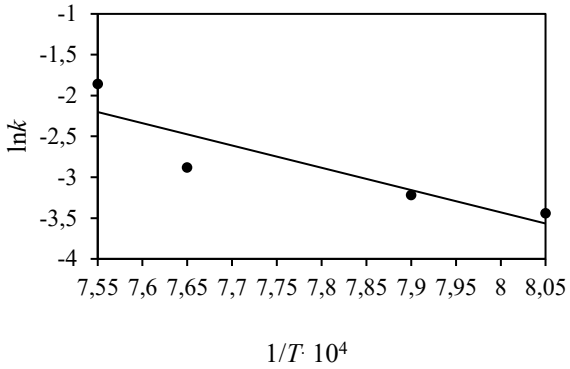

Fig. 3. Graph in Arrhenius coordinates constructed using data from Table 1

Table 1. Results of calculations of coefficients *k* in the Roginsky-Schulz equation

***T*, °C**	***k***	**ln*k***
1050	0.156	-1.858
1030	0.056	-2.882
990	0.04	-3.219
970	0.032	-3.442

logarithms (Table 1). Data from Table 1 is used to plot a graph in Arrhenius coordinates (Fig. 3) and calculate apparent activation energy of process E_a.

Based on obtained graph (Fig. 3) apparent activation energy of process of carbothermic self-healing of dispersed samples of "wustite-graphite" at the first stage was calculated: E_a = 216.16 kJ/mol. It should be noted that such a level of E_a indicates that the reducing agent, which in this case is graphite, has low activity. This is due to peculiarity of its formation at temperatures above 1500 °C. Only in presence of a certain amount of newly formed iron does the process gain noticeable speed. Author of work [24] also points to this.

Using graph shown on Fig. 3 value of k_0 in equation is determined:

$$k = k_0\, exp(-E_a/RT) \quad . \tag{3}$$

From Eq. (3) taking into account found value $k_0 = 2.6 \cdot 10^4$ expression is obtained:

$$k = 2.6 \cdot 10^4\, exp(-216.16/RT) \tag{4}$$

Rate of the process according to the Roginsky-Schulz equation:

$$W = 2.6 \cdot 10^4\, exp(-216.16/RT)\, \alpha^{2/3}. \tag{5}$$

From Eq. (5) degree of transformation:

$$\alpha = [0.867 \cdot 10^4\, exp(-216.16 \cdot 10^3/RT)\, \tau]^3. \tag{6}$$

To evaluate obtained result, experimental points (exp) and points calculated according to Eq. (6) (calc) are plotted on graph of $\alpha(\tau)$ dependence (Fig. 4). Analysis shown on Fig. 4 demonstrates that, contrary to assumptions made in [9], Roginsky-Schulz equation cannot be used for topokinetic analysis of the first stage of carbothermic self-healing of dispersed "wustite-graphite" samples.

Based on obtained results, the experimental data were processed using the Avrami-Erofeev equation. Evaluation of n and β indicators in Eq. (2) is usually carried out using the Hancock-Sharp method [13,14,25]. In accordance with this method, a graph of dependence of ln(-ln(1-α)) on lnτ was constructed and analyzed (Fig. 5(a)). From Fig. 5(a)

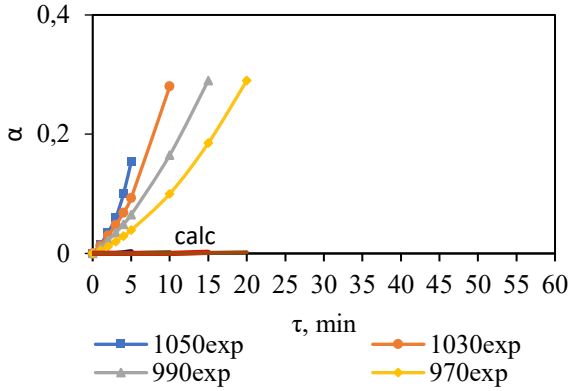

Fig. 4. Comparison of data obtained in the experiment and according to Roginsky-Schulz equation

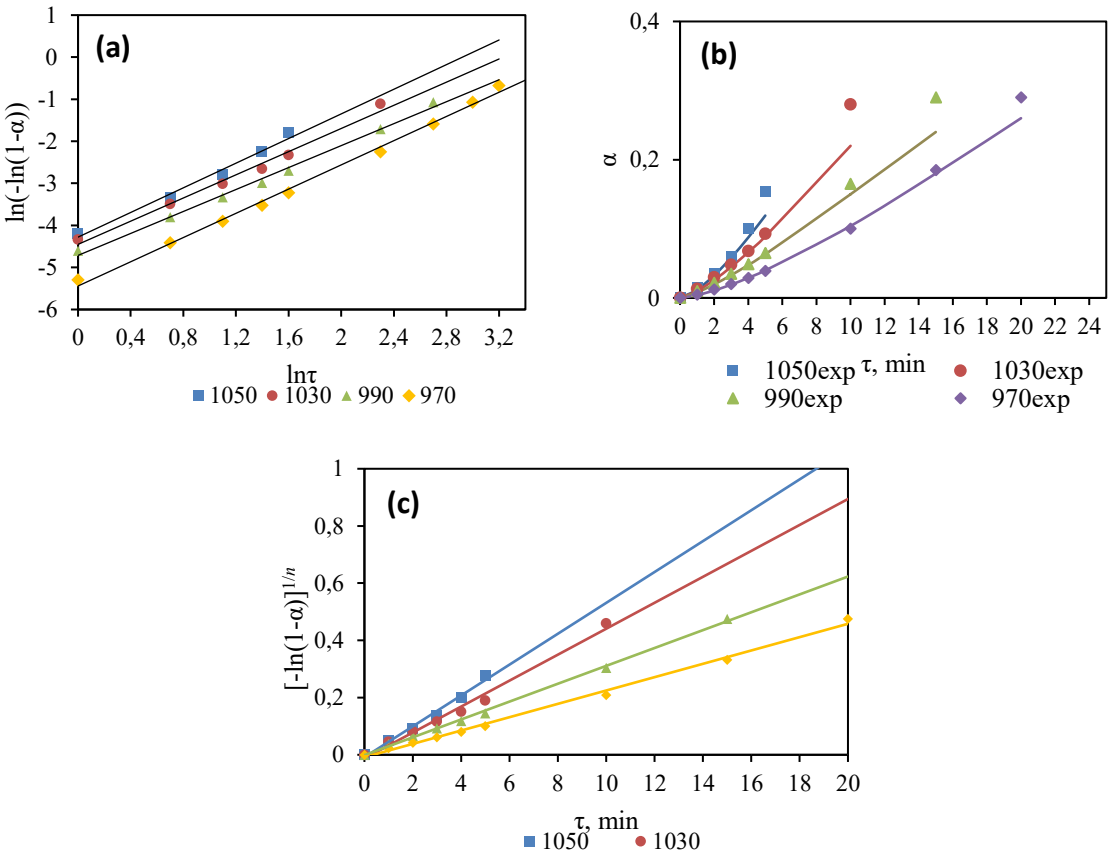

Fig. 5. (a) Dependence of function ln(-ln(1-*α*)) on ln*τ* for experimental conditions;
(b) comparison of data obtained during the experiment and in calculations using the Avrami-Erofeev equation;
(c) dependence of [-ln(1-*α*)]1/n on *τ* under experimental conditions

Table 2. Results of calculations of coefficients of the Avrami-Erofeev equation

No	*T*, °C	*n*	ln*β*	Correlation coefficient, *R*
1	1050	1.465	-4.425	0.990
2	1030	1.380	-4.589	0.994
3	990	1.305	-4.844	0.997
4	970	1.440	-5.585	0.998
Average value		1.398	-4.861	0.995

it follows that function ln(-ln(1-α)) on lnτ is linear at experimental temperatures, i.e., the Avrami-Erofeev equation can be used for the analysis. Based on the analysis of graphs shown on Fig. 5(a) n and β indicators were calculated, and the calculation results are presented in Table 2.

Comparison of results of applying Eq. (2) with experimental data was carried out by analyzing experimental (exp) and calculated curves (calc) shown on Fig. 5(b) and indicates that kinetic model very accurately (with average value of correlation coefficient R = 0.995) describes the process of nucleation and growth of the metallic phase on the surface of wustite particles. Obtained average value $n \approx 1.4$ indicates that process of FeO reduction occurs in kinetic region.

For further calculations the Avrami-Erofeev equation is transformed into form [13]:

$$[-ln(1-\alpha)]^{1/n} = k\tau. \quad (7)$$

Figure 5(c) shows graphical interpretation of Eq. (7) under experimental conditions. Coefficients k in Eq. (7) at different temperatures were calculated using slope of straight lines shown on Fig. 5. Calculation results are given in Table 3.

Table 3. Calculations result of coefficient k in of the Avrami-Erofeev equation (Eq. (7))

No.	T, °C	k	ln$k$
1	1050	0.0540	-2.919
2	1030	0.0454	-3.092
3	990	0.0312	-3.467
4	970	0.0233	-3.760

As in previous case to calculate apparent activation energy of process E_a graph in Arrhenius coordinates was constructed based on data in Table 3 (see Fig. 6). Calculation of E_a performed on the basis of Fig. 6 gives value of apparent activation energy of carbothermic self-recovery process of dispersed samples of "wustite-graphite" of 141.34 kJ/mol. Obtained values are in good agreement with data available in literature concerning reduction of wustite by graphite [24–26].

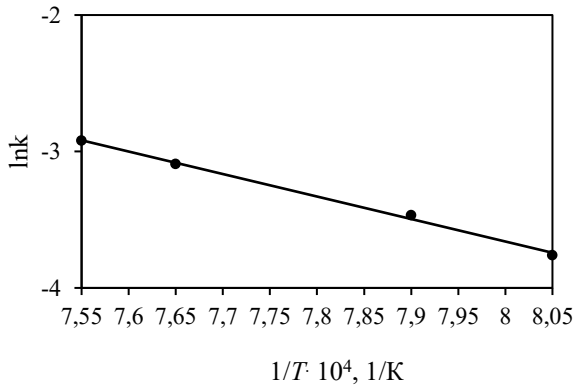

Fig. 6. Graph in Arrhenius coordinates constructed according to data shown in Table 3

In [27], it was found that apparent activation energy of graphite gasification process E_a is 444 kJ/mol. At the same time for complete understanding of the process kinetics [28–30], it is necessary to take into account fact that under considered conditions process

of oxide reduction occurs faster than reaction of CO formation [31–33]. Therefore, in this case it can be concluded that the process is limited by carbon gasification reaction [34,35].

Conclusions

Topokinetic analysis of the process of carbothermic self-healing of dispersed samples of "wustite-graphite" showed following:

1. The Avrami-Erofeev equation can be used in conjunction with the Sharpe-Hancock procedure to describe the process while the Roginsky-Schulz equation does not provide adequate description.
2. Calculated apparent activation energy of this process E_a is equal to 141.34 kJ/mol.
3. The process is limited by carbon gasification reaction.

CRediT authorship contribution statement

Leonid A. Dan: writing – review & editing; **Vladimir A. Maslov**: supervision; **Larisa A. Trofimova**: writing – original draft; **Sergey B. Kargin**: conceptualization; **Viktor G. Artiukh**: investigation; **Daria A. Kitaeva**: data curation; **Nikolay V. Korihin**: data curation.

Conflict of interest

The authors declare that they have no conflict of interest.

References

1. Petrov GV, Boduen AYa, Fokina SB, Popov AA. Chemical concentration of steel-making dusts. *Chernye Metally.* 2016;10: 65–68. (In Russian)
2. Dan L, Maslov V, Trofimova L, Cios G. The Formation, Properties and Use of Dispersed Iron-Graphite Metallurgical Waste. *Journal of Casting & Materials Engineering.* 2022;6(4): 81–92.
3. Chukaeva MA, Matveeva VA, Sverchkov IP. Complex processing of high-carbon ash and slag waste. *Notes of Mining Institute.* 2022;253: 97–104.
4. Li S, Zhang B, Wu D, Li Z, Chu S-Q, Ding X, Tang X, Chen J, Li Q. Magnetic Particles Unintentionally Emitted from Anthropogenic Sources. Iron and Steel Plants. *Environmental Science & Technology Letters.* 2021;8(4): 295–300.
5. Michalik JM, Wilczynska-Michalik W, Gondek L, Tokarz W, Zukrowski J, Gajewska M, Michalik M. Magnetic fraction of the atmospheric dust in Kraków – physicochemical characteristics and possible environmental impact. *Atmospheric Chemistry and Physics.* 2023;23(2): 1449–1464.
6. Aleksandrova TN, Chanturia AV, Kuznetsov VV. Mineralogical and technological features and patterns of selective destruction of ferruginous quartzites of Mikhailovskoye deposit. *Notes of Mining Institute.* 2022;256: 517–526.
7. Petrov G, Zotova I, Nikitina T, Fokina S. Sorption recovery of platinum metals from production solutions of sulfate-chloride leaching of chromite wastes. *Metals.* 2021;11(4): 569.
8. Cheremisina E, Cheremisina O, Ponomareva M, Bolotov V, Fedorov A. Kinetic features of the hydrogen sulfide sorption on the ferro-manganese material. *Metals.* 2021;11(1): 90.
9. Maslov VA, Trofimova LA, Makeev VE, Pustovalov YP. Differential thermal analysis of kinetics of carbothermic self-healing of dispersed wastes of metallurgical production. *Bulletin of Priazovskiy State Technical University. Series: Technical Sciences.* 2003;13: 76–79. (In Russian)
10. Sulimova MA, Sizyakov VM, Litvinova TE, Vasilyev VV. On possibility of the use of metallurgical production wastes as a sorbent in the industrial water cycle. *Chernye Metally.* 2016;8: 43–49. (In Russian)
11. Syrkov AG, Yachmenova LA. Features of obtaining metallurgical products under conditions of solid-state hydride synthesis. *Notes of Mining Institute.* 2022;256: 651–662.
12. El-Rahaiby SK, Rao YK. Kinetics of Reduction of Wustite by Hydrogen-Helium Gas Mixtures at Modest Temperatures. *Transactions of the Iron and Steel Institute of Japan.* 1980;20(5): 287–291.

13. Benoit J, Perry D, Mondal K. Fischer-Tropsch Synthesis in supercritical CO2 – Inhibition of CO2 selectivity for enhanced hydrocarbon production. *Fuel.* 2017;209: 383–393.
14. Yu J, Han Y, Li Y, Gao P, Li W. Mechanism and Kinetics of the Reduction of Hematite to Magnetite with CO-CO_2 in a Micro-Fluidized Bed. *Minerals.* 2017;7(11): 209–220.
15. Kapelyushin Y, Sasaki Y, Zhang J, Jeong S, Ostrovski O. Effects of Temperature and Gas Composition on Reduction and Swelling of Magnetite Concentrates. *Metallurgical and Materials Transactions B.* 2016;47: 2263–2278.
16 Seaton CE, Specht MI, Stellar D. Potential uses of flexicoke for iron ore pelletizing in the Venezuelan steel industry. *Transactions of the Iron and Steel Society of AIME*. 1991;12: 139–144.
17. Varon Cardona LM, Narita CY, Takano C, Breda Mourao M. Characterisation of coal-charcoal composite biocoke as a sustainable alternative for ironmaking. *Canadian Metallurgical Quarterly.* 2017;56(2): 190–198.
18. Mitchell AR, Parker RH. The reduction of SnO_2 and Fe_2O_3 by solid carbon. *Minerals Engineering.* 1988;1: 53–66.
19. Boldyrev VV. Mechanochemical processes with the reaction-induced mechanical activation. Chemo-mechanochemical effect. *Russian Chemical Bulletin.* 2018;67: 933–948.
20. Rozovsky AY. *Kinetics of topochemical reactions*. Moscow: Chemistry; 1974. (In-Russian)
21. Avrami M. Kinetics of Phase Change. I General Theory. *The Journal of Chemical Physics.* 1939;7(12): 1103–1112.
22. Wang H, Thomson WJ. Binary kinetics in the Y-Ba-Cu system: 2. Nanosized particles. *AIChE Journal.* 1995;41(7): 1790–1797.
23. Liu H, Sullivan RM, Hanson JC, Grey CP, Martin JD. Kinetics and Mechanism of the β- to α-$CuAlCl_4$ Phase Transition: A Time-Resolved 63Cu MAS NMR and Powder X-ray Diffraction Study. *Journal of the American Chemical Society.* 2001;123(31): 7564–7573.
24. Trushenski SP, Li K, Philbrook WO. Non-topochemical reduction of iron oxides. *Metallurgical Transactions.* 1974;5: 1149–1158.
25. Hancock JD, Sharp JH. Method of Comparing Solid-State Kinetic Data and Its Application to the Decomposition of Kaolinite, Brucite, and $BaCO_3$. *Journal of the American Ceramic Society.* 2006;55(2): 74–77.
26. Kargin S, Artyukh V, Ignatovich I, Dikareva V. Development and Efficiency Assessment of Process Lubrication for Hot Forging. *IOP Conference Series: Earth and Environmental Science.* 2017;90: 012190.
27. Rao YK. The kinetics of reduction of hematite by carbon. *Metallurgical Transactions.* 1971;2: 1439–1447.
28. Shen J-P, Mobley PD, Douglas LM, Peters JE, Lail M, Norman JS, Turk B. Mechanistic study of CO formation from CO_2 using a mixed-metal oxide of tin, iron, and aluminum. *RSC Advances.* 2014;4(85): 45198–45206.
29. Ha H, Yoo M, An H, Shin K, Han T, Sohn Y, Kim S, Lee S-R, Han JH, Kim HY. Design of Reduction Process of SnO2 by CH4 for Efficient Sn Recovery. *Scientific Reports.* 2017;7(1): 14427.
30. Chernousov PI. Recycling. *Technologies for processing and utilization of man-made formations and waste in ferrous metallurgy*. Moscow: Publishing House MISiS; 2011. (In Russian)
31. Chislavlev VV, Feiler SV. Study of iron and manganese recovery from metallurgical waste. In: Science and youth: problems, searches, solutions. In: Temlyantsev MV. (ed.) *Proceedings of All-Russian Scientific Conference of Students, Postgraduates and Young Scientists.* 2014. p.62–65. (In Russian)
32. Davydov SV. Phase equilibria in carbide region of iron-carbon phase diagram. *Steel.* 2020;1: 22–30.
33. Selivanov EN, Gulyaeva RI, Zaripov RZ, Sel'menskikh NI, Marshuk LA. Effect of calcium oxide on the structure and the thermal properties of granulated high-iron slags. *Russian Metall..* 2020;2020: 121–126.
34. Berdnikov VI, Gudim YA. Chemical reactions in carbon gasification processes. News of higher educational institutions. *Ferrous Metallurgy.* 2019;62(9): 705–712.
35. Kuznetsov YS, Kachurina OI. Thermodynamic analysis of iron oxide reduction processes using carbon and water vapor. News of higher educational institutions. *Ferrous Metallurgy.* 2019;62(5): 394–406.

MATERIALS PHYSICS AND MECHANICS RESEARCH ARTICLE

Submitted: August 12, 2025 **Revised: September 8, 2025** **Accepted: October 7, 2025**

Fabrication and characterization of NiO/AZO heterojunction thin film diodes by radio frequency magnetron sputtering

B.Q. Tran* [1], **T.N.H. Ngo*** [1], **K.B. Nguyen**[2,3], **H.D.T. Duong** [1], **B.K. Thach** [1], **H.P. Pham** [2,3], **H.D. Ngo** [1], **T.K.H. Pham** [1]✉

[1] Ho Chi Minh City University of Technology and Education, Ho Chi Minh City, Vietnam

[2] Nguyen Tat Thanh University Center for Hi-Tech Development, Saigon Hi-Tech Park, Ho Chi Minh City, Vietnam

[3] NTT Hi-Tech Institute, Nguyen Tat Thanh University, Ho Chi Minh City, Vietnam

✉ hangptk@hcmute.edu.vn

*These authors contributed equally to this work.

ABSTRACT

This study focuses on the fabrication and investigation of the properties of the heterojunction *p*-NiO/*n*-Al-doped ZnO via the radio frequency magnetron sputtering method. We conducted a detailed evaluation of the crystal structure, optical properties, and electrical properties of the NiO and Al-doped ZnO monolayers using advanced techniques such as X-ray diffraction, ultraviolet-visible spectroscopy, and Hall effect measurements. X-ray diffraction results show that the NiO thin film crystallizes in the (111) and (200) peaks with a characteristic NaCl-type cubic structure, while the Al-doped ZnO thin film preferentially develops in the (002) peak, exhibiting a hexagonal wurtzite structure. UV–Vis transmission spectrum analysis indicates that the NiO and Al-doped ZnO thin films exhibit transmittance rates of 52 and 92 % in the visible light region, respectively. The optical band gap energy was determined to be 3.45 eV for NiO and 3.36 eV for Al-doped ZnO, respectively. In addition, the carrier concentration in both single layers reached a high level, around 10^{19} cm^{-3}. The *J-V* characteristics under optimal conditions confirmed the formation of the NiO/AZO heterojunction with a turn-on voltage of 0.67 V, an ideality factor of 4.44, and a barrier potential height of 0.5 eV. Especially, the influence of light with a wavelength of 365 nm, this heterojunction clearly exhibited the characteristics of a photodiode. These results demonstrate the remarkable potential applications of the *p*-NiO/*n*-AZO heterojunction in the fields of optoelectronics and light sensors.

KEYWORDS

Al-doped ZnO • NiO • photodiode • heterojunction • RF-magnetron sputtering

Funding. *This work has been supported by the grant of the Ho Chi Minh city university of Technology and Education (SV2025–30).*

Citation: Tran BQ, Ngo TNH, Nguyen KB, Duong HDT, Thach BK, Pham HP, Ngo HD, Pham TKH. Fabrication and characterization of NiO/AZO heterojunction thin film diodes by radio frequency magnetron sputtering. *Materials Physics and Mechanics.* 2025;53(3): 120–130.
http://dx.doi.org/10.18149/MPM.5312025_10

Introduction

UV photodiodes based on semiconductor materials with a large bandgap energy (E_g > 3 eV) are becoming a focal research area due to their widespread applications in the ultraviolet region [1]. Typical materials in the class of transparent conducting oxides (TCOs) include TiO_2, ZnO, NiO, SnO_2, and Ga_2O_3. Among these, ZnO and NiO stand out with their unique optoelectronic properties. They not only have an impressive transmittance (up to 80 %) in the visible region but also possess a low resistivity, around 10^{-3} Ω·cm at room temperature [2–4]. Moreover, their abundant availability, low cost,

and environmental friendliness make them highly attractive for potential large-scale industrial applications. In practice, however, the fabrication of photodiodes based on ZnO/NiO heterojunctions faces significant challenges, particularly in achieving stable *p*-type ZnO (doped with N, P, As, or Sb) and *n*-type NiO (doped with Al, Li, Ag, or Cu). These difficulties arise from the low solubility of dopants, the self-compensation effect, and the limited ability to maintain the desired conductivity type [5–7]. Consequently, heterojunctions employing ZnO or NiO are being actively investigated for optoelectronic applications [8–10].

Zinc oxide (ZnO) is an *n*-type semiconductor belonging to the II-VI group, exhibiting a hexagonal wurtzite structure with space group $P6_3mc$ and lattice constants a = 3.25 Å and c = 5.20 Å [1]. Moreover, its direct bandgap energy of approximately 3.37 eV and a large exciton energy of 60 meV make ZnO highly suitable for a wide range of applications, including UV sensors, UV photoconductive detectors, and white light-emitting devices [11–16]. The *n*-type semiconductor properties of ZnO are primarily formed by intrinsic defects such as zinc interstitial and oxygen vacancy. However, increasing the defect density in the ZnO crystal lattice to enhance its electrical properties inevitably deteriorates both its crystalline quality and optical characteristics. Therefore, to preserve the structural integrity and optoelectronic performance, the carrier concentration of intrinsic ZnO is typically maintained in the range of 10^{16} – 10^{17} cm^{-3} [17]. This procedure causes high resistivity, significantly limiting the performance of the device. To overcome these problems, group IIIA metals like Al, Ga, and In are often added to the ZnO crystal lattice to increase the number of carriers while keeping the crystal's high transparency in the visible range [18–20]. Al is the most common dopant because it works well to replace Zn atoms and is cheaper than In and Ga [21]. Furthermore, high-quality Al-doped ZnO (AZO) thin films can be readily fabricated using various techniques, including radio frequency (RF) magnetron sputtering, metal–organic chemical vapor deposition, and atomic layer deposition.

Nickel oxide (NiO) is a highly promising material for forming *p*–*n* junctions with ZnO. It crystallizes in a face-centered cubic rock-salt structure (space group *Fm-3m*) with a lattice constant of a ~ 4.17 Å [1]. Owing to its oxygen sublattice having a hexagonal symmetry similar to that of Al-doped ZnO, NiO can be effectively deposited on this substrate [22]. As an intrinsic *p*-type semiconductor with a wide direct bandgap of 3.4–4.0 eV, NiO is an attractive candidate for UV sensor applications [23]. Its hole conductivity arises primarily from nickel vacancies and oxygen interstitials; however, its carrier concentration is generally limited. In our previous work, RF-reactive magnetron sputtering was employed to self-dope NiO by controlling the reactive gas flow and the Ni^{3+} content, which serves as a source of free carriers. This approach enabled the carrier concentration to exceed 10^{19} cm^{-3} [24].

Up to now, research on the fabrication and application of NiO/AZO-based heterojunctions remains limited. Shu-Yi Tsai *et al.* fabricated NiO/ZnO heterojunctions via RF magnetron sputtering, reporting carrier concentrations of 7.52×10^{18} and 4.29×10^{19} cm^{-3}, mobilities of 2.26 and 6.02 $cm^2/V{\cdot}s$, and ~ 80 % transmittance in the visible range for single-layer NiO and ZnO, respectively. The resulting heterojunction exhibited an open-circuit voltage of ~2.5 eV and UV sensitivity at 365 nm [25]. Similarly, Gupta R.K. et al. produced *p*-NiO/*n*-ZnO heterojunctions by pulsed laser deposition,

achieving transmittances of 64 and 87 %, carrier concentrations of 7.1×10^{18} and 6.5×10^{19} cm^{-3}, and an open-circuit voltage of 0.45 eV with an ideality factor of about 4.1 and a barrier potential of about 0.35 eV (determined by Norde's method) [26]. However, the large carrier concentration mismatch between NiO and ZnO resulted in a non-optimal electric field distribution in the depletion region, limiting photo-generated carrier collection. NiO/ZnO heterojunctions have been investigated for applications such as photocatalysis, formaldehyde and trimethylamine sensing, UV photodetectors, and supercapacitors [27–31].

In this work, we fabricated a *p*–*n* NiO/AZO heterojunction via RF magnetron sputtering–a widely adopted method offering good uniformity, deposition rate, adhesion, and industrial scalability [32]. Film thickness and properties can be precisely tuned by controlling oxygen flow rate, sputtering power, substrate temperature, and annealing temperature, as demonstrated in our previous studies. Here, we successfully prepared the heterojunction for ultraviolet light sensing applications. While the crystal structure, optical, and electrical properties of the AZO and NiO single layers have been reported previously, this study focuses on investigating the carrier transport mechanism under dark and UV-illuminated (365 nm) conditions through *J*–*V* characterization, which points to possibilities for the potential for practical device applications. XRD, UV–Vis, and Hall effect results are taken from our earlier publications [33, 34].

Materials and Methods

The AZO thin film was fabricated on a glass substrate using the radio frequency (RF) magnetron sputtering, with Al-doped ZnO lab-made targets (2 at. % Al). The glass substrate was thoroughly cleaned with acetone, ethanol, and isopropyl alcohol (IPA), each solution for 5 mins, and then heated in a vacuum chamber at a pressure of 5×10^{-3} Torr to completely remove impurities and moisture. The AZO film deposition process was carried out at a temperature of 200 ºC and a power of 50 W. Next, NiO thin films were sputtered onto the prepared AZO/glass structure, using a Ni metal target with a purity of 99.95% in an argon and oxygen gas environment (Fig. 1). The optimal deposition conditions were established at a pressure of 5×10^{-3} Torr, an RF power of 70 W, and an $Ar:O_2$ gas ratio of 7:3. The substrate temperature is maintained at a stable 250 °C throughout the sputtering process. Indium was used as the electrode material. The contacts were deposited by sputtering through a shadow mask, which allowed indium to contact both the NiO and AZO layers (Fig. 1). The NiO thin film exhibited a thickness of approximately 250 nm, while the AZO thin film showed a thickness of about 280 nm. The crystal structure of the films was analyzed using X-ray diffraction (XRD, D8-ADVANCE).

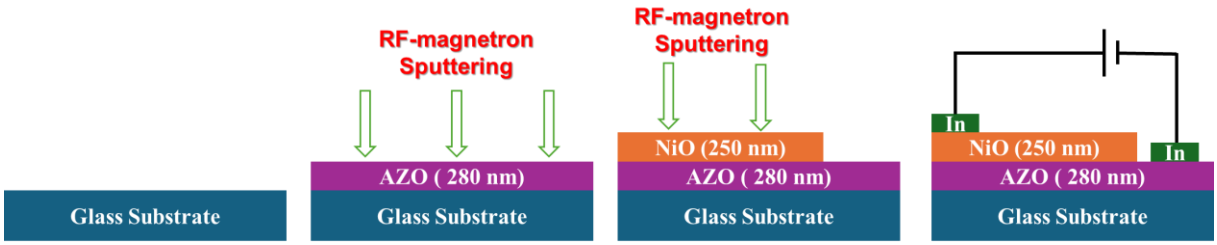

Fig 1. The process of fabricating a *p*-NiO/*n*-AZO heterojunction using the RF-magnetron sputtering method

The optical properties were evaluated through UV-Vis (JASCO, V-550, Japan) transmission spectra, while the electrical characteristics were investigated in detail using Hall effect measurements (BIO-RAD HL5500IU). Finally, the *I–V* characteristics of the diode were measured at room temperature using a Keysight-U2722A current-voltage source.

Results and Discussion

The structural characteristics of AZO and NiO thin films fabricated using the RF-magnetron sputtering method were previously reported in references [33] and [34]. The AZO thin film exhibits a high-intensity difraction peak (002) at an angle of 2θ= 34.54°, with a full width at half maximum (FWHM) of approximately 0.25°. This observation confirms that the AZO thin film crystallizes in the characteristic hexagonal wurtzite structure, with the *c* lattice constant (denoted as a_2) determined to be 5.19 Å [33]. Meanwhile, the diffraction pattern of NiO thin film shows the appearance of two main peaks: (111) at 2θ = 36.43° and (200) at 2θ = 42.73° with corresponding FWHM values of 2.13° and 1.07°, respectively. These peaks represent the characteristic of the cubic structure of NiO, with the lattice constant a (denoted as a_1) estimated to be approximately 4.25 Å [34]. Although the crystal structures of AZO thin films (hexagonal wurtzite) and NiO (NaCl-type cubic) are different, the deposition of high-quality ZnO layers on NiO substrates is still feasible because of the similar oxygen atom configuration (six-fold symmetry) [22].

To further confirm the electrical characterization results and support energy band alignment, an analysis of the lattice mismatch at the NiO/ZnO interface was conducted. The estimation was performed using equations commonly applied to materials with cubic crystal structures [35]. Based on this assumption, the lattice mismatch values were calculated using the following expression:

$$\Delta a = \frac{2(a_1 - a_2)}{a_1 + a_2}, \quad (1)$$

$$N_s = \frac{4(a_1^2 + a_2^2)}{a_1^2 a_2^2}, \quad (2)$$

$$x = \frac{a_1 a_2}{\sqrt{2}\,(a_1 + a_2)}, \quad (3)$$

where a_1, a_2 represents the lattice parameters of the contacting material, N_s is the minimum concentration of surface states at the heterojunction, x is the average distance between NiO and AZO thin films.

Table 1. Lattice mismatch and interfacial parameters of AZO and NiO thin films at the heterojunction

Sample	2θ, °	(hkl)	Lactice parameter		Δ*a*, %	*x*, 10^7 cm	N_s, 10^{-13} cm^{-2}
			a_1, Å	a_2, Å			
AZO	34.54	(002)	–	5.19	-19.92	1.65	3.7
Nio	36.43	(111)	4.25	–			
	42.73	(200)					

The lattice constant deviation between NiO (cubic) and AZO (hexagonal) was calculated to be −19.92%, indicating a significant mismatch at the NiO/AZO heterojunction. In comparison, an ideal heterojunction typically exhibits a lattice mismatch below 7 % [35]. The significant mismatch leads to the formation of interfacial

defects, with an estimated surface state density of 3.7 × 10^{-13} cm^{-2}. These defects facilitate the recombination of charge carriers during the charge transport process. The lattice parameters, mismatch values, and interfacial characteristics of the NiO and AZO thin films, as well as their heterojunction, are summarized in Table 1.

In our previous report [33,34], the optical properties of NiO and AZO thin films were analyzed by using the UV-Vis spectroscopy in the wavelength range from 300 to 1000 nm. The average transmittance was determined to be 92 and 52 % in the visible light region, respectively. Based on the results of the transmission spectrum, the absorption coefficient was determined in the strong absorption region according to the Beer-Lambert law [36]:

$$\alpha = d^{-1}\left[\ln\left(\frac{1}{T}\right)\right], \quad (4)$$

where T is the normalized transmittance and d is the thickness of the film (280 nm for AZO and 250 nm for NiO). The optical band gap (E_g) was then determined using Tauc's formula [36]:

$$\alpha h\nu = A\left(h\nu - E_g\right)^k, \quad (5)$$

where α is the absorption coefficient, A is the band edge constant, $h\nu$ is the photon energy, and k = 1/2 for direct allowed transition, as in the hexangonal wurtzite structure of AZO and the cubic structure of NiO. The optical band gap energy is determined to be 3.36 eV for the AZO thin film and 3.45 eV for the NiO thin film.

Moreover, the electrical properties of AZO and NiO thin films were determined by Hall effect measurements [33,34]. Based on the values indicating the carrier concentration, the NiO and AZO films exhibit *p*-type and *n*-type semiconductor properties, respectively. The carrier concentration and mobility for the AZO thin film were determined to be 2.19 × 10^{19} cm^{-3} and 0.9 $cm^2/V{\cdot}s$, respectively, while for the NiO thin film, they were 2.36 × 10^{19} cm^{-3} and 1.02 $cm^2/V{\cdot}s$, respectively. The parameters characterizing the optical and electrical properties of the AZO and NiO single-layer films are summarized in Table 2.

Table 2. Optical and electrical properties of AZO and NiO thin films

Sample	Thickness, nm	*T* %, 400–800 nm	Optical bandgap, eV	Carrier type	Carrier concentration, 10^{19} cm^{-3}	Mobility, $cm^2/V{\cdot}s$	Ref.
AZO	280	92	3.36	*n*	-2.19	0.9	[33]
NiO	250	52	3.45	*p*	+2.36	1.02	[34]

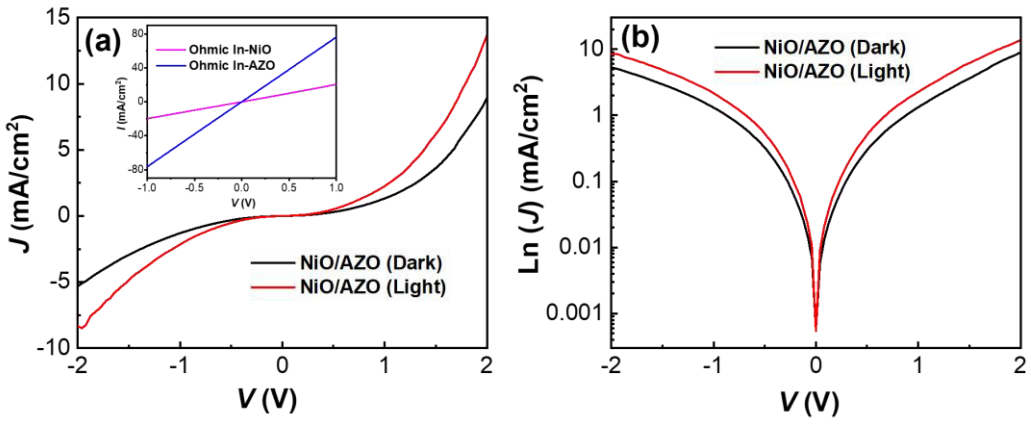

Fig 2. Linear (a) and semi-logarithmic (b) *J*–*V* characteristics of the NiO/AZO diode

Indium metal was used for ohmic contact with the AZO and NiO thin films with a work function of 4.12 eV, as shown in the inset Fig. 2(a). The results show that the p-type semiconductor NiO has formed a heterojunction on the *n*-type AZO semiconductor substrate with the NiO/AZO/glass diode structure. The *J*–*V* characteristics in the dark mode and the changes in characteristics under illumination are shown in Fig. 2(a) (linear) and Fig. 2(b) (semi-logarithmic), with the open-circuit voltage V_{oc} (dark) determined to be 0.67 V, consistent with previous reports [37]. In addition, the relatively large leakage current due to the sputtering fabrication method causes the surface of the AZO film to suffer damage from ion bombardment before the NiO thin film is deposited [3].

The *J*–*V* characteristic curve represents the rectifying relationship between the current density through the diode and the voltage according to the thermionic emission theory given by the expression [24,38]:

$$J = J_0 \cdot \exp\left(\frac{qV}{nK_BT} - 1\right). \quad (6)$$

Here q is the electron charge (1.6×10^{-19} C), K_B is Boltzmann constant ($J \cdot K^{-1}$), T is the absolute temperature (K) and J_0 is the reverse saturation current:

$$J_0 = AA^*T^2\exp\left(\frac{-q\phi_B}{K_BT}\right), \quad (7)$$

where A is the area of the diode (1 cm^2); A^* is the Richardson constant of the *p*-NiO/*n*-ZnO heterojunction (0.062 A $cm^{-2} \cdot K^{-2}$) [39].

The effective barrier height is determined [24,38]:

$$\phi_B = \frac{K_BT}{q} ln \frac{AA^*T^2}{J_0}, \quad (8)$$

with J_0 determined from the extrapolated results in the linear region of the ln(*J*) curve with respect to *V* at the time *V* = 0.

ln(*J*) is determined:

$$\ln J = \frac{qV}{nK_BT} + \ln J_o. \quad (9)$$

The ideal factor (n) is determined:

$$n = \frac{q}{K_BT} \cdot \frac{dV}{dlnJ}. \quad (10)$$

Under dark light, the ideality factor (n) and effective barrier height (ϕ_B) are determined to be 4.44 and 0.50 eV, respectively. The diode operates based on two main mechanisms: thermal transport (TE) and the tunneling effect [40]. The TE mechanism for an ideal diode is the movement of charge carriers due to temperature. Conversely, tunneling allows charge carriers to pass through the energy barrier, often dominating when the diode has a low ideality factor or a large energy barrier. According to the Sah-Noyce-Shockley theory, the ideality factor ranges from 1 to 2, indicating that the primary current mechanism is due to the tunneling effect [40]. If n = 2, the dominant mechanism is due to recombination and emission; if n > 2, the dominant mechanism is leakage current [40]. The high ideality factor value of the NiO/AZO diode is explained by the following reasons: (i) the high series resistance of the two material layers; (ii) the recombination of charge carriers in the depletion region; (iii) the surface morphology of the material; (iv) charge carriers tunneling between states in the bandgap; and (v) inhomogeneous potential barrier [41]. Furthermore, Table 3 shows that the *p*-NiO/*n*-AZO diode fabricated in this study exhibits a threshold voltage significantly lower than that reported in many previous studies on NiO/ZnO systems (1.0 – 3.0 V). This suggests that

the use of Al-doped ZnO, combined with a balanced carrier concentration between the two junction layers, contributes to lowering the threshold voltage, thereby reducing energy consumption and facilitating integration into low-voltage circuits.

Table 3. Comparison of turn-on voltage (V_{on}) and ideality factor (n) for NiO/AZO heterojunction diodes

Heterojunction structure	Method	V_{on}, V	Ideality factor	Ref.
In/NiO/AZO/In	Sputtering	0.67	4.44	This work
Au/NiO/ZnO/Au	PLD	~ 0.35	4.10	[26]
Al/NiO/ZnO/Al	Sputtering	~ 3.00	–	[25]
Au/ZnO/NiO:Li/ITO	PLD	1.00	2.00	[22]
Pt/NiO/ZnO/ITO	Sputtering	0.5–1.1	1.36–1.41	[42]
C/ZnO/NiO_x/Au	Inkjet printing	2.20	–	[43]
Au/NiO/ZnO/Au	Sputtering	1.3	2.7	[44]

Under the condition of illumination with a monochromatic light source at a wavelength of 365 nm (in the near-ultraviolet region), with a power of 10 W, the NiO/AZO heterojunction diode shows a significant increase in current in both polarities, especially in the reverse bias region. Illumination generates electron-hole pairs ($e^- - h^+$) in the *p-n* junction region, thereby increasing the carrier density and significantly contributing to the photocurrent. Under these conditions, the reverse current (photocurrent) increases significantly, reflecting the structure's ability to efficiently absorb photons and effectively separate charge carriers. This shows that the diode operates effectively as an ultraviolet photodiode, with high sensitivity in the light region where the photon energy is greater than the bandgap of the absorbing material. The analysis results show its potential application in optoelectronic devices such as photodiodes or solar cells.

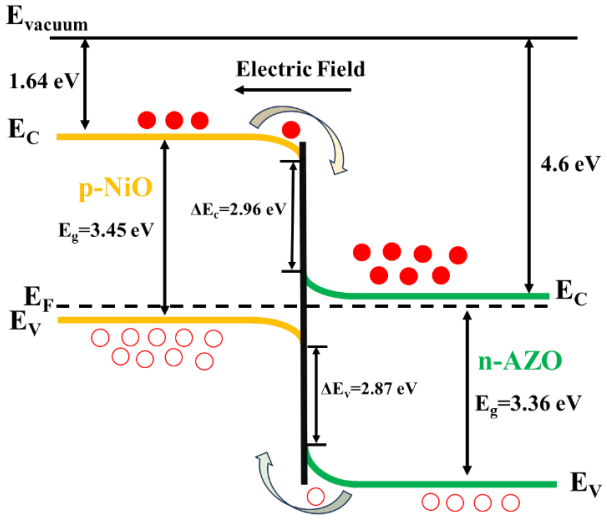

Fig 3. Band diagram of heterojuntion *p*-NiO/*n*-AZO

The energy band structure of the NiO/AZO heterostructure is illustrated in Fig. 3. The work function of the indium electrode is 4.12 eV. The electron affinities (χ) of NiO and AZO are 1.64 eV and 4.60 eV, respectively; the corresponding bandgap energies are 3.45 eV (NiO) and 3.36 eV (AZO) [45,46]. When two materials come into contact to form a

heterostructure, the rearrangement of energy levels leads to the formation of potential barriers at the interface. The conduction band offset (ΔE_C) and valence band offset (ΔE_V) are determined according to equations [35]:

$$\Delta E_C = E_{C1} - E_{C2} = \chi_2 - \chi_1, \quad (11)$$

$$\Delta E_V = E_{V1} - E_{V2} = (\chi_1 + E_{g1}) - (\chi_2 + E_{g2}). \quad (12)$$

The conduction band and valence band offsets were determined to be 2.96 eV and 2.87 eV, respectively, based on the Anderson model, consistent with previous reports [37,47]. These two quantities indicate that the NiO/AZO heterojunction belongs to type II (type-II band alignment), where both the conduction band and valence band of AZO are lower than those of NiO. These two quantities indicate that the NiO/AZO heterojunction belongs to type II, where both the conduction band and the valence band of AZO are lower than those of NiO [48]. The distribution of energy bands in this manner facilitates the separation of electron-hole pairs ($e^- - h^+$). Specifically, electrons in the conduction band of NiO will easily move to the conduction band of AZO with a lower energy level, while holes in the valence band of AZO will move to the valence band of NiO. This process helps prevent recombination, thereby increasing the efficiency of charge separation generated under illumination, contributing to the enhancement of the performance of optoelectronic devices.

Conclusions

The photodiode on a *p*-NiO/*n*-AZO/glass substrate was fabricated using the RF-magnetron sputtering method. The NiO film, which has a cubic structure and a thickness of approximately 250 nm, is deposited on the AZO film, which has a hexagonal wurtzite structure and a thickness of approximately 280 nm. The optoelectronic properties of the single-layer films were determined using UV-Vis and Hall effect, with the NiO thin film (T % = 52 %, E_g = 3.45 eV, n_h = 2.36 × 10^{19} cm^{-3}, μ_h = 1.02 $cm^2/V{\cdot}s$) and the AZO thin film (T % =92 %, E_g = 3.36 eV, n_h = 2.19 × 10^{19} cm^{-3}, μ_h = 0.90 $cm^2/V{\cdot}s$). The J–V characteristics in dark and under illumination with a wavelength of 365 nm show that a heterojunction *p-n* is formed with diode-like properties in the dark, such as turn-on voltage, ideality factor, and barrier potential, which are determined to be 0.67 V, 4.44 and 0.5 eV, respectively, and also demonstrate good photodetection capability under ultraviolet light (356 nm). The results indicate that the NiO/AZO transition has potential applications in photodetectors in the future.

CRediT authorship contribution statement

Bao Quan Tran: writing – review & editing, writing – original draft; **Thi Nhu Huynh Ngo**: writing – review & editing, writing – original draft; **Khac Binh Nguyen**: investigation; **Hong Diu Tho Duong:** investigation; **Bao Khang Thach:** investigation; **Hoai Phuong Pham**: data curation, conceptualization; **Hai Dang Ngo**: data curation, conceptualization; **Thi Kim Hang Pham**: supervision, conceptualization, writing – review & editing.

Conflict of interest

The authors declare that they have no conflict of interest.

References

1. Spencer JA, Mock AL, Jacobs AG, Schubert M, Zhang Y, Tadjer MJ. A review of band structure and material properties of transparent conducting and semiconducting oxides: Ga_2O_3, Al_2O_3, In_2O_3, ZnO, SnO_2, CdO, NiO, CuO, and Sc_2O_3. *Applied Physics Reviews.* 2022;9(1): 011315.
2. Pham TKH, Pham HP, Ngo HDN. Impact of Sputtering Power on Characteristics of Indium-Doped ZnO Thin Films. *Materials Transactions.* 2025;66(9): 1266–1271.
3. Zhang D, Nozaki S, Uchida K. NiO/Si heterostructures formed by UV oxidation of nickel deposited on Si substrates. *Journal of Vacuum Science & Technology B.* 2014;32(3): 031202.
4. Shirshneva-Vaschenko EV, Sosnin IM, Nuryev RK, Gladskikh IA, Liashenko TG, Bezsmertnyĭ VE, Romanov AE. Electrical and optical properties of transparent conducting ZnO:Al/AgNP multilayer films. *Materials Physics and Mechanics.* 2016;29(2): 145–149.
5. Özgür Ü, Alivov YI, Liu C, Teke A, Reshchikov MA, Doğan S, Avrutin V, Cho S-J, Morkoç H. A comprehensive review of ZnO materials and devices. *Journal of Applied Physics.* 2005;98(4): 041301.
6. Egbo KO, Ekuma CE, Liu CP, Yu KM. Efficient p-type doping of sputter-deposited NiO thin films with Li, Ag, and Cu acceptors. *Physical Review Materials.* 2020;4(10): 104603.
7. Sun H, Liao M-H, Chen S-C, Li Z-Y, Lin P-C, Song S-M. Synthesis and characterization of n-type NiO: Al thin films for fabrication of pn NiO homojunctions. *Journal of Physics D: Applied Physics.* 2018;51(10): 105109.
8. Hwang J-D, Lin W-M. Enhancing the photoresponse of p-NiO/n-ZnO heterojunction photodiodes using post ZnO treatment. *IEEE Transactions on Nanotechnology.* 2018;18: 126–131.
9. Tyagi M, Raj VB, Tomar M. High gain NiO/ZnO heterojunction photodiodes operated in Deep-ultraviolet region. *Thin Solid Films.* 2024;798: 140389.
10. Hwang JD, Jiang CI, Hwang SB. P-NiO/n-ZnO heterojunction photodiodes with an MgZnO/ZnO quantum well insertion layer. *Materials Science in Semiconductor Processing.* 2020;105: 104711.
11. Xu Q, Cheng L, Meng L, Wang Z, Bai S, Tian X, Jia X, Qin Y. Flexible self-powered ZnO film UV sensor with a high response. *ACS Appl Mater Interfaces.* 2019;11(29): 26127–26133.
12. Liu KW, Ma JG, Zhang JY, Lu YM, Jiang D, Li B, Zhao DX, Zhang Z, Yao B, Shen DZ. Ultraviolet photoconductive detector with high visible rejection and fast photoresponse based on ZnO thin film. *Solid State Electron.* 2007;51(5): 757–761.
13. Shi Z, Zhang Y, Zhang J, Wang H, Wu B, Cai Xu, Cai Xi, Dong X, Liang H, Zhang B, Du G. High-performance ultraviolet-blue light-emitting diodes based on an n-ZnO nanowall networks/p-GaN heterojunction. *Applied Physics Letters.* 2013;103(2). 021109.
14. Rahman F. Zinc oxide light-emitting diodes: a review. *Optical Engineering.* 2019;58(1): 010901.
15. Rackauskas S, Talka T, Kauppinen EI, Nasibulin AG. Zinc oxide tetrapod synthesis and application for UV sensors. *Materials Physics and Mechanics.* 2012;13(2): 175–180.
16 Khan M, Alam MS, Ahmed SF. Effect of nickel incorporation on structural and optical properties of zinc oxide thin films deposited by RF/DC sputtering technique. *Materials Physics and Mechanics.* 2023;51(1): 19–32.
17. Vyas S. A short review on properties and applications of zinc oxide based thin films and devices: ZnO as a promising material for applications in electronics, optoelectronics, biomedical and sensors. *Johnson Matthey Technology Review.* 2020;64(2): 202–218.
18. Bhosle V, Tiwari A, Narayan J. Electrical properties of transparent and conducting Ga doped ZnO. *Journal of Applied Physics.* 2006;100(3): 033713.
19. Hafdallah A, Ynineb F, Aida MS, Attaf N. In doped ZnO thin films. *Journal of Alloys and Compounds.* 2011;509(26): 7267–7270.
20. Takci DK, Senadim Tuzemen E, Kara K, Yilmaz S, Esen R, Baglayan O. Influence of Al concentration on structural and optical properties of Al-doped ZnO thin films. *Journal of Materials Science: Materials in Electronics.* 2014;25: 2078–2085.
21. Kadam P, Agashe C, Mahamuni S. Al-doped ZnO nanocrystals. *Journal of Applied Physics.* 2008;104(10): 103501.

22. Ohta H, Kamiya M, Kamiya T, Hirano M, Hosono H. UV-detector based on pn-heterojunction diode composed of transparent oxide semiconductors, p-NiO/n-ZnO. *Thin Solid Films.* 2003;445(2): 317–321.
23. Al-Hardan NH, Ahmed NM, Almessiere MA, Aziz AA. Low-intensity UV light sensor based on p-NiO/n-Si heterojunction. *Materials Research Express.* 2020;6(12): 126332.
24. Pham TKH, Tran BQ, Nguyen KB, Pham NYN, Nguyen THY, Nguyen AH-T, Nguyen NP, Ngo HD, Pham HP. Oxygen partial pressure effects on nickel oxide thin films and NiO/Si diode performance. *Materials Advances.* 2025;6(5): 1719–1725.
25. Tsai S-Y, Hon M-H, Lu Y-M. Fabrication of transparent p-NiO/n-ZnO heterojunction devices for ultraviolet photodetectors. *Solid State Electron.* 2011;63(1): 37–41.
26. Gupta RK, Ghosh K, Kahol PK. Fabrication and characterization of NiO/ZnO p–n junctions by pulsed laser deposition. *Physica E: Low-dimensional Systems and Nanostructures.* 2009;41(4): 617–20.
27. San X, Li M, Liu D, Wang G, Shen Y, Meng D, Meng F. A facile one-step hydrothermal synthesis of NiO/ZnO heterojunction microflowers for the enhanced formaldehyde sensing properties. *Journal of Alloys and Compounds.* 2018;739: 260–269.
28. Wei C, Xu J, Shi S, Bu Y, Cao R, Chen J, Xiang J, Zhang X. The improved photoresponse properties of self-powered NiO/ZnO heterojunction arrays UV photodetectors with designed tunable Fermi level of ZnO. *Journal of Colloid and Interface Science.* 2020;577: 279–289.
29. Li C, Feng C, Qu F, Liu J, Zhu L, Lin Y, Wang Y, Li F, Zhou J, Ruan Sh. Electrospun nanofibers of p-type NiO/n-type ZnO heterojunction with different NiO content and its influence on trimethylamine sensing properties. *Sensors and Actuators B: Chemical.* 2015;207: 90–96.
30. Wang T, Liu J, Ma Y, Gu C, Lian J. P-N heterojunction NiO/ZnO electrode with high electrochemical performance for supercapacitor applications. *Electrochimica Acta.* 2021;392: 138976.
31. Tsai SY, Fung KZ. Enhancement of p-NiO/i-ZnO nanorods/n-ZnO ultraviolet detectors through the incorporation of ZnO nanorods. *Journal of Physics and Chemistry of Solids.* 2026;208: 113015.
32. Reddy AM, Reddy AS, Lee K-S, Reddy S. Growth and characterization of NiO thin films prepared by dc reactive magnetron sputtering. *Solid State Sciences.* 2011;13(2): 314–320.
33. Tran BQ, Nguyen KB, Vo NT, Le VT, Do TH, Ngo H, Pham TKH. Effect of limited oxygen gas flux on properties of Al-doped ZnO films. *Dong Thap University Journal of Science.* 2024;13(5): 113–120.
34. Binh NK, Yen Nhi PN, Quan TB, Tam PM, Phuong NN, Tuan DM, Hang PTK, Phuong PH. Impact of in situ heating on the structure, morphology, and electrical and optical properties of RF-sputtered NiO thin films. *Journal of Vacuum Science & Technology B.* 2024;42(6): 062205.
35. Yermakov M, Pshenychnyi R, Opanasyuk A, Klymov O, Mu˜noz-Sanjos´e V. Optical and electrical properties of ZnO/NiO heterojunctions obtained by the spray-pyrolysis method. *Journal of Material Science.* 2024;59: 15738–15751.
36. Chen Z, Dinh HN, Miller E. *UV-vis Spectroscopy. Photoelectrochemical Water Splitting: Standards, Experimental Methods, and Protocols.* New York: Springer; 2013.
37. Ishida Y, Fujimori A, Ohta H, Hirano M, Hosono H. Potential profiling of the nanometer-scale charge-depletion layer in n-ZnO/p-NiO junction using photoemission spectroscopy. *Applied Physics Letters.* 2006;89(15): 153502.
38. Hoai Phuong P, Ngo HD, Bui HT, Phuong NN, Nguyen AHT, Nguyen THY, Tuoi LT, Tran QT, Tuan NM. Effect of sodium doping on characteristics of p-SnOx films prepared by reactive direct current magnetron sputtering. *Ceramics International.* 2022;48(9): 13047–13054.
39. Jlassi M, Sta I, Hajji M, Ben Haoua B, Ezzaouia H. Effect of annealing atmosphere on the electrical properties of nickel oxide/zinc oxide p-n junction grown by sol-gel technique. *Materials Science in Semiconductor Processing.* 2014;26(9): 395–403.
40. Lok R, Dogan MU, Kaya S, Soykan U, Terzioglu C. Gamma radiationinduced modifications in structural, optical, and electrical characteristics of p-NiO/n-Si heterojunction diodes. *Radiation Physics and Chemistry.* 2025;229: 112519.
41. Pham HP, Nguyen THY, Nguyen AH-T, Vo NT, Thuy TGL, Nguyen HH, Hoa HTM, Tran QT. Effects of substrate temperature on characteristics of the p-type Ag-doped SnOx thin films prepared by reactive DC magnetron sputtering. *Journal of Photochemistry and Photobiology A: Chemistry.* 2020;388: 112157.
42. Tyagi M, Tomar M, Gupta V. Trap assisted space charge conduction in p-NiO/n-ZnO heterojunction diode. *Materials Research Bulletin.* 2015;66: 123–131.

43. Gonzalez S, Vescio G, Frieiro JL, Hauser A, Linardi F, Lopez-Vidrier J, Oszajca M, Hernandez S, Ciera A, Garrido B. Inkjet-Printed p-NiO/nZnO Heterojunction Diodes for Photodetection Applications. *Advanced Materials Interfaces.* 2023;10(15): 2300035.
44. Huang J, Li B, Hu Y, Zhou X, Zhang Z, Ma Y, Tang K, Wang L, Lu Y. Transparent p-NiO/n-ZnO heterojunction ultraviolet photodetectors prepared on flexible substrates. *Surface and Coatings Technology.* 2019;362: 57–61.
45. Lin X-Y, Chang H-C, Huang B-L, Lin Y-J. Induced transition from Schottky to ohmic contact in In/n-type Si owing to $(NH_4)_2S_x$ treatment. *Indian Journal of Physics.* 2022;96: 3137–3141.
46. Hakkoum H, Moumen A, Ghougali M, Sengouga N, Comini E. The effect of structural characteristics of ZnO and NiO thin films on the performance of NiO/ZnO photodetectors. *Journal of Materials Science: Materials in Electronics.* 2022;33: 26604–26618.
47. Deng R, Yao B, Li YF, Zhao YM, Li BH, Shan CX, Zhang ZZ, Zhao DX, Zhang JY, Shen DZ, Fan XW. X-ray photoelectron spectroscopy measurement of n-ZnO/p-NiO heterostructure valence-band offset. *Applied Physics Letters.* 2009;94(2): 022108.
48. Grundmann M, Karsthof R, von Wenckstern H. Interface recombination current in type II heterostructure bipolar diodes. *ACS Applied Materials & Interfaces.* 2014;6(17): 14785–14789.

MATERIALS PHYSICS AND MECHANICS RESEARCH ARTICLE

Submitted: November 25, 2023 **Revised: December 14, 2023** **Accepted: February 22, 2024**

Комплексное исследование вязкоупругопластических свойств нанокомпозитов с повышенной износостойкостью на основе Фторопласта-4. Часть 2

А.В. Хохлов [1-3]✉, А.А. Охлопкова [2], С.А. Слепцова [2], Н.Н. Лазарева [2], П.Н. Тарасова [2], А.В. Бабайцев [4], О.С. Вотинова [2], А.В. Шапорев [3], В.В. Гулин [1-3]

[1] НИИ механики МГУ имени М.В. Ломоносова, Москва, Россия

[2] Институт естественных наук, СВФУ им. М.К. Аммосова, Якутск, Россия

[3] Московский центр фундаментальной и прикладной математики, Москва, Россия

[4] Московский авиационный институт (НИУ), Москва, Россия

✉ andrey-khokhlov@ya.ru

АННОТАЦИЯ

Описаны технологии изготовления композитов с повышенной износостойкостью на основе фторопласта-4 (ПТФЭ), полученных введением в качестве наполнителей механоактивированных слоистых силикатов (каолинит, серпентин, бентонит) и шпинели магния, основные результаты по исследованию износостойкости, структуры и химического состава поверхности трения методами электронной микроскопии и ИК-спектроскопии, и данные механических испытаний: семейства кривых растяжения с разными скоростями до разрушения, кривых нагружения и разгрузки с разными скоростями и кривых ползучести и восстановления для разных уровней напряжения, полученные в испытаниях ПТФЭ и шести композитов, дисперсно-наполненных серпентином и шпинелью магния с массовой долей от 1 до 5 %. Проведен первичный анализ выраженности наследственных свойств материалов, в частности скоростной чувствительности, способности к течению при постоянном напряжении, ползучести и восстановлению после разгрузки, и влияния на них состава, состояния и доли наполнителей. Определены базовые характеристики материалов: мгновенный модуль, предел текучести, напряжение и деформация при разрыве в зависимости от скорости нагружения. После механических испытаний на сканирующем электронном микроскопе исследованы изменения микроструктуры ПТФЭ и композитов с разным содержанием наполнителей в зонах разрушения образцов (по сравнению с исходной структурой). При анализе накопленного объема данных испытаний обнаружены высокая деформативность материалов, выраженные наследственные свойства, способность материалов ползти (течь) при постоянной нагрузке и накапливать необратимую (пластическую) деформацию, очень высокая скоростная чувствительность, сильное влияние малых долей наполнителей на структуру и механические свойства. Хотя износостойкость полученных композитов значительно выше, чем ПТФЭ (в 2000 раз), их кривые деформирования качественно мало отличаются от кривых ПТФЭ: на всех кривых есть длинная площадка текучести и стадия упрочнения после нее, напряжения растут с ростом скорости растяжения, причем предел прочности гораздо слабее зависит от скорости, чем предел текучести и деформация при разрушении. В испытаниях на нагрузку-разгрузку обнаружен интересный физический эффект: на кривых разгрузки при достаточно больших максимальных напряжениях продолжается заметный рост деформации и на начальном этапе разгрузки, максимум деформации запаздывает по сравнению с пиком нагружения. Этот "инерционный" эффект свидетельствует о сильно выраженной памяти истории нагружения и наблюдается как у чистого ПТФЭ, так и у всех испытанных композитов.

КЛЮЧЕВЫЕ СЛОВА

политетрафторэтилен • нанокомпозиты • эффекты и модели вязкоупругопластичности, квазистатические испытания • диаграммы деформирования • скоростная чувствительность, кривые нагрузки-разгрузки • кривые ползучести и восстановления • кривые релаксации

Финансирование. *Работа выполнена при поддержке Российского научного фонда (грант № 22-13-20056).*

Citation: Хохлов АВ, Охлопкова АА, Слепцова СА, Лазарева НН, Тарасова ПН, Бабайцев АВ, Вотинова ОС, Шапорев АВ, Гулин ВВ. Комплексное исследование вязкоупругопластических свойств нанокомпозитов с повышенной износостойкостью на основе Фторопласта-4. Часть 2. *Materials Physics and Mechanics*. 2025;53(4): 131–168.
http://dx.doi.org/10.18149/MPM.5342025_11

Systematic all-round examination of the viscoelastoplastic properties of nanocomposites with increased wear resistance based on polytetrafluoroethylene. Part 2

A.V. Khokhlov [1-3]✉, A.A. Okhlopkova [2], S.A. Sleptsova [2], N.N. Lazareva [2], P.N. Tarasova [2], A.V. Babaytsev [4], O.S. Votinova [2], A.V. Shaporev [3], V.V. Gulin [1-3]

[1] Lomonosov Moscow State University, Moscow, Russia

[2] North-Eastern Federal University, Yakutsk, Russia

[3] Moscow Center of Fundamental and Applied Mathematics, Moscow, Russia

[4] Moscow Aviation Institute (National Research University), Moscow, Russia

✉ andrey-khokhlov@ya.ru

ABSTRACT

A description of the technology for manufacturing composites with increased wear resistance based on polytetrafluoroethylene (PTFE) is given. The composites were obtained by introducing mechanically activated layered silicates (kaolinite, serpentine, bentonite) and magnesium spinel as fillers. The main results of the study on wear resistance, structure and chemical composition of the friction surface using electronic microscopy and infrared spectroscopy and mechanical test data are presented, including families of tensile-to-failure curves at different strain rates, loading and unloading curves at different rates, and creep and recovery curves for different stress levels obtained in tests of pure PTFE and six PTFE composites particulate-filled with serpentine and magnesium spinel with a mass fraction ranging from 1 to 5 %. A primary analysis of materials loading history dependence was carried out, in particular: strain rate sensitivity, ability to flow under constant stress, deformability resource and ability to recover after unloading, and the influence of the composition, condition and proportion of fillers. The basic characteristics of materials have been determined: instantaneous modulus, yield strength, stress and strain at failure depending on the loading rate, etc. After examination using a scanning electron microscope, changes in the microstructure of PTFE and composites with different filler contents in the destruction zones of the samples were studied (compared to the original structure). When analyzing the accumulated volume of experimental data, high deformability of materials, pronounced loading history dependence, the ability of materials to creep (flow) under constant load and accumulate irreversible (plastic) strain, very high strain rate sensitivity, and a strong influence of small amounts of fillers on the structure and mechanical properties were discovered. Although the wear resistance of the studied composites is significantly higher than pure polytetrafluoroethylene (about 2000 times), their stress-strain curves are qualitatively little different from the PTFE curves: all curves have a long yield plateau and a hardening stage after it, stress increases with increasing tensile speed, and the tensile strength much less dependent on strain rate than the yield strength and strain at failure. An interesting physical effect is observed in load-unloading tests for sufficiently large given upper stress: a noticeable increase in strain continues at the initial stage of unloading and the maximum strain lags behind the loading peak. This "inertial" effect indicates a pronounced memory of the loading history and is observed both in pure PTFE and in all tested composites based on it.

KEYWORDS
polytetrafluoroethylene • nanocomposites • wear resistance • viscoelastoplastic properties • stress-strain curves family,strain rate sensitivity • failure strains • loading and unloading curves • creep and recovery curves

Funding. *The research was carried out at the expense of a grant from the Russian Science Foundation, No. Russian Science Foundation (Grant No. 22-13-20056).*

Citation: Khokhlov AV, Okhlopkova AA, Sleptsova SA, Lazareva NN, Tarasova PN, Babaytsev AV, Votinova OS, Shaporev AV, Gulin VV. Systematic all-round examination of the viscoelastoplastic properties of nanocomposites with increased wear resistance based on polytetrafluoroethylene. Part 2. *Materials Physics and Mechanics*. 2025;53(4): 131–168. (In Russian)
http://dx.doi.org/10.18149/MPM.5342025_11

Введение

Данная статья – прямое продолжение (вторая часть) статьи [1]. В [1] описаны технологии изготовления композитов с повышенной износостойкостью на основе ПТФЭ с разными мелкодисперсными наполнителями и основные результаты работ по исследованию структуры и химического состава поверхности трения методами электронной микроскопии и ИК-спектроскопии и повышению износостойкости этих материалов за счет образования пленки переноса и вторичных структур в результате трибоокислительных процессов. Описаны цели и система программ квазистатических испытаний полимеров и композитов для всестороннего изучения их вязкоупругопластических свойств (совокупности всех наблюдаемых в испытаниях эффектов), возможности линейного определяющего соотношения (ОС) вязкоупругости

$$\varepsilon(t) = \int_0^t \Pi(t-\tau)\, d\sigma(\tau),\ \sigma(t) = \int_0^t R(t-\tau)\, d\varepsilon(\tau),\ t \geq 0 \qquad (1)$$

и четырех более общих физически нелинейных ОС вязкоупругопластичности с широкими областями применимости [2–13] (одно из которых учитывает взаимное влияние эволюции структуры материала и процесса деформирования [11,12]) по описанию указанных эффектов и методология анализа данных испытаний и выбора адекватных определяющих соотношений для их моделирования. В частности, в [1] рассмотрены признаки физической нелинейности поведения материалов, т.е. индикаторы неприменимости линейного ОС (1) с произвольными функциями ползучести и релаксации $\Pi(t)$ и $R(t)$ (эти материальные функции не независимы, а связаны условием взаимной обратности операторов (1) в виде интегрального уравнения Вольтерры [4,9]), которые можно обнаружить в испытаниях по разным программам нагружения, способы очертить диапазон линейности поведения вязкоупругого материала. Описаны испытания для экспресс-диагностики типа поведения материала, если характеризовать его категориями упругий, вязкоупругий, вязкопластичный, упруговязкопластичный, и методология выбора адекватной модели для описания поведения конкретного материала.

Во второй части статьи приводятся данные испытаний на растяжение по разным программам нагружения образцов ПТФЭ и композитов на его основе: семейства диаграмм растяжения с разными скоростями до разрушения, кривых нагружения и разгрузки с разными скоростями, кривых ползучести и восстановления для разных уровней напряжения. Будет исследована выраженность наследственных свойств материалов (скоростная чувствительность, способность к течению при постоянном напряжении, ресурс деформативности и способность к восстановлению после

разгрузки, особенности кривой разгрузки), определены мгновенный модуль, предел текучести, напряжение и деформация при разрыве в зависимости от скорости нагружения, начат анализ влияния на них состава, доли и размеров частиц наполнителей. Экспериментальные кривые будут сопоставлены с модельными кривыми [1, Рис. 5–16], порождаемыми разными ОС [2–13] при нагружениях по тем же программам.

Задачи всестороннего экспериментального изучения вязкоупругопластических свойств материалов (полимеров, металлов и сплавов, керамик, композитов с разными типами матриц и наполнителей) при разных температурах и режимах нагружения, создания (удобного для пользователей) банка этих свойств в виде наборов кривых испытаний по разным базовым и специальным программам нагружения и наблюдаемых эффектов, а не только нескольких простейших скалярных характеристик (модуль упругости, предел прочности при растяжении, сжатии или изгибе, деформация при разрушении), проблема выбора адекватного определяющего соотношения (ОС) и надежного моделирования процессов деформирования и разрушения, длительной прочности и долговечности вязкоупругопластичных материалов и элементов конструкций с учётом физической и геометрической нелинейностей, наследственности и скоростной чувствительности по-прежнему остаются актуальными в механике, материаловедении и практике инженерных расчётов. Из-за быстрого роста количества новых материалов и моделей для описания их поведения и повышения требований к весу, размерам, удельной прочности, долговечности, надежности и экономичности элементов конструкций и механизмов, первостепенную роль играют вопросы построения или выбора (из сотни существующих) адекватных ОС, анализа и паспортизации их свойств, возможностей и области применимости, сфер влияния их материальных функции (МФ) и феноменологических ограничений на них. С этим вопросами тесно связаны задачи разработки информативных, но экономичных комплексных программ испытаний образцов материала (желательно не слишком длительных и многочисленных), методик определения материальных параметров и функций ОС по их результатам (идентификации) и верификации ОС (см. статьи [2–13] и др., посвященные анализу, аттестации и идентификации линейного ОС (1) и пяти более общих физически нелинейных ОС вязкоупругопластичности с произвольными материальными функциями (МФ).

Политетрафторэтилен (ПТФЭ, фторопласт-4) – широко используемый во всем мире полимер, он обладает большим набором полезных (и во многом уникальных) химических и физико-механических свойств [14–86]: 1) очень низкий коэффициент трения, 2) гидрофобность и отсутствие налипания других материалов, включая и адгезивы, к поверхности изделий из ПТФЭ, 3) низкие водопоглощение и газопроницаемость, высокая стойкость к агрессивным средам, к воздействию воды, света, УФ-излучения, природных загрязнений, 4) высокие деформативность и пластичность (обеспечивающие широкое применение ПТФЭ в качестве материала для уплотнений и герметиков [14–22,26,27]), 5) физиологическая нейтральность, 6) сохранение многих ценных физико-механических свойств и возможность эксплуатации при низких и криогенных температурах (от -260 до +260 С) [20,22,24,27]. Благодаря этим свойствам ПТФЭ имеет широкий спектр приложений в разных

отраслях промышленности и техники: машиностроении, транспорте углеводородов, строительстве, электротехнике, медицине, пищевой, швейной, химической промышленности, военной и аэрокосмической технике. ПТФЭ особенно эффективен в качестве уплотнительного и триботехнического материала [14–22,26,27,31–86].

Из-за низкого коэффициента трения ПТФЭ широко применяется в качестве основы композитов для изготовления деталей самых ответственных узлов трения (подшипников, опор мостов и т.п). [14,17,20,22,31–86]. Он не заменим в узлах «сухого» трения, поскольку не только имеет низкий коэффициент трения по стали, но и обладает самосмазывающими свойствами. Одно из основных преимуществ ПТФЭ и КМ на его основе перед другими полимерами – обеспечение работоспособности узла трения без применения смазки в условиях циклического образования и удаления пленки переноса [85]. Детали, изготовленные на основе таких КМ, имеют меньшую массу и снижают транспортные расходы, не боятся низких температур и агрессивных сред, работают практически бесшумно, обладают демпфирующей способностью, повышают надежность и долговечность (хорошо спроектированных) узлов машин.

Однако у ПТФЭ есть и недостатки: он обладает низкой износостойкостью, большим коэффициентом линейного термического расширения, высокой деформативностью (это свойство полезно в применениях ПТФЭ в качестве уплотнений и герметиков, но вредно во многих других областях применения) и быстро накапливает пластическую деформацию как при постоянной, так и при циклической нагрузках: подвержен ползучести (хладотекучести) и рэтчетингу даже при небольших нагрузках в нормальных условиях. Для улучшения свойств и расширения области применения в ПТФЭ вводят разные наполнители [17–86]: углеродные и стеклянные волокна, оксиды металлов, силикаты, детонационные наноалмазы, порошки бронзы, дисульфида молибдена, графита, кокса, слюды, меди, нитрида бора. Большинство промышленно выпускаемых материалов на основе ПТФЭ – композиции с высокой долей наполнителей (более 15–30 %), что приводит к избыточному повышению жесткости и хрупкости материала. На рынке России широко представлены следующие марки КМ на основе ПТФЭ: Ф-4К20, Ф-4К20М5, Ф4С15, Флубон-15 и Флубон-20 [22,26,32]. Эти высоконаполненные КМ обладают повышенными износостойкостью (до 1000 раз по сравнению с исходным ПТФЭ) и модулем упругости, но значительно меньшей податливостью и ресурсом деформативности, что снижает их эффективность в уплотнениях.

В работах [34,36,65–81] показано, что заметное повышение износостойкости достигается при введении малого количества (до 5 %) наполнителей (серпентин, каолинит, вермикулит, бентонит, цеолит, оксид алюминия, оксид магния, оксид кремния, базальтовое волокно, углеродное волокно) при этом деформационно-прочностные характеристики получаемого КМ сохраняются на уровне чистого ПТФЭ или повышаются (см. ниже). В работах [65–70,73,74,76–80] показано, что введение минеральных слоистых силикатов в ПТФЭ приводит к снижению износа в 700–2000 раз.

Волокнистые наполнители придают КМ на основе ПТФЭ прочность, жесткость и износостойкость [51]. В работах [70–72,77] установлено, что введение 5 % коротких углеродных волокон повышает износостойкость КМ в 70–80 раз по сравнению с исходным ПТФЭ. Основной недостаток углеродного волокна – его высокая цена (в зависимости от типа и качества углеродного волокна, от спроса на него в разных

сегментах рынка его цена может существенно различаться). А сырье для производства может быть в 5–25 раз дороже, чем у стекловолокна. Возможный более дешевый наполнитель для ПТФЭ – базальтовые волокна [50,81]: они обладают высокими механическими характеристиками и термической и химической стойкостью, но технология их производства значительно проще и менее энергоемка, сырье (природного происхождения) не ограничено и значительно дешевле, а отработавшие волокна не загрязняют окружающую среду. Первые испытания показали [81], что введении 5 % коротких базальтовых волокон (диаметром 8–10 мкм) снижает износ КМ в 55 раз по сравнению с ПТФЭ.

Необходимость освоения регионов Арктики рождает повышенный спрос на разработку и применение в технических устройствах морозостойких материалов с длительным сроком службы. ПТФЭ и разрабатываемые КМ на его основе очень перспективны для решения этих задач. Перспективным представляется и сочетание указанных наполнителей с методом радиационной модификации ПТФЭ облучением малыми дозами в расплаве (чуть выше температуры плавления кристаллитов 327 °С), которое изменяет надмолекулярную структуру ПТФЭ [41,42,46,83]; работа в этом направлении ведется в сотрудничестве с С.А. Хатиповым. Таким образом, создание КМ на основе ПТФЭ с улучшенным комплексом эксплуатационных свойств представляет большой научный и практический интерес. Исследования КМ на основе ПТФЭ, применение новых наполнителей для повышения физико-механических свойств и развитие технологий изготовления КМ – важные задачи, решение которых требует комплексного подхода, включающего материаловедческие, технологические, механико-математические и экономические аспекты.

Эта работа – вводная статья цикла статей, посвященных всестороннему экспериментальному исследованию вязкоупругопластических свойств и моделированию поведения фторопласта-4 и нескольких семейств КМ с повышенной износостойкостью на его основе, полученных в последние 20 лет в лабораториях "Технологии полимерных нанокомпозитов" и "Полимерные композиты для Севера" Северо-Восточного федерального университета им. М.К. Аммосова введением в качестве наполнителей слоистых силикатов (механоактивированные каолинит и серпентин, шпинель магния) и коротких базальтовых или углеродных волокон [34,36,65–81]. В данном цикле из 8–10 статей внимание будет сосредоточено на системном исследовании всего комплекса вязкоупругопластических свойств ПТФЭ и указанных нанокомпозитов (а не их отдельных характеристик) и разработке системы программ квазистатических термомеханических испытаний, позволяющих получить максимально полную информацию о реологических свойствах исследуемых материалов (которые в дальнейшем будут использованы для паспортизации КМ и подбора определяющего соотношения и моделирования их деформирования и разрушения [2–13,87–93]). В данной статье, составляющей с [1] единое целое, приведена часть полученных за последние три года данных испытаний образцов ПТФЭ и КМ на его основе: семейства диаграмм растяжения с разными скоростями до разрушения, кривых нагружения и разгрузки с разными скоростями, кривых ползучести и восстановления для разных уровней напряжения. В дальнейшем будет подробно представлен весь накопленный объем данных испытаний и обнаруженных эффектов, будут детально проанализированы и сопоставлены семейства кривых

деформирования при растяжении нескольких семейств КМ, кривые нагружения и разгрузки, их скоростная чувствительность и зависимость от температуры, кривые ползучести и восстановления при разных уровнях напряжения и температуры и проведен сравнительный анализ структурных изменений исследуемых КМ под действием разных программ нагружения. По семействам построенных кривых деформирования, нагружения и разгрузки и ползучести, и восстановления будет осуществляться выбор и проверка индикаторов применимости к описанию деформирования исследуемых материалов пяти физически нелинейных ОС вязкоупругопластичности, построенных и детально изученных ранее в цикле статей [2–13,91,92] и др.

Результаты испытаний образцов ПТФЭ на растяжение до разрыва

Целесообразно начать экспериментальные исследования с испытаний ПТФЭ и КМ на растяжение по программе $\varepsilon(t) = at$ до разрушения образца и построения ДД с постоянными скоростями, точнее – с разными постоянными скоростями движения траверсы, поскольку (минимальные и максимальные) напряжения и деформации при разрушении послужат важными ориентирами при планировании испытаний без разрушения образца, при выборе параметров более сложных программ нагружений (на нагрузку-разгрузку, ползучесть и восстановление, ступенчатое и циклическое нагружение и др. – см. Рис. 6–16 статьи [1]). По результатам этих испытаний можно исследовать наличие площадки текучести, оценить жесткость, прочность, ресурс пластичности материала и его скоростную чувствительность [88]: выраженность зависимости диаграмм, мгновенного и касательного модуля, предела текучести, напряжения и деформации при разрушении от скорости деформирования (скорости движения захвата) при фиксированных величинах температуры; исследовать существование (ненулевой) равновесной диаграммы (предельной при скорости деформирования, стремящейся к нулю) [1,88,90,92].

В 2022–2023 гг. А.В. Хохловым, А.В. Бабайцевым и О.С. Вотиновой проведены нескольких серий квазистатических испытаний на растяжение с постоянными скоростями движения траверсы (до разрушения) образцов из чистого ПТФЭ и девяти композитов на его основе с повышенной износостойкостью, полученных в последние годы в СВФУ им. М.К. Аммосова введением в качестве наполнителей слоистых силикатов (механоактивированные каолинит и серпентин), шпинели магния и коротких углеродных или базальтовых волокон [34,36,65–81]. Образцы имели форму лопаток с длиной рабочей части 70 мм, толщиной 3 ± 0.1 мм и (средней) площадью поперечного сечения 31.8 ± 0.8 мм^2. Испытания проводились на универсальной электромеханической машине Instron 5969, снабженной программным обеспечением Bluehill, контактным экстензометром Instron 2620-602 SN:3301 и видеоэкстензометром (2663-821 SN:5478) с полем обзора 60 × 500 мм^2. Использовался датчик нагрузки с 50kN 2210-920 Expansion Channel Module, по измеренному усилию вычислялось номинальное напряжение σ делением на начальную площадь сечения. Применялись пневматические захваты бокового действия с губками 25 × 25 мм^2 с прорезиненной поверхностью. Нагружение проводилось с постоянными скоростями движения траверсы V = 0.6; 6; 60; 600 мм/мин и

V = 1; 15; 150; 300; 450; 600 мм/мин. Для измерения деформации видео-экстензометром на образце ставились метки по стандартному трафарету с базой равной 20 мм. Перед испытанием осуществлялось предварительное нагружение до 7 Н, при этой нагрузке проводилась балансировка всех средств измерений (ASTM E4, DIN 51221, ISO 75001).

Результаты испытаний ПТФЭ со скоростями V = 0.6; 6; 60; 600 мм/мин (средние по времени и рабочей части образца скорости деформации: a = 0.143; 1.43; 14.3; 143·10^{-3} с$^{-1}$), приведены на Рис. 1: начальные участки графиков номинального напряжения от времени $\sigma(t,a)$ (Рис. 1(a)) и зависимости напряжения от деформации, т.е. диаграммы деформирования (ДД) $\sigma(\varepsilon,a)$, которые получаются исключением параметра $t = \varepsilon/a$ в зависимостях $\sigma(t,a)$ с Рис. 1(a). На всех ДД есть длинная площадка текучести и стадия упрочнения после нее. С увеличением скорости растяжения графики $\sigma(t,a)$ и ДД $\sigma(\varepsilon,a)$ смещаются вверх (напряжения растут), значительно уменьшается абсолютное удлинение при разрыве и время при разрыве. Деформации и напряжения в момент разрыва ε_* и σ_* и пределы текучести видны на Рис. 1: $\sigma_*(a)$ практически не зависит от a и лежит в диапазоне 18 ÷ 20 МПа, предел текучести сильно зависит и монотонно возрастает по a (на 70 %), а $\varepsilon_*(a)$ убывает по a (почти в 2 раза). Время до разрыва при V = 0.6 мм/мин (черная кривая) составило 27600 с, при V = 6 мм/мин(голубая кривая) – 2108 с, при V = 60 мм/мин (красная кривая) –172 с, а при V = 600 мм/мин (зеленая кривая) – 14.7 с.

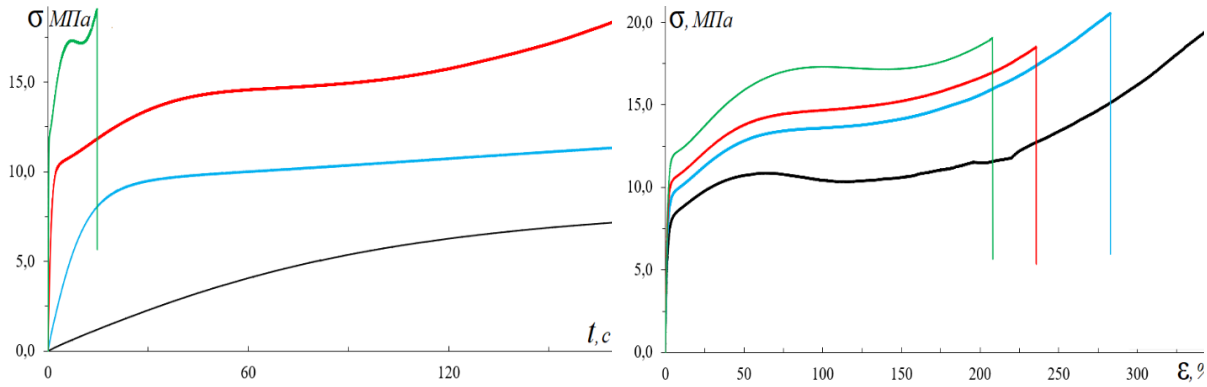

Рис. 1. Начальные участки графиков σ(*t*,*a*) (a) и диаграммы деформирования σ(ε,*a*) (b) образцов ПТФЭ для скоростей траверсы V = 0.6; 6; 60; 600 мм/мин (черная, синяя , красная и зеленые кривые), т.е. для средних по времени и рабочей части образца скоростей деформации a = 0.14; 1.4; 14; 143·10^{-3} 1/с

Fig. 1. Initial sections of the graphs σ(*t*,*a*) (a) and stress-strain curves σ(ε,*a*) (b) of PTFE samples at crosshead speeds V = 0.6; 6; 60; 600 mm/min (black, blue, red, and green curves), i.e., for average strain rates a = 0.14; 1.4; 14; 143·10^{-3} 1/s

Проведены еще 14 испытаний образцов-лопаток ПТФЭ на растяжение до разрыва со скоростями траверсы V = 0.6; 6; 60; 600 мм/мин (соответствующие средние по времени и рабочей части образца скорости деформации: a = 0.14; 1.4; 14; 143·10^{-3} с$^{-1}$). По полученным данным были построены таблица всех размеров образцов до и после испытаний (не приводится в этой статье), Табл. 1 с временами, нормальными силами, деформациями, номинальными и истинными напряжениями в момент разрыва $(t_*,\varepsilon_*,P_*,\sigma_*,s_*)$ в зависимости от скорости траверсы V, графики напряжения $\sigma(t,a)$ (Рис. 2(a,b)) и ДД $\sigma(\varepsilon,a)$ (Рис. 3).

Таблица 1. Времена, деформации и напряжения при разрыве образца ПТФЭ в зависимости от скорости *V*

№ испытания	V мм/мин	t_* с	Δl_* мм	P_* Н	σ_* МПа	ε_* %	s_* МПа
1	0.6	27600.0	276.0	614.0	19.5	344.0	86.6
2	1.0	17556.0	293.0	613.0	18.0	267.0	66.1
3	1.0	15125.0	252.0	515.0	16.4	343.0	72.7
4	6,0	2108.0	211.0	630.0	20.5	283.0	78.5
5	15.0	820.0	205.0	521.0	16.5	281.0	62.9
6	60,0	171.0	172.0	567.0	18.5	236.0	62.2
7	150.0	78.7	197.0	582.0	18.3	284.0	70.3
8	150.0	84.2	211.0	598.0	18.9	251.0	66.4
9	150.0	60.7	152.0	480.0	15.9	134.0	37.2
10	300.0	44.1	206.0	491.0	15.5	236.0	52.1
11	450.0	27.8	209.0	537.0	16.6	249.0	57.9
12	450.0	24.4	183.0	581.0	18.1	255.0	64.3
13	450.0	28.9	217.0	611.0	18.7	226.0	62.9
14	600.0	14.9	148.0	586.0	18.0	203.0	54.5
15	600.0	16.1	160.0	501.0	15.9	94.0	30.8
16	600.0	19.6	196.0	586.0	19.5	260.0	70.2
17	600.0	21.6	215.0	641.0	20.4	255.0	72.4
18	600.0	14.7	147.0	593.0	19.1	209.0	59.0

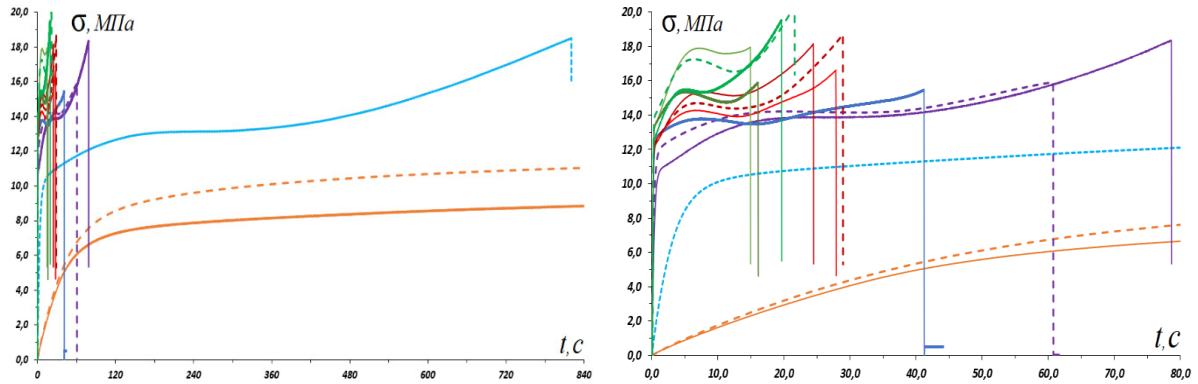

(a) (b)

Рис. 2. График зависимостей σ(*t*,*a*) в зависимости от скорости: (а) в интервале до 840 с (до разрушения образца при *V* = 15 мм/мин), (б) до 80 с (увеличены σ(*t*,*a*) при больших скоростях)

Fig. 2. Graph of the dependences σ(*t*,*a*) with different strain rates: (a) in the interval up to 840 s (until the specimen failure at *V* = 15 mm/min), (b) – up to 80 s (magnified graphs σ(*t*,*a*) at higher strain rates)

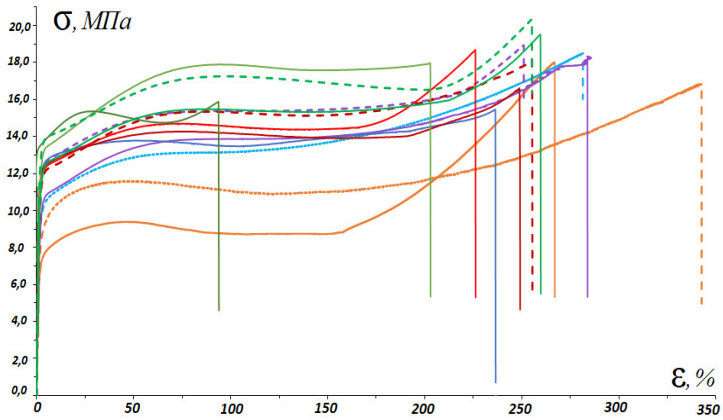

Рис. 3. Диаграммы деформирования ПТФЭ σ(ε,*a*) со скоростями *a* = 0.23; 3.6; 36; 71; 107; 143·10^{-3} 1/с

Fig. 3. Stress-strain curves of PTFE σ(ε,*a*) at strain rates *a* = 0.23; 3.6; 36; 71; 107; 143·10^{-3} 1/s

У образцов ПТФЭ в опыте на одноосное растяжение до разрыва наблюдается большое относительное удлинение: от 200 до 340 % (см. Табл. 1 и Рис. 2, 3). С увеличением скорости растяжения графики $\sigma(t,a)$ и ДД $\sigma(\varepsilon,a)$ смещаются вверх (напряжения растут, растет и предел текучести), значительно уменьшаются удлинение Δl_*, деформация $\varepsilon_*(a)$ и время t_* при разрыве.

Номинальное напряжение $\sigma_*(a)$ при разрыве у всех испытанных образцов находится в диапазоне $15.5 \div 20.0$ МПа (среднее значение равно 18 МПа), $\sigma_*(a)$ практически не зависит от a (Рис. 1, 3). Истинное напряжение при разрыве $s_* = (\varepsilon_* + 1)\sigma_*$ изменяется в диапазоне 55–87 МПа (среднее по образцам убывает с ростом a и стабилизируется на уровне 60 МПа при $V \geq 15$ мм/мин, т.е. $a \geq 3.6{\cdot}10^{-3}$ с$^{-1}$). При малой скорости траверсы $V = 1$ мм/мин ($a \geq 2.3{\cdot}10^{-4}$ с$^{-1}$) время и деформация при разрушении очень велики: деформация при разрыве ($\varepsilon_* \approx 340$ %) – почти в два раза больше, чем при $V = 600$ мм/мин ($\varepsilon_* \approx 200$ %), а время при разрыве двух образцов равно 15125 с (более 4 ч) и 17556 с (около 5 ч), т.е. в 20 раз больше, чем для $V = 15$ мм/мин (голубая кривая), почти в 250 раз больше, чем для $V = 150$ мм/мин (фиолетовые кривые), в 850 раз больше, чем для $V = 450$ мм/мин (три красные кривые), и почти в 1000 раз больше, чем при $V = 600$ мм/мин ($a \geq 0.143$ с$^{-1}$, зеленые кривые), когда оно лежит в диапазоне от 15 до 21 с (см. четыре последних строки Табл. 1). Поэтому на Рис. 2(a) две оранжевые кривые для $V = 1$ мм/мин обрезаны при $t = 840$ с (они качественно похожи на голубую кривую для $V = 15$ мм/мин с временем разрыва 820 с: после локального максимума и течения при почти постоянном напряжении наблюдается длинный участок упрочнения пред разрывом). На Рис. 2(b) приведены те же графики $\sigma(t,a)$, но на интервале до 80 с, чтобы увеличить графики при больших скоростях.

На Рис. 1(b) и Рис. 3 приведены диаграммы деформирования ПТФЭ $\sigma(\varepsilon,a)$ (после исключения параметра t в зависимостях $\sigma(t,a)$ с Рис. 2). На них наблюдаются три характерных участка: возрастающий выпуклый вверх до локального максимума (вязкоупругий), длинный почти горизонтальный участок течения при постоянном напряжении (площадка текучести) при всех скоростях и возрастающий выпуклый вниз участок ускоренного упрочнения (особенно выраженный при малых скоростях). Отметим, что ДД, перестроенные в истинных напряжениях и деформациях $s = (\varepsilon + 1)\sigma$, $p = ln(\varepsilon + 1)$ (они будут проанализированы в последующих статьях цикла), монотонно возрастают (не имеют локальных максимума и минимума), но сохраняют выраженную площадку текучести и точку перегиба в начале участка упрочнения.

Таким образом, в испытаниях первой серии установлена высокая деформативность ПТФЭ во всем диапазоне квазистатических скоростей деформации (кратность растяжения до 4.5 при скоростях $a = 1.4{\cdot}10^{-4}$ и $a = 1.4{\cdot}10^{-4}$ с$^{-1}$, кратность растяжения около 3 при $a = 0.143$ с$^{-1}$), выраженные наследственные свойства, способность к течению при постоянной нагрузке и накоплению большой необратимой (пластической) деформации и очень высокая скоростная чувствительность материалов: при увеличении скорости растяжения ПТФЭ в 600 раз измеряемые напряжения (в частности, пределы текучести) увеличились примерно на 70–80 % (при одинаковых деформациях), а деформация при разрушении ε_* уменьшилась почти в два раза (с 340 до 200 %). Высокая скоростная чувствительность тормозит и останавливает локализацию деформации, задерживает и останавливает развитие

шейки и обеспечивает выраженную площадку текучести, довольно длительный участок упрочнения за ней и, в итоге, большой ресурс пластичности (большую деформацию при разрушении). Структурные корни этих свойств (и накопления необратимой деформации при ползучести и циклическом нагружении с малыми нагрузками – см. ниже) – ламеллярное строение кристаллитов ПТФЭ и низкая прочность кристаллитов на сдвиг (и растяжение), из-за которой кристаллиты не могут препятствовать развитию деформации (скольжению и перестройкам фибрилл). Деформативность материалов является преимуществом при использовании в уплотнениях, но это недостаток, если применять ПТФЭ в узлах трения скольжения, где необходимы достаточная жесткость и высокая износостойкость. Измеренные в этой серии испытаний напряжение и деформация при разрыве (диапазоны их изменения в зависимости скорости растяжения – см. Табл. 1) служат важными ориентирами при задании параметров более сложных программ нагружений в последующих сериях испытаний (испытания на ползучесть и восстановление, на нагрузку-разгрузку-восстановление и др. – см. ниже).

Результаты испытаний композитов на основе ПТФЭ на растяжение до разрыва

Проведены испытания на растяжение с разными скоростями до разрыва образцов-лопаток из шести КМ на основе ПТФЭ с шестью разными содержаниями наполнителей: образцы материалов КМс-1, КМс-2, КМс-5 содержали 1, 2 или 5 % серпентина (по массе), а в образцы материалов КМсш-1, КМсш-2, КМсш-5 была добавлена еще шпинель магния (суммарное содержание наполнителей – 1, 2 и 5 %) и они имели состав: КМсш-1: ПТФЭ + С 0.9% + ШМ 0.1%; КМсш-2: ПТФЭ + С 1.5% + ШМ 0.5%; КМсш-3: ПТФЭ + С 3.8% + ШМ 1.2% (ШМ – шпинель магния, С – серпентин). Исходные материалы и технология изготовления этих дисперсно-наполненных КМ, исследование их коэффициентов трения, скоростей износа, структуры и химического состава поверхности трения методами электронной микроскопии и ИК-спектроскопии, влияния добавок микроскопии и ИК-спектроскопии, влияния добавок шпинели магния на ИК-спектры композитов с серпентином, на ускорение трибоокислительных процессов и значительное снижение износа композитов приведены в первой части статьи [1].

По данным испытаний на растяжение были построены таблица всех размеров образцов до и после испытаний, таблица с временами, нормальными силами, деформациями, номинальными и истинными напряжениями в момент разрыва $(t_*,\varepsilon_*,P_*,\sigma_*,s_*)$ в зависимости от скорости траверсы V, аналогичная Табл. 1 (они не приводится в этой статье для краткости), и графики напряжения от времени $\sigma(t,a)$ (Рис. 4, 6) и ДД $\sigma(\varepsilon,a)$ (Рис. 4–7).

На Рис. 4 приведены начальные участки графиков $\sigma(t,a)$ (Рис. 4 (a,c,e)) и ДД $\sigma(\varepsilon,a)$ (Рис. 4(b,d,f)) материалов КМс-1, КМс-2, КМс-5 для скоростей V = 0.6; 6; 60; 600 мм/мин (черная, синяя, красная и зеленая кривые – как на Рис. 1), т.е. для средних по времени и рабочей части образца скоростей деформации a = 0.143; 1.43; 14.3; 143·10^{-3}с$^{-1}$: (a,b) КМс-1, (c,d) КМс-2, (e,f) КМс-5 (на этих рис. приведены две черные кривые по результатам двух испытаний с минимальной скоростью).

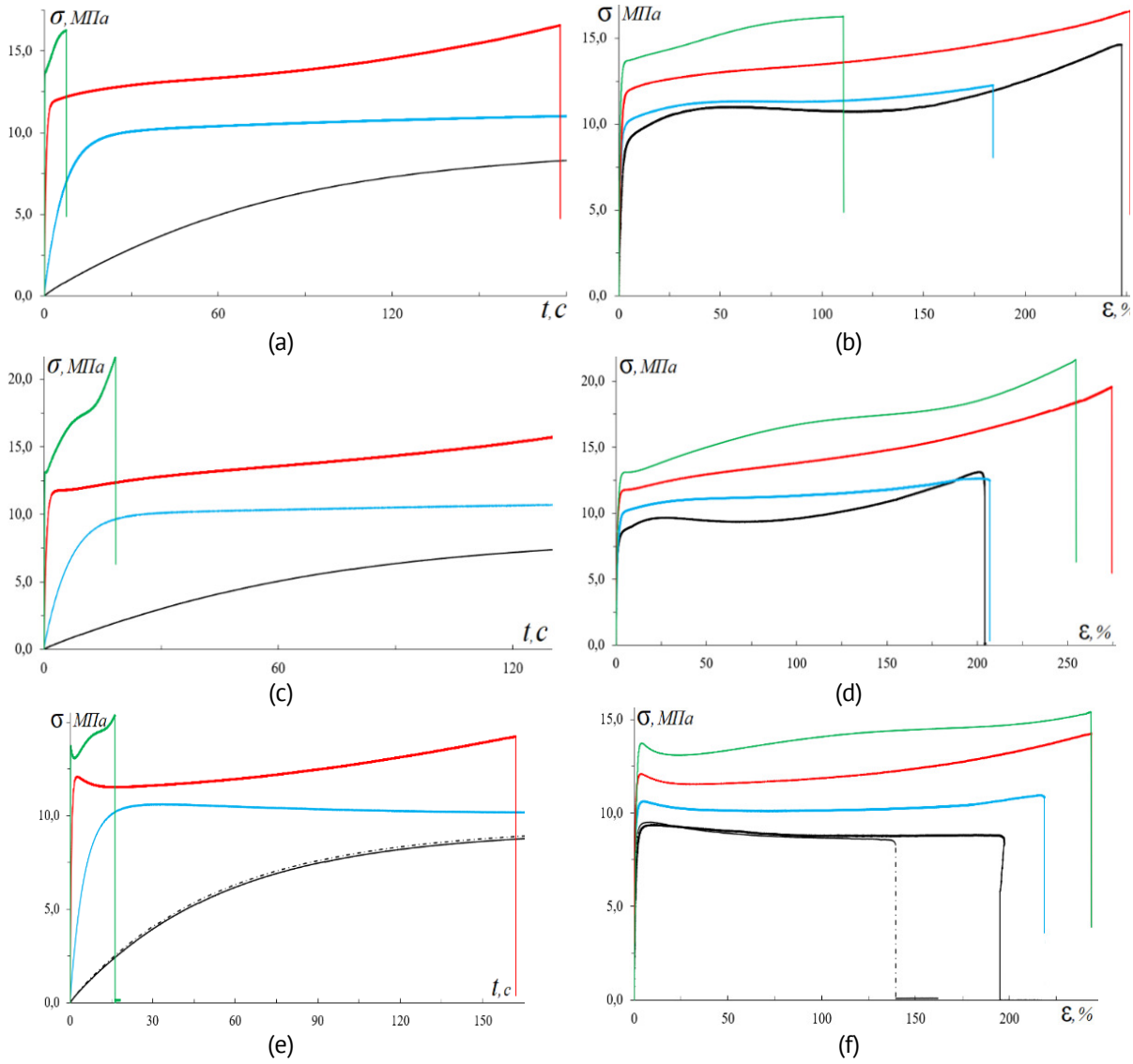

Рис. 4. Начальные участки графиков σ(*t*,*a*) (a,c,e) и диаграммы деформирования σ(ε,*a*) (b,d,f) композитов с серпентином КМс-1, КМс-2, КМс-5 для 4 скоростей траверсы *V* = 0.6, 6, 60, 600 мм/мин (черная, синяя, красная и зеленые кривые), т.е. для средних скоростей деформации *a* = 0.14; 1.4; 14; 143·10^{-3} 1/с: (a,b) КМс-1, (c,d) КМс-2, (e,f) КМс-5

Fig. 4. Initial sections of the graphs σ(*t*,*a*) (a,c,e) and stress-strain curves σ(ε,*a*) (b,d,f) of composite CMs-1, CMs-2, CMs-5 samples (PTFE filled with 1, 2 or 5% of serpentine) at crosshead speeds *V* = 0.6, 6, 60, 600 mm/min (black, blue, red, and green curves), i.e., for average strain rates *a* = 0.14; 1.4; 14; 143·10^{-3} 1/s: (a,b) CMs-1, (c,d) CMs-2, (e,f) CMs-5

На всех ДД есть длинная площадка текучести и стадия упрочнения после нее, как и у ПТФЭ (Рис. 3). С увеличением скорости растяжения графики $\sigma(t,a)$ и ДД $\sigma(\varepsilon,a)$ смещаются вверх (напряжения растут, жесткость материалов повышается, растет предел текучести), значительно уменьшается время при разрыве (как у чистого ПТФЭ).

Деформации и напряжения в момент разрыва $\varepsilon_*(a)$ и $\sigma_*(a)$ видны на Рис. 4(b,d,f) и Рис. 5. Предел прочности $\sigma_*(a)$ у всех КМ при всех скоростях немного ниже, чем у ПТФЭ, и демонстрирует тенденцию к повышению с ростом *a* (у КМс-1 наблюдается немонотонность $\sigma_*(a)$) особенно ярко выраженную у КМс-5, у которого $\sigma_*(a)$ возрастает от 9 до 15 МПа (у чистого ПТФЭ он слабо зависит от *a* и у всех образцов

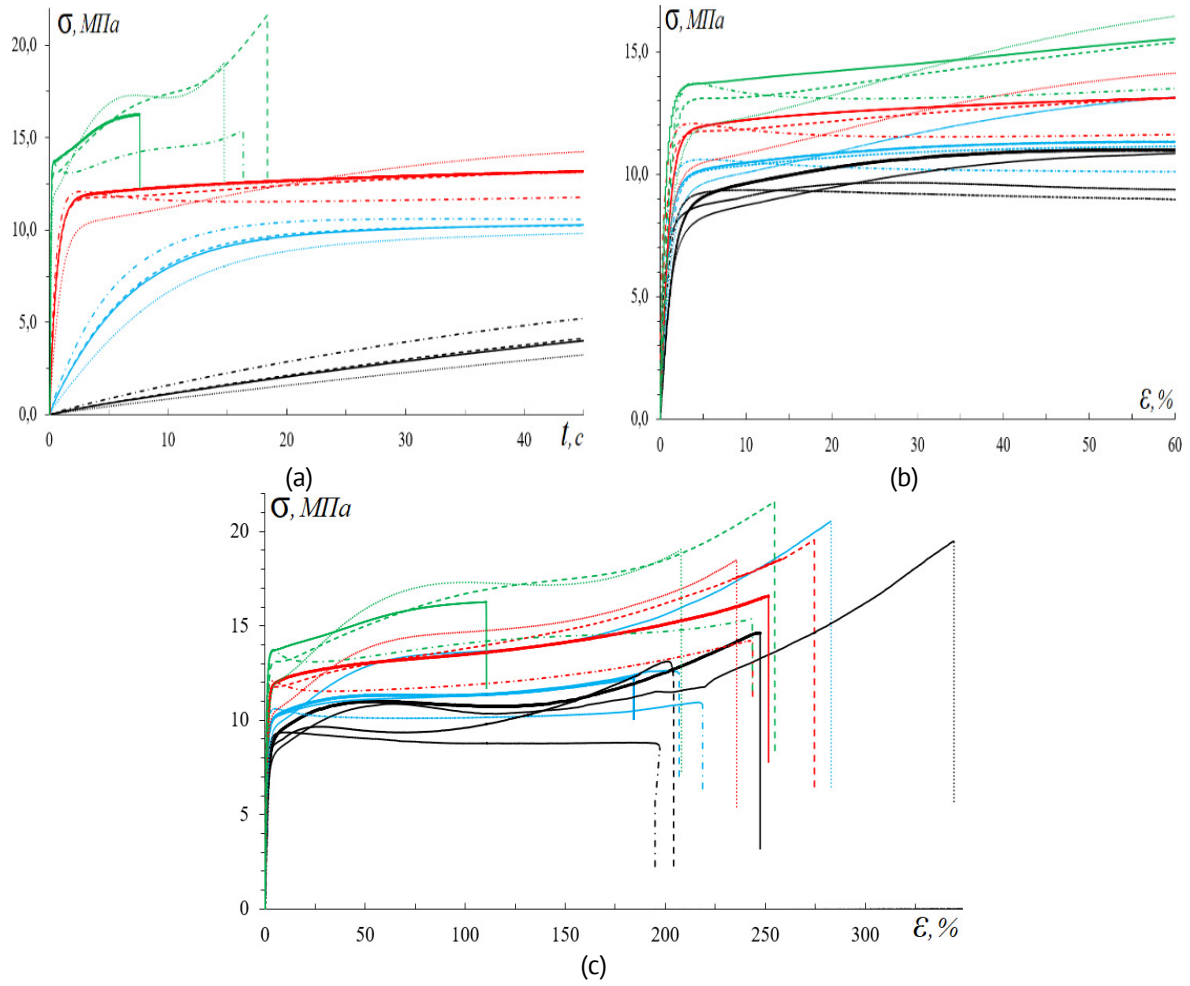

Рис. 5. Сравнение начальных участков графиков σ(*t*,*a*) (a) и диаграмм деформирования σ(ε,*a*) (b,c) чистого ПТФЭ (пунктирные линии) и композитов КМс-1, КМс-2 и КМс-5 (сплошные, штриховые и штрих-пунктирные линии) с разными долями серпентина для 4 скоростей траверсы *V* = 0.6, 6, 60, 600 мм/мин (черные, синие, красные и зеленые кривые

Fig. 5. Comparison of initial sections of the graphs σ(*t*,*a*) (a) and stress-strain curves σ(ε,*a*) (b,c) of pure PTFE (dot lines) and composites CMs-1, CMs-2, and CMs-5 (solid, dashed, and dash-dotted lines) at crosshead speeds *V* = 0.6, 6, 60, 600 mm/min

находится в диапазоне 15÷20 МПа – Рис. 1, 3). При этом предел текучести у ПТФЭ и всех КМ монотонно возрастает с увеличением *a* на 40–60 % (Рис. 4, 5). Деформация при разрыве $\varepsilon_*(a)$ ведет себя по разному с ростом скорости растяжения, в зависимости от содержания серпентина: у чистого ПТФЭ $\varepsilon_*(a)$ убывает по *a* от 340 до 220 % (см. Рис. 1, 3 и Табл. 1), у КМс-2 и КМс-5 – наоборот возрастает от 200 до 250 % (Рис. 4(d,f)), а у КМс-1 функция $\varepsilon_*(a)$ немонотонна (ныряет вниз при $a = 0.0014 \cdot c^{-1}$ и при $a = 14 \cdot c^{-1}$ – см. Рис. 4(b)). Зависимость $\varepsilon_*(a)$ КМ и влияние на нее доли наполнителя требует изучения в большем количестве опытов, сбора и обработки статистики. Время до разрыва при *V* = 0.6 мм/мин составило 21700 с для образца КМс-1 (на 20 % меньше, чем у чистого ПТФЭ: 27600 с), 22880 с для образца КМс-2, 9140 с для образца КМс-5. Времена до разрыва при *V* = 6 мм/мин (голубые ДД) для КМс-1, КМс-2 и КМс-5 составили 1050, 1543 и 1406 с, т.е. на 25–50 % меньше, чем уПТФЭ (2108 с), а при *V* = 60 мм/мин – 178, 206 и 162 с, что почти совпадает с

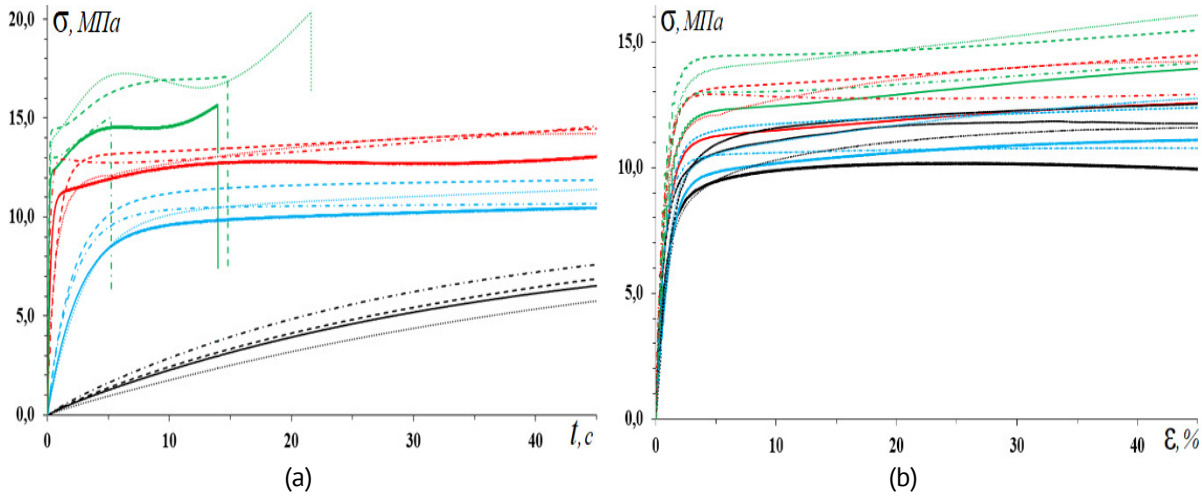

Рис. 6. Сравнение начальных участков графиков σ(*t*,*a*) (a) и диаграмм деформирования σ(ε,*a*) (b) ПТФЭ и композитов КМсш-1, КМсш-2, КМсш-5 с разным содержанием серпентина и шпинели магния для 4 скоростей траверсы *V* = 1, 15, 150, 600 мм/мин (черная, синяя, красная и зеленые кривые), т.е. для средних скоростей деформации *a* = 0.14, 1.4, 14, 143·10^{-3} с$^{-1}$

Fig. 6. Comparison of initial sections of the graphs σ(*t*,*a*) (a) and stress-strain curves σ(ε,*a*) (b) of PTFE and composites CMsMsp-1, CM-2sMsp, and CMsMsp-5 with different contents of serpentine and magnesium spinel (0.9+0.1%, 1.5+0.5% or 3.8+1.2%) for four crosshead speeds *V* = 1, 15, 150, 600 mm/min (black, blue, red, and green curves), i.e., for average strain rates *a* = 0.14, 1.4, 14, 143·10^{-3} 1/s

временем разрыва ПТФЭ, равным 172 с (соответственно близки и деформации при разрыве: 252, 259, 244 и 246 %). При *V* = 600 мм/мин времена до разрыва 7.6, 18.4, 16.3 и 14.7 с, а деформации – 111, 255, 245 и 209 %.

На сводном Рис. 5 совмещены для сравнения начальные участки графиков $\sigma(t,a)$ (a) и ДД $\sigma(\varepsilon,a)$ (Рис. 5(b,c)) при скоростях *V* = 0.6; 6; 60; 600 мм/мин (черные, синие, красные и зеленые кривые – как и на Рис. 1 и 4) для образцов из четырех материалов с разной долей серпентина: чистого ПТФЭ (пунктирные линии), КМс-1, (сплошные линии), КМс-2 (штриховые), КМс-5 (штрих-пунктирные линии). На Рис. 5(c) приведены полные ДД до разрушения, а на Рис. 5(b) увеличены их начальные участки (по ним можно качественно оценить зависимость мгновенного модуля и предела текучести от скорости и от содержания наполнителя).

Композиты КМс-1, КМс-2 и КМс-5 с серпентином не уступают ПТФЭ в деформативности при скоростях деформации, больших *a* = 0.014 с$^{-1}$ (красные и зелены ДД на Рис. 5), но проигрывают по величине $\varepsilon_*(a)$ 20–50 % в диапазоне скоростей $a \le 0.0014$ с$^{-1}$ (черные и синие ДД на Рис. 5). Все КМ уступают ПТФЭ по прочности в диапазоне скоростей $a \le 0.0014$ с$^{-1}$, где у них $\sigma_*(a) < 12$ МПа, что примерно на 30–40 % ниже, чем у ПТФЭ. В диапазоне $a \le 0.0014$ с$^{-1}$ отличие по величине $\sigma_*(a)$ не превосходит 20–25 %. Самыми прочными оказались образцы КМс-2 (Рис. 4(d)), в диапазоне скоростей $a \le 0.0014$ с$^{-1}$ они даже превзошли ПТФЭ как по $\varepsilon_*(a)$, так и по $\sigma_*(a)$. При увеличении доли серпентина до 5 % $\varepsilon_*(a)$ практически не изменилась (Рис. 5(c)), предел прочности $\sigma_*(a)$ понизился на 20–30 % при всех скоростях растяжения, а на ДД появился "зуб текучести" (Рис. 4(f) и 5(b)), которого не было у ПТФЭ и остальных КМ. Деформации и напряжения в момент разрыва $\varepsilon_*(a)$ и $\sigma_*(a)$ образцов КМсш-1, КМсш-2, КМсш-5 видны на Рис. 7. Они меняются примерно в том же диапазоне, как и у КМс-1, КМс-2 и КМс-5 (таблица всех величин не приводится, чтобы не увеличивать объем

статьи). Условный предел прочности $\sigma_*(a)$ при всех скоростях у большинства КМ на Рис. 7 немного ниже, чем у ПТФЭ (на 10–15 %)и немного выше (на 10–15 %), чем у большинства образцов КМс-1 и КМс-5 (Рис. 5); напряжение $\sigma_*(a)$ у КМсш, как и у чистого ПТФЭ (Табл. 1) практически не зависит от a (различие для каждого КМ не превышает 10 %) и у всех испытанных образцов КМ находится в диапазоне 13…18 МПа. При этом предел текучести существенно возрастает с увеличением a (примерно на 50 % у ПТФЭ и КМсш-1 и на 30 % у КМсш-2, КМсш-5 – Рис. 6(b), 7). Деформация при разрыве $\varepsilon_*(a)$ у КМсш-2 и КМсш-5 ниже, чем у ПТФЭ и КМсш-1, и вообще говоря, понижается с увеличением доли наполнителей и с ростом a (см. сплошные ДД КМсш-1 на Рис. 7). Только у КМсш-2 $\varepsilon_*(a)$ оказалась не зависящей от скорости: $\varepsilon_*(a)$=145 ± 7 % (штриховые ДД на Рис. 7), но результатов единичных испытаний пока недостаточно для определенного вывода – проводятся повторные испытания. КМсш-1 (сплошные ДД) не уступает ПТФЭ по величине $\varepsilon_*(a)$ во всем диапазоне скоростей. КМсш-2 и КМсш-5 проигрывают ПТФЭ по деформативности во всем диапазоне скоростей 40–60 и 35–75 % соответственно.

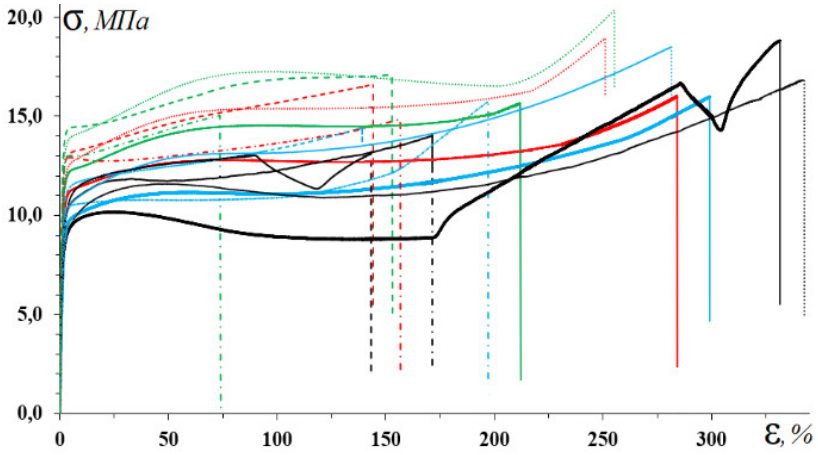

Рис. 7. Диаграммы деформирования σ(ε,*a*) до разрыва ПТФЭ и композитов КМсш-1, КМсш-2, КМсш-5 для 4 скоростей траверсы *V* = 1; 15; 150; 600 мм/мин (как на Рис. 6)

Fig. 7. Stress-strain curves σ(ε,*a*) until failure of PTFE and composites CMsMsp-1, CMsMsp-2, CMsMsp-5 at crosshead speeds *V* = 1; 15; 150; 600 mm/min (black, blue, red, and green curves), i.e., for average strain rates *a* = 0.23; 3.6; 36; 143·10^{-3} 1/s (as at the Fig. 6)

Более подробное представление всего объема данных испытаний на растяжение до разрыва (в частности ДД в истинных напряжениях и деформациях, таблицы основных механических характеристик в зависимости от доли наполнителей и скоростей растяжения), системное исследование вязкоупругопластических свойств этих и других КМ с разным содержанием наполнителей (скоростной чувствительности, зависимостей модуля упругости, напряжения течения, напряжения и деформации при разрыве от скорости растяжения и от вида и содержания наполнителя, особенностей локализации и делокализации деформации и разрушения) и изменений микроструктуры КМ в зонах разрушения образцов на сканирующем электронном микроскопе, а также их детальный сравнительный анализ и обнаружение корреляций с износостойкостью – темы последующих статей цикла в 2024–2025 гг.

Первичный анализ показал, что свойства ДД композитов КМс-1, КМс-2 и КМс-5 и КМсш-1, КМсш-2 и КМсш-5 качественно не отличаются и количественно близки к ДД чистого ПТФЭ (Рис. 3–7), хотя износостойкость КМ значительно выше. Предел прочности $\sigma_*(a)$ при всех скоростях у большинства КМ немного ниже (на 10–30 %), чем у ПТФЭ (кроме КМс-2, у которого выше). С увеличением доли наполнителей до 5 % наблюдается снижение величины $\varepsilon_*(a)$ на 20–50%, но многие КМ не уступают ПТФЭ в деформативности в определенных диапазонах скоростей деформации. Таким образом, разработанные технологии получения КМ ведут к изменению свойств КМ в нужном для триботехнических приложений направлении и следует их совершенствовать и определять оптимальные содержания наполнителей и режимы термомеханической обработки КМ на стадии получения.

Испытания ПТФЭ на нагрузку-разгрузку-восстановление

Программы испытаний имеют вид по трехстадийным программам нагружения:
$\sigma(t) = bt$ при $t \in [0; t_1]$, $\sigma(t) = -bt + 2bt_1$ при $t \in (t_1; 2t_1)$, $\sigma(t) \equiv 0$ при $t > 2t_1$, (2)
и состоят из трех стадий: нагружение со скоростью $b = b_i$ (длительность нагружения t_1) до максимального напряжения $\hat{\sigma}_i = b_i t_1$, полная разгрузка с той же скоростью, восстановление при нулевом напряжении (в течение 3 ч). Заданные параметры нагружения t_1 и $\hat{\sigma}_i$ (Рис. 8(a)): длительности стадии нагружения t_1 = 300; 900; 1500 с; $\hat{\sigma}_i = i\sigma_*/10, i = 1,\ldots,6, \sigma_* = 16$ МПа (минимальное напряжение при разрыве, найденное в испытаниях п.1), т.е. $\hat{\sigma}_i$ = 1.6; 3.2; 4.8; 6.4; 8.0; 9.6 МПа (ломаные *1–6, 7–12* и *13–18*). Использовались пневматические захваты бокового действия с губками 25 × 25 мм^2 с прорезиненной поверхностью. Деформация образцов измерялась контактным экстензометром Instron 2620-602 SN:3301, отвечающий требованиям ISO 9513, BS 3846 и ASTM E 83, с погрешностью измерений не более 0.15 %. Для фиксации деформаций на образце ставились метки по стандартному трафарету с базой 25 мм.

Испытаны образцы семи материалов: чистого ПТФЭ (Рис. 8, 9), ПТФЭ, наполненного серпентином до массовой доли 1, 2 или 5 % и ПТФЭ, наполненного коротким базальтовым волокном до 1, 2 или 5%. Для КМ с серпентиномы базальтовым волокном программ испытаний было меньше (Рис. 10(a)): длительности нагружения t_1 = 300; 900; 1500 с; $\hat{\sigma}_i = i\sigma_*/10, i = 1,\ldots,5$ (σ_* =16 МПа – минимальное напряжение при разрыве, найденное ранее), т.е. $\hat{\sigma}_i$ = 1.6; 3.2; 4.8; 6.4; 8.0 МПа для t_1 = 300 с (ломаные *1–5*), $\hat{\sigma}$ = 4.8; 9.6 для t_1 = 900 с (ломаные *11,12*) и $\hat{\sigma}$ = 8.0 для t_1 = 1500 с; скорость нагружения $b_1 = 5.33{\cdot}10^{-3}$ МПа/с одинакова для программ *1,11,15*, а $b_2 = 10.67{\cdot}10^{-3}$ МПа/с – для программ *2* и *12*).

На Рис. 8(a,b) приведены программы испытаний на нагружение-разгрузку и восстановление ПТФЭ при разных скоростях нагружения и разгрузки и графики измеренной деформации образцов от времени $\varepsilon(t; t_1, b_i)$: кривые *1–6* $\sigma(\varepsilon;\mathrm{t}_1, \mathrm{b}_\mathrm{i})$ соответствуют нагружениям (2) с t_1 = 300 с, кривые *7–12* – с t_1 = 900 с, кривые *7–12* – с t_1 = 1500 с. На Рис. 8(c) увеличены стадии нагрузки-разгрузки тех же графиков $\varepsilon(t; t_1, b_i)$, поместившиеся в диапазон $\varepsilon \le 2$ %, $t \le 3600$ с. После исключения параметра времени построены кривые нагружения-разгрузки и восстановления (КНР) $\sigma(\varepsilon;t_1, b_i)$ при разных t_1 и $\hat{\sigma}_i$: на Рис. 8(d) приведены КНР $\sigma(\varepsilon;t_1, b_i)$ *1–6* для нагружений с t_1 = 300 с,

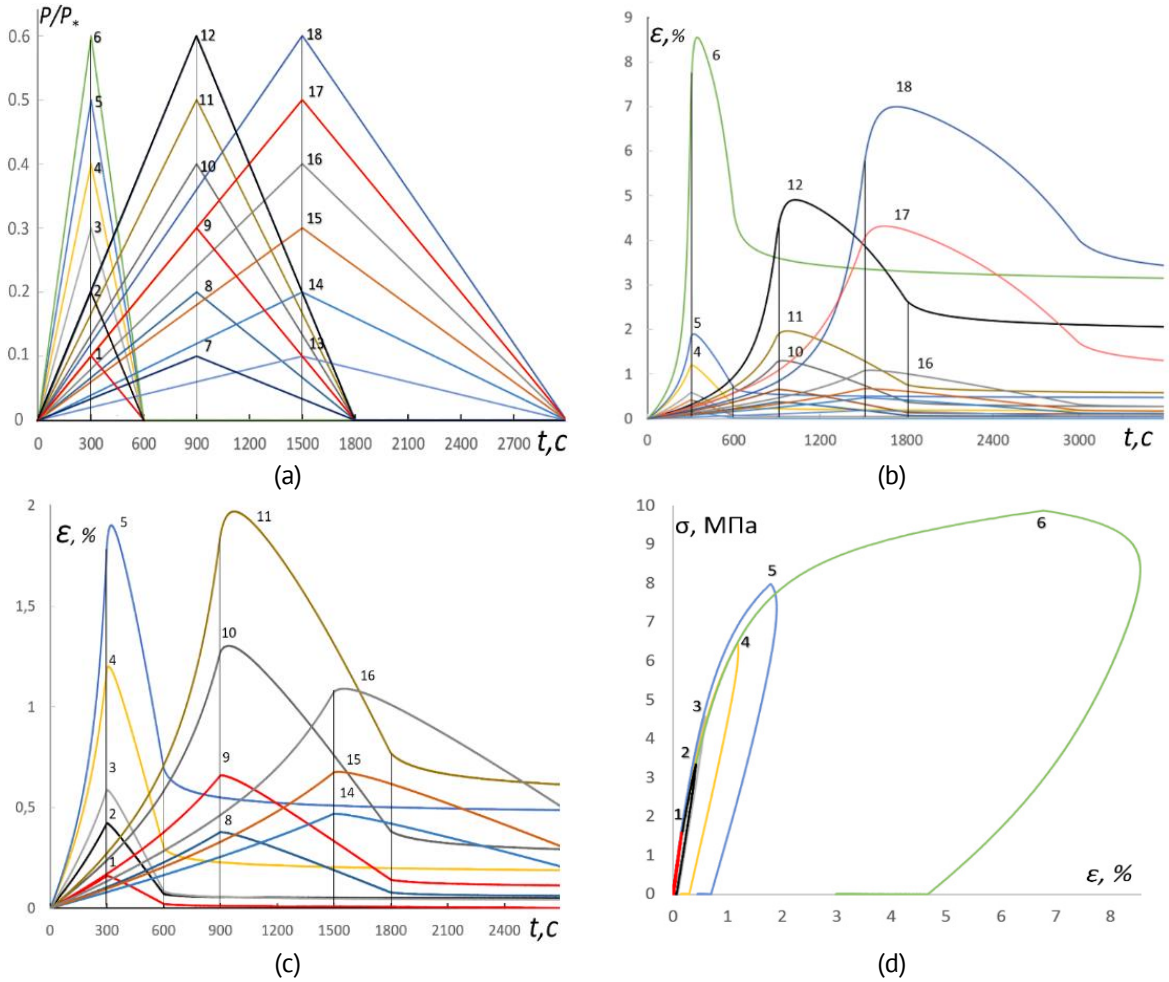

Рис. 8. Программы испытаний на нагружение-разгрузку-восстановление (2) при разных t_1, $\hat{\sigma}_i$ (a), графики измеренной деформации образцов ПТФЭ от времени $\varepsilon(t;t_1,b_i)$ (b,c) и кривые нагружения-разгрузки-восстановления $\sigma(\varepsilon;t_1,b_i)$ в испытаниях *1–6* (d)

Fig. 8. Loading programs for loading-unloading-recovery test (2) at different values of loading parameters t_1, $\hat{\sigma}_i$ (a); measured strain of PTFE samples over time $\varepsilon(t;t_1,b_i)$ (b,c), and loading-unloading-recovery curves $\sigma(\varepsilon;t_1,b_i)$ in tests *1–6* (d)

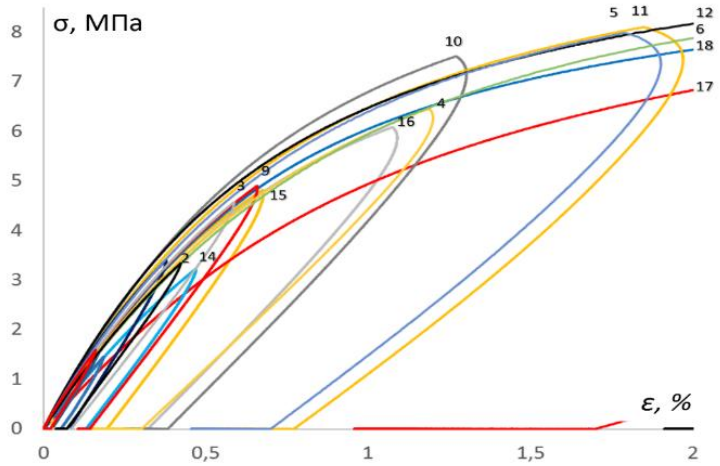

Рис. 9. Кривые нагружения-разгрузки-восстановления ПТФЭ $\sigma(\varepsilon;t_1,b_i)$ (испытания *1–18* на Рис. 8(a,b)) в диапазоне $\varepsilon \leqslant 2\%$, $\sigma \leqslant 8.5$ МПа

Fig. 9. Loading-unloading-recovery curves $\sigma(\varepsilon;t_1,b_i)$ of PTFE (tests *1–18* in Fig. 8(a,b)) in the range of $\varepsilon \leqslant 2\%$, $\sigma \leqslant 8.5$ MPa

а на сводном Рис. 9 приведены увеличенные КНР $\sigma(\varepsilon;t_1,b_i)$ *1–18* при разных параметрах нагружения t_1 и $\hat{\sigma}_i$, поместившиеся в диапазон $\varepsilon \leq$ 2 %, $\sigma \leq$8.5 МПа.

Рисунок 8(c,d) полезно сравнить с Рис. 8(c,d) и 16 статьи [1], на которых приведены кривые $\varepsilon(t;t_1,b_i)$ и $\sigma(\varepsilon;t_1,b_i)$, порождаемые нелинейным ОС типа Максвелла [6] и ОС, учитывающим взаимное влияние эволюции структуры и процесса деформирования [11,12,93].

Отклики образцов ПТФЭ на треугольный импульс нагрузки (Рис. 8) с деформацией, продолжающей расти и в начале разгрузки, и с большими остаточными деформациями качественно весьма сходны с наблюдаемыми в испытаниях асфальтобетонов, твердых топлив и других материалов. Этот эффект не связан с нелинейностью поведения материала: его описывает даже линейное ОС (1), даже простейшая линейная модель Максвелла [6]. КНР, порождаемые нелинейным ОС типа Максвелла [1,6] и нелинейным ОС для тиксотропных сред, учитывающим эволюцию структуры [1,11,12,93], качественно схожи по форме с КНР ПТФЭ и композитов на его основе, поэтому (после проверки системы индикаторов по КНР и по кривым ползучести [6,91]) эти ОС можно примерить к описанию поведения ПТФЭ [1].

Испытания на нагрузку-разгрузку-восстановление ПТФЭ-композитов с серпентином

В этом разделе приведем данные испытаний на растяжение по программам вида (2) образцов-лопаток композитов КМс-1, КМс-2 и КМс-5, т.е. ПТФЭ, наполненного мелкодисперсным серпентином до массовой доли 1, 2 или 5 % [1]. Диаграммы деформирования до разрушения этих КМ приведены на Рис. 4, 5. Образцы каждого КМ испытывались по 8 программам нагружения (2) с разными при разными параметрами t_1 и $\hat{\sigma}_i = b_i t_1$ (теми же, что и в испытаниях ПТФЭ, но в меньшем количестве); они изображены на Рис. 10(a).

Измеренные зависимости деформации от времени $\varepsilon(t;t_1,b_i)$ для ПТФЭ с 5 % серпентина в испытаниях по программам Рис. 10(a) приведены Рис. 10(b). На Рис. 10(c) увеличены кривые *1–5* для t_1 = 300 с на более узком интервале времени $4t_1$ = 1200 с. КНР $\sigma(\varepsilon;t_1,b_i)$ этого композита при разных при разных t_1 и $\hat{\sigma}_i$ приведены на Рис. 10(d). На Рис. 8, 9 и 10(b-d) хорошо заметен интересный физический эффект на кривых разгрузки: при достаточно больших напряжениях $\hat{\sigma}$ продолжается заметный рост деформации и на начальном этапе разгрузки (кривые *4–6, 10–12, 15–18*, на Рис. 8, 9 и кривые *4, 5, 12, 15* на Рис. 10, т.е. при $\hat{\sigma} \geq 0.4\sigma_*$), максимум $\varepsilon(t)$ запаздывает по сравнению с пиком нагружения (эта "инерционность" материала свидетельствует о сильно выраженной памяти предыстории нагружения). Этот эффект наблюдается как у чистого ПТФЭ, так и у всех испытанных КМ на его основе (Рис. 11), причем запаздывание максимума деформации примерно одинаково для всех четырех материалов: оно составляет примерно 40 с для нагружений с t_1 = 300 с и примерно 120 с для нагружений с t_1 = 900 с Этот эффект был ранее обнаружен у модельных кривых нагружения-разгрузки, порождаемых как физически нелинейным определяющим соотношением типа Максвелла [6], так и линейными моделями вязкоупругости при определенных ограничениях на материальные функции (Рис. 8(c,d) статьи [1]).

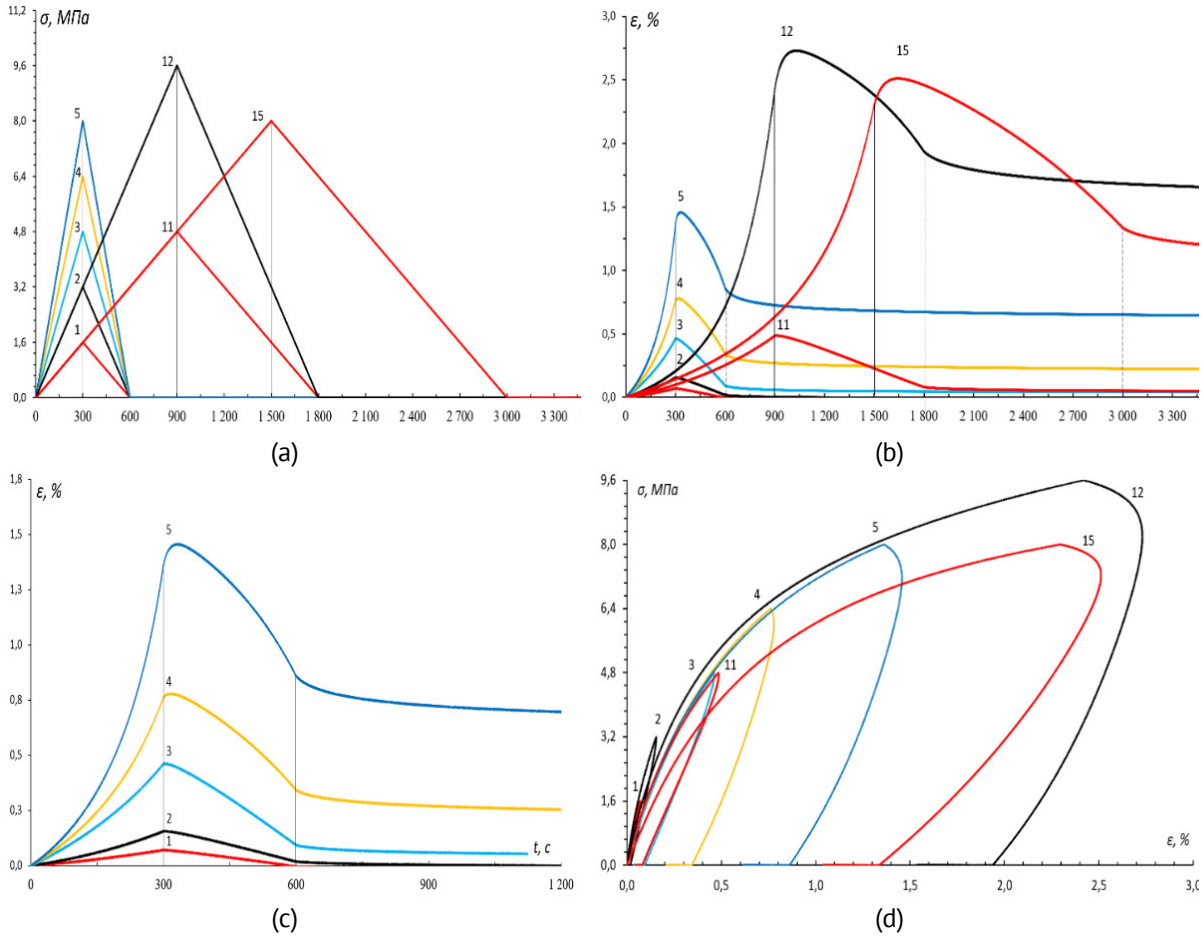

Рис. 10. Испытания на нагрузку-разгрузку и восстановление по программе (2): (a) нагружения (1) с разными параметрами *t1, bi, $\hat{\sigma}$*; (b) измеренные зависимости *ε(t;t₁,bᵢ)* для ПТФЭ с 5 % серпентина при t_1 = 300, 900, 1500 с и $\hat{\sigma}_i$ = 1.6, 3.2, 4.8, 6.4, 8.0, 9.6 МПа; (c) увеличенные кривые 1–5 для t_1 = 300 с; (d) кривые нагружения-разгрузки и восстановления *σ(ε;t₁,bᵢ)* при t_1 = 300, 900, 1500 с и разных b_i

Fig. 10. Loading-unloading and recovery tests according to program (2): (a) loadings (1) with different parameters t_1, b_i, $\hat{\sigma}$; (b) measured strain ε(t;t_1,b_i) for the composite CMs-5 (PTFE filled with 5 % serpentine) at t_1 = 300, 900, 1500 s and $\hat{\sigma}_i$ = 1.6, 3.2, 4.8, 6.4, 8.0, 9.6 MPa; (c) zoomed curves *1–5* for t_1 = 300 s; (d) loading-unloading-recovery curves σ(ε;t_1,b_i) at t_1 = 300, 900, 1500 s and different rates b_i

На сводном Рис. 11(a) приведены измеренные зависимости деформации от времени $\varepsilon(t; t_1, b_i)$ для нагружений (2) с t_1 = 300 с и пятью разными $\hat{\sigma}_i$ =1.6; 3.2; 4.8; 6.4; 8.0 МПа (по программам *1-5* с Рис. 11(a)) для образцов из четырех материалов: ПТФЭ (пунктирные линии), ПТФЭ с 1 % серпентина (сплошные линии), ПТФЭ с 2 % серпентина (штриховые), ПТФЭ с 5 % серпентина (штрих-пунктирные линии). Стадия восстановления (ее длительность – 3 ч) обрезана, чтобы увеличить начальный участок кривых нагружения-разгрузки. На сводном Рис. 11(b) приведены аналогичные зависимости для нагружений с t_1 = 900 с и t_1 = 1500 с(по программам *11,12,15*). Видно насколько существенно различаются кривые $\varepsilon(t)$ при разном содержании серпентина.

На сводном Рис. 12(a) приведены (соответствующие Рис. 8) КНР $\sigma(\varepsilon;t_1, b_i)$ при разных скоростях b_i для нагружений (2) с t_1 = 300 с и пятью разными $\hat{\sigma}_i$ =1.6; 3.2; 4.8; 6.4; 8.0 МПа (по программам *1–5* на Рис. 10(a)) для образцов из четырех материалов: ПТФЭ (пунктирные линии), ПТФЭ с 1 % серпентина (сплошные линии), ПТФЭ с 2 % серпентина (штриховые линии), ПТФЭ с 5 % серпентина (штрих-

пунктирные линии). На Рис. 12(b) приведены аналогичные зависимости для нагружений с t_1 = 900 си t_1 = 1500 (по программам *11, 12, 15*).

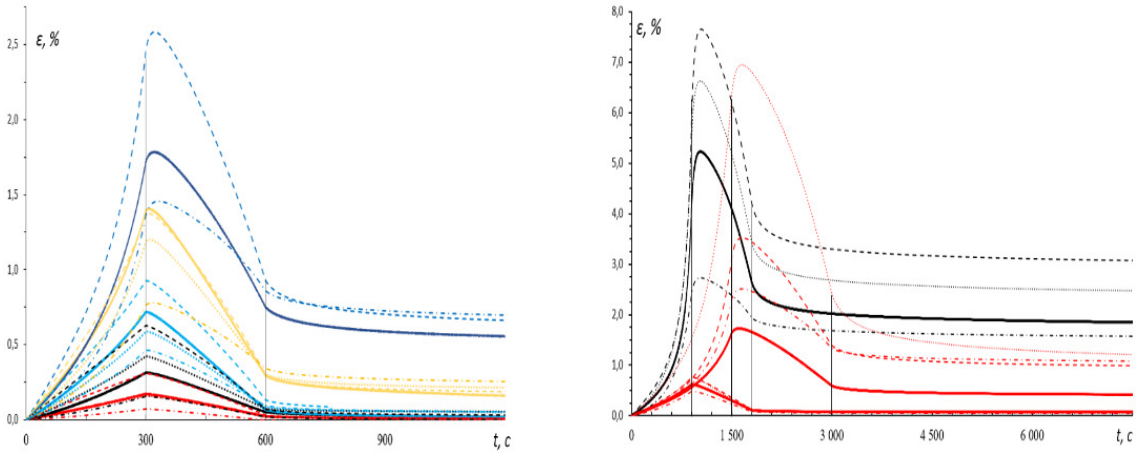

(a) (b)

Рис. 11. Измеренные зависимости деформации от времени $\varepsilon(t;t_1,b_i)$ для нагружений по программе (2) с t_1 = 300 с и пятью разными $\hat{\sigma}_i$ (a) и с t_1 = 900 с и t_1 = 1500 с (b) для образцов из четырех материалов: ПТФЭ (пунктирные линии), ПТФЭ с 1 % серпентина (сплошные линии), ПТФЭ с 2 % серпентина (штриховые линии), ПТФЭ с 5 % серпентина (штрих-пунктирные линии)

Fig. 11. Measured strain dependences on time $\varepsilon(t;t_1,b_i)$ for loadings according to program (2) with t_1 = 300s and five different values of maximal stress $\hat{\sigma}_i$ (a) and with t_1 = 900 s and t_1 = 1500 s (b) for PTFE (dot lines) and three composites with different contents of serpentine: CMs-1 (solid lines), CMs-2 (dashed lines), CMs-5 (dash-dot lines)

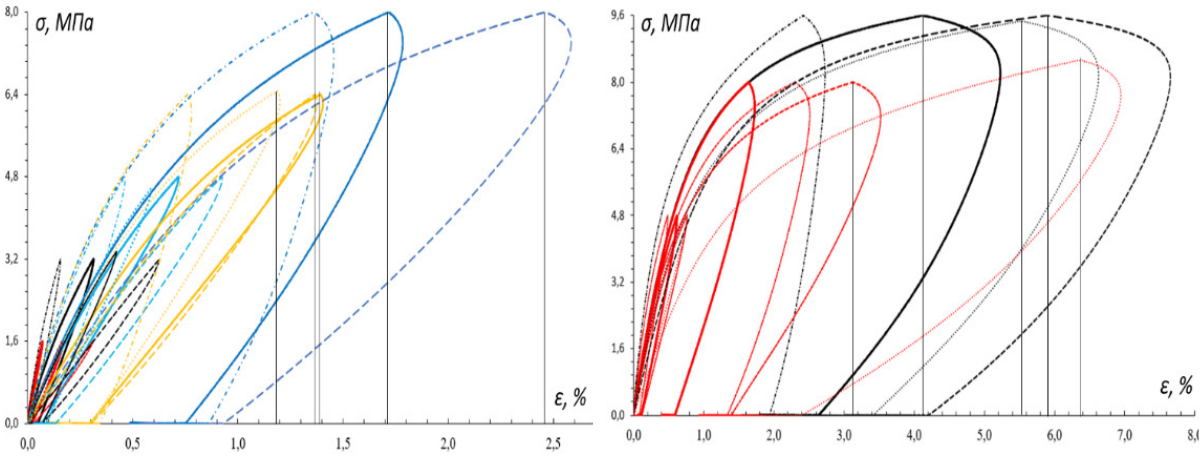

(a) (b)

Рис. 12. КНР $\sigma(\varepsilon;t_1,b_i)$ при разных скоростях b_i для нагружений (2) с t_1 = 300 с и пятью разными $\hat{\sigma}_i$ (a) и с t_1 = 900 с и t_1 = 1500 с (b) для образцов из четырех материалов: ПТФЭ (пунктирные линии), материалов: ПТФЭ с 1 % серпентина (сплошные линии), ПТФЭ с 2 % серпентина (штриховые линии), ПТФЭ с 5 % серпентина (штрих-пунктирные линии)

Fig. 12. Loading-unloading curves $\sigma(\varepsilon;t_1,b_i)$ at different rates b_i for programs (2) with t_1 = 300 s and five different values of $\hat{\sigma}_i$ (a) and with t_1 = 900 s and t_1 = 1500 s (b) for PTFE (dot lines) and three composites with different contents of serpentine: CMs-1 (solid lines), CMs-2 (dashed lines), CMs-5 (dash-dot lines)

Подробный сравнительный анализ кривых нагружения-разгрузки и восстановления ПТФЭ и КМ на его основе – в последующих статьях.

Испытания образцов ПТФЭ на ползучесть и восстановление

Испытания образцов ПТФЭ и КМ на ползучесть и восстановление при растяжении с целью построения семейства кривых ползучести и восстановления (КПВ) $\varepsilon(t;\bar{\sigma},T)$ проводились (при комнатной температуре) на универсальной электромеханической испытательной машиной Instron 5969 по программам вида:

$$\sigma(t)=\bar{\sigma}[h(t)-h(t-T)],\ \bar{\sigma}>0,\ T>0, \qquad (3)$$

с $T=4$ ч и разными уровнями нагрузки: $\bar{\sigma}=i\sigma_*/10$, $i=1,\ldots,7$, $\sigma_*=16$ МПа для ПТФЭ, т.е. $\hat{\sigma}_i$ =1.6; 3.2; 4.8; 6.4; 8.0; 9.6; 11.2 МПа (продольные силы $P_i=iP_*/10$, $i=1,\ldots,7$, P_* =500 Н – минимальное усилие разрыва образца, определенное в серии испытаний до разрыва – см. Табл. 1 и Рис. 1, 3). Образцы имели форму лопаток с длиной рабочей части 70 мм, толщиной 3 ± 3 мм (средней) площадью поперечного сечения 31.8 ± 0.8 мм^2. Задавалась общая программа нагружения по растягивающей силе, а напряжение $\bar{\sigma}$ для каждого образца рассчитывалось по начальной площади его поперечного сечения, и потому их разброс составлял около 5–7 % от целевых величин $\bar{\sigma}$. Для уточнения поведения КПВ проведены испытания и для нагрузок P =175; 225; 275 Н ($\bar{\sigma}\approx 0.35\sigma_*, 0.45\sigma_*, 0.55\sigma_*$). Длительности стадий ползучести при постоянном напряжении $\bar{\sigma}$ и стадии восстановления при нулевой нагрузке (при техническом нуле $0.01P_*$) – по 4 ч (длительность каждого испытания – чуть более 8 ч).

Испытания при каждом уровне нагрузки проводились по следующей программе (Рис. 13):

0. Пред-нагрузка 7 Н для выбора люфтов по ГОСТ 18197-2014 "Пластмассы. Метод определения ползучести при растяжении".

1. Три предварительных треугольных цикла нагружения с постоянной скоростью 10 Н/с (с примерной средней скоростью деформации 0.0001 с$^{-1}$) до заданной малой нагрузки P_c и полной разгрузки (до технического нуля) с той же скоростью (Рис. 13а)). Для образцов-лопаток из ПТФЭ было задано $P_c=150$ Н в испытаниях с $P_i\geq 150$ (длительность каждого цикла – 30 с). В испытаниях при малых силах P =50;100 Н амплитуда $P_c=25$ Н (нижняя кривая на Рис. 13(а)). Эта стадия нагружения общая для всех испытаний серии с разными *P*, она позволяет набрать статистику для осреднения экспериментальных величин модуля упругости и оценить разброс свойств образцов из партии (контролировать их относительную

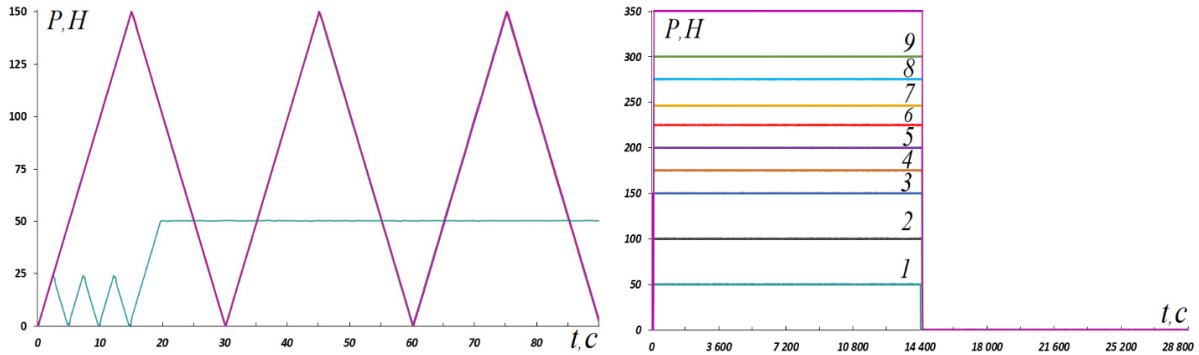

(a) (b)

Рис. 13. Программы нагружения с заданием растягивающей силы как функции времени: (а) три цикла нагружения и разгрузки начальной стадии, (b) на стадиях ползучести и восстановления

Fig. 13. Loading programs specifying tensile force as a function of time: (a) three cycles of loading and unloading at the initial stage, (b) stages of creep and recovery

стабильность). Модуль упругости E каждого образца вычисляется как среднее значение по трем циклам нагружения, а модуль материала – еще и осреднением по всем испытанным образцам.

2. Быстрое нагружение (со скоростью 10 Н/с) до целевого уровня нагрузки P выдержка в течение 4 ч при постоянной нагрузке для исследования ползучести

3. Быстрая разгрузка (со скоростью 10 Н/с) до почти нулевой нагрузки (до технического нуля).

4. Выдержка в течение 4 ч при нулевой нагрузке (в 7 Н) для измерения деформации, т.е. для наблюдения эффекта восстановления (обратной ползучести).

5. Быстрое увеличение нагрузки с постоянной скоростью траверсы 15 мм/мин до разрушения образца, чтобы сравнить, как восьмичасовое испытание на ползучесть и восстановление влияет на модуль Юнга, напряжение и деформацию при разрушении (сравнить с данными испытаний на нагружение с постоянной скоростью до разрыва из Табл. 1). Эта финальная стадия одинакова для всех образцов. После испытания проводились исследования изменений микроструктуры ПТФЭ и КМ в зонах разрушения образцов на сканирующем электронном микроскопе (см. ниже).

По полученным данным построены таблицы всех размеров образцов до и после испытаний и основных измеренных характеристик деформации (не приводятся в этой статье), и графики измеренной осевой деформации от времени, т.е. семейство КПВ $\varepsilon(t;\bar{\sigma},T)$ (Рис. 14). Во всех испытаниях даже при самых малых нагрузках в $\bar{\sigma} = 0.1\sigma_*$ *наблюдалась ползучесть* при постоянной нагрузке и накопление необратимых деформаций: быстрый рост деформаций без заметного замедления и выхода на асимптоту, неполное восстановление с выходом на ненулевую асимптоту (Рис. 14(a)). Структурные корни этих свойств – ламеллярное строение кристаллитов ПТФЭ и низкая прочность кристаллитов на сдвиг (и растяжение), из-за которой кристаллиты не могут препятствовать развитию деформации (скольжению, распрямлению и перестройкам фибрилл).

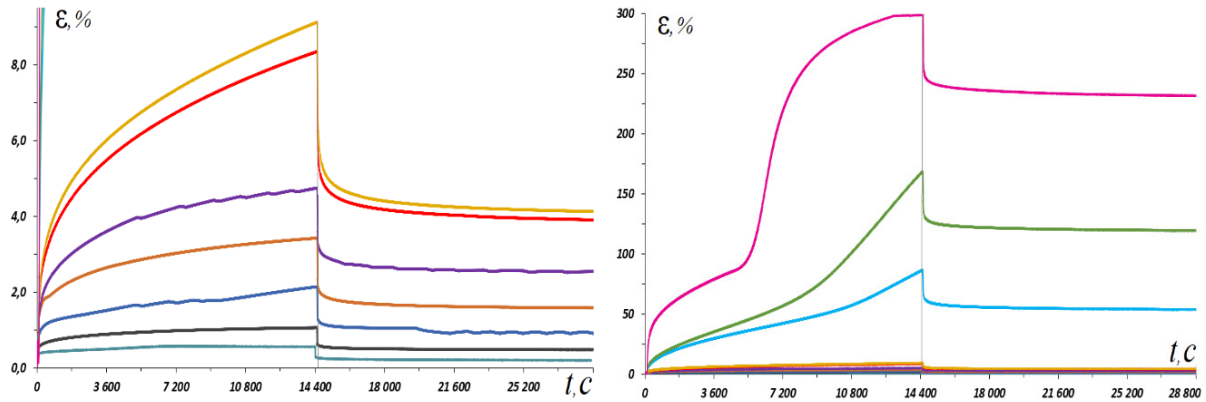

Рис. 14. Кривые ползучести и восстановления ПТФЭ: (a) при растягивающих усилиях $P \leq 0.5P_*$, т.е. P = 50; 100; 150; 175; 200; 225; 250 Н; (b) при больших усилиях P = 275; 300; 350 Н

Fig. 14. Creep and recovery curves of PTFE: (a) under tensile forces $P \leq 0.5P_*$, i.e., P = 50; 100; 150; 175; 200; 225; 250 N; (b) under greater forces P = 275; 300; 350 N

Как и следовало ожидать, семейство КПВ $\varepsilon(t;\bar{\sigma},T)$ монотонно возрастает по параметру $\bar{\sigma}$, причем особенно быстрый рост деформации (интенсификация

ползучести) начинается с нагрузки $P > 0.45P_* = 225$ Н (красная кривая); в частности, возрастают средняя скорость ползучести и остаточная (пластическая) деформация после снятия нагрузки и выдержки в течение 4 ч. КПВ приведены на двух Рис. 14, поскольку максимальные деформации при уровнях нагрузки $P \le 0.5P_*$, т.е. $P \le 250$ Н (Рис. 14(a)), не превосходят 9 % (и КПВ имеют обычную форму, типичную для большинства вязкоупругопластичных материалов) [1,4,8,92], а при больших усилиях $P > 0.5P_*$, т.е. P =275; 300; 350 Н (Рис. 14(b)), превышают 80 % и достигают 300 % для $P = 0.7P_* = 350$ Н (верхняя кривая на Рис. 14(b)), а остаточная деформация после снятия нагрузки и выдержки в течение 4 ч превышает 60 % и достигает 230 %. Для $P \le 0.4P_*$ остаточная деформация не превышает 3 % (фиолетовая кривая на Рис. 14(a) – для $P = 0.4P_*$).

По Рис. 14(a) хорошо видно, что уже при $P = 0.3P_* = 150$ Н наблюдается заметное отклонение от подобия кривых ползучести (их пропорциональности уровню напряжения и одной и той же функции времени); это означает, что ПТФЭ можно считать линейно вязкоупругим лишь при нагрузках, не превышающих $\bar{\sigma} = 0.2\sigma_*$ (или менее) и можно попытаться описывать зависимость деформации $\varepsilon(t)$ от истории нагружения $\sigma(t)$ линейным интегральным оператором (линейным ОС) вязкоупругости, а проявлениями физической нелинейности можно пренебречь (это гипотеза, которую требуется подтвердить значительно большим количеством испытаний). При бОльших напряжениях (усилиях) нельзя пренебрегать эффектами физической нелинейности при моделировании и надо выбирать физически нелинейное ОС.

При $P = 0.55P_* = 275$ Н кривые ползучести ПТФЭ меняют свою форму (Рис. 14(b)): появляется третья стадия ползучести с растущей скоростью (ее не было при нагрузках $P \le 0.5P_*$) и деформации резко растут. Очень интересна форма кривых ползучести $P = 350$ Н (Рис. 14(b)): после третьей стадии ползучести снова наблюдается упрочнение, резкое понижение скорости ползучести (кривые ползучести такой формы встречаются крайне редко и свидетельствуют об очень высокой скоростной чувствительности и большом деформационном ресурсе материала). Отметим, что при больших нагрузках изменения размеров поперечного сечения при ползучести велики (толщина уменьшилась с 3 до 2 мм, ширина – с 10 до 6 мм, площадь с 30 до 12 мм^2), т.е. истинное напряжение (при постоянстве усилия) заметно растет и в конце стадии ползучести превышает номинальное почти в три раза (но все же материал стабилизирует быстрое нарастание деформации и скорость ползучести уменьшается на последней стадии почти до нуля).

Отметим, что уже на предварительной стадии циклического нагружения с малой амплитудой цикла $P_c = 0.3P_* = 150$ Н, т.е. $\bar{\sigma}_c \approx 4.8$ МПа, и периодом в 30 с (Рис. 13(a)), явственно наблюдается накопление вязкопластических деформаций с каждым циклом у всех образцов (Рис. 15) и искривление ветви разгрузки (Рис. 15(b)). На Рис. 15(a) приведены начальные участки откликов $\varepsilon(t;\bar{\sigma},T)$, $t \le 240$ с, для нагружений с P =150; 175; 200; 225; 250; 275 Н, включая отклик на три предварительных цикла нагружения с фиксированной амплитудой $P_c = 150$ Н, а на Рис. 15(b) – соответствующие кривые циклического нагружения $\sigma - \varepsilon$ для образцов №9 и №10 (отнулевой цикл, скорость нагружения и разгрузки равна 10 Н/с). *Даже при низкой нагрузке и малых скоростях деформирования наблюдаются ярко выраженные неупругие свойства ПТФЭ*. При этом после первого цикла нагрузки у всех десяти

образцов наблюдалось заметное увеличение жесткости (увеличение касательного модуля при $\sigma = 0$), уменьшение приращения остаточной и деформации и сужение петли гистерезиса на каждом цикле (Рис. 15(b)).

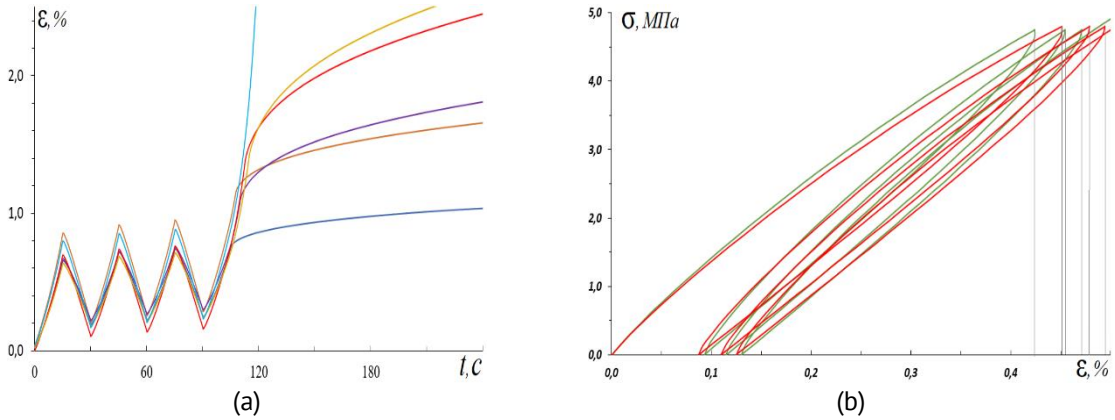

Рис. 15. (a) Начальные участки откликов $\varepsilon(t;\bar{\sigma},T)$, $t \leqslant 240$ с, для нагружений с P = 150; 175; 200; 225; 250 Н, включая отклик на три предварительных цикла нагружения с амплитудой P_c = 150 Н ($\bar{\sigma}_c \approx 4.8$ МПа) и длительностью 30 с; (b) диаграммы мягкого циклического нагружения σ-ε образцов №9 и №10 (отнулевой цикл, скорость нагружения и разгрузки равна 10 Н/с)
Fig. 15. (a) Initial sections of responses $\varepsilon(t;\bar{\sigma},T)$, t ⩽ 240 s, for loadings with P = 150; 175; 200; 225; 250 N, including the response to three preliminary loading cycles with the amplitude of P_c = 150 N ($\bar{\sigma}_c \approx 4.8$ MPa) and duration of 30 s; (b) stress-strain curves σ-ε under cyclic loading of samples No. 9 and No. 10 (zero-to-tension stress cycle, loading and unloading rates are equal to 10 N/s)

Обнаружение в испытаниях выраженных эффектов ползучести и восстановления показывает, что при комнатной температуре и нагрузках $\bar{\sigma} > 0.1\sigma_*$, $\sigma_* = 16$ МПа (даже достаточно малых по сравнению с пределом прочности при растяжении) ПТФЭ (и исследованные КМ на его основе) *нельзя считать упругим или упругопластическим*, а *необходимо учитывать наследственные свойства и эффекты* (память, зависимость от истории нагружения, скоростную чувствительность, способность к ползучести и релаксации), т.е. *моделировать ПТФЭ как вязкоупругопластический и учитывать физическую нелинейность его реологических свойств* [1,92].

Более подробное представление всего объема данных испытаний (в частности кривых ползучести ПТФЭ и КМ в истинных напряжениях и деформациях) и обнаруженных эффектов (зависимости средних скоростей ползучести и восстановления и остаточной деформации от уровня нагрузки и от вида и содержания наполнителя, особенностей локализации и делокализации деформации и др.), их детальный сравнительный анализ и обнаружение корреляций с износостойкостью – темы последующих статей цикла в 2025–2026 гг.

Микроскопия зон разрушения ПТФЭ и композитов на его основе при растяжении

После механических испытаний проводились исследования изменений микроструктуры ПТФЭ и КМ в зонах разрушения образцов на сканирующем электронном микроскопе (СЭМ) Jeol JSM-7800F (JEOL, Япония) в режиме вторичных электронов.

На Рис. 16 приведены фотографии (с увеличением в 1000 раз) зон разрушения образцов ПТФЭ в испытаниях на растяжение со скоростями движения траверсы V =1; 15; 150; 600 мм/мин (соответствующие средние по времени и рабочей части образца скорости деформации: a = 0.23; 3.6; 107; $143 \cdot 10^{-3} c^{-1}$). Светлые пятна-выступы по всему рельефу – оборванные фибриллы, а красными кругами отмечены микропоры (их средний размер – 5…20 мкм).

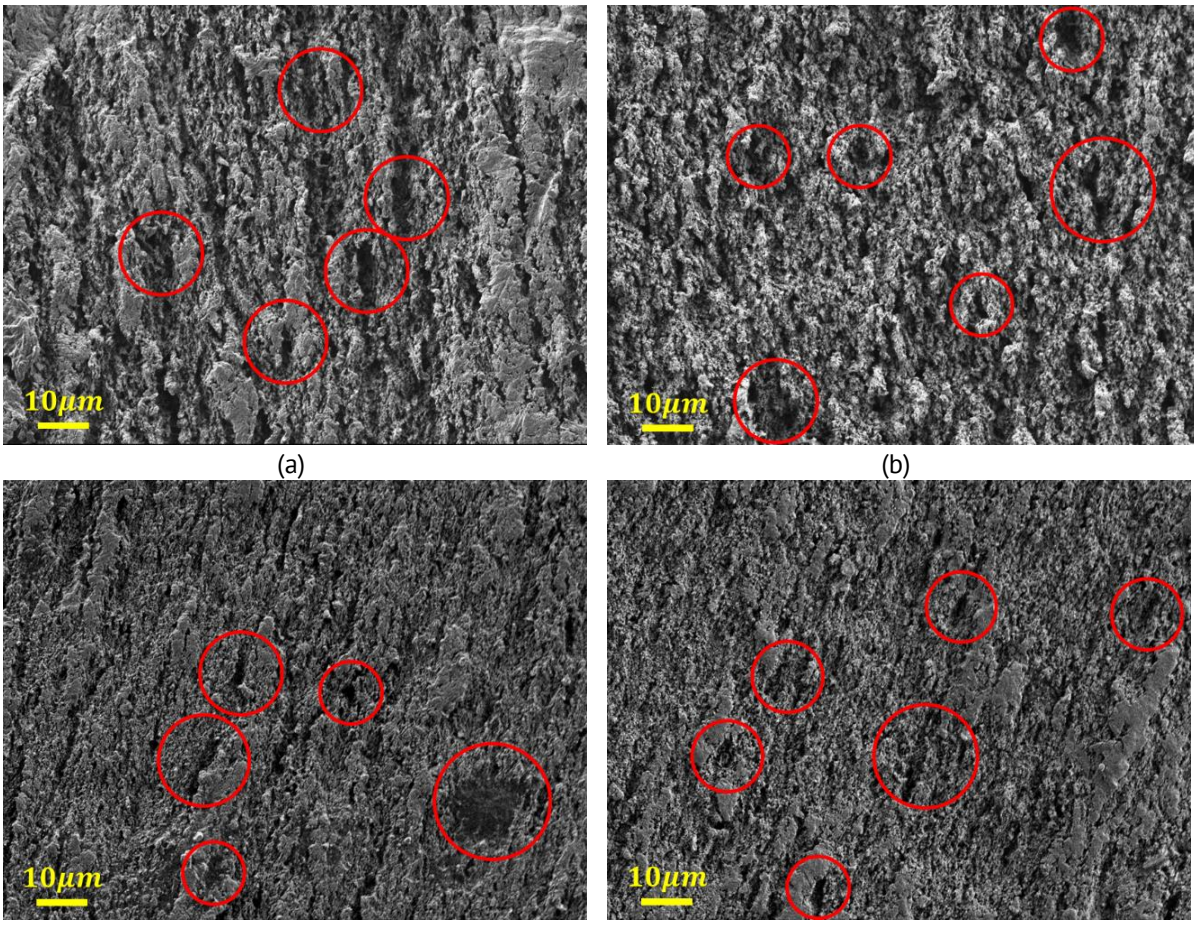

Рис. 16. Микрофотографии зон разрушения ПТФЭ при четырех разных скоростях деформирования a = 0.23; 3.6; 107; $143 \cdot 10^{-3}$ 1/c (a–d)

Fig. 16. Microphotographs of fracture zones of PTFE samples in four tests at different strain rates a = 0.23; 3.6; 107; $143 \cdot 10^{-3}$ 1/s (a–d)

Разрушение образцов ПТФЭ при комнатной температуре и указанных (малых) скоростях деформации протекает по вязкому механизму, с накоплением больших пластических деформаций (Рис. 1, 3, Табл. 1). При растяжении образца по всему объему происходит образование множества микропор, которые постепенно растут, полимер между соседними порами вытягивается в направлении нагрузки, образуются фибриллярные мостики, обладающие повышенной жесткостью благодаря ориентированности цепей. Формирование фибрилл представляет собой процесс распутывания кристаллических доменов с образованием ориентированной лентовидной кристаллической структуры в направлении нагрузки [86,94]. С ростом нагрузки и локализации напряжения фибриллы все больше растягиваются и

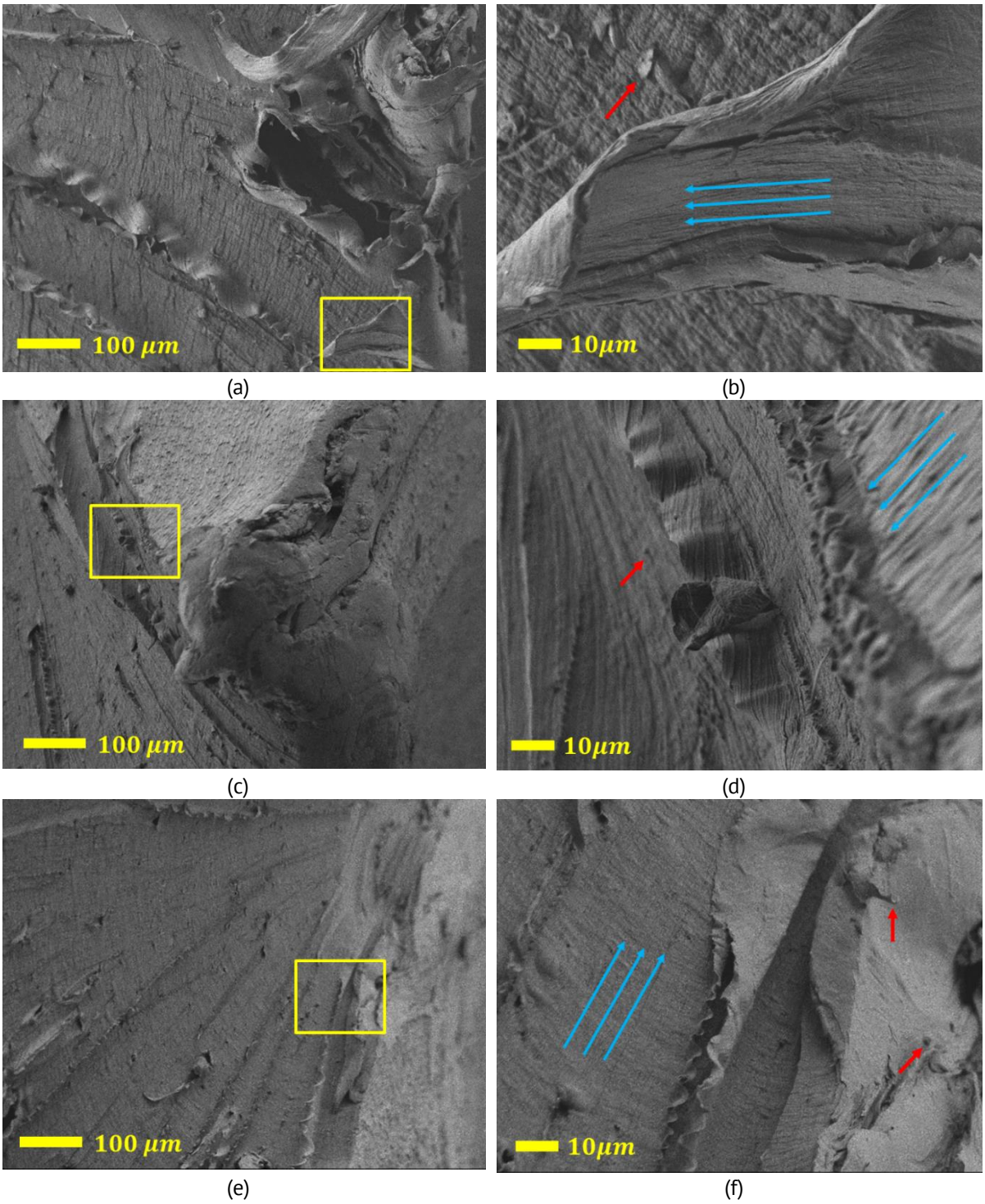

Рис. 17. Микрофотографии зон разрушения образцов из КМсш-1 (с наполнением 0.9 % серпентина и 0.1 % шпинели магния), доведенных до разрыва после испытаний на ползучесть и восстановление: (a,b) при нагрузке 100 Н (образец №42); (c,d) при нагрузке 150 Н (образец №43); (e,f) при нагрузке 250 Н (образец №45); увеличение в 150 раз на фрагментах (a,c,e) и в 1000 раз – на фрагментах (b,d,f)

Fig. 17. Microphotographs of the fracture zones of the composite CMsMsp-1 samples (with 0.9% serpentine and 0.1% magnesium spinel), loaded to failure after creep and recovery tests: (a,b) creep under a load of 100 N; (c,d) under a load of 150 N; (e,f) under a load of 250 N; magnification 150 times in (a,c,e) and 1000 times in (b,d,f)

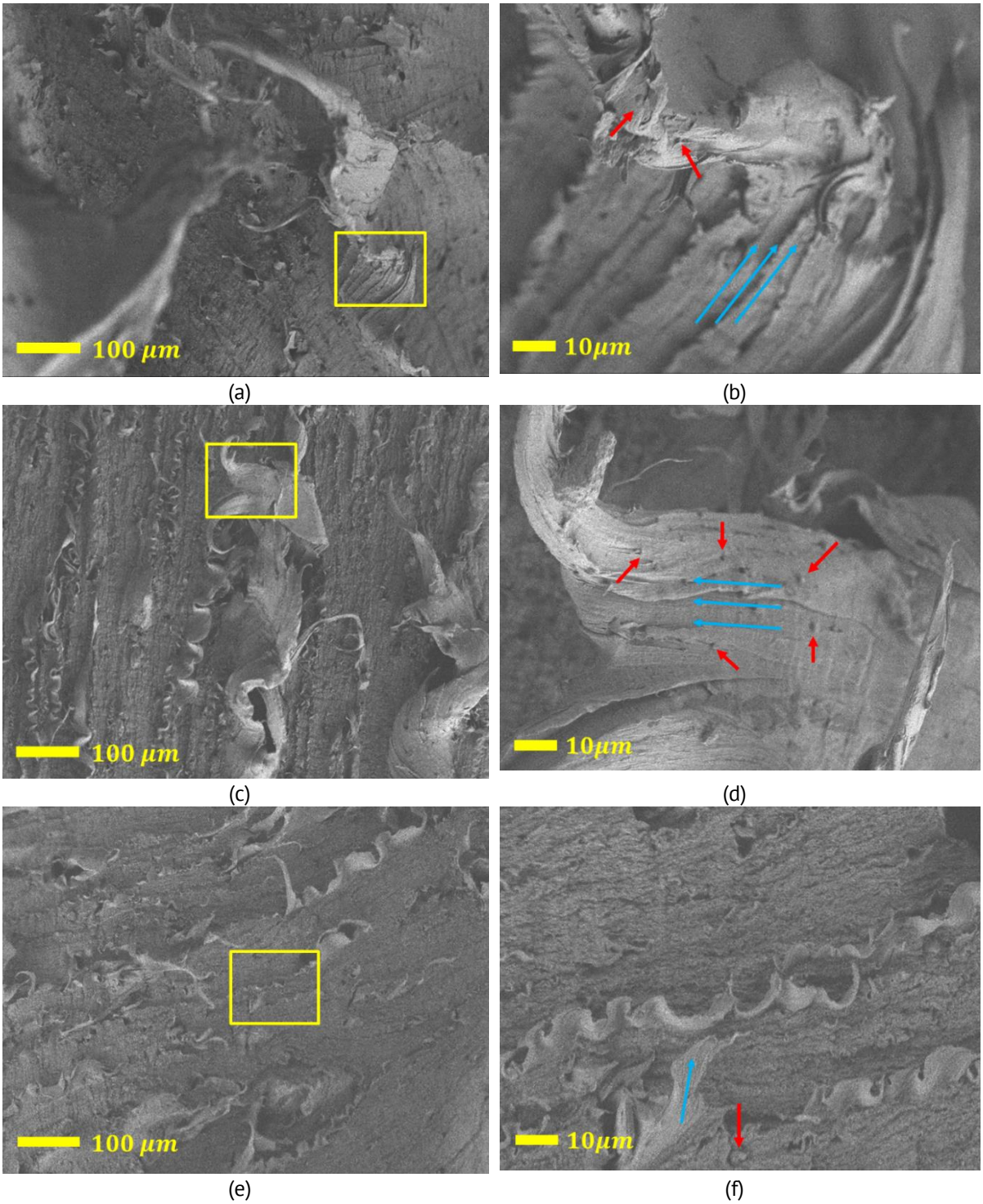

Рис. 18. Микрофотографии зон разрушения образцов из КМсш-2 с наполнением 1.5 % серпентина и 0.5 % шпинели магния, доведенных до разрыва после испытаний на ползучесть и восстановление: (a,b) при нагрузке 50 Н (образец №61); (c,d) при нагрузке 150 Н (образец №63); (д,е) при нагрузке 250 Н (образец №65); увеличение в 150 раз на фрагментах (a,c,e) и в 1000 раз – на фрагментах (b,d,f)]
Fig. 18. Microphotographs of the fracture zones of the composite CMsMsp-2 samples with 1.5 % serpentine and 0.5 % magnesium spinel, loaded to failure after creep and recovery tests: (a,b) creep under a load of 50 N; (c,d) under a load of 150 N; (e,f) under a load of 250 N; magnification 150 times in (a,c,e) and 1000 times in (b,d,f)

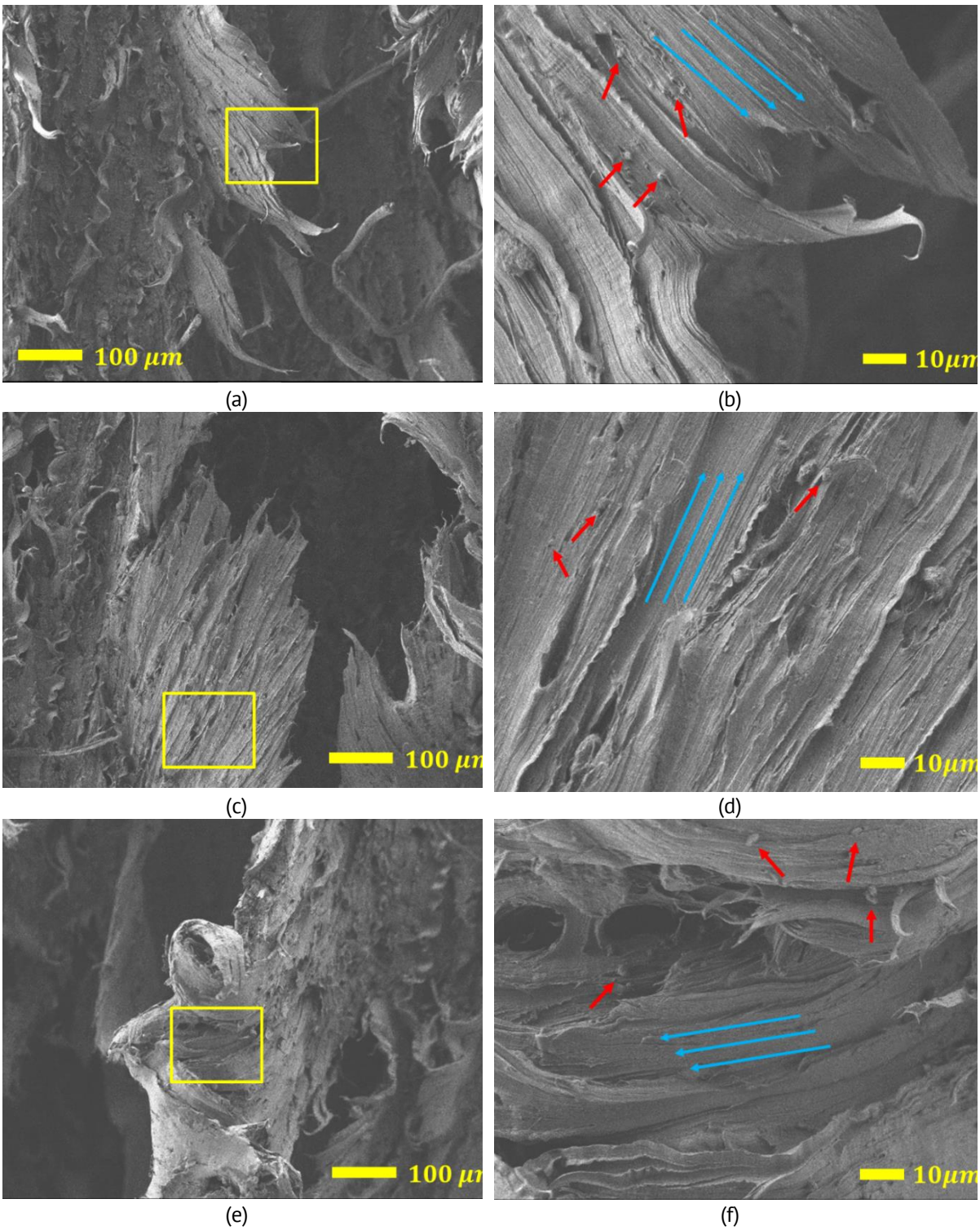

Рис. 19. Микрофотографии зон разрушения образцов из КМсш-5 с наполнением 3.8 % серпентина и 1.2 % шпинели магния, доведенных до разрыва после испытаний на ползучесть и восстановление: (a,b) при нагрузке 50 Н (образец №81); (c,d) при нагрузке 150 Н (образец №83); (e,f) при нагрузке 250 Н (образец №85); увеличение в 150 раз на фрагментах (a,c,e) и в 1000 раз – на фрагментах (b,d,f)
Fig. 19. Microphotographs of the fracture zones of the composite CMsMsp-5 samples with 3.8% serpentine and 1.2% magnesium spinel, loaded to failure after creep and recovery tests: (a,b) under a load of 50 N; (c,d) under a load of 150 N; (e,f) under a load of 250 N; magnification 150 times in (a,c,e) and 1000 times in (b,d,f)

ориентируются, потом начинают рваться, соседние микропоры сливаются и укрупняются (разрыв соседних стенок-мостиков приводит к процессу, аналогичному "расстегиванию молнии"), образуются трещины в плоскости, перпендикулярной направлению растяжения; дальнейшее растяжение вызывает разрывы оставшихся фибрилл, замедляющих развитие трещин, и рост трещин приводит к разрыву образца. На Рис. 16 хорошо видны оборванные концы фибриллярных мостиков (светлые выступы по всему рельефу). Поверхности разрыва при малой скорости деформирования $a = 0.23 \cdot 10^{-3} с^{-1}$ или $a = 3.6 \cdot 10^{-3} с^{-1}$(Рис. 16(a,b)) характеризуются более вытянутыми фибриллярными выступами, чем при больших скоростях $a = 107; 143 \cdot 10^{-3} с^{-1}$ (Рис. 16(c,d)), это свидетельствует о постепенном охрупчивании материала с увеличением скорости растяжения. На макроуровне это выражается в резком уменьшении деформации при разрыве (Рис. 1, 3 и Табл. 1). Как известно, процесс скоростного охрупчивания приводит к тому, что при больших скоростях деформирования (за пределами исследуемого квазистатического диапазона) происходит гораздо более резкое охрупчивание ПТФЭ и разрушение становится хрупким.

На Рис. 17–19 приведены микрофотографии зон разрушения образцов из КМ трех составов (рассмотренных ранее) с разным содержанием наполнителей: КМсш-1 (с 0.9 % серпентина и 0.1 % шпинели магния по массе), КМсш-2 (с 1.5 % серпентина и 0.5 % шпинели магния) и КМсш-2 (с 3.8 % серпентина и 1.2 % шпинели магния). Образцы доведены до разрушения после описанных испытаний на ползучесть и восстановление (в течение 4 + 4 ч) при разных нагрузках от 50 до 250 Н, т.е. от 1.6 до 8 МПа (см. Рис. 13, 14). В левом столбце – снимки с увеличением в 150 раз, в правом – в 1000 раз, желтые рамки обозначают зоны увеличения. Красные стрелки указывают частицы наполнителей; голубые – направление фибрилл.

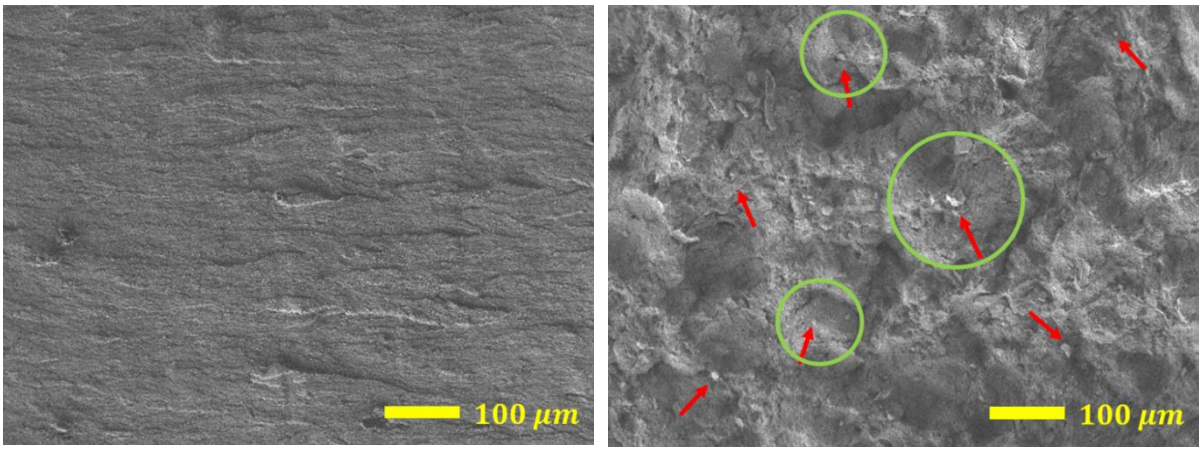

(a) (b)

Рис. 20. Надмолекулярная структура ПТФЭ (a) и КМ с 1.5% серпентина и 0.5% шпинели магния (b)
Fig. 20. Supramolecular structure: (a) ribbon-striped structure of the original PTFE; (b) spherulitic structure of composite filled with 1.5 % serpentine and 0.5 % magnesium spinel

Надмолекулярная структура исходного ПТФЭ характеризуется формированием ленточно-полосчатой структуры (Рис. 20(a)). Введение в ПТФЭ серпентина и шпинели магния способствует трансформации надмолекулярной структуры в направлении образования сферолитов (Рис. 20(b)). На микрофотографиях видно, что частицы наполнителей служат центрами кристаллизации, от которых идет рост

сферолитоподобных образований (зеленые круги). В результате измельчения и механоактивации наполнителей в мельнице при дальнейшем сухом смешивании с ПТФЭ, прессовании и термообработке активные сегменты макромолекул адсорбируются на поверхности наполнителя, вызывая радиальную ориентацию макромолекул в аморфной фазе, что приводит к росту сферолитов и изменению соотношения между кристаллической и аморфной составляющей матрицы [22,45]. Повышение физико-механических свойств композитов может возникнуть, когда наполнители, концентрируясь в аморфных областях, и увеличивают плотность упаковки.

На микрофотографиях зон разрушения образцов КМ (Рис. 17–19) видно, что пучки макромолекул ПТФЭ в процессе деформирования растягиваются и образуют ориентированную структуру, отчетливо наблюдаются фибриллы полимера. Фибриллы ориентируются из точки концентрации напряжения (на микрофотографиях отчетливо наблюдаются частицы наполнителей) в основном в направлении растяжения. Способность фибрилл связывать берега трещины и их прочность, заметно замедляет или даже блокирует развитие трещин. Стабильность вытягивания фибрилл (локального ориентирования пучков макромолекул) в первую очередь определяется температурой и кристаллической фазой, а также зависит от вида напряженного состояния, интенсивности нагрузки, скорости нагружения и анизотропии микроструктуры [95].

Заключение

Статья посвящена комплексному экспериментальному изучению вязкоупругопластических свойств политетрафторэтилена и нескольких семейств композитов (КМ) с повышенной (в 2000 раз) износостойкостью на его основе, полученных в последние годы в лабораториях Института естественных наук СВФУ им. М.К. Аммосова введением в качестве наполнителей слоистых силикатов (механоактивированные вермикулит, каолинит, серпентин, бентонит), шпинели магния и коротких базальтовых или углеродных волокон. В первой части статьи [1] описаны технологии изготовления композитов и основные результаты работ по исследованию структуры и химического состава поверхности трения методами электронной микроскопии и ИК-спектроскопии и повышению износостойкости этих материалов за счет образования пленки переноса и вторичных структур в результате трибоокислительных процессов. Описана система программ квазистатических испытаний полимеров и композитов для всестороннего изучения их вязкоупругопластических свойств (совокупности всех наблюдаемых в испытаниях эффектов), возможности линейного интегрального соотношения вязкоупругости Больцмана-Вольтерры и четырех физически нелинейных определяющих соотношений вязкоупругопластичности (одно из которых учитывает взаимное влияние эволюции структуры и процесса деформирования) по их описанию и методология анализа данных испытаний и выбора адекватных определяющих соотношений для их моделирования. В частности, рассмотрены признаки физической нелинейности поведения материалов, т.е. индикаторы неприменимости линейного интегрального соотношения вязкоупругости Больцмана-Вольтерры, которые можно

обнаружить в испытаниях по разным программам нагружения, способы очертить диапазон линейности поведения вязкоупругого материала. Описаны испытания для предварительной диагностики типа поведения материала (в первом приближении), если характеризовать его категориями упругий, вязкоупругий, вязкопластичный, упруговязкопластичный, и методология выбора адекватной модели для описания поведения конкретного материала [1].

Во второй части статьи приведены данные испытаний на растяжение по разным программам образцов-лопаток из чистого ПТФЭ и шести КМ на его основе с наполнением серпентином или серпентином и шпинелью магния (до 5 % по массе): семейства диаграмм растяжения $\sigma(\varepsilon,a)$ с разными скоростями до разрушения, кривых нагружения-разгрузки-восстановления $\varepsilon(t;t_1,b_i)$ и $\sigma(\varepsilon;t_1,b_i)$ с разными скоростями и длительностями стадии нагружения и кривых ползучести и восстановления $\varepsilon(t;\bar{\sigma},T)$ для разных уровней постоянной нагрузки и длительностей ее приложения (Рис. 1–15). Проведен первичный анализ выраженности наследственных свойств материалов, в частности скоростной чувствительности, способности к течению при постоянном напряжении, ресурса деформативности и способности к восстановлению после разгрузки, и влияние на них состава и доли наполнителей. Определены базовые скалярные характеристики материалов: мгновенный модуль, предел текучести, напряжение и деформация при разрыве в зависимости от скорости нагружения и др. После механических испытаний на сканирующем электронном микроскопе проведены исследования изменений микроструктуры ПТФЭ и композитов с разным содержанием наполнителей в зонах разрушения образцов (по сравнению с исходной структурой). Установлено сильное влияние малых долей наполнителей на структуру и многие вязкоупругопластические свойства материалов.

При анализе накопленного за два года объема данных испытаний обнаружены высокая деформативность ПТФЭ и КМ на его основе во всем диапазоне квазистатических скоростей деформации (кратность растяжения до 4.5 при скоростях $a = 1.4\cdot10^{-4}$ и $a = 2.3\cdot10^{-4}$ с$^{-1}$, кратность растяжения около 3 при $a = 0.143$ с$^{-1}$), выраженные наследственные свойства даже при низкой нагрузке (менее 10 % от разрывной), способность материалов к ползучести и течению при постоянной нагрузке и накоплению большой необратимой (пластической) деформации, способность упрочняться после длинной площадки текучести и очень высокая скоростная чувствительность (Рис. 1–7): при увеличении скорости растяжения ПТФЭ в 1000 раз измеряемые напряжения увеличились на 70–80 % (при одинаковых деформациях), деформация при разрушении уменьшилась почти в 2 раза (с 340 до 200 %), предел текучести ПТФЭ и всех исследованных КМ монотонно возрастал с увеличением скорости деформирования на 40–60 %. Вместе с тем предел прочности $\sigma_*(a)$ у ПТФЭ и всех КМ гораздо слабее зависит от скорости (меняется не более, чем на 20–30 %) и не всегда монотонно. Высокая скоростная чувствительность материалов тормозит и останавливает локализацию деформации, задерживает и останавливает развитие шейки и обеспечивает выраженную площадку текучести, довольно длительный участок упрочнения за ней и, в итоге, большой ресурс пластичности (деформацию при разрушении). Деформативность материалов (и способность к восстановлению) является преимуществом при использовании в

уплотнениях, но это недостаток, если применять ПТФЭ в узлах трения скольжения, где необходимы достаточная жесткость и высокая износостойкость.

Первичный анализ данных испытаний показал, что свойства диаграмм деформирования $\sigma(\varepsilon,a)$ всех исследованных КМ качественно не отличаются и количественно близки к ДД чистого ПТФЭ (на всех ДД есть длинная площадка текучести и стадия упрочнения после нее – Рис. 3–7), хотя износостойкость КМ значительно выше (в 2000–2500 раз), жесткость как правило, немного повышается с увеличением доли наполнителя, а деформации ползучести и способность материалов к восстановлению снижаются. Предел прочности $\sigma_*(a)$ при всех скоростях у большинства КМ немного ниже (на 10–30 %), чем у ПТФЭ. С увеличением доли наполнителей до 5 % наблюдается снижение величины $\varepsilon_*(a)$ на 20–50 %, но многие КМ не уступают ПТФЭ в деформативности в определенных диапазонах скоростей деформации. Таким образом, разработанные технологии получения КМ ведут к изменению свойств КМ в нужном для триботехнических приложений направлении и следует их совершенствовать и определять оптимальные содержания наполнителей и режимы термомеханической обработки КМ на стадии получения (эта работа продолжается).

В испытаниях на нагрузку-разгрузку обнаружен интересный физический эффект: на кривых разгрузки при достаточно больших максимальных напряжениях (кривые *4–6, 10–12, 15–18*, на Рис. 8, 9 и кривые *4, 5, 12, 15* на Рис. 10) продолжается заметный рост деформации и на начальном этапе разгрузки, максимум деформации запаздывает по сравнению с пиком нагружения (эта "инерционность" материала свидетельствует о сильно выраженной памяти истории нагружения). Этот эффект наблюдается как у чистого ПТФЭ, так и у всех испытанных КМ (Рис. 8–12).

Обнаружение выраженных эффектов ползучести, скоростной чувствительности, течения при постоянном напряжении, накопления необратимой деформации и частичного восстановления в проведенных сериях испытаний показывает, что при комнатной температуре и нагрузках $\bar{\sigma} > 0.1\sigma_*$,$\sigma_*$ =16 МПа (даже достаточно малых по сравнению с номинальным пределом прочности σ_* при растяжении) ПТФЭ и КМ на его основе нельзя считать упругими или упруго пластическими материалами, а необходимо учитывать наследственные свойства и эффекты (зависимость откликов от истории нагружения, скоростную чувствительность, способность к ползучести и релаксации и т.п. [1]), т.е. *моделировать эти материалы как вязкоупругопластические, причем учитывать физическую нелинейность их реологических свойств и, возможно, эволюцию структуры при деформировании и ее влияние на механические свойства* [11,12,93]. Исходя из отмеченных особенностей поведения исследуемых материалов для его моделирования следует выбрать физически нелинейное определяющее соотношение (ОС), описывающее широкий спектр эффектов, свойственных вязкоупругопластическим материалам. В качестве основных кандидатов для описания поведения исследуемого материала (на данном этапе экспериментального исследования) можно взять нелинейное ОС Работнова или нелинейное ОС типа Максвелла [3–9] и его обобщения [10–13], поскольку каждое из них способно описывать весь спектр обнаруженных в испытаниях эффектов (как доказано в работах [3–13,91–93] и др.), а при надлежащем выборе материальных функций способны

описывать и линейно вязкоупругое поведение материала при не слишком высоких температурах и достаточно малых напряжениях.

Более подробное представление всего объема данных испытаний образцов разных КМ на основе ПТФЭ и обнаруженных эффектов (в частности, скоростной чувствительности диаграмм деформирования, чередования участков разупрочнения и упрочнения на кривых ползучести, накопления необратимых деформаций, особенностей локализации и делокализации деформации и разрушения при разных видах нагружения), системное исследование свойств изучаемых КМ с разным содержанием наполнителей, их детальный сравнительный анализ и обнаружение корреляций с износостойкостью – темы последующих статей цикла в 2024–2025 гг. По семействам построенных диаграмм деформирования, кривых нагружения и разгрузки и кривых ползучести и восстановления будет осуществляться выбор и проверка индикаторов применимости к описанию деформирования исследуемых материалов пяти физически нелинейных ОС вязкоупругопластичности, построенных и детально изученных ранее в цикле статей [2–13,91–93] и др. Одна из важных задач всего цикла статей – комплексная характеризация и системное описание свойств ПТФЭ и КМ на его основе, проведение и анализ испытаний одних и тех же материалов по разным информативным программам: даже по чистому ПТФЭ (да и другим материалам) в научной литературе представлены только разрозненные данные испытаний по отдельным программам образцов ПТФЭ, изготовленных из разного сырья в разных условиях по разным технологиям, которые нельзя использовать вместе для выбора, идентификации и всесторонней верификации ОС для описания всего комплекса реологических свойств ПТФЭ.

Авторский вклад

Андрей Владимирович Хохлов: разработка концепции, проведение исследования, курирование данных, написание рукописи и редактирование, научное руководство; **Айталина Алексеевна Охлопкова**: разработка концепции, научное руководство; **Сардана Афанасьевна Слепцова**: разработка концепции,; **Надежда Николаевна Лазарева**: проведение исследования, курирование данных; **Прасковья Николаевна Тарасова**: investigation; **Арсений Владимирович Бабайцев**: проведение исследования; **Ольга Сергеевна Вотинова** : проведение исследования; **Артемий Валерьевич Шапорев**: проведение исследования; **Вячеслав Владимирович Гулин**: проведение исследования.

CRediT authorship contribution statement

Andrew V. Khokhlov: conceptualization, investigation, data curation, writing – original draft & editing, supervision; **Aitalina A. Okhlopkova**: conceptualization, supervision; **Sardana A. Sleptsova**: conceptualization; **Nadezhda N. Lazareva**: investigation, data curation; **Praskovia N. Tarasova**: investigation; **Arseny V. Babaytsev**: investigation; **Olga S. Votinova**: investigation; **Artemii V. Shaporev**: investigation; **Vyacheslav V. Gulin**: investigation.

Конфликт интересов

Авторы заявляют об отсутствии конфликта интересов.

Conflict of interest

The authors declare that they have no conflict of interest.

Литература / References

1. Хохлов АВ, Охлопкова АА, Слепцова СА, Лазарева НН, Тарасова ПН, Бабайцев АВ, Шапорев АВ, Гулин ВВ. Комплексное исследование вязкоупругопластических свойств нанокомпозитов с повышенной износостойкостью на основе Фторопласта-4. Часть 1. *Materials Physics and Mechanics.* 2025;53(3): 177–218. (Khokhlov AV, Okhlopkova AA, Sleptsova SA, Lazareva NN, Tarasova PN, Babaytsev AV, Shaporev AV, Gulin VV. Systematic all-round examination of the viscoelastoplastic properties of nanocomposites with increased wear resistance based on polytetrafluoroethylene. Part 1. *Materials Physics and Mechanics.* 2025;53(3): 177–218. (In Russian))
2. Khokhlov AV. Fracture criteria under creep with strain history taken into account, and long-term strength modelling. *Mech. Solids.* 2009;44: 596–607.
3. Хохлов АВ. Нелинейная модель вязкоупругопластичности типа Максвелла: моделирование влияния температуры на кривые деформирования, релаксации и ползучести. *Вестник Самарского гос. техн. ун-та. Сер. физ.-мат. науки.* 2017;21(1): 160–179. (Khokhlov AV. The nonlinear Maxwell-type model for viscoelastoplastic materials: Simulation of temperature influence on creep, relaxation and strain-stress curves. *J. Samara State Tech. Univ., Ser. Phys. Math. Sci.* 2017; 21(1): 160–179. (In Russian))
4. Хохлов АВ. Анализ и сравнение свойств кривых релаксации и ползучести при ступенчатых нагружениях, порождаемых нелинейным определяющим соотношением Работнова и линейной теорией вязкоупругости. *Композиты и Наноструктуры.* 2024;16(1): 20–55. (Khokhlov AV. Comparative analysis of properties of stress relaxation curves and creep curves under multi-step loadings generated by the Rabotnov quasi-linear relation and the Boltzmann-Volterra linear viscoelasticity relation. *Composites and Nanostructures.* 2024; 16(1): 20–55. (In Russian))
5. Хохлов АВ. Идентификация нелинейной модели упруговязкопластичности типа Максвелла по кривым ползучести с начальной стадией нагружения. Часть 2. Методики. *Деформация и разрушение материалов.* 2017;10: 2–9. (Khokhlov AV. Identification methods of Maxwell-type nonlinear viscoelastoplastic model, based on creep curves with initial ramp loading. Part II. Methods. *Deformatsiya I razrushenie materialov.* 2017;(10): 2–9. (In Russian))
6. Khokhlov AV. Applicability indicators and identification techniques for a nonlinear Maxwell–type elastoviscoplastic model using loading–unloading curves. *Mechanics of Composite Materials.* 2019;55(2): 195–210.
7. Khokhlov AV. Analysis of Properties of Ramp Stress Relaxation Curves Produced by the Rabotnov Nonlinear Hereditary Theory. *Mechanics of Composite Materials.* 2018;54(4): 473–486.
8. Хохлов АВ. Индикаторы применимости и методики идентификации нелинейной модели типа Максвелла для реономных материалов по кривым ползучести при ступенчатых нагружениях. *Вестник МГТУ им. Н.Э. Баумана. Сер. Естественные науки.* 2018;6: 92–112. (Khokhlov AV. Applicability Indicators and Identification Techniques for a Nonlinear Maxwell-Type Elasto-Viscoplastic Model using Multi-Step Creep Curves. *Herald of the Bauman Moscow State Technical University. Natural Sciences.* 2018;(6): 92–112. (In Russian))
9. Khokhlov AV. Properties of the Set of Strain Diagrams Produced by Rabotnov Nonlinear Equation for Rheonomous Materials. *Mechanics of Solids.* 2019;54(3): 384–399.
10. Khokhlov AV. Generalization of a nonlinear Maxwell-type viscoelastoplastic model and the simulation of creep recovery curves. *Mechanics of Composite Materials.* 2023;59(3): 441–454.
11. Khokhlov AV, Gulin VV. Analysis of the Properties of a Nonlinear Model for Shear Flow of Thixotropic Media Taking into Account the Mutual Influence of Structural Evolution and Deformation. *Phys Mesomech.* 2023;26: 621–642.
12. Khokhlov AV, Gulin VV. Families of stress-strain, relaxation, and creep curves generated by a nonlinear model for thixotropic viscoelastic-plastic media accounting for structure evolution. Part 2. Relaxation and stress-strain curves. *Mechanics of Composite Materials.* 2024;60(2): 259–278.
13. Khokhlov AV. Hybrid of a nonlinear Maxwell-type viscoelastoplastic model with the linear viscoelasticity constitutive constitutive equation and properties of crossbred creep and stress-strain curves.

Materials Physics and Mechanics. 2024;52(4): 114–140.
14. Черский ИН. *Полимерные материалы в современной уплотнительной технике*. Якутск: Якутское книжное изд-во, 1975. (Cherskiy IN. *Polymer materials in modern sealing technology*. Yakutsk: Yakutskoe knizhnoe izdatel'stvo; 1975. (In Russian))
15. Уолл Л. *Фторполимеры*. Москва: Мир; 1975. (Knunyanca IL, Ponamorenko VA. *Fluoropolymers*. Moscow: Mir; 1975. (In Russian))
16. Паншин ЮА, Малкевич СГ, Дунаевская ЦС. *Фторопласты*. Ленинград: Химия; 1978. (PanshinYuA, Malkevich SG, Dunaevskaya CS. *Fluoroplastics*. Leningrad: Himiya; 1978. (In Russian))
17. Истомин НП , Семенов АП. *Антифрикционные свойства композиционных материалов на основе фторполимеров*. Москва: Наука; 1981. (Istomin NP, Semenov AP. *Antifriction properties of composite materials based on fluoropolymers*. Moscow: Nauka; 1981. (In Russian))
18. Пугачев АК, Росляков ОА. *Переработка фторопластов в изделия*. Ленинград: Химия; 1987. (Pugachev AK, Roslyakov OA. *Processing of fluoroplastic into products*. Leningrad: Himiya; 1987. (In Russian))
19. Булманис ВН. *Рекомендации по применению фторопластовых композитов для уплотнительных устройств*. Якутск: ЯФ СО АН СССР; 1988. (Bulmanis VN. *Recommendations for the use of fluoroplastic composites for sealing devices*. Yakutsk: YaF SO AN SSSR; 1988. (In Russian))
20. Машков ЮК, Полещенко КН, Поворознюк СН, Орлов ПВ. *Трение и модифицирование материалов трибосистем*. Москва: Наука; 2000. (Mashkov YuK, Poleschenko KN, Povoroznyuk SN, Orlov PV. *Friction and modification of tribosystem materials*. Moscow: Nauka; 2000. (In Russian))
21. Хрулев ВМ. *Полимерсиликатные композиции в строительстве*. УФА: ТАУ; 2002. (Hrulev VM. *Polymer silicate compositions in construction*. Ufa: TAU; 2002. (In Russian))
22. Машков ЮК, Овчар ЗН, Суриков ВИ, Калистратова ЛФ. *Композиционные материалы на основе политетрафторэтилена*. Москва: Машиностроение; 2005. (Mashkov YuK, Ovchar ZN, Surikov VI, Kalistratova LF. *Composite materials based on polytetrafluoroethylene*. Moscow: Mashinostroeniye; 2005. (In Russian))
23. Бузник ВМ, Фомин ВМ, Алхимов АП, Игнатьева ЛН. *Металлополимерные нанокомпозиты*. Новосибирск: Изд-во СО РАН; 2005. (Buznik VM, Fomin VM, Alhimov AP, Ignat'eva LN. *Metal-polymer nanocomposites*. Novosibirsk: Izdatel'stvo SO RAN; 2005. (In Russian))
24. Михайлин ЮА. *Термоустойчивые полимеры и полимерные материалы*. СПб: Профессия; 2006. (Mihajlin YuA. *Heat-resistant polymers and polymer materials*. Saint Petersburg: Professiya; 2006. (In Russian))
25. Козлов ГВ, Заиков ГЕ, Стоянов ОВ, Кочнев АМ. *Дисперсно-наполненные полимерные нанокомпозиты*. Казань: КНИТУ; 2012. (Kozlov GV, Zaikov GE, Stoyanov OV, Kochnev AM. *Dispersion-filled polymer nanocomposites*. Kazan: KNITU; 2012. (In Russian))
26. Авдейчик СВ. *Машиностроительные фторокомпозиты: структура, технология, применение*. Гродно; 2012. (Avdeychik SV. *Mechanical fluorocomposites: structure, technology, application*. Grodno: Grodnenskiygosudarstvennyyuniversitetimeni Yanki Kupaly; 2012. (In Russian))
27. Логинов БА, Виллемсон АЛ, Бузник ВМ. *Российский фторполимеры: история, технологии, перспективы*. Москва: Гиицветмет; 2013. (Loginov BA, Villemson AL, Buznik VM. *Russian fluoropolymers: history, technology, prospects*. Moscow: Giicvetmet; 2013. (In Russian))
28. Stan F, Fetecau C. Study of stress relaxation in polyteyrafluoroethylene composites by cylindrical macroindentation. *Composites*. 2013;(47): 298–307.
29. Полуэктов ВЛ, Баронин ГС, Бузник ВМ, Худяков ВВ, Полуэктова СЛ. Упрочняющая твердофазная технология получения профилированных изделий из нанокомпозитов на основе Ф-4 с использованием интенсивной пластической деформации. *Вестник Тамбовского университета. Серия: Естественные и технические науки*. 2016;21(3): 1250–1254. (Poluektov VL, Baronin GS, Buznik VM, Hudyakov VV, Poluektova SL. Strengthening solid-phase technology for producing profiled products from nanocomposites based on F-4 using severe plastic deformation. *Bulletin of Tambov University. Series: Natural and technical sciences*. 2016;21(3): 1250–1254. (In Russian))
30. Николаева ИП, Огородов ЛИ, Яковлева ЕЛ. Ползучесть модификаций политетрафторэтилена при различных режимах нагружения. *Строительство уникальных зданий и сооружений*. 2017;3(54): 7–17. (Nikolaeva IP, Ogorodov LI, Yakovleva EL. Creep of polytetrafluoroethylene modifications under various loading conditions. *Construction of unique buildings and structures*. 2017;54(3): 7–17. (In Russian))
31. Tanaka K, Kawakami S. Effect of various fillers on the friction and wear of polytetrafluoroethylene-based composites. *Wear*. 1982;79(2): 221–234.
32. Сиренко ГА. *Антифрикционные карбопластики*. Киев: Техника; 1985. (Sirenko GA. *Anti-friction carboplastics*. Kazan: Tekhnika; 1985. (In Russian))
33. Biswas SK, Vijayan K. Friction and wear of PTFE. *Wear*. 1992;158(1–2):193–211.

34. Охлопкова АА. *Физико-химические принципы создания триботехнических материалов на основе политетрафторэтилена и ультрадисперных керамик. Дисс. д-ра техн. наук.* Гомель; 2000. (Okhlopkova AA. *Physico-chemical principles of creating tribological materials based on polytetrafluoroethylene and ultradisperse ceramics.* Gomel; 2000. (In Russian))
35. Суриков ВИ. *Повышение эксплуатационных свойств композитов на основе политетрафторэтилена путем структурной многоуровневой модификации: дис. д-ра техн. наук.* Омск; 2001. (Surikov VI. *Improving the performance properties of polytetrafluoroethylene-based composites through multi-level structural modification.* Omsk; 2001. (In Russian))
36. Охлопкова АА, Адрианова ОА, Попов СН. *Модификация полимеров ультрадисперсными соединениями.* Якутск: Якутский филиал АН СО РАН; 2003. (Okhlopkova AA, Adrianova OA, Popov SN. *Modification of polymers with ultrafine compounds*. Yakutsk: Yakutskiy filial AN SO RAN; 2003. (In Russian))
37. Friedrich K, Zhang Z, Schlarb A. Effects of various fillers on the sliding wear of polymer composites. *Compos. Sci. Technol.* 2005;65(15-16):2329–2343.
38. Shi Y, Feng X, Wang H, Lu X. Tribological properties of PTFE composites filled with surface-treated carbon fiber. *J. Mater. Sci.* 2007;42: 8465–8469.
39. Ignat'eva LN, Buznik VM. IR-spectroscopic examination of polytetrafluoroethylene and its modified forms. *Russ J Gen Chem.* 2009;79: 677–685.
40. Shi Y, Feng X, Wang H, Lu X. The effect of surface modification on the friction and wear behavior of carbon nanofiber-filled PTFE composites. *Wear.* 2008;264(11-12):934–939.
41. Hatipov SA, Artamonov NA. A new antifriction and sealing material based on radiation-modified polytetrafluoroethylene. Russ *J Gen Chem.* 2009;79: 616–625.
42. Khatipov SA, Konova EM, Artamonov NA. Radiation-modified polytetrafluoroethylene: Structure and properties. *Russ J Gen Chem.* 2009;79: 2006–2015.
43. Vail JR, Burris DL, Sawyer WG. Multifunctionality of single-walled carbon nanotube-polytetrafluoroethylene nanocomposites. *Wear.* 2009;267: 619–624.
44. Zhu J, Shi Y, Feng X, Wang H, Lu X. Prediction on tribological properties of carbon fiber and TiO2 synergistic reinforced polytetrafluoroethylene composites with artificial neural networks. *Materials & Design.* 2009;30(4): 1042–1049.
45. Машков ЮК, Кропотин ОВ. Трибофизика и структурная модификация материалов трибосистем. Омск, 2009. (Mashkov YuK, Kropotin OV. *Tribophysics and structural modification of materials of tribosystems.* Omsk: Izdatel'stvo OmGTU; 2009. (In Russian))
46. Khatipov SA, Serov SA, Sadovskaya NV, Konova EM. Morphology of irradiated polytetrafluoroethylene. *Polym. Sci. Ser. A.* 2012;54: 684–692.
47. Chen B, Wang J, Yan F. Boston ivy-like clinging of dendritic polytetrafluoroethylene nano-ribbons to the surface of carbon fiber. *Composites Part A: Applied Science and Manufacturing.* 2012;43(7): 1028–1031.
48. Chen B, Wang J, Yan F. Synergism of carbon fiber and polyimide in polytetrafluoroethylene-based composites: Friction and wear behavior under sea water lubrication. *Materials & Design.* 2012;36: 366–371.
49. Ye J, Khare HS, Burris DL. Transfer film evolution and its role in promoting ultra-low wear of a PTFE nanocomposite. *Wear.* 2013;297(1-2): 1095–1102.
50. Wang J, Chen B, Liu N, Han G, Yan F. Combined effects of fiber/matrix interface and water absorption on the tribological behaviors of water-lubricated polytetrafluoroethylene-based composites reinforced with carbon and basalt fibers. *Composites Part A: Applied Science and Manufacturing.* 2014;59: 85–92.
51. Кропотин ОВ, Машков ЮК, Егорова ВА, Кургузова ОА. Влияние углеродных модификаторов на структуру и износостойкость полимерных нанокомпозитов на основе политетрафторэтилена. *Журнал Технической Физики.* 2014;84(5): 66–70. (Kropotin OV, MashkovYuK, Egorova VA, Kurguzova OA. The influence of carbon modifiers on the structure and wear resistance of polymer nanocomposites based on polytetrafluoroethylene. *Journal of Technical Physics.* 2014;84(5): 66–70. (In Russian))
52. Higaki Y, Ishige R, Takahara A. Fluoropolymer Surfaces/Interfaces. In: *Handbook of Fluoropolymer Science and Technology*. 2014. p.433–450.
53. Harris KL, Pitenis AA, Sawyer WG, Krick BA, Blackman GS, Kasprzak DJ, Junk CP. PTFE tribology and the role of mechanochemistry in the development of protective surface films. *Macromolecules.* 2015;48(11): 3739–3745.
54. Kropotin OV, Mashkov YK, Egorova VA, Kurguzova OA. Effect of carbon modifiers on the structure and wear resistance of polytetrafluoroethylene-based polymer nanocomposites. *Technical Physics.* 2014;59: 696–700.
55. Ebnesajjad S. Filled fluoropolymer compounds. In: *Fluoroplastics.* 2nd ed. Oxford: William Andrew Publishing; 2015. p.336–381.
56. Будник ОА. Структурные изменения матрицы ПТФЭ-композитов. *Вестник БГТУ им. В.Г. Шухова.* 2015;(4): 104–112. (Budnik OA, Berladir KV, Budnik AF, Rudenko PV. Structural changes in the matrix of PTFE composites. *Bulletin of BSTU named after. V.G. Shukhova*. 2015;(4): 104–112. (In Russian))
57. Harris KL, Pitenis AA, Sawyer WG, Krick BA, Blackman GS, Kasprzak DJ, Junk CP. PTFE tribology and the role of mechanochemistry in the development of protective surface films. *Macromolecules.* 2015;48(11): 3739–3745.

58. Кропотин О.В. *Износостойкие ПТФЭ-композиты для повышения надежности металлополимерных герметизирующих устройств изделий машиностроения. Диссертация, к.т.н.* Омск; 2016. (Kropotin OV. *Wear-resistant PTFE composites to improve the reliability of metal-polymer sealing devices for mechanical engineering products*. Omsk; 2016. (In Russian))
59. Son F, Wan Q, Wang T. Effects of glass fiber and molybdenum disulfide on tribological behaviors and PV limit of chopped carbon fiber reinforced polytetrafluoroethylene composites. *Tribology International.* 2016;104: 392–401.
60. Wang L, Wang S, Wen D, Wang G, Yang L. The study of the composite material Go/CF/PTFE tribological property. *MATEC Web of Conferences.* 2017;130: 09005.
61. Негров ДА, Еремин ЕН, Корусенко ПМ, Несов СН. Влияние ультразвуковой активации на структурообразование политетрафторэтилена, модифицированного нитридом бора. *Омский научн. вестник. Сер. Авиац.-ракетн. и энергетич. машиностроение.* 2017;1(2): 57–63. (Negrov DA, Eremin EN, Korusenko PM, Nesov SN. Effect of ultrasonic activation on the structure formation of polytetrafluoroethylene modified with boron nitride. *Omsk Scientific Bulletin. Aviation, missile and power engineering series*. 2017;1(2): 57–63. (In Russian))
62. Машков ЮК, Рубан АС, Рогачев ЕА, Чемисенко ОВ. Изменение структуры и износостойкости ПТФЭ-нанокомпозитов при различных методах структурной модификации. *Динамика систем, механизмов и машин.* 2017;5(2): 188–193. (MashkovYuK, Ruban AS, Rogachev EA, Chemisenko OV. Changes in the structure and wear resistance of PTFE nanocomposites with various methods of structural modification. *Dynamics of systems, mechanisms and machines*. 2017;5(2): 188–193. (In Russian))
63. Машков ЮК, Кургузова ОА, Рубан АС. Разработка и исследование износостойких полимерных материалов. *Вестник СибАДИ*. 2018;15(1): 36–45. (MashkovYuK, Kurguzova OA, Ruban AS. Development and research of wear-resistant polymer materials. *SibADI Bulletin*. 2018;15(1): 36–45. (In Russian))
64. Чемисенко ОВ. *Структура и свойства нанокомпозита на основе политетрафторэтилена, модифицированного диоксидом кремния и скрытокристаллическим графитом. Диссертация, к.т.н.* Омск; 2018. (Chemisenko OV. *Structure and properties of a nanocomposite based on polytetrafluoroethylene modified with silicon dioxide and cryptocrystalline graphite*. Omsk; 2018. (In Russian))
65. Okhlopkova AA, Sleptsova SA. Influence of Nanoceramics on the Properties of Polytetrafluoroethylene. *Mechanics of Composite Materials.* 2003;39: 123–128.
66. Okhlopkova AA, Sleptsova SA, Parnikova AG, Ul'yanova TM, Kalmychkova OY. Triboengineering and physicomechanical properties of nanocomposites based on PTFE and aluminum oxide. *Journal of Friction and Wear.* 2008;29:466–469.
67. Sleptsova SA, Afanas'eva ES, Grigor'eva VP. Structure and tribological behavior of polytetrafluoroethylene modified with layered silicates. *J. Frict. Wear.* 2009;30: 431–437.
68. Gogoleva OV, Okhlopkova AA, Petrova PN. Development of self-lubricating antifriction materials based on polytetrafluoroethylene and modified zeolites. *Journal of Friction and Wear.* 2014;35: 383–388.
69. Kirillina YV, Lazareva NN, Sleptsova SA, Okhlopkova AA. Effect of organomodified layered silicates on the properties and structure of polytetrafluoroethylene. *Polym. Sci. Ser. A.* 2016;58: 95–101.
70. Охлопкова АА, Стручкова ТС, Алексеев АГ, Васильев АП. Разработка и исследование полимерных композиционных материалов на основе активации политетрафторэтилена и углеродных наполнителей. *Вестник СВФУ.* 2015;4(48): 51–63. (Okhlopkova AA, Struchkova TS, Alekseev AG, Vasil'ev AP. Development and research of polymer composite materials based on the activation of polytetrafluoroethylene and carbon fillers. *NEFU Bulletin*. 2015;4(48): 51–63. (In Russian))
71. Okhlopkova AA, Struchkova TS, Vasilev AP, Alexeev AG. Studying the properties and structure of polytetrafluoroethylene filled with Belum modified carbon fibers. *Journal of Friction and Wear.* 2016;37: 529–534.
72. Васильев АП, Охлопкова АА, Стручкова ТС, Алексеев АГ, Иванова ЗС. Разработка антифрикционных материалов на основе политетрафторэтилена с углеродными волокнами. *Вестник СВФУ*. 2017;59(3): 39–47. (Vasil'ev AP, Okhlopkova AA, Struchkova TS, Alekseev AG, Ivanova ZS. Development of antifriction materials based on polytetrafluoroethylene with carbon fibers. *NEFU Bulletin*. 2017;59(3): 39–47. (In Russian))
73. Sleptsova SA, Kapitonova YV, Lazareva NN, Makarov MM. Wear-resistant polymer composites based on polytetrafluoroethylene and layered silicates. *KnE Materials Science.* 2016;2016: 149–154.
74. Sleptsova SA, Okhlopkova AA, Kapitonova IV, Lazareva NN, Makarov MM, Nikiforov LA. Spectroscopic study of tribooxidation processes in modified PTFE. *Journal of Friction and Wear.* 2016;37: 129–135.
75. Sleptsova SA, Lazareva NN, Fedoseeva VI, Kapitonova YV, Okhlopkova AA. The Influence of Metal Cations of Mechanoactivated Bentonite on Tribochemical Processes in PTFE. *Journal of Friction and Wear.* 2018;39(6): 469–475.
76. Лазарева НН. *Разработка триботехнических материалов на основе политетрафторэтилена и механоактивированных слоистых силикатов Дис. канд. техн. наук.* Якутск, 2019. (Lazareva NN. *Development of tribological materials based on polytetrafluoroethylene and mechanically activated layered silicates*. Yakutsk; 2019. (In Russian))

77. Vasilev AP, Struchkova TS, Nikiforov LA, Okhlopkova AA, Grakovich PN, Shim EL, Cho JH. Mechanical and tribological properties of polytetrafluoroethylene composites with carbon fiber and layered silicate fillers. *Molecules.* 2019;24(2): 224.
78. Gladkina NP, Sleptsova SA, Fedoseeva VI, D'yakonov AA. Effect of Silica Modified with Aluminum Ions on the Structure and Properties of Composite Materials Based on Polytetrafluoroethylene. *Polymer Science, Series A.* 2022;64(3):187–193.
79. Kapitonova IV, Lazareva NN, Tarasova PN, Okhlopkova AA, Laukkanen S, Mukhin VV. Morphology analysis of friction surfaces of composites based on PTFE and layered silicates. *Polymers.* 2022;14(21): 4658.
80. Kapitonova IV, Tarasova PN, Okhlopkova AA, Lazareva NN, Khokhlov AV. Frictional Properties and Wear of Composites Based on PTFE/Layered Silicates. *Tribology Online.* 2023;18(2): 10–17.
81. Ushkanov AA, Sleptsova SA, Okhlopkova AA, Lazareva NN, Khokhlov AV, Gorohova SV, Ammosova AP. The influence of basalt fiber on the properties and structure of composites based on polytetrafluoroethylene. *Composites andNanostructures.* 2022;14(2): 117–129.
82. Obvintsev AYu, Serov SA, Sadovskaya NV, Khatipov SA, Bouznik VM. Mechanism of the Effect of Gamma Irradiation on the Surface Properties of Polytetrafluoroethylene. *J. Surf. Investig.* 2018;12: 988–993.
83. Campbell KL, Sidebottom MA, Atkinson CC, Babuska TF, Kolanovic CA, Boulden BJ, Junk CP, Krick BA. Ultralow Wear PTFE-Based Polymer Composites—The Role of Water. *Macromolecules.* 2019;52(14): 5268–5277.
84. Sedakova EB, Kozyrev YP. Estimation of the Tribotechnical Efficiency of Polytetrafluoroethylene Filling (review). *Journal of Machinery Manufacture and Reliability.* 2021;50(3): 236–242.
85. Barylski A, Swinarew AS, Aniołek K, Kaptacz S, Gabor J, Stanula A, Waśkiewicz Z, Knechtle B. Tribological and Mechanical Behavior of Graphite Composites of Polytetrafluoroethylene (PTFE) Irradiated by the Electron Beam. *Polymers.* 2020;12(8): 1676.
86. Luo C, Pei J, Zhuo W, Niu Y, Li G. Phase transition behavior and deformation mechanism of polytetrafluoroethylene under stretching. *RSC Advances.* 2021;11(63): 39813–39820.
87. Khokhlov AV. Two-sided estimates for the relaxation function of the linear theory of heredity via the relaxation curves during the ramp-deformation and the methodology of identification. *Mechanics of Solids.* 2018;53(3): 307–328.
88. Хохлов АВ. Общие свойства показателя скоростной чувствительности диаграмм деформирования, порождаемых линейной теорией вязкоупругости, и существование максимума у его зависимости от скорости. *Вестник Самарского гос. техн. ун-та. Сер. Физ.-мат. науки.* 2020;24(3): 469–505. (Khokhlov AV. Properties of the strain rate sensitivity function produced by the linear viscoelasticity theory and existence of its maximum with respect to strain and strain rate. *J. Samara State Tech. Univ., Ser. Phys. Math. Sci.* 2020;24(3): 469–505. (In Russian))
89. Хохлов АВ. Анализ общих свойств кривых ползучести при циклических ступенчатых нагружениях, порождаемых линейной теорией наследственности. *Вестник Самарского гос. техн. ун-та. Сер. Физ.-мат. науки.* 2017;21(2): 326–361. (Khokhlov AV. Analysis of creep curves produced by the linear viscoelasticity theory under cyclic stepwise loadings. *J. Samara State Tech. Univ., Ser. Phys. Math. Sci.* 2017;21(2): 326–361. (In Russian))
90. Хохлов АВ. Анализ влияния объемной ползучести на кривые нагружения с постоянной скоростью и эволюцию коэффициента Пуассона в рамках линейной теории вязкоупругости. *Вестник Самарского гос. техн. ун-та. Сер. Физ.-мат. науки.* 2019;23(4): 671–704. (Khokhlov AV. Analysis of the bulk creep influence on stress-strain curves under tensile loadings at constant rates and on Poisson's ratio evolution based on the linear viscoelasticity theory. *J. Samara State Tech. Univ., Ser. Phys. Math. Sci.* 2019;23(4): 671–704. (In Russian))
91. Khokhlov AV. Creep and long-term strength of a laminated thick-walled tube of nonlinear viscoelastic materials loaded by external and internal pressures. *Mechanics of Composite Materials.* 2021;57(6): 731–748.
92. Хохлов А.В. Особенности поведения вязкоупругопластических материалов, модели и система программ квазистатических испытаний полимеров и композитов для комплексного изучения их свойств и выбора и идентификации определяющих соотношений. *Высокомолекулярные соединения.* 2024;66(3): 157–211. (Khokhlov AV. The Main Features of Viscoelastoplastic Materials Behavior, Models, and the System of Quasi-static Tests for Polymers and Composites aimed at All-round Study of Their Properties and Selection and Identification of Constitutive Relation. *Polymer Science.* 2024;66(3): 157–211. (In Russian))
93. Khokhlov AV, Gulin VV. Influence of Structural Evolution and Load Level on the Properties of Creep and Recovery Curves Generated by a Nonlinear Model for Thixotropic Viscoelastoplastic Media. *Phys Mesomech.* 2025;28: 66–90.
94. Kitamura T, Okabe S, Tanigaki M, Kurumada KI, Ohshima M, Kanazawa SI. Morphology change in polytetrafluoroethylene (PTFE), porous membrane caused by heat treatment. *Polymer Engineering & Science.* 2000;40(3): 809–817.
95. Brown EN, Dattelbaum DM. The role of crystalline phase on fracture and microstructure evolution of polytetrafluoroethylene (PTFE). *Polymer.* 2005;46(9): 3056–3068.

MATERIALS PHYSICS AND MECHANICS

53 (4) 2025

УЧРЕДИТЕЛИ

Санкт-Петербургский политехнический университет Петра Великого
Адрес: 195251, Санкт-Петербург, Политехническая ул., д. 29

Институт проблем Машиноведения Российской академии наук
Адрес: 199178, Санкт-Петербург, Большой пр-кт В.О., д. 61

ИЗДАТЕЛЬ

Санкт-Петербургский политехнический университет Петра Великого
Адрес: 195251, Санкт-Петербург, Политехническая ул., д. 29

Журнал зарегистрирован в Федеральной службе по надзору в сфере связи, информационных технологий и массовых коммуникаций (РОСКОМНАДЗОР), свидетельство ПИ №ФС77-69287 от 6 апреля 2017 года.

АДРЕС И ТЕЛЕФОН РЕДАКЦИИ

199178, Санкт-Петербург, Большой пр-кт В.О., д. 61

Тел. редакции: +7(812)552 77 78, доб. 224

E-mail редакции: mpmjournal@spbstu.ru

Компьютерная верстка Л.И. Гузилова

Подписано в печать 31.11.2025 г. Выход в издания в свет: 26.12.2025 г.
Формат 60x84/8. Печать цифровая
Усл. печ. л. 10,0. Тираж 100. Заказ___.
Цена: Бесплатно

Отпечатано в **Издательско-полиграфическом центре Политехнического университета Петра Великого**
Адрес: 195251, Санкт-Петербург, Политехническая ул., 29
Тел.: +7(812)552 77 17

MPM SCIENTIFIC JOURNAL

MPM, Vol. 53, No. 4, 2025